Imperial College London

The Impact Behaviour of High Performance Fibre Composites

by

Syed Idros Bin Syed Abdullah

Department of Aeronautics
Imperial College London
South Kensington Campus
London SW7 2AZ
United Kingdom

This thesis is submitted for the degree of Doctor of Philosophy
October 2018

For my parents
Syed Abdullah bin Syed Mohamed
Rugayah binti Syed Ali

"A man can do all things if he wills"

Leon Battista Alberti (1404-1472)

Abstract

The use of composite materials as structural reinforcements has increased significantly throughout the years. In aircraft structures, composite materials have replaced conventional materials such as aluminium to more than 50% of the aircraft's total mass. The advantages of composite materials include a high strength-to-weight ratio, and corrosion resistance. This has attracted designers to utilise these materials to enable a more cost-effective design, without compromising the aircraft's structural integrity. However, composite materials are highly vulnerable to transvere impact loading. The need to improve their impact resistance is essential to achieve a more reliable and safer design.

The research presented in this PhD aims to investigate the impact performance of laminated composites, both in low and high velocity regimes. The investigation involves impact loading on three different fibre composites, namely Carbon fibre (IM7), Glass fibre (S2-Glass), and Thermotropic Liquid Crystal Polymer (Vectran), in a thermosetting epoxy matrix. Prior to this, all three laminates were characterised to obtain their in-plane mechanical properties, as well as the Mode I and II interlaminar fracture toughness. For the Vectran composite, the Mode I translaminar (fibre tensile) response was characterised to obtain its strain energy release rate, G_c, as well as understanding the complex failure mechanisms which contributes to its fracture toughness. All experimentally obtained properties were used for numerical modelling using the non-linear explicit Finite Element Method (FEM) software, LS-Dyna. Finally, an energy-based plane-stress User MATerial (UMAT) model was developed for the Vectran composite. The UMAT was used to simulate the in-plane, as well as the low and high velocity impact response of the Vectran composite. For carbon and glass composites, the commercially available energy-based material model in LS-Dyna was utilised to numerically reproduce the experimentally obtained impact response.

Declaration of Originality

The work presented hereafter is based on research carried out by the author at the Department of Aeronautics of Imperial College London and it is all the author's own work except where otherwise acknowledged. No part of the present work has been submitted elsewhere for another degree or qualification

Syed Idros Bin Syed Abdullah

Copyright Declaration

The copyright of this thesis rests with the author and is made available under a Creative Commons Attribution Non-Commercial No Derivatives licence. Researchers are free to copy, distribute or transmit the thesis on the condition that they attribute it, that they do not use it for commercial purposes and that they do not alter, transform or build upon it. For any reuse or redistribution, researchers must make clear to others the licence terms of this work.

Contents

1 Introduction **1**

1.1 Background 1

1.2 Motivation and objectives 3

1.3 Thesis outline 5

1.4 Publications 6

2 Literature Review **7**

2.1 Introduction 7

2.2 Impact on Composite Structures 8

2.2.1 Polymer fibre composites under impact 13

2.3 Modelling impact on composite structures 18

2.3.1 Modelling damage 22

2.3.2 Modelling delamination 24

2.4 Summary 29

3 Material Characterisation **31**

3.1 Introduction 31

3.2 Data Reduction 32

3.2.1 Tension 32

3.2.2 Compression 33

3.2.3 $\pm 45^{\circ}$ In-plane shear 33

3.3 Manufacturing 34

3.4 Testing 36

3.5 Results 37

3.5.1 Tensile response . . . 37
3.5.2 Compressive response . . . 42
3.5.3 ±45° In-plane shear response . . . 46
3.6 Summary of the in-plane characterisation for all composite materials . . 50
3.7 Determination of the fibre volume fraction . . . 50
3.7.1 Introduction . . . 50
3.7.2 Procedure . . . 51
3.8 Interlaminar fracture toughness . . . 54
3.8.1 Data Reduction . . . 56
3.8.2 Manufacturing . . . 57
3.8.3 Testing . . . 59
3.8.4 Results . . . 59
3.8.5 On Fractography . . . 66
3.9 Summary . . . 70

4 Translaminar Fracture Toughness of Vectran Composite 72

4.1 Introduction . . . 72
4.2 Specimen design . . . 73
4.2.1 Design development in Finite Element . . . 75
4.2.2 Specimen manufacturing . . . 77
4.3 Test method and experimental setup . . . 78
4.4 Data reduction . . . 79
4.4.1 ASTM E399 . . . 79
4.4.2 Area method . . . 80
4.4.3 Compliance calibration . . . 81
4.4.4 Fibre tensile failure . . . 82
4.5 Results . . . 83
4.5.1 Specimen inspection . . . 83
4.5.2 Test results . . . 85
4.6 Discussions . . . 86
4.6.1 Fibre-matrix de-bonding . . . 88

4.6.2 Fibre pull-out . . . 89
4.6.3 Vectran fibre failure . . . 90
4.6.4 Fibre-bridging phenomenon . . . 91
4.7 Summary . . . 92

5 The Impact Response of Composite Laminates 94
5.1 Introduction . . . 94
5.2 Laminate manufacturing . . . 95
5.3 Experimental procedure . . . 96
5.3.1 Low Velocity Impact . . . 96
5.3.2 High Velocity Impact . . . 96
5.4 Results . . . 101
5.4.1 Low Velocity Impact . . . 101
5.4.2 High Velocity Impact . . . 119
5.4.3 On delamination . . . 125
5.5 Discussions . . . 142
5.5.1 Energy absorption . . . 142
5.5.2 Damage types . . . 145
5.5.3 Delamination . . . 146
5.6 Summary . . . 147

6 An Energy-Based Damage Model for Vectran Composite 149
6.1 Introduction . . . 149
6.2 Vectran fibres . . . 150
6.3 Governing equations . . . 151
6.3.1 Effective stress-strain relationship . . . 151
6.3.2 Stress-strain-damage relationship . . . 153
6.3.3 Damage propagation . . . 156
6.3.4 Mesh dependency . . . 164
6.4 Model validation . . . 166
6.4.1 Model set-up . . . 166

6.4.2 Tension . . . 167
6.4.3 Compression . . . 169
6.4.4 ±45° In-plane shear . . . 170
6.5 Discussions . . . 173
6.5.1 Tensile behaviour . . . 173
6.5.2 Compressive behaviour . . . 173
6.5.3 ±45° In-plane shear . . . 173
6.5.4 Mesh dependency . . . 174
6.6 Summary . . . 174

7 Modelling the impact response of composite laminates 175
7.1 Introduction . . . 175
7.2 FEM model set-up . . . 176
7.2.1 Element type and boundary conditions . . . 176
7.2.2 Material models . . . 177
7.2.3 Cohesive algorithm . . . 178
7.2.4 Mesh sensitivity study . . . 179
7.2.5 Delamination sensitivity analysis . . . 182
7.3 Results . . . 184
7.3.1 Low velocity impact . . . 184
7.3.2 High velocity impact . . . 206
7.4 Discussion . . . 215
7.4.1 Permanent indentation . . . 215
7.4.2 Strain-rate effects . . . 216
7.4.3 Delamination . . . 217
7.4.4 Numerical accuracy . . . 218
7.5 Summary . . . 221

8 Further Discussions 223
8.1 Introduction . . . 223
8.2 Key research areas . . . 224

8.2.1 Material characterisation 224
8.2.2 Translaminar fracture toughness of Vectran fibre composites . . . 226
8.2.3 Impact performance of composite materials 226
8.2.4 Development of a plane-stress material model for Vectran/MTM57 228
8.2.5 Numerical modelling of impact loading 229

9 Conclusion and Future Work 231

9.1 Introduction 231
9.2 Conclusion 231
9.3 Future work 234
9.4 Potential application of Vectran fibres 235

Appendix:

A New Sabot Stripper Design 259

B Analytical prediction on the ballistic limit 265

C Flowchart of LS-Dyna implementation 267

List of Figures

1.1 Percentage use of composite materials for the past 30 years 2

2.1 Response types for impacted composite structures 9
2.2 (a) Pine tree pattern (b) Reversed pine tree pattern 10
2.3 Types of matrix failure (a) Tensile crack (b) Shear crack 11
2.4 (a) Load-displacement response for laminates subjected to impact loads of 1.55 J - no damage (b) Load-time response of laminates subjected to 6.24 J of damage - delamination damage 11
2.5 (a) Variation of damage in low velocity impact loading (b) Peanut-shaped delamination with respect to fibre orientation 12
2.6 Speed of sound versus mass-based energy absorption capacity for a number of high performance fibres based on Cuniff velocity, U^*. Red contours represent U^* 14
2.7 Alternative softening laws for fibre tension and compression failures (a) Bi-linear softening law (b) Exponential softening law 19
2.8 Calculation of l_c from different approaches (a) Geometrical (b) Element shape function (isoparametric coordinates) 21
2.9 RUV of the CF/Epoxy laminate (a) Optical micrograph of the fibre arrangement (b) The Hexagonal RUV model 23
2.10 (a) The modified unit cell model (b) The idealised geometry unit cell . . 24
2.11 The VCCT method 25
2.12 The Floating Node Method 26

2.13 (a) R-curve with an increasing trend (b) Illustration of fibre-bridging in a Double Cantilever Beam (DCB) specimen 28

3.1 Typical cutting plans for quasi-static in-plane characterisation (a) Tensile. [1] denotes longitudinal tensile, and [2] denotes transverse and orthotropic tensile (b) Compression (c) ±45 °In-plane shear. Close up image showing the width of the water jet cutting line 35
3.2 Typical specimen schematic (a) Top view (b) Side view 36
3.3 Average tensile stress-strain response for each of the composite material 37
3.4 Tensile strength for all three composite laminates. Error bars represent the variation of tensile strength between five specimens 38
3.5 Failed longitudinal (0 °) IM7/8552 tensile specimens (a) Top view (b) Side view 39
3.6 Failed transverse (90 °) IM7/8552 tensile specimens 39
3.7 (a) Typical failed S2-Glass/MTM57 tensile specimens (b) Close up view of on the white square in (a) 40
3.8 (a) Typical failed Vectran/MTM57 tensile specimens (b) Close up view of on the white square in (a) 41
3.9 Average compressive stress-strain response from each fibre reinforced composite used 42
3.10 Defibrillation in Vectran (a) Defibrillation in a single fibre under tensile loading (b) Defibrillation in a laminate under ±45 ° in-plane shear loading 43
3.11 (a) Typical failed Vectran/MTM57 compressive specimens (b) Close up image on the failure region shown in (a) - bottom (c) Close up image on the failure region shown in (a) - top 43
3.12 Compressive strength for all three composite laminates. Error bars represent the variation of compressive strength between five specimens . . . 44
3.13 Typical failed IM7/8552 longitudinal (0 °) compressive specimens 45
3.14 (a) Failed IM7/8552 transverse (90 °) compressive specimens (b) Close up image on the failure region shown in (a) - top 45

3.15 (a) Failed S2-Glass/MTM57 compressive specimens (b) Close up image on the failure region shown in (a) - top 46
3.16 Average ±45° in-plane shear response from each fibre reinforced composite 46
3.17 ±45° In-plane strength for all three composite laminates. Error bars represent the variation of shear strength between five specimens 47
3.18 (a) Failed ±45° in-plane shear IM7/8552 specimens (b) Close up image on the failure region shown in (a) - top 48
3.19 (a) Failed ±45° in-plane shear Vectran/MTM57 specimens (b) Close up image on the failure region in specimen 3 49
3.20 (a) Failed ±45° in-plane shear S2-Glass/MTM57 specimens (b) Close up image on the failure region in specimen 3 49
3.21 Typical optical images of the composite laminates used in FVF determination (a) IM7/8552 (b) S2-Glass/MTM57 (c) Vectran/MTM57 52
3.22 Illustration of the cut NCF fabric used for FVF measurement (a) Vectran (b) S2-Glass 53
3.23 Mode I test specimens 55
3.24 Mode II test specimens 55
3.25 Schematic of the Mode I and Mode II specimens (a) Illustration of the plate for Mode I and Mode II specimen (b) DCB (c) 4ENF. For S2-Glass/MTM57, a monolithic sequence is used instead 57
3.26 Cured T800s/M21/Vectran/MTM57 hybrid specimen 58
3.27 Radiograph images of the failed DCB and 4ENF specimens for S2-Glass/MTM57 and T800s/M21/Vectran/MTM57 hybrid composites 60
3.28 Mode I load-displacement response for all five S2-Glass/MTM57 specimens 61
3.29 Flatbed scan view of the delaminated area of S2-Glass/MTM57 61
3.30 Mode I resistance curve for all five S2-Glass/MTM57 specimens 62
3.31 Mode I load-displacement response for all five Vectran/MTM57 specimens 63
3.32 Mode I resistance curve for all five Vectran/MTM57 specimens 63
3.33 Mode II load-displacement response for all five S2-Glass/MTM57 specimens 64
3.34 Mode II resistance curve for all five S2-Glass/MTM57 specimens 64

3.35 Mode II load-displacement response for all five Vectran/MTM57 specimens 65
3.36 Mode II resistance curve for all five Vectran/MTM57 specimens 65
3.37 SEM image on S2-Glass/MTM57 fracture surface showing (a) Crack growth morphology before a stitch (b) Crack growth morphology after the stitch. Note the presence of a broken fibre end due to fibre-bridging. Dotted lines indicate riverlines 66
3.38 SEM images on Vectran/MTM57 fracture surface (a) Fibrils on Vectran/MTM57 fracture surface (b) SEM image around the specimen insert (c) Close up image of the black square in Figure 3.38b. Dashed lines represent riverlines (d) Fibre-bridging seen on Vectran/MTM57 DCB specimen 67
3.39 Visual appearance of cusps under the Scanning Electron Microscope (SEM) 68
3.40 Fracture surface of S2-Glass under mode II loading. White arrows indicate large-sized cusps whilst yellow arrows indicate smaller-sized cusps. Crack growth direction is shown in black 69
3.41 Fracture surface of Vectran/MTM57 under Mode II loading. Yellow arrows indicate cusps. Crack growth direction is shown in black 70

4.1 Possible failure locations of conventional Compact Tension (CT) specimen 73
4.2 Schematic of the individual/final parts in the current Compact Tension (CT) specimen design 74
4.3 CT specimen modelled with LS-Dyna, utilising symmetry. Contours represent the out-of-plane displacement (units in mm). Small dark triangles represent the 'tiebreak' contact used in the simulation 76
4.4 Final FEM results for Vectran/MTM57 CT specimen (a) Tension and compression. Contour represents tensile and compressive strength (b) $\pm 45^\circ$ In-plane shear. Contour represent $\pm 45^\circ$ in-plane shear strength. All units are in kN/mm^2 77
4.5 Lay-up process for Vectran/MTM57 CT specimen manufacture 78
4.6 (a) Vectran/MTM57 CT specimen used during testing. (b) Close up image from the white square shown in (a). Note the residual floss produced after using the diamond saw cutter 79

4.7 The area method 80
4.8 Typical compliance versus crack length curve obtained from the CC method 81
4.9 Representative unit cell for Vectran/MTM57 82
4.10 Radiograph images of tested Vectran/MTM57 CT specimen (a) Front view (b) Top view. The delamination failure occured before experimental testing 84
4.11 Load-displacement response for Vectran/MTM57, including IM7/8552 for comparison purposes 85
4.12 R-curve deduced by area method for all three Vectran/MTM57 specimens 85
4.13 R-curve deduced by the CC method for all three Vectran/MTM57 specimens 86
4.14 R-curve deduced by the MCC method using FEM. Also shown are the representative of AM and CC method for comparison 86
4.15 Evidence of fibre-matrix de-bonding present on the fracture surface of Vectran/MTM57 CT specimen (a) Fracture surface of Vectran/MTM57 showing multiple fibre pull-out with varying lengths indicated by yellow arrrows. (b) Close-up image of the white square in (a) showing fibre-matrix debonding 88
4.16 Evidence of shear cusps on the fibres (a) multiple cusps seen across the fibre indicated by white arrows (b) Close up image of the shear cusps shown by the black arrow 90
4.17 (a) Skin-core morphology of Vectran showing the path of failure beginning with failure at the skin which then propagates to the core (b) Close-up image on Vectran fibres 91
4.18 Fibre-bridging development on Vectran/MTM57 CT specimen (a) a=12 mm: Fibre-bridging phenomenon can be slightly observed (b) a=17 mm: Fibre-bridging phenomenon fully visible, with evidence of fibre pull-off in the wake of the crack 92

5.1 Typical impact specimen dimensions 96
5.2 (a) Instron 9350 drop tower. Blue square represents close up image in (b) 97

5.3 Illustration of the 'wrap-around' type breech system employed in the gas gun in this study. (a) Before firing sabot is held in place (b) Upon firing, pressure is released into the main barrel via the annular ports to propel the sabot (and projectile 97
5.4 HVI testing setup (top view) 98
5.5 Velocity-pressure calibration curve 99
5.6 Load-time response for 40 J impact loading of all three impacted S2-Glass/MTM57 laminates 102
5.7 Load-deflection response for 40 J impact loading of all three impacted S2-Glass/MTM57 laminates 103
5.8 Load-time response for 40 J impact loading of all three impacted Vectran/MTM57 laminates 103
5.9 Load-deflection response for 40 J impact loading of all three impacted Vectran/MTM57 laminates 103
5.10 Load-time response for 40 J impact loading of all three impacted IM7/8552 laminates. 'DTL' indicates the Delamination Threshold Load 104
5.11 Load-deflection response for 40 J impact loading of all three impacted IM7/8552 laminates.'DTL' indicates the Delamination Threshold Load . 104
5.12 (a) Cross-sectional view of Vectran/MTM57 laminate under 40 J impact. (b) Optical micrograph of the black square shown in (a). No observable damage can be seen on the laminate cross-section 105
5.13 (a) Cross-sectional view of S2-Glass/MTM57 laminate under 40 J impact. (b) Optical micrograph of the black square shown in (a) (c) Close up view of the black square in (b) showing kink-bands and intralaminar damage inidicating compressive and matrix failure 106
5.14 (a) Cross-sectional view of IM7/8552 laminate under 40 J impact showing multiple damage types (b) Close-up view on the vicinity of impact showing matrix and fibre failure, as well as delamination 107
5.15 Load-time response for 100 J impact loading of all three impacted S2-Glass/MTM57 laminates 108

5.16 Load-deflection response for 100 J impact loading of all three impacted S2-Glass/MTM57 laminates 109
5.17 Load-time response for 100 J impact loading of all three impacted Vectran/MTM57 laminates 109
5.18 Load-deflection response for 100 J impact loading of all three impacted Vectran/MTM57 laminates 109
5.19 Load-time response for 100 J impact loading of all three impacted IM7/8552 laminates 110
5.20 Load-deflection response for 100 J impact loading of all three impacted IM7/8552 laminates 110
5.21 (a) Cross-sectional view of S2-Glass/MTM57 laminate under 100 J impact (b) Close-up view showing intralaminar and fibre failure 111
5.22 (a) Cross-sectional view of Vectran/MTM57 laminate under 100 J impact showing permanent indentation (b) Optical micrograph of the black square shown in (a) 112
5.23 (a) Cross-sectional view of IM7/8552 laminate under 100 J impact. (b) Optical micrograph of the white square shown in (a) showing delamination and fibre failure at every ply 113
5.24 Load-time response for 160J impact loading of all three impacted S2-Glass/MTM57 laminates 114
5.25 Load-deflection response for 160J impact loading of all three impacted S2-Glass/MTM57 laminates 115
5.26 Load-time response for 160J impact loading of all three impacted Vectran/MTM57 laminates 115
5.27 Load-deflection response for 160J impact loading of all three impacted Vectran/MTM57 laminates 115
5.28 Load-time response for 160J impact loading of all three impacted IM7/8552 laminates 116
5.29 Load-deflection response for 160 J impact loading of all three impacted IM7/8552 laminates 116

5.30 (a) Cross-sectional view of S2-Glass/MTM57 laminate after 160 J impact. (b) Optical micrograph of the black square shown in (a) showing extensive fibre failure at every ply 117
5.31 (a) Cross-sectional view of Vectran/MTM57 laminate under 160 J impact. (b) Optical micrograph showing extensive fibre failure at every ply . . . 118
5.32 (a) Cross-sectional view of IM7/8552 laminate under 160 J impact. (b) Optical micrograph of the white square shown in (a) showing extensive delamination, intralaminar failure, and delamination at every ply 119
5.33 Ballistic curve for all three materials used in this study 120
5.34 Montage of HVI events on Vectran/MTM57 at 171.2 m/s (a) Before impact (b) During impact (c) Partial penetration (d) penetrated. White arrow indicates projectile 121
5.35 Montage of HVI events on S2-Glass/MTM57 at 183.08 m/s (a) Before impact (b) During impact (c) Partial penetration (d) Penetrated. White arrow indicates projectile 121
5.36 Montage of HVI events on IM7/8552 at 115.75 m/s (a) Before impact (b) During impact (c) Partial penetration (d) Penetrated. White arrow indicates projectile 121
5.37 Cross-sectional view of S2-Glass/MTM57 under HVI load (a) 136.19 m/s - below V_{50} (b) 137.43 m/s - close to V_{50} (c) 196.14 m/s - above V_{50}. White arrow indicates delamination whilst the black dashed line indicates fibre failure. The black arrow in (a) and (b) shows fibre failure 122
5.38 Cross-sectional view of Vectran/MTM57 under HVI load (a) 152.87 m/s - below V_{50} (b) 165.15 m/s - close to V_{50} (c) 212 m/s - above V_{50}. White arrows indicates delamination, whilst the red arrow indicates fibre failure 123
5.39 Cross-sectional view of IM7/8552 under HVI load (a) 60.25 m/s - below V_{50} (b) 79.91 m/s - close to V_{50} (c) 115.75 m/s - above V_{50}. White arrows indicates delamination, whilst the blue arrow indicates intralaminar failure 124

5.40 Cross-sectional view of an impacted Vectran/MTM57 laminate (≈ 210 m/s) under HVI loading. Note the multiple delamination extending towards the laminate boundary (shown with white arrows). Dashed lines represents penetration path 126
5.41 Typical fracture surface of IM7/8552 under low velocity impact loading. Blue arrows indicate shear cusps whilst white arrows indicate riverlines 126
5.42 Damaged S2-Glass/MTM57 specimen under 40 J of impact load (a) Front face (b) Back face (c) Radiograph image of the specimen showing matrix cracks (d) Specimen under ultrasonic C-scan 130
5.43 Damaged Vectran/MTM57 specimen under 40 J of impact load (a) Front face (b) Back face (c) Radiograph image of the specimen showing matrix cracks (d) Specimen under ultrasonic C-scan 131
5.44 Damaged IM7/8552 specimen under 40 J of impact load (a) Front face (b) Back face (c) Radiograph image of the specimen showing matrix cracks (d) Specimen under ultrasonic C-scan 132
5.45 Damaged S2-Glass/MTM57 specimen under 100 J of impact load (a) Front face (b) Back face (c) Radiograph image of the specimen showing matrix cracks (d) Specimen under ultrasonic C-scan 133
5.46 Damaged Vectran/MTM57 specimen under 100 J of impact load (a) Front face (b) Back face (c) Radiograph image of the specimen showing matrix cracks (d) Specimen under ultrasonic C-scan 134
5.47 Damaged IM7/8552 specimen under 100 J of impact load (a) Front face (b) Back face (c) Radiograph image of the specimen showing matrix cracks (d) Specimen under ultrasonic C-scan 135
5.48 Damaged S2-Glass/MTM57 specimen under 160J of impact load (a) Front face (b) Back face (c) Radiograph image of the specimen showing matrix cracks (d) Specimen under ultrasonic C-scan 136
5.49 Damaged Vectran/MTM57 specimen under 160J of impact load (a) Front face (b) Back face (c) Radiograph image of the specimen showing matrix cracks (d) Specimen under ultrasonic C-scan 137

5.50 Damaged IM7/8552 specimen under 160J of impact load (a) Front face (b) Back face (c) Radiograph image of the specimen showing matrix cracks (d) Specimen under ultrasonic C-scan 138
5.51 Damaged S2-Glass/MTM57 specimen under HVI loading close to V_{50} (a) Front face (b) Back face (c) Radiograph image of the specimen showing matrix cracks (d) Specimen under ultrasonic C-scan 139
5.52 Damaged Vectran/MTM57 specimen under HVI loading close to V_{50}. Note that the specimen was split into two halves (a) Front face (b) Back face (c) Radiograph image of the specimen showing damage on the front and back face (d) Specimen under ultrasonic C-scan showing delamination on the front and back face 140
5.53 Damaged IM7/8552 specimen under HVI loading close to V_{50} (a) Front face (b) Back face (c) Radiograph image of the specimen showing matrix cracks (d) Specimen under ultrasonic C-scan 141
5.54 Average normalized absorption per unit weight for all laminates under LVI loading 142
5.55 Average normalized energy absorption per unit weight for all laminates under HVI loading 143

6.1 The three-tier model established for TLCP fibres 151
6.2 Direct stress component with unloading 156
6.3 Failure envelope for tensile and compressive direct stresses. Shaded area represents G_c. Also shown is the elastic-perfectly plastic assumption under compressive loading 158
6.4 Typical experimental compressive response for Vectran/MTM57 laminates. ϕ represents the kink-band angle 159
6.5 Cyclic and monotonic $\pm 45^\circ$ in-plane shear response for Vectran/MTM57 162
6.6 $\pm 45^\circ$ in-plane shear response including the loading and unloading behavior shown in black. Initial phase is shown in yellow, strain-hardening phase in red, and linear degradation in blue. Shaded area highlights G_c 162

6.7 Effects of strain-rate enhancement of Vectran/MTM57 ±45° in-plane shear behaviour 163
6.8 Sigmoid relation to define the shear strain-rate enhancement 163
6.9 Square specimens loaded in tension with different mesh densities. Failed elements are highlighted in red 164
6.10 Load-displacement response of specimens with different mesh densities loaded in tension 164
6.11 Unstructured mesh with different mesh densities (a) 3^2 (b) 5^2 165
6.12 Vectran NCF used in this study (a) NCF fabric (b) Schematic of the RUC 166
6.13 Progression of damage in the FEM model (top) damage band in the FEM model prior to final failure (bottom) final failure 168
6.14 Failed Vectran/MTM57 specimen under quasi-static tensile loading . . . 168
6.15 FE prediction on the tensile stress-strain response for Vectran/MTM57 169
6.16 FEM prediction on the compressive stress versus strain response for Vectran/MTM57 169
6.17 Vectran/MTM57 under quasi-static compression loading (a) FEM prediction on the damaged region (b) Failed Vectran/MTM57 specimen (c) Close-up image of the black square in (b) showing the kink-bands 170
6.18 Shear stress versus shear strain curve for Vectran/MTM57 171
6.19 Vectran/MTM57 under quasi-static ±45° in-plane shear loading (a) FEM prediction on the damaged region (b) Close-up image of the black square in (a) showing the damage bands (c) Experimental specimen 172
6.20 Comparison between experimental and FEM predicted longitudinal and transverse shear strain component versus total shear strain 172

7.1 FEM model used in the low velocity impact case 176
7.2 (a) Trilinear law to represent tensile and compressive fibre failure (b) Bilinear law to represent tensile and compressive failure in the transverse (matrix) direction. l represent the characteristic element length 178
7.3 Contact algorithm for interlaminar properties (a) Bi-linear initiation-propagation law (b) Mixed-mode I and II iinitiation-propagation law . . 179

7.4 Load-time curve for 40 J impact loading of Vectran/MTM57 using three different mesh sizes 181
7.5 Load-deflection response for 40 J impact loading of Vectran/MTM57 using three different mesh sizes 181
7.6 Load-time response for 40 J impact loading of IM7/8552 using three different mesh sizes 181
7.7 Load-deflection response for 40J impact loading of IM7/8552 using three different mesh sizes 182
7.8 Side view of the FEM model. Note that the distance between each layers is slightly increased to illustrate the placement of each cohesive surface . 182
7.9 Load-time response for 100 J impact loading of Vectran/MTM57 with varying layer of cohesive surface 183
7.10 FEM prediction on the delamination damage under 100 J loading at the middle layer (a) One cohesive layer (b) Two cohesive layer (c) Three cohesive layer 184
7.11 FEM prediction of delamination under 100 J LVI loading using three cohesive surfaces (a) Average envelope (b) Individual interface 184
7.12 FEM prediction of the load-time response for 40 J impact loading on IM7/8552 and compared with three experimental results 185
7.13 FEM prediction of the load-deflection response for 40 J impact loading on IM7/8552 and compared with three experimental results 185
7.14 FEM prediction of the load-time response for 100 J impact loading on IM7/8552 and compared with three experimental results 186
7.15 FEM prediction of the load-deflection response for 100 J impact loading on IM7/8552 and compared with three experimental results 186
7.16 FEM prediction of the load-time response for 160J impact loading on IM7/8552 and compared with three experimental results 187
7.17 FEM prediction of the load-deflection response for 160J impact loading on IM7/8552 and compared with three experimental results 187

7.18 Comparison of experimental and simulation results for 40 J impact load on IM7/8552 (a) FEM prediction of damage on the laminate back face. Contours showing the damage associated with tensile fibre failure (b) Experimental back face damage (c) FEM prediction on delamination damage (d) C-scan results 188
7.19 Comparison of experimental and simulation results for 100 J impact load on IM7/8552 (a) FEM prediction of damage on the laminate back face. Contours showing the damage associated with tensile fibre failure (b) Experimental back face damage (c) FEM prediction on delamination damage (d) C-scan results 189
7.20 Comparison of experimental and simulation results for 160J impact load on IM7/8552 (a) FEM prediction of damage on the laminate back face. Contours showing the damage associated with tensile fibre failure (b) Experimental back face damage (c) FEM prediction on delamination damage (d) C-scan results 190
7.21 FEM prediction of the load-time response for 40 J impact loading on S2-Glass/MTM57 and compared with three experimental results 192
7.22 FEM prediction of the load-deflection response for 40 J impact loading on S2-Glass/MTM57 and compared with three experimental results . . 192
7.23 FEM prediction of the load-time response for 100 J impact loading on S2-Glass/MTM57 and compared with three experimental results 192
7.24 FEM prediction of the load-deflection response for 100 J impact loading on S2-Glass/MTM57 and compared with three experimental results . . 193
7.25 FEM prediction of the load-time response for 160J impact loading on S2-Glass/MTM57 and compared with three experimental results 193
7.26 FEM prediction of the load-deflection response for 160J impact loading on S2-Glass/MTM57 and compared with three experimental results . . 193

7.27 Comparison of the simulation and experimental results for 40 J impact load on S2-Glass/MTM57 (a) FEM prediction of damage on the laminate back face (b) Experimental back face damage (c) FEM prediction on delamination damage (d) C-scan results 194
7.28 Comparison of the simulation and experimental results for 100 J impact load on S2-Glass/MTM57 (a) FEM prediction of damage on the laminate back face (b) Experimental back face damage (c) FEM prediction on delamination damage (d) C-scan results 195
7.29 Comparison of the simulation and experimental results for 160J impact load on S2-Glass/MTM57 (a) FEM prediction of damage on the laminate back face (b) Experimental back face damage (c) FEM prediction on delamination damage (d) C-scan results 196
7.30 FEM prediction of the load-time response for 40 J impact loading on Vectran/MTM57 and compared with three experimental results 197
7.31 FEM prediction of the load-deflection response for 40 J impact loading on Vectran/MTM57 and compared with three experimental results . . . 197
7.32 Impact response mechanism of Vectran/MTM57 laminates under low velocity impact loads (a) Before impact (b) During impact (c) After impact 198
7.33 Front face of Vectran/MTM57 after 40 J impact loading (a) Experimental front face damage (b) Close-up view of the permanent indentation . . . 198
7.34 FEM prediction of the load-time curve for 100 J impact loading on Vectran/MTM57 and compared with three experimental results 199
7.35 FEM prediction of the load-deflection curve for 100 J impact loading on Vectran/MTM57 and compared with three experimental results 199
7.36 Damage observed in the Vectran/MTM57 specimen under 100 J of LVI loading (a) Optical micrograph showing fibre failure (b) Predicted failure in the FEM model including fibre failure and delamination. Contours representing fibre tensile damage 200

7.37 Damage observed in the Vectran/MTM57 specimen under 160 J of LVI loading (a) Optical micrograph showing extensive fibre failure at every ply (b) Damage prediction from the FEM model showing complete penetration. Contours representing fibre tensile damage 201
7.38 FEM prediction of the load-time curve for 160J impact loading on Vectran/MTM57 and compared with three experimental results 202
7.39 FEM prediction of the load-deflection curve on for 160J impact loading on Vectran/MTM57 and compared with three experimental results . . . 202
7.40 Comparison of the simulation and experimental results for 40 J impact load on Vectran/MTM57 (a) FEM prediction of damage on the laminate back face (b) Experimental back face damage (c) FEM prediction on delamination damage (d) C-scan results 203
7.41 Comparison of the simulation and experimental results for 100 J impact load on Vectran/MTM57 (a) FEM prediction of damage on the laminate back face (b) Experimental back face damage (c) FEM prediction on delamination damage (d) C-scan results 204
7.42 Comparison of the simulation and experimental results for 160J impact load on Vectran/MTM57 (a) FEM prediction of damage on the laminate back face (b) Experimental back face damage (c) FEM prediction on delamination damage (d) C-scan results 205
7.43 Impact versus residual velocity for FEM predictions and experimental measurements for IM7/8552 206
7.44 HVI events on IM7/8552 at $V_i \approx 115$ m/s. (a) - (d) Experimental HVI events (e) - (h) FEM predictions. Black arrow showing projectile 207
7.45 Comparison of damage on IM7/8552 laminate under ≈ 92 m/s impact velocity. The black arrows represent ply-splitting whilst the red arrow represents fibre fracture. Contours represents fibre damage. (a) FEM prediction (b) Experimental specimen (c) FEM delamination prediction (d) C-scan results 208

7.46 Impact versus residual velocity for FEM predictions and experimental measurements for S2-Glass/MTM57 209
7.47 HVI events on S2-Glass/MTM57 at ≈ 183 m/s. (a) - (d) Experimental HVI events (e) - (h) FEM predictions. Black arrow showing ply-splitting 210
7.48 Comparison of damage on IM7/8552 laminate under ≈ 92 m/s impact velocity. White arrows represent ply-splitting whilst blue arrow represents fibre fracture. Contours represents fibre damage. (a) FEM prediction (b) Experimental Vectran/MTM57 specimen (c) FEM delamination prediction (d) C-scan results 211
7.49 Impact versus residual velocity for FEM predictions and experimental measurements for Vectran/MTM57 212
7.50 HVI events on Vectran/MTM57 at ≈ 170 m/s. (a) - (d) Experimental HVI events (e) - (h) FEM predictions. Black arrow showing ply-splitting 213
7.51 Comparison of damage on Vectran/MTM57 laminate under ≈ 170 m/s impact velocity. Black arrows represent matrix damage. Contours representing shear strain. White arrow represent penetration/fibre failure (a) FEM prediction (b) Experimental Vectran/MTM57 specimen (c) FEM delamination prediction (d) C-scan results 214
7.52 A comparison between the average normalized absorbed energy for all laminates under LVI loading - FEM versus experiments 219
7.53 Illustration of the bi-linear approach using MAT262 for the ±45 ° in-plane shear response of IM7/8552 220
7.54 Average normalized energy absorption per unit weight under HVI loading between the FEM and experimental results 220
7.55 A comparison between the average normalized peak load for all laminates under LVI loading - FEM versus experiments 221

A.1 Velocity-Pressure calibration curve. Note the change in velocity with respect to pressure with different sabot material 260
A.2 Complete schematic of the modified sabot catcher 261
A.3 Main Frame 262

A.4 Disc Frame 263

A.5 Sabot 264

C.1 Flowchart illustrating the implemented UMAT into LS-Dyna explicit. t_n represents the current time, t_f represents the termination (final) time, and $\varepsilon_{t,c}$ represents the strain under tension and compression, respectively 268

List of Tables

2.1 Cuniff velocity for chosen fibres 15

3.1 Properties for selected fibres and its constituents 32
3.2 Nominal plate dimension and orientation for appropriate tests 35
3.3 Nominal specimen dimensions: In-plane 36
3.4 In-plane material characterisation properties 50
3.5 Recorded fabric properties for FVF determination 53
3.6 Recorded specimen properties for FVF determination 53
3.7 Measured FVF for all materials involved 54
3.8 Mode I and II interlaminar fracture toughness for IM7/8552: Available values from the literature 56
3.9 Nominal plate and specimen dimensions: IFT characterisation 58
3.10 Fibre and matrix material properties calculated using the rule of mixtures 70

4.1 Some mechanical properties of Vectran/epoxy composite 89

5.1 Layup and material physical properties 95
5.2 Average measured delamination area. Units are in mm^2 127
5.3 Delamination Threshold Load: Measured and calculated 128
5.4 Relevant mechanical properties for all the composites used 144

6.1 Mechanical properties used in the FEM analysis 167
6.2 Modelling constants 167

7.1 Fracture toughness inputs for composite materials used in this study . . 178

7.2 Inputs for delamination prediction 179

7.3 Comparison of FEM prediction and experiments on the measured delamination area under LVI. Units in mm^2 218

B.1 Ballistic limit predicted using Walker's relationship 266

Acknowledgements

All praises are due to God Almighty, owner of the universe, for with his blessings and permission, I am given the chance to complete this PhD project, and to understand with this limited mind, the field of structural, composites, and impact engineering.

The utmost dedication is to my parents, Syed Abdullah bin Syed Mohamed, Rugayah binti Syed Ali, and my brother, Syed Mohamed bin Syed Abdullah. They are indeed my strongest source of support and strength throughout this PhD journey. A special thank you to the lovely Hannah Mohd Jeran, and the wonderfully adorable Syed Luthfan for being in my life. Perhaps the best family one could ask for.

To my respective supervisors, Professor Lorenzo Iannucci and Professor Emile Greenhalgh, I would like to thank them for giving me the opportunity to learn and be guided by their great amount of experience and knowledge. Most importantly, for giving me the opportunity to study at Imperial College.

To my friends, acquaintances, and colleagues, I thank you for your support and help in times of need. Dr. Nick Fogell, Dr. Sang Nguyen, Dr. Frank Gomer, Mr. Atrash Mohsin, Mr. Tomas Katafiasz, Mrs. Michelle Willows, Mr. Joseph Meggyesi, Mr. Gary Senior, and Mr. Jon Cole, I wish you the best of luck and success in your life.

Nomenclature

Lower case Roman letters

a ..... crack length
a ..... fitting parameter for Vectran/MTM57 non-linear shear curve
a_0 ..... half crack length
b ..... fitting parameter for Vectran/MTM57 non-linear shear curve
c ..... fitting parameter for Vectran/MTM57 non-linear shear curve
c_0 ..... sonic velocity
d ..... fitting parameter for Vectran/MTM57 non-linear shear curve
d ..... displacement
d ..... impactor diameter
d_c ..... critical displacement at specific crack length
d_f ..... fibre diameter
d_i ..... damage. i=1,2,3,4,5
d_x ..... combined tension-compression damage in the warp direction
d_y ..... combined tension-compression damage in the weft direction
g_c ..... specific fracture energy
h ..... thickness
l_c ..... characteristic element length
l_c ..... critical fibre length
l_e ..... element size in the direction of crack propagation
l_{po} ..... fibre pull-out length
p ..... Jonas-Lambert fitting parameter
t ..... specimen thickness
t ..... time
t ..... thickness for cross-sectional area
t_f ..... final (termination) time
t_n ..... current time
v_f ..... fibre volume fraction
v_m ..... matrix volume fraction
v_m ..... matrix volume fraction

v_s ..... stitch volume fraction
w ..... specimen width for stress intensity factor calculation
x ..... x-direction global coordinate
y ..... y-direction global coordinate
x' ..... x-direction material coordinate
y' ..... y-direction material coordinate

Upper case Roman letters

A ..... cross-sectional area
A ..... fracture cross-sectional area
A_i ..... image area for FVF calculation
A_p ..... projectile cross-sectional area
C ..... compliance
E ..... Young's Modulus
E^0 ..... initial Young's Modulus
E_f ..... flexural Young's Modulus
$E_{i,j}$ ..... Young's modulus in the i or j direction. i=1 and j=2
$E^0_{i,j}$ ..... initial Young's modulus in the i or j direction. i=1 and j=2
E_y ..... transverse Young's Modulus
E_z ..... out-of-plane Young's Modulus
G_{12} ..... $\pm 45°$ in-plane shear modulus
G^0_{12} ..... $\pm 45°$ initial in-plane shear modulus
G_{Ic} ..... Mode I Critical strain energy strain release rate
G_{IIc} ..... Mode II Critical strain energy strain release rate
G_c ..... Critical strain energy strain release rate
G_m ..... matrix shear modulus
G_{po} ..... fibre pull-out fracture energy
K_{Ic} ..... stress intensity factor
N ..... fitting parameter for Vectran/MTM57 tensile stress-strain curve
N_e ..... number of element insider the cohesive zone
N_f ..... number of fibres
M ..... fitting parameter for Vectran/MTM57 tensile stress-strain curve
P ..... load
P_0 ..... initial gas pressure
P_c ..... critical load at specific crack length
P_c ..... critical load to cause fracture
P_c ..... critical load to initiate delamination
R ..... ratio of matrix tensile to shear strength
T_m ..... melting temperature

U ..... energy
U^* ..... Cuniff velocity
V_{50} ..... velocity at 50% probability of penetration/no-penetration
V_{50}^{Exp} ..... experimental velocity at 50% probability of penetration/no-penetration
V_{50}^{FE} ..... FE predicted velocity at 50% probability of penetration/no-penetration
V_f ..... volume of fibres in RUC
V_i ..... impact velocity
V_m ..... volume of matrix in RUC
V_r ..... residual velocity
V_s ..... volume of stitch in RUC
V_{bl} ..... ballistic velocity
W_0 ..... initial specimen width
W_f ..... fibre weight
W_{stitch} ..... stitch weight
W_{warp} ..... warp weight
W_{weft} ..... weft weight
X_i ..... horizontal force at node i
X_C ..... compressive strength for maximum stress criterion
X_T ..... tensile strength for maximum stress criterion
X_{po} ..... fibre pull-out strength
Z_i ..... vertical force at node i

Lower case Greek letters

α ..... fitting parameter for compliance calibration curve
α_c ..... constant for shear-rate enhancement
β ..... constant for irreversible strain
β ..... fitting parameter for compliance calibration curve
β ..... kink-band angle
γ ..... fitting parameter for compliance calibration curve
γ ..... gas adiabatic exponent
γ ..... shear strain
γ_Y ..... matrix shear yield strain
γ_{12}^0 ..... $\pm 45^\circ$ in-plane shear yield strain
γ_{12}^e ..... $\pm 45^\circ$ elastic (recoverable) in-plane shear strain
γ_{12}^p ..... $\pm 45^\circ$ inelastic (permanent) in-plane shear strain
γ_{12}^t ..... total $\pm 45^\circ$ in-plane shear strain
γ_{12}^{max} ..... $\pm 45^\circ$ ultimate in-plane shear strain
$\dot{\gamma}_{12}$ ..... $\pm 45^\circ$ in-plane shear strain-rate
ε ..... strain-to-failure

ε ..... tensile strain-to-failure
ε_0 ..... strain at damage onset
ε_c ..... compressive strain
ε_l ..... longitudinal strain
ε_p ..... irreversible (permanent) strain
ε_t ..... transverse strain
$\varepsilon_{e,t}$ ..... tensile or compressive strainl
ε_{max} ..... strain at final failure (d=1)
θ ..... ply angle
κ ..... Jonas-Lambert fitting parameter
κ ..... material parameter defining the $\pm 45^\circ$ in-plane shear strain-rate
ν ..... Poisson's ratio
ν_{12} ..... major Poisson's ratio
ν_{21} ..... minor Poisson's ratio
ν_{12}^0 ..... initial major Poisson's ratio
ν_{21}^0 ..... initial minor Poisson's ratio
ρ ..... density
σ_i ..... strength at the i direction. i=1,2,3
σ_f ..... fibre fracture strength
$\sigma_{t,c}$ ..... failure strength tension or compression
$\bar{\sigma}$ ..... effective strength
τ^0 ..... interfacial shear strength
τ_{12} ..... $\pm 45^\circ$ in-plane shear strength
τ_{12}^u ..... $\pm 45^\circ$ ultimate in-plane shear strength
τ_{ij}^u ..... shear strength in the (i,j) plane , ij=12,13,23
$\bar{\phi}$ ..... initial misalignment angle
$\bar{\tau}^0$ ..... interfacial strength

Acronyms

3PB ..... Three Point Bending
4PB ..... Four Point Bending
ASTM ..... American Standard for Testing Materials
BFD ..... Back Face Deflection
BVID ..... Barely Visible Impact Damage
CAI ..... Compression After Impact
CDM ..... Continuum Damage Mechanics
CFRP ..... Carbon Fibre Reinforced Plastics
CC ..... Compact Compression

CC ..... Compliance Calibration
CCD ..... Charged-Coupled Device
CLT ..... Classical Laminate Theory
CNT ..... Centre Notched Tension
CT ..... Compact Tension
CV ..... Coefficient of Variation
CZM ..... Cohesive Zone Model
DCB ..... Double Cantilever Beam
DEN ..... Double Edge Notched
DIC ..... Digital Image Correlation
DTL ..... Delamination Threshold Load
ECM ..... Equivalent Constraint Model
ECT ..... Edge Compact Tension
ELS ..... Edge Loaded Split
ENF ..... End Notched Flexure
FEM ..... Finite Element Method
FNM ..... Floating Node Method
FRMM ..... Fixed Rate Mixed-Mode
FOD ..... Foreign Object Damage
FVF ..... Fibre Volume Fraction
GFRP ..... Glass Fibre Reinforced Plastics
HAT ..... ASTM failure code: tHrough-thickness At Tab
HIT ..... ASTM failure code: tHrough-thickness Inside Tab
HVI ..... High Velocity Impact
ICSTM ..... Imperial College Standard for Testing Material
IFT ..... Interlaminar Fracture Toughness
LEFM ..... Linear Elastic Fracture Mechanics
LGM ..... ASTM failure code: Lateral Gauge Middle
LVI ..... Low Velocity Impact
MBT ..... Modified Beam Theory
MCC ..... Modified Compliance Calibration
MMB ..... Mixed-Mode Bending
MMF ..... Micro-Mechanics Failure
NCF ..... Non Crimp Fabric
NFLS ..... Normal Failure Stress
RFI ..... Resin Film Infusion
RUV ..... Representative Unit Volume
RUC ..... Representative Unit Cell
SEM ..... Scanning Electron Microscope
SEN ..... Single Edge Notched

SERR ..... Strain Energy Release Rate
SGM ..... ASTM failure code: Splitting Gauge Middle
SC ..... Surface Cracked
TLCP ..... Thermotropic Liquid Crystal Polymer
UD ..... Uni-Directional
UMAT ..... User Defined Material Model
VCCT ..... Virtual Crack Closure Technique
VIC ..... Vickers Indentation Crack
WIF ..... Wedge Insert Fracture
XUU ..... ASTM failure code: eXplosive Unkonwn Unknown

Chapter 1

Introduction

1.1 Background

While the first use of composite structures dates back to 1500 B.C., their significant development began in 1940 [1], when Glass Fibre Reinforced Plastics (GFRPs) were used in the marine industry to replace traditional wood or metal structures. The appealing properties such as a high stiffness-to-weight ratio, corrosion resistant, and increased fatigue life, have attracted many designers to adopt GFRP in the production of boats and ships. In aeronautical structures such as commercial aircraft, the use of composite materials has seen a rapid increase beginning in the late 1980s. Airbus introduced large primary aerodynamic structures such as the vertical and horizontal stabiliser built from Carbon Fibre Reinforced Plastics (CFRPs) in its A320 family. Today, the Airbus A350 XWB and its American counterpart, the Boeing 787 Dreamliner, are constructed of more than 50% composite materials. Figure 1.1 shows the evolution of composite material used in Airbus commercial aircraft families over the past 30 years.

The rapid increase in the use of composite materials within structural components has also stimulated a significant amount of research. Focus has been on understanding of the mechanics of the composite, as well as the ability to predict failure under a range of loading conditions. This includes impact, which can generate a considerable amount of damage in the composite. In the aerospace industry, operational threats during service, such as runaway debris [2, 3], bird strike [4, 5], and hail ice impact [6, 7] have the potential to cause a severe damage on the primary aircraft structure, incurring very expensive costs, and in extreme cases, severe injuries or even fatalities. Therefore, a

comprehensive understanding of the composite material behaviour is important towards a safer and a more cost effective aircraft design.

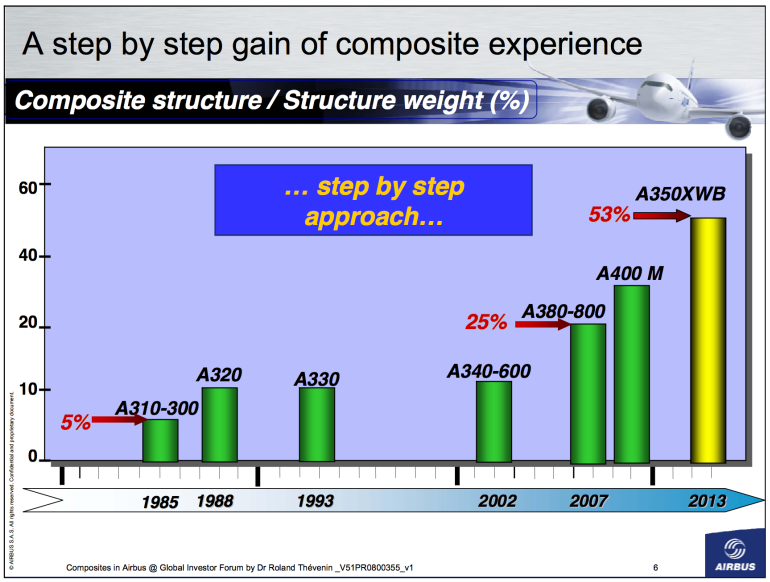


Figure 1.1: Percentage use of composite materials for the past 30 years [8]

Failure of composite structures is often a complex process and require a significant amount of time to examine and understand. This is particularly true for high performance fibres, where the mechanics of failure have yet to be thoroughly understood. For instance, the use of polymer based fibres such as Vectran and Dyneema in the defence and aerospace industries have seen a considerable increase in the past few decades. Owing to this, research on polymer based fibre composites have also undergone an appreciable increase. However, many aspects of these composites remain unclear and not fully understood. For example, although the impact performance of polymer fibre based composites has been well documented, their delamination behaviour has yet to be studied. This is an important area since delamination resistance of a composite material often determines its impact performance.

Thus, the need to fully understand the mechanics of failure is essential for a number of reasons. First, with a comprehensive understanding, engineers could exploit the full potential of the composite, without the need to 'over-design' to ensure that the composite structure meets all safety requirements. This would result in a more cost-effective design, with minimal material consumption and fewer man-hours. Secondly, an accurate prediction of failure can be made, leading to a more reliable design since the

mechanics of the composite are fully understood. Thirdly, physically based constitutive equations can be derived, which can be implemented as a material model for Finite Element Method (FEM) modelling. The material model can then be used to reduce the number of experimental tests required, leading to a reduction in the total design cost.

1.2 Motivation and objectives

The motivation for this research emerged from the increasing use of composite materials, particularly in the aeronautical industry. The poor impact performance of conventional fibre composites such as carbon and glass fibres warrants the need for further research to improve their impact resistance. One strategy in improving the impact performance is by composite hybridisation, where two (or more) types of reinforcements are included in a matrix material [9]. Some of the reinforcements include polymer based fibres such as Aramid and Vectran, due to their superior impact performance. However, polymer fibres often possess poor compressive properties, both in strength and modulus [10]. Therefore, fibres which are superior in compression, such as carbon fibres are often included in a hybrid composite system along with polymer based fibres to ensure its structural integrity whilst having a high impact resistance.

However, it is important to understand the behaviour of polymer based fibre composites, before including it as a reinforcement in a hybrid system. Therefore, the research presented in this thesis focuses on understanding the behaviour of polymer based fibre composites, especially their response under impact loading. In addition, the impact behaviour of high performance fibre composites was also investigated and compared to the response of polymer based fibre composites. Factors influencing the impact performance were also studied, such as the quasi-static in-plane response, and the delamination behavour [11, 12]. These factors generally determine the impact performance of laminated composites. For instance, the tensile strain-to-failure is often one of the main attributes which determines the impact performance of laminated composites [13]. A large tensile strain-to-failure is commonly an indication of a superior performing composite under impact, due to the large energy absorbing potential.

Furthermore, the results obtained from the quasi-static characterisation can also be

used to derive constitutive relations for a composite material. The constitutive relations can then be implemented into a non-linear FEM software such as LS-Dyna, to numerically simulate the composite response under quasi-static loading, as well as impact. The experimental results can be used to validate the numerical model, confirming its reliability and accuracy for future use in a more complex composite study.

To summarise, the objectives of the PhD programme are:

(i) To evaluate the impact performance of three composite materials under low and high velocity impact loading. The composite materials are:

- IM7/8552 - Unidirectional Carbon/Epoxy supplied by Hexcel;
- S2-Glass/MTM57 - 0°/90° Non-Crimp Fabric (NCF) with Epoxy resin. The fabric is supplied by Sigmatex and the resin is supplied by Cytec;
- Vectran/MTM57 - 0°/90° Non-Crimp Fabric (NCF) with Epoxy resin. The fabric is supplied by Sigmatex and the resin is supplied by Cytec.

(ii) To characterise the quasi-static in-plane mechanical properties of the composites including tension, compression, and ±45° in-plane shear;

(iii) To evaluate the Mode I and II delamination behaviour of Vectran/MTM57 and S2-Glass/MTM57 composites by way of the Double Cantilever Beam (DCB) and Four End Notched Flexure (4ENF) tests;

(iv) To measure the translaminar fracture toughness due to the tensile fibre failure of the Vectran/epoxy composite material;

(v) To develop a 2D numerical damage model which will be implemented in LS-Dyna for Vectran/MTM57. The numerical model will be used to validate experimental testing such as the quasi-static in-plane tests, as well low and high velocity impact.

1.3 Thesis outline

The chapters in this thesis are outlined as follows:

Chapter 1: An introduction to the PhD project, along with the objectives;

Chapter 2: A comprehensive review on the existing literature related to the impact behaviour of high performance fibre composites. In addition, the current research on composite impact modelling is also discussed in detail;

Chapter 3: Results of the quasi-static in-plane and Interlaminar Fracture Toughness (IFT) tests are presented for all three composite materials used in this PhD project;

Chapter 4: Results of the translaminar fracture toughness test for Vectran/MTM57 are presented. In addition, outcomes from the fractographic investigation are discussed to understand the mechanism which contributes to the overall tensile fibre fracture energy;

Chapter 5: Results of the low and high velocity impact loading on all three composite materials. Impacted specimens are examined using an optical microscope to characterise the types of damage present in each composites. Additionally, the extent of interlaminar damage (delamination) is ascertained using an ultrasonic C-scan and radiographic imaging technique;

Chapter 6: The constitutive relations derived for Vectran/MTM57 are presented. The constitutive relations are then implemented into LS-Dyna as a User MATerial model (UMAT 41v). In addition, the UMAT is used to simulate in-plane tests (tension, compression, and $\pm 45^{\circ}$ in-plane shear) and compared with the experimental results;

Chapter 7: Results from the low and high velocity impact modelling are presented. In addition, the predicted damage types are also discussed and compared with the experimental results. An energy-based damage model previously developed by Maimi et al. [14, 15] is utilised to simulate the behaviour of IM7/8552 and S2-Glass/MTM57 composites due to their linear-elastic behaviour. For Vectran/MTM57, the UMAT developed in this study is employed;

Chapter 8: Further discussions on the results and observations obtained in the PhD study are presented;

Chapter 9: The conclusions of the PhD study were presented, along with recommendations for future research .

1.4 Publications

The work presented in this thesis have resulted in the following publications:

Journal papers

- S. I. B. Syed Abdullah, L. Iannucci, E. S. Greenhalgh, On the translaminar fracture toughness of Vectran/epoxy composite material. *Composite Structures*, 202:566-577,2018
- S. I. B. Syed Abdullah, L. Iannucci, E. S. Greenhalgh, A plane stress damage model for Vectran/Epoxy composites. *Composite Science and Technology, Submitted*, 2018
- S. I. B. Syed Abdullah, L. Iannucci, E. S. Greenhalgh, The impact performance of fibre reinforced polymers. *International Journal of Impact Engineering, Under preparation for submission*, 2018

Conference oral presentations

- S. I. B. Syed Abdullah, L. Iannucci, E. S. Greenhalgh, An experimental study of the Mode I interlaminar fracture toughness of Vectran/Epoxy composites. 17th European Conference on Composite Materials (ECCM17). Munich, Germany, 26th-30th June 2016.

Chapter 2

Literature Review

2.1 Introduction

In the past few decades, composite materials have been widely utilised as a substitute for conventional materials such as steel and aluminium in the aeronautical and automotive industries. This is due to their attractive properties such as high strength-to-weight ratio, corrosion resistant, and ease of manufacture. However, the susceptibility of composite materials to impact induced loads remains one of its greatest drawbacks. The ability of composite materials to absorb impact energies are often inferior to that of metallic materials such as steel and aluminium. One of the main reasons for this weakness is due to the large energy absorbing potential by way of plasticity of metallic materials, when compared to polymer composites. For instance, Karthikeyan et al. [16] investigated the ballistic performance of cured IM7/8552 (CF/Epoxy) with 304 stainless steel plates. It was concluded that the uncured 304 stainless steel plates showed significant inelastic deformation before penetration, resulting in superior ballistic performance. In contrast, the brittle nature of IM7/8552 restricts its energy absorbing potential to the elastic regime, limiting in a poor impact performance compared with the metallic system. Thus, it is essential that the performance of composite materials under impact induced loads is improved.

In recent years, the use of polymer fibre based composites has emerged as a potential solution to improve their impact performance. Polymer fibres such as Kevlar and Vectran offer enhanced mechanical properties, such as a high tensile modulus and strain-

to-failure, ultimately resulting in a better performing composite system under impact. Moreover, the increased understanding in the field of composite mechanics have led to better composite design, ultimately yielding to a superior performing material. Recent advancement in the prediction of composite failure using the Finite Element Method (FEM) with advanced energy-based damage models has resulted in more accurate and comprehensive modelling of composites, significantly reducing the time and cost for structural design using composite materials. Increasingly more detailed experimental data on the impact performance of various composite structures has led to a better understanding of the different types of damage which form due to impact induced loading. Furthermore, extensive evidence provides excellent validation resources for determining the accuracy of numerical models, hence ensuring its reliability in a more complex application.

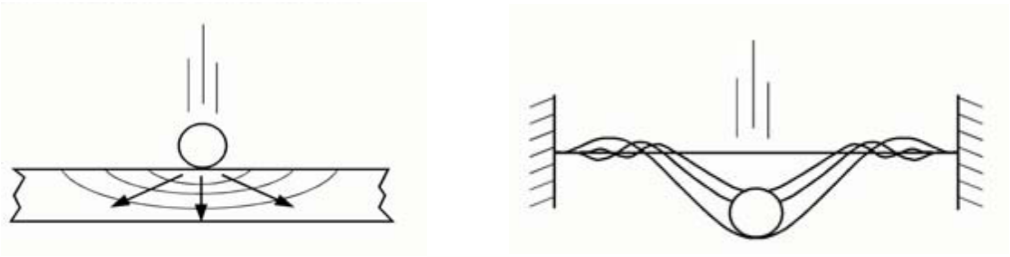
In the following subsections, an extensive review of the literature available to-date is presented. This includes literature on low and high velocity impacts, particularly with respect to high performance fibre composites. In addition, a review of the current state of composite modelling, especially energy-based damage models is discussed.

2.2 Impact on Composite Structures

The problem of impact on composite structures has been a subject of review for more than three decades. To date, many review papers have been written by researchers [11,12,17–23], reporting the advances observed in the field of impact mechanics on composite materials. These advances, which include those made in damage prediction using numerical methods such as FEM, have strengthened our understanding of more damage tolerant structures, designed for various applications. Mathematical models such as the spring-mass model, the energy-balance model and the Delamination Threshold Load (DTL) [24, 25] have greatly helped in determining the performance of the composite structure under transverse impact loading.

Foreign Object Damage (FOD), characterised by the velocity of impact, is of particular importance due to its relevance in real-life applications. Research normally centres around two types of velocity regime - low and high velocity impact. Although argument

exists with regards to the distinction of velocity range between low and high velocity impact, researchers have agreed that the threshold velocity defining low velocity impact is up to 10 m/s^{-1} [11, 12, 23, 26], and more generally by Abrate [20] for velocities below 100 m/s^{-1}. Additionally, Davies and Robinson [27] define Low Velocity Impact (LVI) as one in which through-thickness stress waves in the specimen play no significant part in the stress distribution at any time during the impact event. Hence, a global deformation can be observed in the laminate, shown in Figure 2.1b, due to the long impact duration. In contrast, a High Velocity Impact (HVI) event is usually stress wave dominated, Figure 2.1a, therefore the effects of boundary conditions can be neglected [11, 18–20].



(a) Stress wave dominated event (b) Boundary dominated event

Figure 2.1: Response types for impacted composite structures [11]

Godwin and Davies [28] proposed a simple technique to evaluate the transition velocity in which stress wave effects dominate. The relationship is based on the propagation of stress waves from the front face, which then progress towards the rear of the laminate. Therefore, the compressive strain, ε_c, can be calculated by using the relationship given by [27]:

$$\varepsilon_z = \frac{V_i}{C_z} = \frac{V_i}{\sqrt{\frac{E_z}{\rho}}} \tag{2.1}$$

where V_i is the impact velocity, C_z is the through-thickness speed of sound in the material, E_z is the out-of-plane Young's modulus, and ρ is the material's density. For instance, the transition velocity into a stress wave dominated event would occur at an impact velocity of approximately 20 ms^{-1} and above for a Uni-Directional (UD) CF/Epoxy composite with $E_y = E_z = 9.4$ GPa, $\varepsilon_c \approx 0.6\%$, and $\rho = 1.3$ g/cm^3.

Under High Velocity Impact (HVI) load, the longitudinal and transverse stress waves

propagate from the point of impact upon initial contact between the projectile and the composite. The longitudinal wave propagates towards the edge of the laminate and is reflected back towards the centre, whilst the transverse wave propagates towards the composite back face, usually travelling at a velocity much lower than the longitudinal wave. The repeated reflections of the longitudinal stress waves typically decreases in intensity throughout the impact event, which was shown experimentally by Pandya et al. [29].

When the impact velocity (or impact energy) is considerably lower than the V_{50} (or penetration energy for LVI loading), minimal to no damage will be observed in the laminate. V_{50} is defined as the velocity at which a projectile has a 50% probability of penetrating the target material (in this case composite laminates) [30]. The contact stress between the projectile (or impactor) and the laminate would generally induce minimal damage in the form of matrix cracking [31]. These cracks would saturate as a result of coalescence between multiple microcracks [32–35]. Depending on the thickness of the laminate, the damage pattern would differ due to the difference in the energy absorbing mechanism. For a typical brittle fibre-matrix system such as Carbon Fibre/Epoxy (CF/EPoxy) and Glass Fibre/Epoxy (GF/Epoxy), the cross-sectional damage normally resembles the so-called "pine tree" pattern. For thin laminates, a reversed pine tree pattern, Figure 2.2b, can usually be observed from the cross-section of the impact area. This is due to the high bending load at the rear side of the laminate, hence initiating shear matrix failure, Figure 2.3b. On the contrary, matrix cracks in thick laminates will often result in a pine tree pattern, Figure 2.2a. This is because the normal in-plane stresses have exceeded the transverse tensile stress of the front plies, therefore initiating matrix failure. For both pine tree patterns, extensive experimental evidence exists for CF/Epoxy composites [36–40], and GF/Epoxy [41–44].

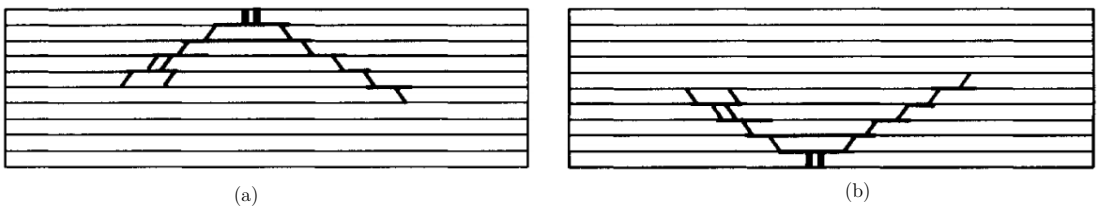
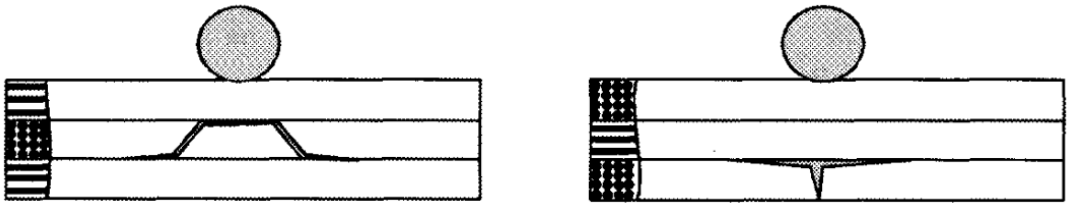


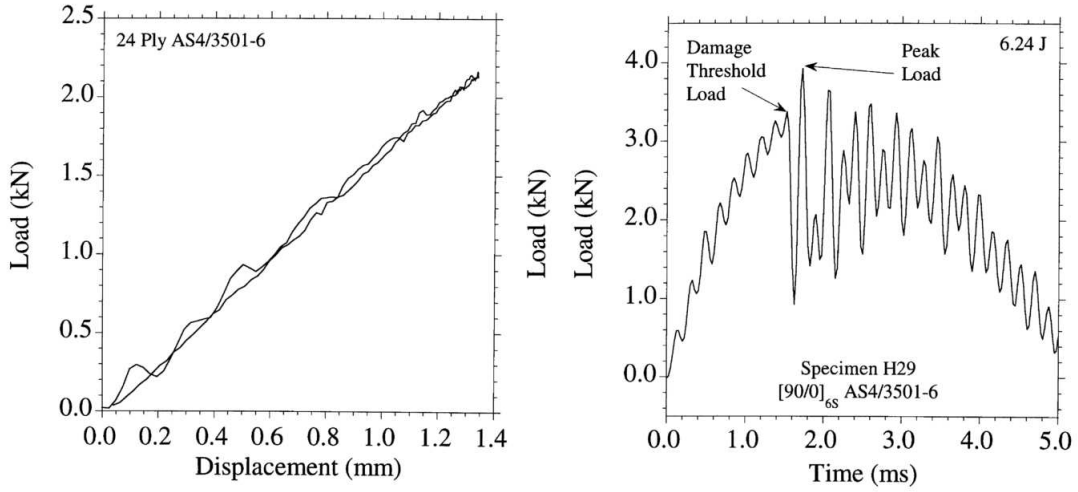
Figure 2.2: (a) Pine tree pattern (b) Reversed pine tree pattern [20]



(a) (b)

Figure 2.3: Types of matrix failure (a) Tensile crack (b) Shear crack [20]

The saturation of matrix cracks would typically lead to interlaminar failure, often known as delamination damage, which severely degrades the laminate's capability to carry further loads. An obvious drop in the load-time history (or load-displacement history) response [24] can be observed indicating a delamination has occured. For some materials (usually brittle materials such as CF/Epoxy and GF/Epoxy), violent oscillations may also be observed following delamination damage, Figure 2.4 (b), due to the unstable propagation of delamination [24]. Also, a noticeable change in stiffness can be seen in the load-displacement history [20], illustrated clearly in Figure 2.4 (b).



(a) (b)

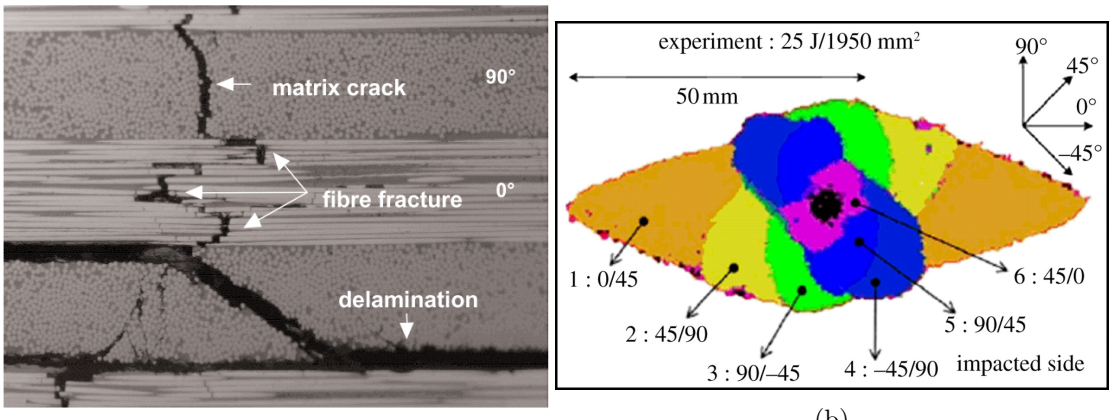
Figure 2.4: (a) Load-displacement response for laminates subjected to impact loads of 1.55 J - no damage (b) Load-time response of laminates subjected to 6.24 J of damage - delamination damage [24]

A closed form solution for the prediction of delamination damage has also been defined by Davies et al. [45], utilising fracture mechanics given by:

$$P_c^2 = \frac{8\pi^2 E_f h^3}{9(1-\nu^2)} G_{IIc} \tag{2.2}$$

where P_c is the critical load to initiate delamination, G_{IIc} is the Mode II critical strain energy, ν is the Poisson's ratio, E_f is the laminate flexural modulus, and h is the laminate thickness. The high dependence on the shear properties for LVI loading is apparent, resulting in the inclusion of Mode II critical strain energy in Equation 2.2. This is not surprising since LVI is a flexural dominated event, hence interlaminar shear properties are central to the impact performance of laminated composites. A closed form approximation has also been derived by Olsson et al. [25, 46] to predict delamination initiation and propagation under HVI loading. It was found that the threshold load to initiate delamination is approximately 21% higher compared to its quasi-static value. This is due to the dynamic nature of the HVI event, inducing very high contact stresses localizing at the point of impact [25].

It must be noted that delamination failure normally occurs only at interfaces with different fibre orientation (Figure 2.5a) [12, 20, 47]. This is associated with the adjacent plies which have different fibre orientations possessing different bending stiffnesses, therefore promoting delamination failure due to the property mismatch (Figure 2.5b). From this, peanut-shaped delamination extending along the fibres can normally be observed, increasing in size with an increase in the misalignment angle (i.e. a larger size should be present for a 0°/90° alignment compared to a 0°/45° fibre alignment) [11, 12, 20, 48].



(a) (b)

Figure 2.5: (a) Variation of damage in low velocity impact loading [11] (b) Peanut-shaped delamination with respect to fibre orientation [48]

If the velocity is increased (i.e. closer to the laminate ballistic limit or penetration energy), further damage would be seen due to higher contact stresses as well as a greater amount of energy transfer between the projectile and the laminate. For thin laminates, the energy transfer will normally result in tensile straining of the fibres, usually known as a cone formation at the rear of the laminate [49–51]. This is due to the high flexural load experienced by the laminate, with high tensile strain, particularly at the laminate back face. Penetration of the laminate is therefore governed by the amount of fibre failure; full penetration indicates that all fibres are broken, and no penetration indicates that zero or a minimal number of fibres have failed [49]. Fibre failure normally initiates from the laminate back-face, extending through-the-thickness towards the front face [11, 12, 20]. For thick laminates, penetration is normally associated with shear failure, specifically in the transverse direction resulting in a shear-plug formation [12]. The depth of penetration depends on the severity of damage and includes other factors such as the type and shape of the impactor [12, 20, 23, 42, 52, 53]. The energy related to laminate penetration is proposed by Dorey et al. [54] given as:

$$E_p = \pi \gamma t d \tag{2.3}$$

where E_p is the penetration energy, γ is a coefficient property related to the fibre fracture energy, d is the diameter of the impactor, and t is the laminate thickness. It is clear from Equation 2.3, that the energy absorption due to penetration increases with increasing thickness. This has been confirmed experimentally by researchers [12, 20, 42, 55, 56], and have concluded that the energy absorption (hence impact resistance) significantly increases with increasing thickness.

2.2.1 Polymer fibre composites under impact

As mentioned earlier, the use of a polymer fibre as an alternative to conventional brittle fibres such as CF and GF offer a potential solution to the poor impact performance of composite materials. Its superior mechanical properties often results in an enhanced impact performance, both under LVI and HVI. A key step in understanding the impact performance of high performance fibre composites was proposed by Cuniff [30] using a

dimensionless analysis based on the fibre specific toughness and longitudinal strain wave velocity, given by:

$$U^* = \frac{\sigma\varepsilon}{2\rho}\sqrt{\frac{E}{\rho}} \tag{2.4}$$

where U^* is the so-called "Cuniff velocity", σ is the fibre ultimate axial tensile strength, ε is the fibre ultimate tensile strain, ρ is the fibre density, and E is the fibre tensile modulus. Note the linear assumption in Equation 2.4, which could be misleading for fibre (or composite) possessing a non-linear tensile response. Moreover, through-thickness stresses, as well as the in-plane shear properties were not considered in Equation 2.4.

This may present a significant difference in the composite impact performance if the selection is based purely on U^*. However, Equation 2.4 does allow for a quick analysis in selecting the appropriate fibre for composite design. Table 2.1 presents the calculated Cuniff velocity for the fibres used in this PhD study. Consequently, Figure 2.6 presents the U^* for several commercially available high performance fibres.

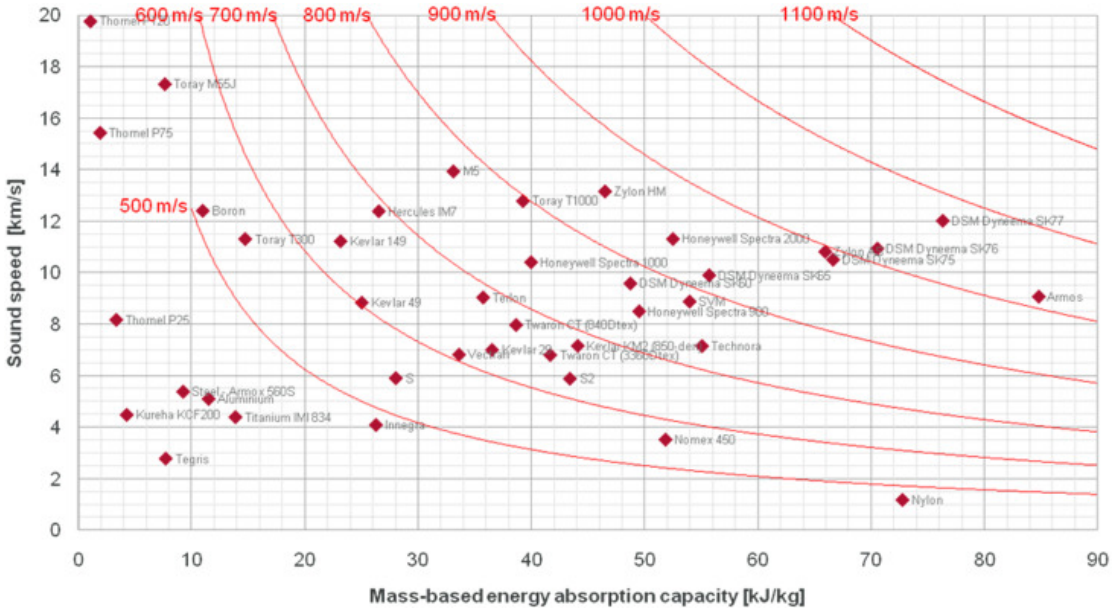


Figure 2.6: Speed of sound versus mass-based energy absorption capacity for a number of high performance fibres based on Cuniff velocity, U^*. Red contours represent U^* [57]

Table 2.1: Cuniff velocity for chosen fibres

Fibre type	U^* (m/s)
IM7 (CF)	721.65
S2-Glass (GF)	634.05
Vectran	616.12

From Table 2.1, it can be easily observed that IM7 possesses the highest U^* when compared to the selected fibres. This should indicate that IM7 should possess excellent impact performance although in reality, this is not the case. It was found that IM7 composite was the worst performing composite when compared to Vectran and S2-Glass composites. This result is associated with several factors. First, the low tensile strain-to-failure of IM7 ($\approx$ 1.9 [58]) compared to Vectran ($\approx$ 3.8 [59]) and S2-Glass ($\approx$ 5.7 [60]) limits the 'elongation' of the fibre to prevent impactor penetration. A recent investigation by Heimbs et al. [61] found that Dyneema HB26 showed superior HVI performance compared to CF and GF composites, whilst a comparable LVI performance with GF composite. Furthermore, in both impact events (LVI and HVI), CF composite exhibits the worst impact performance among all three composite materials. The superior performance can be partly attributed to the relatively high tensile strain-to-failure of Dyneema HB26 laminate, in addition to other factors such as the low $\pm 45^\circ$ in-plane shear properties (both stiffness and strength). This is consistent with the works of Reddy et al. [62] when investigating the impact performance (LVI and HVI) of GF/Epoxy and Dyneema HB26 laminates. The influence of shear strength on the ballistic performance has also been investigated by Karthikeyan et al. [16], which found a significantly higher V_{50} for the uncured IM7/8552 (CF/Epoxy) if compared to its cured counterpart. More importantly, the low $\pm 45^\circ$ in-plane shear properties have resulted in a superior impact performance of Dyneema HB26 and HB50 laminates; at least 50% higher than the uncured IM7/8552.

Recently, Hazzard et al. [63] investigated the effect of fibre orientation of Dyneema HB26 under LVI loading. A large Back Face Deflection (BFD) due to the low $\pm 45^\circ$ in-plane shear properties was observed for the $0^\circ/90^\circ$ orientation of Dyneema HB26

laminates. However, no penetration was observed even for large impact energies of up to 150J impacted on a 2 mm thick laminate. The effects of fibre orientation of Dyneema HB26 under HVI loading have also been investigated by Karthikeyan et al. [64], whereby a large BFD was observed for the $0\,^{\circ}/90\,^{\circ}$ orientation compared to other types of layup such as Unidirectional (UD) and helicoidal (hybridised $0\,^{\circ}/90\,^{\circ}$ orientation). In spite of this, the $0\,^{\circ}/90\,^{\circ}$ orientation yielded the highest V_{50} compared to the other orientation types. It must be noted that a large BFD may not necessarily be a positive characteristic concerning composite structural design. In certain structural design, particularly in defence applications, a large BFD may imply a severe weakness due to the 'soft' nature of the structure, enabling rapid (and excessive) membrane loading at the point of impact.

Secondly, the inherently large fracture energy of polymer fibre composites partly contributes to its superior impact performance. An earlier work by Park et al. [65] highlights the considerably large impact absorption energy of Aramid when compared to GF composites (6.3 J and 58.43 J for a 2 mm thick GF and Aramid laminates, respectively) under LVI loading. A similar observation was seen by Sikarwar and co-workers [66] when investigating the behaviour GF/Epoxy and Kevlar/Epoxy laminates, where a considerably higher specific energy absorption capacity was found for Kevlar/Epoxy laminates ($\approx 36\%$ higher) when compared to Glass/Epoxy laminates. This is consistent with the findings of Evci and Gulgec [67], where a superior impact performance was observed for Aramid laminates if compared to GF composites under LVI.

The high fracture energy of polymer fibres (or polymer composite systems) enables a large energy absorption under impact loading, partly due to its unique fibre structure. For instance, the so-called'skin-core' structure of Vectran fibre typically results in a tougher system, due to its inherent energy absorption mechanisms such as fibre pull-out and interfacial sliding. A recent investigation on the tensile fracture properties of Vectran/Epoxy laminates [68] revealed a much higher value of fracture toughness; up to 48.26% and 95.27% higher for initiation and propagation for some CF/Epoxy [69] composite system, and 9.93% and 68.6% higher for initiation and propagation for some GF/Epoxy [70] composite system. The high fracture energy of Vectran is partly attributed to the 'skin-core' nature of the fibre, resulting from its manufacturing process.

During fibre extrusion, the 'skin' cools much quicker than the 'core' resulting in a highly oriented crystalline region at the 'skin', whilst a less oriented, amorphous region at the 'core'. Hence, a noticeable difference in the mechanical properties may be found, whereby the 'skin' is much stiffer when compared to the 'core', resulting in a path of failure which initiated first at the 'skin' and then propagating towards the 'core'.

Thirdly, the sensitivity to strain-rate effects was evident, particularly in polymer fibre composites. A recent report by Singh [71] attempts to collate existing strain-rate research on high performance fibre composites. It was found that GF (or GF composites) display considerable sensitivity towards strain-rate, with enhancements close to 200% observed at 10^3/s compared to the quasi-static case. A similar response was seen for Kevlar fibres, although its enhancement is not as significant as GF, with an increase of up to 50% in tensile strength. This is consistent with the works of Wang and Xia [72], when investigating the effect of strain-rate (0.0001/s - 1350/s) on Kevlar 49 fibre bundles. The authors found an approximately 22% increase on its tensile strength modulus and strength, including a 15% increase in its tensile strain-to-failure. Tan et al. [73] investigated the tensile response of Twaron CT716 yarns at strain-rates of up to 480/s and found a 28% and 36% increase on the tensile modulus and strength, respectively. In a follow-up study, Koh et al. [74] investigated the strain-rate effects of Spectra 900 yarns and found a 150% increase in the tensile modulus and 40% increase in the tensile strength.

Despite the excellent impact performance of polymer fibres, the significantly low compressive properties severely restrict their use as a structural component. This is due to the weak (van der Waals) bonds between molecules, which easily fails when the fibres are loaded in compression. Specifically for Vectran, the fibrillar nature of the fibre tends to de-fibrillate almost instantly under compression loads, resulting in a compressive property of approximately 10% of its tensile component [75]. Hence, it is common that polymer fibre composites should be utilised as a reinforcement in a hybrid composite system.

Park et al. [65, 76] investigated the impact performance of Aramid fibre/glass fibre hybrid composite and found a markedly higher impact performance when compared to

the monolithic GF composite system. Sikarwar et al. [66] observed a 20% increase in the HVI performance of GF/Kevlar hybrid composites when compared to the monolithic GF composite system. Bandaru et al. [77] investigated the ballistic performance hybrid thermoplastic Kevlar and basalt composite system and found a 26.27% increase in the impact performance compared to Basalt monolithic composite system. A recent review by Iannucci [78] highlights the advantages of composite hybridization by incorporating polymer fibres with conventional materials such as CF and GF. Some of the benefits include potential weight savings and enhanced impact performance, whilst achieving the desired compressive properties to be used as a structural component.

2.3 Modelling impact on composite structures

The use of numerical models for the prediction of mechanical properties or impact response can considerably reduce the time and cost related to composite structural design. Numerical techniques such as the Finite Element Method (FEM), is often utilised to predict damage due to impact loading in a composite material. In recent years, the use of energy-based models has seen an appreciable increase due to their accuracy and reliability in damage prediction. Mathematical models such as the Classical Laminate Theory (CLT) are used in conjuction with energy-based theories such as fracture mechanics to describe laminate failure. For example, the energy required for fibre failure is taken as the energy obtained from standard fracture mechanics tests such as the Compact Tension (CT) or Compact Compression (CC). This energy is commonly known as the strain energy release rate, G_c, and is assumed to be the area enclosed under the stress versus strain curve of the relevant modes. Upon reaching the failure strength (tension or compression), laminate stiffness is degraded to zero.

The concept of degradation is essentially part of a more general Continuum Damage Mechanics (CDM) approach, which was first introduced by Kachanov [79] and later by Rabotnov [80] when attempting to describe the creep behaviour in metals. CDM is an attractive approach since it provides a method in which accurate determination of the material condition can be made - from a pristine condition (no damage) until final failure (full damage). Unlike the earlier approach to modelling composite laminate using stress

(or strain) based criteria [81–83], in which the stress is immediately reduced to zero, upon reaching its threshold strength. This is a gross over-simplification which neglects the post-failure behaviour of a laminated composite.

The earliest implementation of energy-based damage mechanics approach is proposed by Ladeveze [84]. In-plane testing of various laminate orientation was simulated using the CDM approach and later compared with the experimental results. Damage onset was taken as the failure strength of relevant modes, and then linearly degraded until zero. Excellent correlation between the experimental and simulation results was obtained. Later, Matzenmiller et al. [85] utilise the CDM approach by considering the post-failure behaviour as a function of the Weibull distribution of strength. Williams et al. [86] implemented the approach suggested by Matzenmiller et al. [85] into LS-Dyna as a plane stress material model. Following this, Iannucci et al. [87–91] employed the CDM approach to model thin laminated composites (UD and woven) under LVI and HVI loadings. All numerical prediction including the force-time/displacement histories were in close agreement with the experimental results.

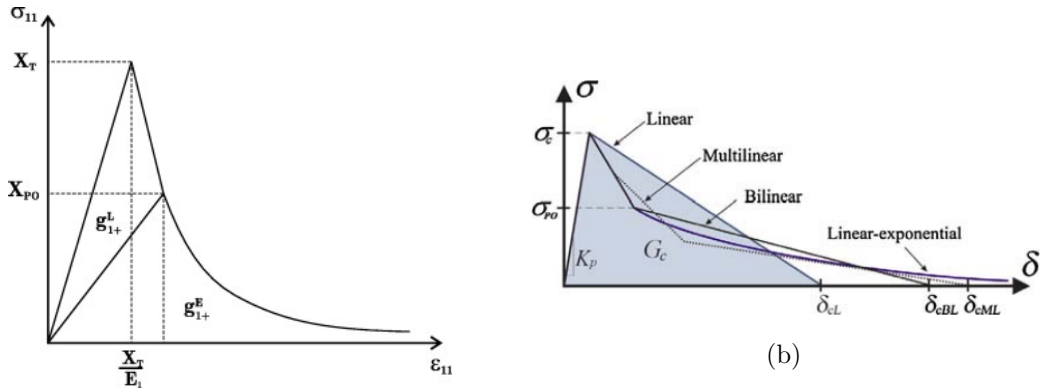


Figure 2.7: Alternative softening laws for fibre tension and compression failures (a) Bi-linear softening law [92] (b) Exponential softening law [15]

The linear degradation model, originally proposed by Bazant [93], has been widely used due to its ability to reproduce excellent force-time/deflection histories [11, 94]. However, this approach is rather simplified and does not involve any physical reasoning. For this reason, Maimi et al. [14,15] proposed a linear-exponential softening law, Figure 2.7a, which was later super-imposed by Davila et al. [92] to a bi-linear softening law

involving two linear curves to represent damage propagation. These softening laws were based on the processes typically involved in fibre failure (i.e. matrix failure, fibre-bridging, fibre pull-out etc.). For instance, at damage onset, stress will be linearly degraded until reaching the fibre pull-out strength, X_{po}, followed by an exponential softening until zero stress.

These alternative softening laws not only provide a sound physical justification for damage degradation, but were also reported to yield more accurate results. This was shown by Davila and co-workers [92], when comparing the linear and bi-linear softening laws in a Compact Tension (CT) simulation. It was found that the bi-linear softening law was able to closely predict the shape of the Resistance curve (R-curve) with the experimental results if compared to the linear softening law.

Apart from describing an accurate determination of the material condition, the CDM approach also allows for the alleviation of mesh dependency in numerical analysis. This is because CDM is based on a representative unit volume and therefore the energy related to this unit volume must be made constant regardless of the element dimension. Thus, a length parameter is introduced, typically known as the element characteristic length, l_c, to ensure constant energy dissipation throughout the analysis. This approach is commonly known as the smeared formulation, whereby the fracture energy is smeared over the full volume of the element [95].

However, the calculation of l_c is not always straightforward and may require a separate algorithm in the material model. Some of the methods proposed by previous researchers include the use of the element shape functions, or purely from a geometrical approach. This was discussed by Ehrich et al. [96], which investigated both strategies for the l_c calculation. For the former (using geometrical approach), the nodal coordinates from the element nodal connectivity were accessed and then stored as a history variable, which was then called back to calculate the coordinate global to local coordinate transformation based on the ply angle, θ, given by:

$$x' = cos(\theta)x + sin(\theta)y \tag{2.5}$$

$$y' = -sin(\theta)x + cos(\theta)y \tag{2.6}$$

where (x' ,y') are the material coordinates, and (x ,y), are the global coordinates. Upon transformation, the characteristic element length, l_c can be calculated using the desired approach (geometry or element shape functions). For the geometrical approach, l_c will be calculated from the element sub-intervals giving the characteristic length for each strip, Figure 2.8a, which is then used to calculate the l_c for the entire element.

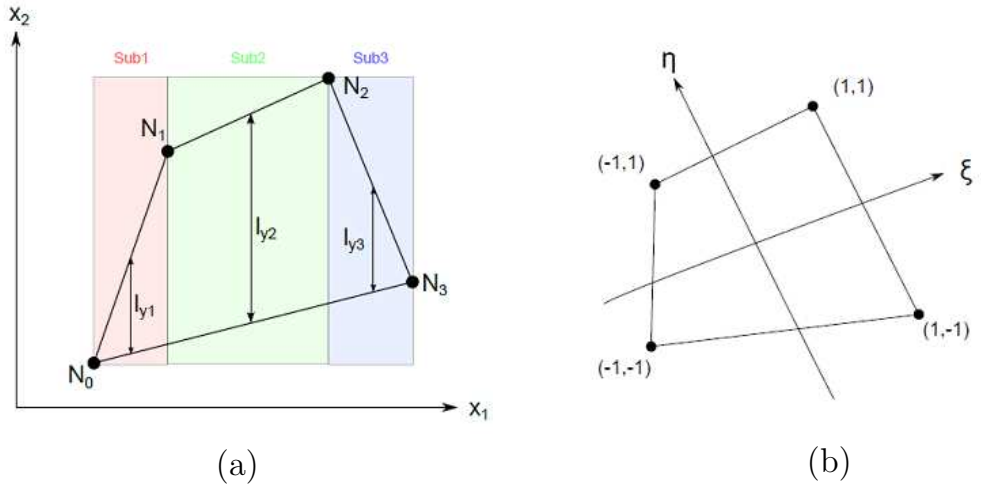


Figure 2.8: Calculation of l_c from different approaches (a) Geometrical (b) Element shape function (isoparametric coordinates) [96]

Conversely, when utilising the element shape function approach, l_c, is calculated using the isoparametric nodal coordinates which is used in the partial differential equation originally proposed by Oliver [97] given by:

$$g_c = G_c \frac{\partial v(x', y')}{\partial x'} = \frac{G_c}{l_c} \tag{2.7}$$

where g_f is the specific fracture energy, and G_c is the critical fracture energy of the material.

Donadon and co-workers [98, 99] utilised the smeared formulation to accommodate irregular/non-structured mesh, by utilising the element shape functions approach to calculate l_c for use in the smeared formulation. Ehrich [96] has also implemented these modifications into plane stress elements in Abaqus explicit. Raimondo et al. [100] proposed an alternative approach in alleviating mesh dependency. The method is based on the maximum crack density, which is suggested to be a material characteristic in a composite laminate. Hence, a crack density parameter was introduced into their degradation

model to account for the total energy dissipated in one element.

2.3.1 Modelling damage

In the context of CDM, damage initiates when the current stress reaches the maximum strength of the material (d=0), and then degraded to zero stress (d=1). Each failure modes (tension, compression, and shear) are typically assigned with a damage variable, hence allowing the current state of the model to be examined. Failure normally initiate as matrix cracks and then followed by delamination, similar to the experimental observation. While the interaction between matrix failure and delamination are sometimes treated separately, a study performed by Bouvet et al. [101], attempts to capture this interaction by using discrete intra-ply (matrix) zero-thickness cohesive elements (or cohesive surfaces). These elements are based on non-linear springs and follow the well known bi-linear traction-separation law, similar to the one proposed by Bazant and Oh [93]. The authors reported a remarkable correlation between the experimental results, in spite of a couple of drawbacks. First, the approach is computationally costly due to the number of cohesive algorithms utilised in the model. Secondly, and most importantly, the authors reported a significant mesh sensitivity in the model. Perhaps it is worth noting that the model is restricted to UD materials due to the inherent nature of the approach. In a follow-up study, Bouvet et al. [102] utilised the previous model to simulate the Compression After Impact (CAI) response of CF/Epoxy laminates. Similar to the previous study, both the impact and the CAI response were in excellent agreement with the experimental observations. Recently, Lopes and co-workers [103] utilised the approach proposed by Bouvet et al. [101] in modelling intra-ply failure. For the in-plane response, the authors employed the constitutive relations proposed by Maimi et al. [14, 15]. Although the approach is computationally costly, accurate prediction of damage types, in particular matrix cracking and delamination were achieved.

Over the last few years, multi-scale modelling has also been an active topic of research, due to its ability to predict not only the response of composite in the macro-scale but also the fibre-matrix interaction in the micro-scale. More importantly, the multi-scale approach would allow for a minimal number of laboratory testing, hence

considerably reducing the cost and time required for composite design. In a multi-scale model, a reference Representative Unit Volume (RUV) of the microstructure is usually defined [104], which could then be utilised to predict the material properties of a laminate on a macro-scale level.

Recently, Liao et al. [105] developed a multi-scale model to predict the LVI response of CF/Epoxy utilising Hexagonal RUV model (shown in Figure 2.9) and Micro-Mechanics Failure (MMF) criterion originally developed by Jin et al. [106]. The MMF is partly based on the rule-of-mixtures which predict the 'macro' properties of the RUV. In addition, the MMF considers the interaction between the fibre and the matrix including interfacial fibre-matrix shear stresses derived using a simple linear relation. Apart from the good correlation between the impact experiments, the model developed by Liao et al. [105] was also capable of analysing the stress-state of the RUV at the micromechanical level.

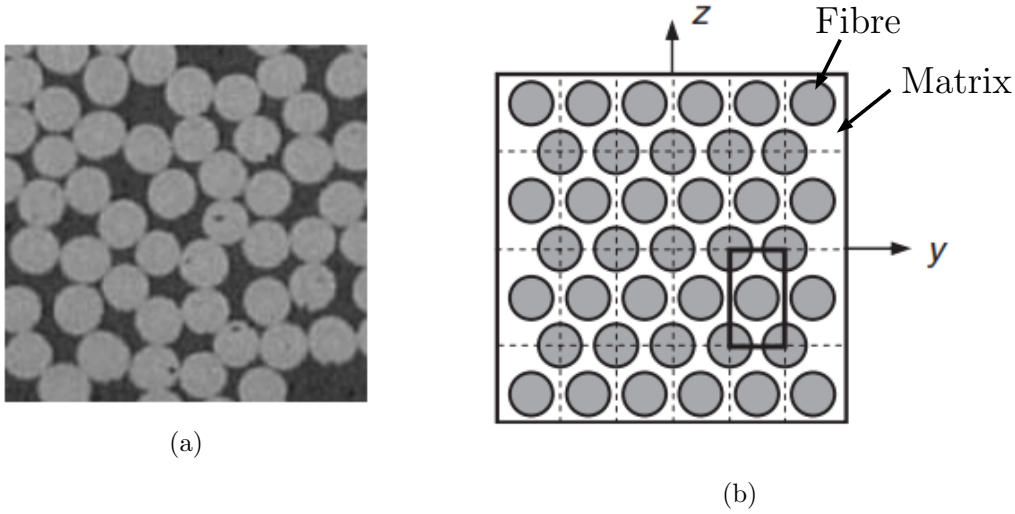
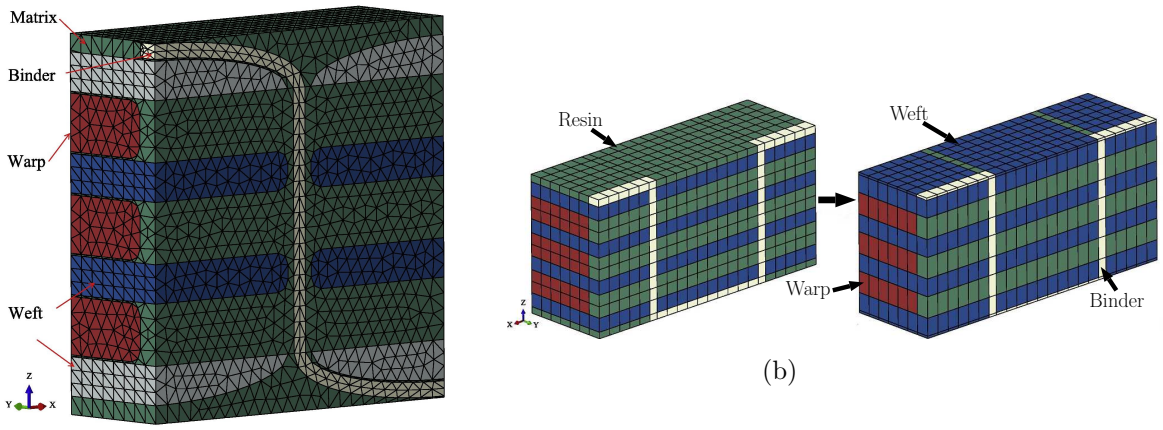


Figure 2.9: RUV of the CF/Epoxy laminate (a) Optical micrograph of the fibre arrangement (b) The Hexagonal RUV model [105]

Lopes et al. [107] developed a virtual 3D RUV model to calculate the in-plane mechanical properties of AS4/8552 composite. It was found that the predicted in-plane mechanical properties using the RUV are in very close agreement with the available literature data. Later, the properties obtained from the RUV are passed on to the macro-scale model which was then utilised to analyse the LVI response of the laminate discussed earlier [103]. Dai and Cunningham [108] studied the progression of damage

in a 3D woven composite loaded in tension by utilising an idealised geometry unit cell model, Figure 2.10b, and a modified mosaic cell model, Figure 2.10a. The elastic properties of the RUV were calculated using the modified rule-of-mixture approach (Chamis rule [109]).



(a) (b)

Figure 2.10: (a) The modified unit cell model (b) The idealised geometry unit cell [108]

The types of damage predicted in the model include matrix cracking, tow debonding, tow transverse tensile failure, and tow longitudinal tensile failure, with the transverse weft tow failing first, followed by matrix cracking, weft and warp tow debonding, and finally warp tow tensile failure. Additionally, the tensile strength and modulus predicted by the unit cell and mosaic cell models were about 10% higher than the experimentally measured values.

A recent review is provided by Bogenfeld et al. [110], highlighting key numerical strategies in modelling composite laminates under LVI. Alternatively, Iannucci [78] provides an up-to-date survey on the available numerical methods for HVI modelling on high performance fibre composites. In both cases, special attention is given to the CDM and multi-scale modelling approach.

2.3.2 Modelling delamination

Laminated composites can fail in a number of damage modes, typically matrix cracking, delamination, and fibre failure. Due to the inherently low through-thickness strength in laminated composites, delamination could easily occur which would seriously impair

the load bearing capability of the structure. This is particularly in an impact event, especially LVI, where Barely Visible Impact Damage (BVID) is a hidden menace often causing delamination.

In recent years, many numerical strategies have been proposed to predict delamination. Well known methods such as the DTL [27] offers analytical estimation to predict the load for delamination onset. However, numerical methods such as the FEM is still required to predict the extent of delamination damage in a composite structure. A recent review by Tabiei and Zhang [111] and Bogenfeld et al. [110], highlights the two most famous methods in delamination modelling: the Virtual Crack Closure Technique (VCCT) and the Cohesize Zone Model (CZM). The VCCT approach, initially built on the works of Irwin [112], is based on the assumption that "when a crack extends by a small amount, the energy released in the process is equal to the energy required to close the crack to its original length".

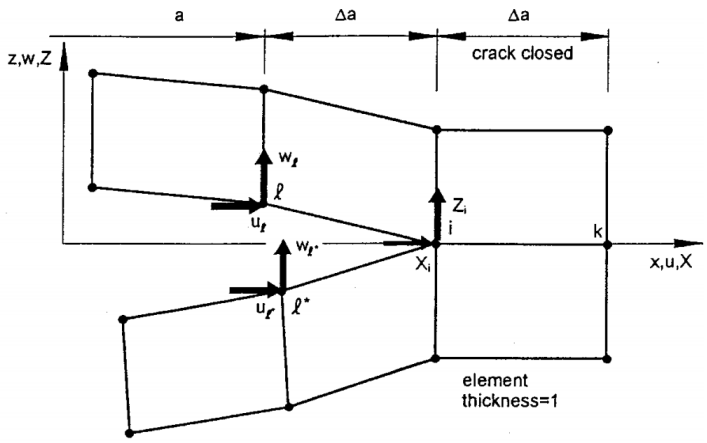


Figure 2.11: The VCCT method [112]

Consider an FEM implementation as illustrated in Figure 2.11. The Strain Energy Release Rate (SERR) can then be approximated by multiplying the forces at node $\mathbf{Z}_i$ (or $\mathbf{X}_i$ for Mode II SERR) and the displacements at node l, shown in Equations 2.8 and 2.9. An extensive review on the VCCT method was given by Krueger [112].

$$\mathrm{G}_I = -\frac{1}{2\Delta a} Z_i (w_l - w_{l^*}) \tag{2.8}$$

$$G_{II} = -\frac{1}{2\Delta a} X_i (u_l - u_{l^*}) \tag{2.9}$$

In spite of the straightforward process, the VCCT method has some disadvantages which are inherent in its approach. First, the method requires an initial crack to be determined before the analysis could be performed, and this could be difficult in a more complex analysis such as impact. Secondly, advanced remeshing techniques needs to be employed to accommodate the advancing crack so as to obtain a consistent or reliable values of G_c. Perhaps more importantly, the VCCT method requires a pre-defined delamination path in order to simulation crack growth. While this may be sufficient in modelling a simple Double Cantilever Beam (DCB) test, in a more complex analysis such as impact, the VCCT method may not be suitable. To overcome these problems, Chen et al. [113] proposed the Floating Node Method (FNM). The FNM employs 'floating' nodes which are not activated until any failure criterion is met. This is crudely illustrated in Figure 2.12, where it can be observed that the element is 'split' into two once the failure criterion is met. Compared to the original VCCT method, the FNM does not require any delamination path to be defined, as well as allowing multiple cracks to occur in an element. This is a desirable advantage, especially for impact modelling due to the complex nature of the impact event.

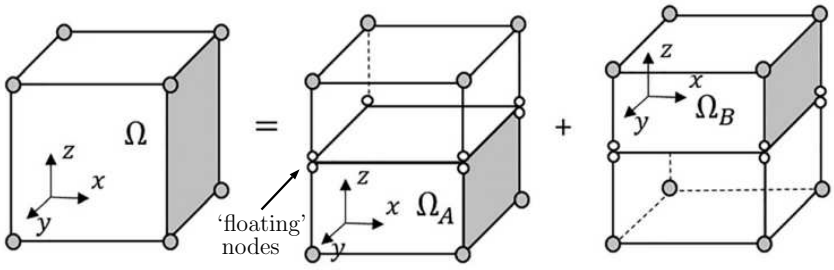


Figure 2.12: The Floating Node Method [111]

The CZM, perhaps the most widely used approach to model delamination, was originally built on the works of Dugdale [114] and Barenblatt [115]. The method is based on non-linear springs which connects the relevant parts (normally discretized into a finite number of elements between the top and bottom), and utilises fracture and damage mechanics to describe its behaviour. Upon reaching the tensile strength (delamina-

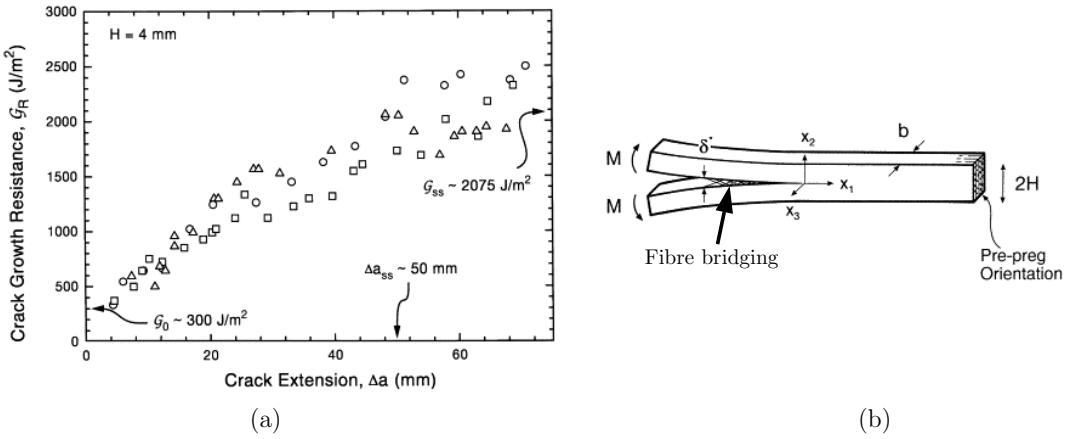
tion onset), the stiffness of the non-linear springs will be degraded until reaching zero strength. This region of strain softening (commonly known as delamination propagation) is normally identified as the process zone, in which mechanisms such as fibre-bridging or fibre pull-out is suggested to take place [116, 117]. Therefore, it is important that the properties related to the process zone is carefully selected to obtain reliable and accurate modelling results. Furthermore, it has been reported that a minimum number of element is required to capture the process zone behaviour. Following this, Turon et al. [118] proposed a method to artificially enlarge the cohesize zone length by reducing the interfacial strength, given by:

$$\bar{\tau}^0 = \sqrt{\frac{9\pi E G_c}{32 N_e^0 l_e}} \tag{2.10}$$

where E is the Young's modulus, G_c is the critical SERR, N_e is the minimum number of element inside the cohesive zone, and l_e is the mesh size in the direction of crack propagation. The authors reported that the method allows the use of large elements in the cohesive zone, hence significantly reducing the computational time, without compromising the results. Harper and co-workers [117] further investigated the original idea proposed by Turon et al. [118] by modifiying the interfacial strength to accommodate the use of coarse mesh sizes.

Later, Gutkin et al. [119] investigated the use of a tri-linear law following initial works by Sorenson et al. [120] to accurately describe the interlaminar behaviour of laminated composites, therefore resulting in a better correlation of the R-curve, especially for the one which has an increasing trend. It is generally understood that an R-curve which has an increasing trend (shown in Figure 2.13a) is normally associated with micromechanical strengthening mechanisms, such as the fibre-bridging effect (shown in Figure 2.13b). Furthermore, for some matrices, such as a thermoplastic resin, the influence of the matrices, inherent misalignment of the fibres, or even poor fibre-matrix debonding could further improve the delamination resistance of the composite, therefore requiring greater energy for each crack advance [121–123]. In general, a linear strain-softening has been utilised by many researchers [116, 117, 124–127] to represent the process zone during delamination propagation due to its simplistic approach, as well as being able to produce

reasonable prediction which correlates well with experimental results. However, some researchers argue that the bi-linear law is a crude approach in modelling delamination.



(a) (b)

Figure 2.13: (a) R-curve with an increasing trend (b) Illustration of fibre-bridging in a Double Cantilever Beam (DCB) specimen [120]

For this, advanced models such as the bridging law [120] were proposed to accommodate for such effects. Recently, Shokrieh et al. [128] proposed a multi-linear model which accommodate a single spring during loading and multiple springs during unloading (strain softening). Excellent agreement with the experimental results can be observed with a tri-linear softening (three springs during unloading) compared to a linear softening (one spring during unloading). Heidari-Rarani et al. [129] investigated the response of four different softening laws (linear, exponential, trapezoidal, and bi-linear) on End Notched Flexure (ENF) specimens for UD Glass/Epoxy laminates. It was found that the bi-linear softening (two linear slope during softening) produces the best result which agrees very well with the experimental results.

Further, mixed-mode delamination modelling has also been investigated by many researchers [116, 124–127], with most work built upon the original investigation by Benzeggagh and Kenane [130] and the mixed-mode failure criteria outlined by Reeder [131]. Mixed-mode simulations were then evaluated with experimental tests such as the Fixed Rate Mixed Mode (FRMM) or the Mixed-Mode Bending (MMB). Recently, de Moura et al. [132] proposed a novel energy-based mixed-mode CZM to predict the delamination behaviour of laminated composites. They argued that the existing CZM has inherent inconsistencies due to the inherent relative displacement formulation in the approach. The

novel numerical approach yields better stability and consistency under several 'mode-mixity', as well being able to accurately predict the critical fracture energy at each mode.

Recently, alternative approaches to simulate the interaction between matrix cracking and delamination (typically known as delamination migration) have been explored. The use of the VCCT method coupled with FNM has also been proposed to model delamination migration in laminated composite [133]. An alternative approach to model delamination migration was studied by Shi and co-workers [134] using the Equivalent Constraint Model (ECM), in which interface cohesive elements were inserted parallel to the fibre direction and equally spaced so as to represent matrix failure. Kumar et al. [135] extended the works of Shi et al. [134] by expanding the zero-thickness interface elements to include delamination failure so as to predict inter-ply and intra-ply crack growth.

Finally, a note on the two commonly used cohesive models: cohesive surfaces and cohesive elements. Although the formulation behind the two models is very similar, in which both models employ the stress-based traction-separation law, some subtle differences exist. First, the cohesive surface is based on a contact algorithm, where the 'slave and master' nodes (top and bottom nodes of the relevant parts) are usually in contact. Upon failure, the nodes which are in contact is released, representing crack growth. In the cohesive elements model, the 'slave and master' elements are connected with explicit elements. Failure occurs when the imposed criterion is met, and the elements can either be assigned zero-stress or be deleted from the analysis.

2.4 Summary

The literature review covered in this chapter highlights several important features in the problem of impact on composite structures. There is a good qualitative understanding of the mechanics of impact, and the damage types associated with the type of impact loading, in particular, LVI and HVI. There is also a consensus in whether the impact event should be categorised as LVI or HVI, allowing researchers to characterise the damage types associated with each velocity regime. More importantly, the review highlights

the potential use of polymer fibre composites as a substitute for conventional fibre types such as CF and GF. This is due to their excellent mechanical properties, resulting in an enhanced impact performance. However, the poor compressive properties, both in strength and modulus restricts the use of polymer fibre composites as structural components. Thus, to overcome this drawback, an alternative solution is explored to improve the compressive properties of polymer fibre composites, without compromising their impact performance. One potential solution is composite hybridisation, where the polymer fibre composite is combined with composite laminates possessing superior compressive properties. The final laminate yields enhanced compressive properties and an excellent resistance to impact loading.

A critical step in optimising the hybrid composite is with the use of numerical techniques, such as the FEM. However, this requires a detailed understanding of the composite behaviour, potentially involving extensive laboratory experiments. In recent years, the increasing maturity of numerical models for predicting damage and failure of laminated composite enables an accurate analysis to be performed, hence reducing the number and complexity of tests required. The development of energy-based models, used in conjunction with damage mechanics, allows accurate determination of the composite material status to be determined, thus enabling the full potential of the composite to be exploited. The recent interest in multi-scale modelling may well be a future direction to reduce the number of mechanical testing, since only the fibre and matrix information would be required as input. Ideally, this information should be readily available from the manufacturer, which would greatly minimise the number of tests to be performed. Models could be developed at the micro-scale level, which may then be analysed using analytical techniques. The information derived at the micro-scale level could then passed to the meso-scale level, and then the macro-scale which can then be used to model complex design problems such as impact. However, a complete understanding of the composite behaviour must be achieved, to enable accurate and reliable models to be developed.

Chapter 3

Material Characterisation

3.1 Introduction

The determination of the elastic properties of laminated composites, particularly the stiffness, strength, and strain-to-failure is important for design purposes. These are also important because they can be used to validate numerical models. The characterisation of laminated composites usually only covers the in-plane properties of the laminate, and the through-thickness properties are often estimated or ignored. This is due to several reasons, including:

(i) Economical reasons - time and cost involved;

(ii) Often, laminated composites are analysed using simplified theories, such as the Classical Laminate Theory (CLT), which ignores the through-thickness properties. Therefore, through-thickness properties are not always needed.

Thus, in the current testing programme, only the in-plane properties are measured which include tension[1], compression[2], and $\pm 45^\circ$ in-plane shear.

[1] 0° and 90° for carbon/epoxy and only orthotropic tension for Vectran/MTM57 and S2-Glass/MTM5

[2] 0° and 90° for carbon/epoxy and only orthotropic compression for Vectran/MTM57 and S2-Glass/MTM57

Three different laminated fibre composites were used in this PhD, namely:

(i) IM7/8552 - Unidirectional Carbon/Epoxy supplied by Hexcel;

(ii) S2-Glass/MTM57 - 0°/90° Non-Crimp Fabric (NCF) with an epoxy resin. The fabric is supplied by Sigmatex and the resin is supplied by Cytec;

(iii) Vectran/MTM57 - 0°/90° Non-Crimp Fabric (NCF) with an epoxy resin. The fabric is supplied by Sigmatex and the resin is supplied by Cytec.

For reference, the mechanical properties obtained from the literature for each of the fibre, matrix, and fabric properties are described in Table 3.1. The following subsections presents the results of the characterisation tests for all of the composites stated.

Table 3.1: Properties for selected fibres and its constituents [58–60, 136]

Properties	Fibre/resin			
	IM7/8552	S2-Glass	Vectran	MTM57
Density (g/cm^3)	1.58	2.48	1.41	1.19
Thickness (mm)	0.125	0.126	0.224	0.178
Tensile Strength (MPa)	2600	4890	3200	80.1
Tensile Modulus (GPa)	165	86.9	75	2.68
Tensile strain-to-failure (%)	1.6	5.7	3.8	3.9
Areal weight (gsm)	134	312	312	212/319

3.2 Data Reduction

3.2.1 Tension

Tension tests were performed in accordance with the ASTM standard [137] for tensile testing of composite laminates. For IM7/8552, two different strength and stiffnesses were measured to obtain the longitudinal (0°) and transverse (90°) properties of the laminate. In contrast, only one stiffness and strength value was determined for S2-Glass/MTM57 and Vectran/MTM57. This is due to the cross-ply nature of the fabric, where the longitudinal and transverse properties were assumed to be the same. The strength

values were recorded at the point of failure, and the tensile moduli were calculated using the strength values measured at longitudinal strain levels of approximately 0.1% and 0.3% (corresponding to the elastic region of the composite). Finally, the Poisson's ratio was calculated by dividing the transverse and longitudinal strains at strain values of approximately 0.1% to 0.3%.

3.2.2 Compression

For compression, testing was performed following the Imperial College London procedure for testing in compression [138]. The procedure and specimen dimensions are very similar to that of the recommended ASTM standard [139]. The only differences are the geometry of the loading fixture and the length of the specimen.

Two different strength and stiffness values were computed for IM7/8552 to obtain the properties corresponding to the longitudinal (0°) and transverse (90°) direction of the laminate. Similar to tensile, only one strength and stiffness value was computed for S2-Glass/MTM57 and Vectran/MTM57 under compressive loads. The strength values were recorded at the point of failure, and the compressive moduli were calculated using the strength values measured between the longitudinal strain levels of approximately 0.1% and 0.3% (corresponding to the elastic region of the composite).

3.2.3 ±45° In-plane shear

±45° in-plane shear testing was performed in accordance to the recommended ASTM standard [140]. The maximum shear strain, γ, was computed from the longitudinal, ϵ_l, and transverse, ϵ_t, strains as:

$$\gamma = \epsilon_l - \epsilon_t \tag{3.1}$$

Finally, the shear stress can be computed from the applied uniaxial load, P, and the cross-sectional area, A, of the specimen, as shown below:

$$\tau = \frac{P}{2A} \tag{3.2}$$

The shear modulus, G_{12}, was determined between strain levels of approximately 0.2%

to 0.6%. The change in the specimen width due to fibre rotation can be determined by expanding Equation 3.2 to give [95]:

$$\tau = \frac{P}{A} \sin\left(\frac{\pi}{4} - \gamma\right) \cos\left(\frac{\pi}{4} - \gamma\right) \tag{3.3}$$

where A in Equation 3.3 is the specimen's cross-sectional area considering the width reduction, given by:

$$A = t \times W_0(1 - |\varepsilon_t|) \tag{3.4}$$

where W_0 is the initial specimen width and t is the thickness.

3.3 Manufacturing

The Resin Film Infusion (RFI) was employed for S2-Glass/MTM57 and Vectran/MTM57 laminates due to the use of resin films (MTM57). The resin films are placed between the NCF layers up to the desired thickness. No resin films were employed for IM7/8552, since the fibres (IM7) were already impregnated with the 8552 matrix. Table 3.2 presents the nominal plate dimensions for each in-plane test.

The stacked laminates were then placed under a vacuum table to remove any excess air pockets or bubbles in the fabric/resin interface. Especially for Vectran/MTM57 and S2-Glass/MTM57, the Resin Film Infusion (RFI) technique was utilised in the autoclave cure due to the use of resin films (MTM57) in the layup. The completed layup was cured in an autoclave following the recommended cure cycle from the respective resin supplier [141, 142]. Upon curing, laminates were then examined for any defects using an ultrasonic C-scan, before cutting them into specific dimensions using a water-jet cutter. This is illustrated in Figure 3.1, with the plated dimensions presented in Table 3.2. A schematic of the specimen is shown in Figure 3.2, with the dimensions specific for each test shown in Table 3.3. Laminates were then examined for any defects using an ultrasonic C-scan, before placing end tabs on each specimen, as shown in Figure 3.1. A two part epoxy-hardener (Araldite 2011) was used to bond the end tabs to the specimen. Specimens were then left overnight under a vacuum table to ensure good adhesion.

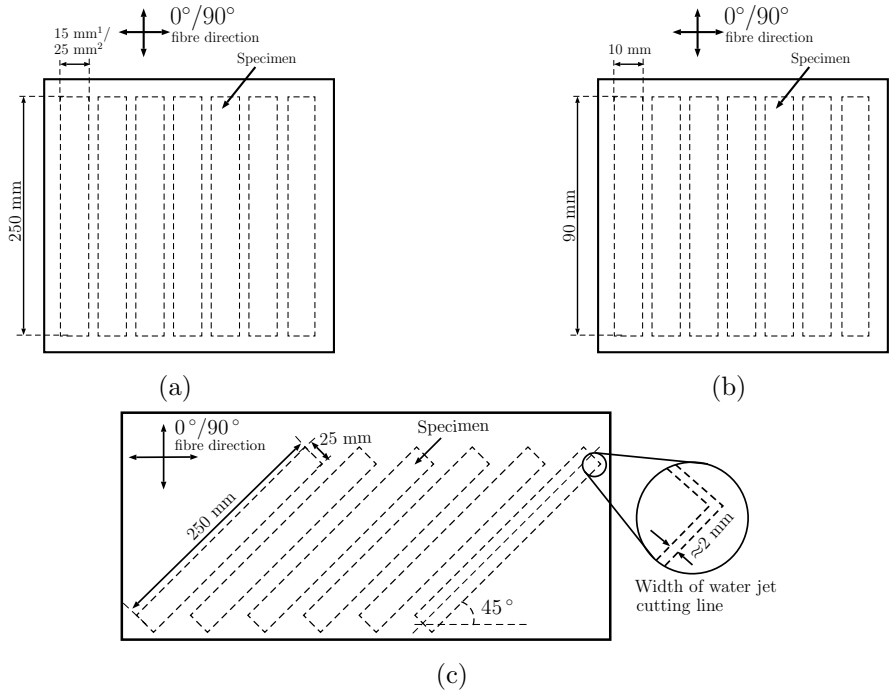


Figure 3.1: Typical cutting plans for quasi-static in-plane characterisation (a) Tensile. [1] denotes longitudinal tensile, and [2] denotes transverse and orthotropic tensile (b) Compression (c) ±45 °In-plane shear. Close up image showing the width of the water jet cutting line

Table 3.2: Nominal plate dimension and orientation for characterisation tests

Plate	Test	Dimensions (mm)	Layup	Thickness (mm)
1	Tensile (0 °)[3]	300 x 300	$[0\,^\circ]_8$	1
2	Tensile (90 °)[3]	300 x 300	$[90\,^\circ]_{16}$	2
3	Tensile orthotropic[4]	300 x 300	$[0\,^\circ/90\,^\circ]_3$	2
4	Tensile orthotropic[5]	300 x 300	$[0\,^\circ/90\,^\circ]_{4s}$	2
5	±45 °In-plane shear[3]	450 x 450	$[0\,^\circ/90\,^\circ]_{8s}$	2
6	±45 °In-plane shear[4]	450 x 450	$[0\,^\circ/90\,^\circ]_{3s}$	2
7	±45 °In-plane shear[5]	450 x 450	$[0\,^\circ/90\,^\circ]_{4s}$	2
8	Compression (0 °) [3]	110 x 80	$[0\,^\circ]_{16}$	2
9	Compression (90 °) [3]	110 x 80	$[0\,^\circ]_{32}$	4
10	Compression orthotropic[4]	110 x 80	$[0\,^\circ/90\,^\circ]_{6s}$	4
11	Compression orthotropic[5]	110 x 80	$[0\,^\circ/90\,^\circ]_{8s}$	4

[3]IM7/8552
[4]Vectran/MTM5
[5]S2-Glass/MTM57

Table 3.3: Nominal specimen dimensions: In-plane

Specimen	L (mm)	W (mm)	t (mm)	b (mm)	h (mm)
tL[6]	250	15	1	50	1.5
tT[7]	250	25	2	50	1.5
tO[8]	250	25	2	50	1.5
ipS[9]	250	25	2	50	1.5
cO[10]	90	9.5	4	40	1.5

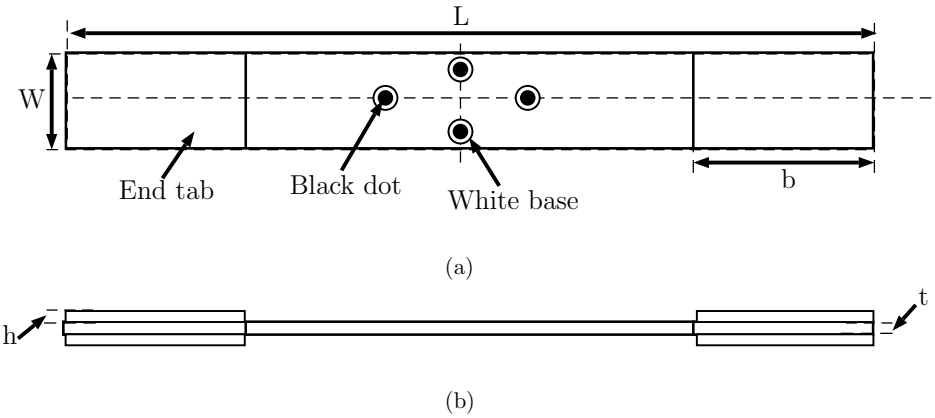


Figure 3.2: Typical specimen schematic (a) Top view (b) Side view

3.4 Testing

Testing was performed using the Instron 5960 with a load cell rated to a maximum load of 50 kN. The load cell has an accuracy of ±0.5% when reading down to 1/1000 of the load cell capacity. At least five specimens were tested for each composite, with a fixed loading rate of 2 mm/min, in-line with the recommmendation from relevant standards [137, 138, 140]. Except for compression specimens, four black and white dots of approximately 3 mm in diameter were made on the specimen prior to testing. The black and white dots were used as reference points by the Imetrum video extensometer to measure the longitudinal and transverse strains. The Imetrum optical strain video

[6] denotes tensile longitudinal (0 °)
[7] denotes tensile transverse (90 °)
[8] denotes tensile orthotropic (0 °/90 °)
[9] denotes ±45 ° in-plane shear
[10] denotes compression orthotropic (0 °/90 °)

extensometer is based on the Digital Image Correlation (DIC) system, with resolutions of up to 1/500th pixel and a measurement accuracy within 1% of the experimental value. Further, it has the advantage of measuring strain values of more than 5% (whereupon strain gauges would fail), which is desirable since some of the testing (such as the $\pm 45\,^{\circ}$ in-plane shear) involves strain values of up to 75%.

The white base was fabricated using a 'tipp-ex' correction fluid, and the inner black dots using a black extra-fine tip pen. Figure 3.2a illustrates the typical specimen configuration for use with the Imetrum video extensometer. For compression specimens, strain gauges were placed on the front and back surface of the specimen to measure the strain values under compression loading.

3.5 Results

Subsections 3.5.1 to 3.5.3 present results of the in-plane characterisation for IM7/8552, Vectran/MTM57, and S2-Glass/MTM57 composite laminates. The results are presented to enable a direct comparison on the behaviour of each composite material.

3.5.1 Tensile response

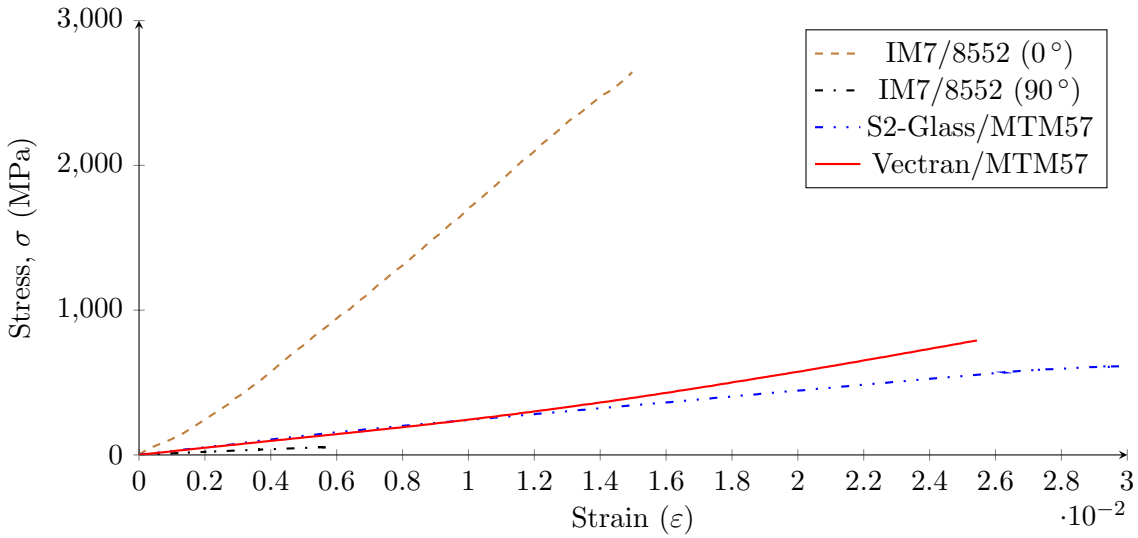


Figure 3.3: Average tensile stress-strain response for each of the composite material

Figure 3.3 illustrates the average stress-strain response for all composites used in this study. It can be observed that IM7/8552 has the highest strength and stiffness when loaded in the longitudinal direction. When loaded perpendicular to the fibre direction, the tensile stiffness, strength, and strain-to-failure were significantly lower. The average longitudinal and transverse strengths for IM7/8552 are shown in Figure 3.4. The average calculated longitudinal strength and modulus was 2681 MPa (CV: 4.58%) and 131.4 GPa (CV: 8.29%), respectively. The transverse strength and modulus were computed to be 64.1 MPa (CV: 8.72%) and 9.7 GPa (CV:6.5%), respectively.

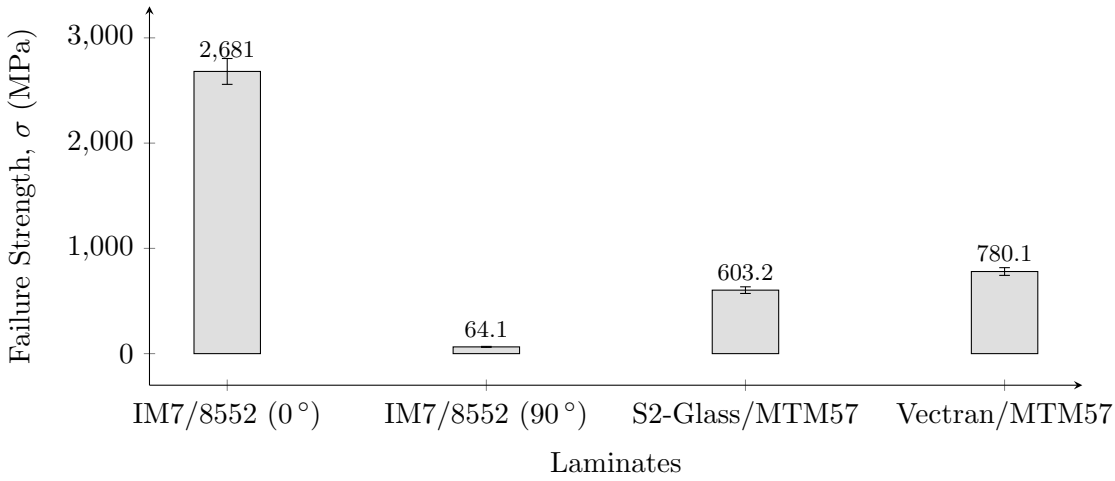
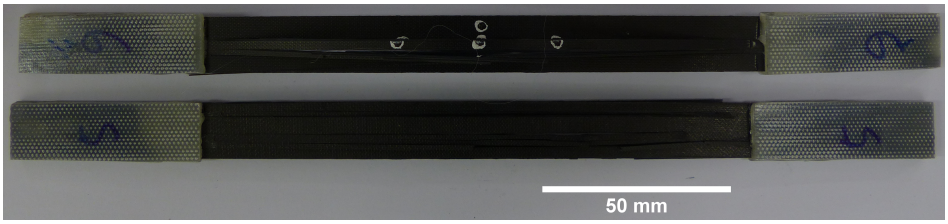


Figure 3.4: Tensile strength for all three composite laminates. Error bars represent the variation of tensile strength between five specimens

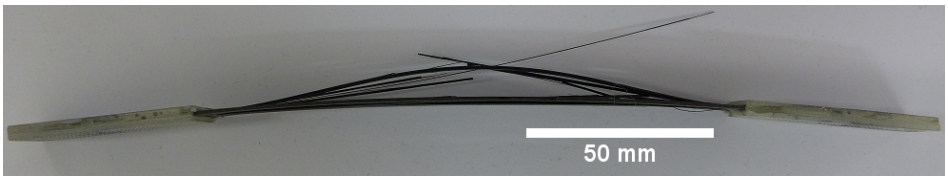
Failure was explosive for all longitudinal specimens (ASTM designation: XUU [137]), shown in Figure 3.5, whilst a sudden failure across the specimens (parallel to the fibre direction) was observed for the transverse specimens (ASTM designation: LGM), shown in Figure 3.6.

For S2-Glass/MTM57 laminates, a significantly higher tensile strain-to-failure was observed, with a strain value of up to 3%, compared to IM7/8552 ($\varepsilon_l \approx 1.6\%$). However, a considerably lower tensile strength and modulus were obtained if compared to IM7/8552, computed to be 603.2 MPa (CV: 5.18%) and 28.7 GPa (CV: 5.06%) respectively. This is thought to be due to a higher presence of surface flaws, which are an inherent characteristic of glass fibres [143]. The tensile strength for S2-Glass/MTM57

specimen is shown in Figure 3.4. In general, a sudden failure (ASTM designation: SGM) was observed, due to the cross-ply architecture of the fabric, shown in Figure 3.8a.



(a)



(b)

Figure 3.5: Failed longitudinal (0 °) IM7/8552 tensile specimens (a) Top view (b) Side view

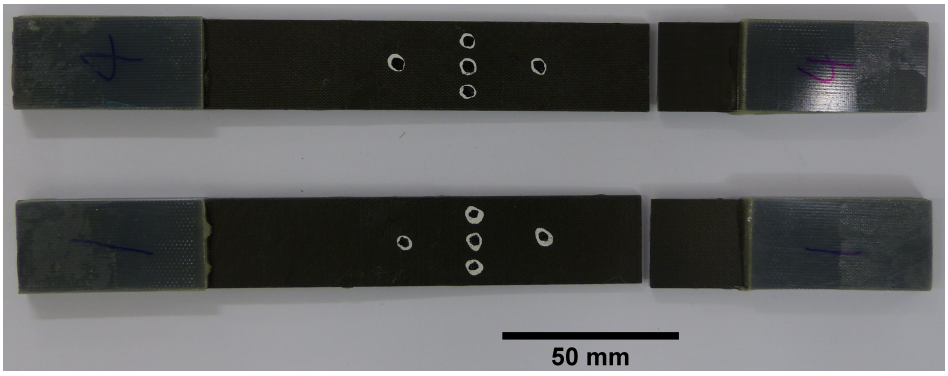
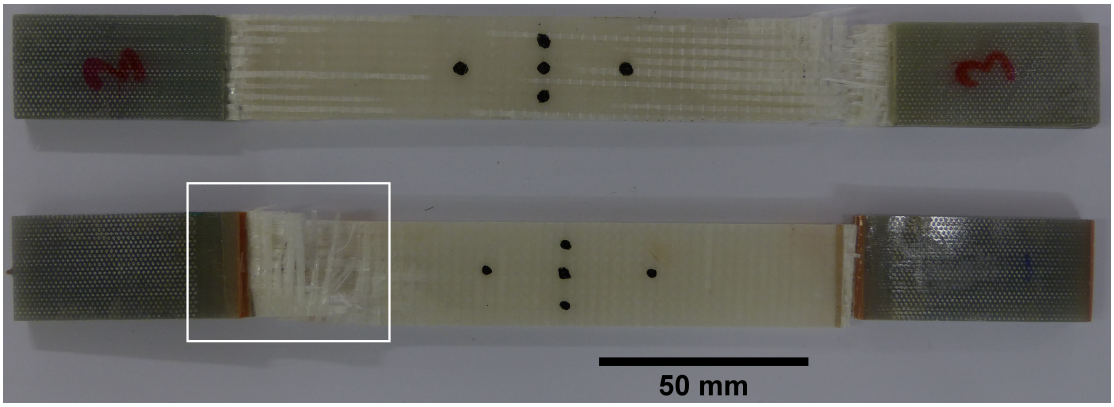
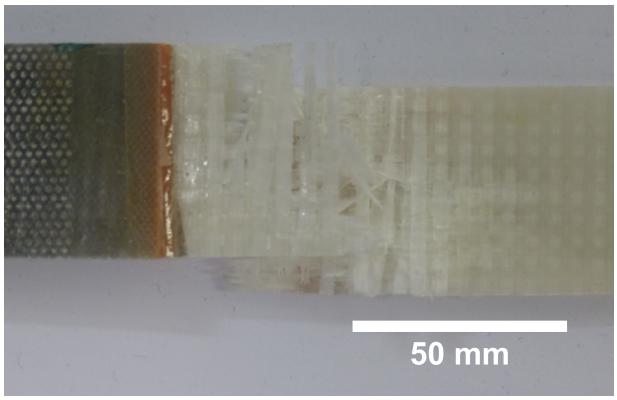


Figure 3.6: Failed transverse (90 °) IM7/8552 tensile specimens



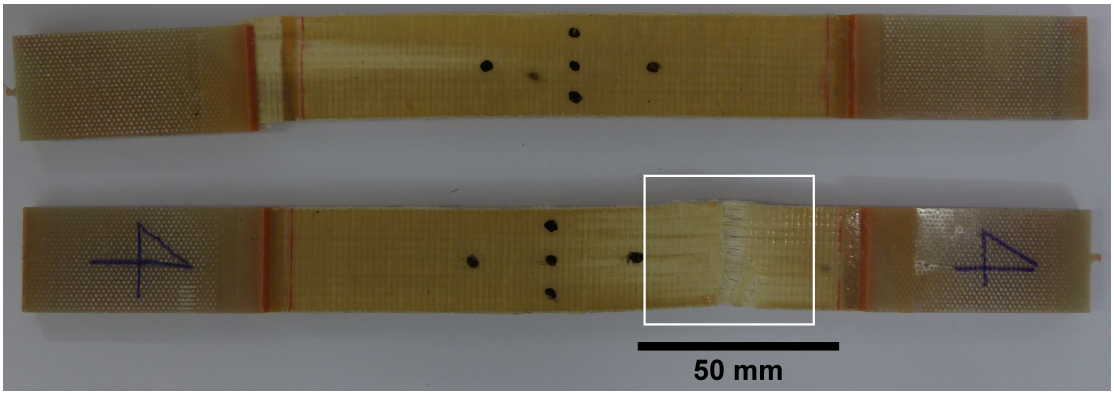
(a)



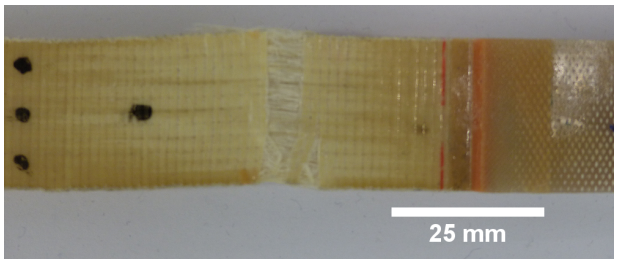
(b)

Figure 3.7: (a) Typical failed S2-Glass/MTM57 tensile specimens (b) Close up view of on the white square in (a)

The tensile strength for Vectran/MTM57 specimen is presented in Figure 3.4. The average tensile strength was calculated to be 780.1 MPa (CV: 4.62%), and the average tensile modulus was 24.2 GPa (CV: 1.86%). Images of the failed specimens are presented in Figure 3.8, where the majority of failures occured at the gauge region (ASTM designation: LGM). A non-linear response can be observed in Figure 3.3, where it was thought to be due to the 'cold-drawing' process [144,145] of the polymeric macromolecules during the tensile test. A similar behaviour was also exhibited by other low modulus fibres such as Kevlar 29, Kevlar 119, Kevlar 129, and Twaron [144]. Another possible explanation could be due to the so-called 'skin-core' morphology of Thermotropic Liquid Crystal Polymer (TLCP) fibres [146–148].



(a)



(b)

Figure 3.8: (a) Typical failed Vectran/MTM57 tensile specimens (b) Close up view of on the white square in (a)

The 'skin-core' structure is a manifestation of the manufacturing process of Vectran fibres, which is highly sensitive to the processing condition (i.e. temperature, draw ratio, etc.). Upon being drawn, the outermost surface 'solidifies' quicker compared to other structures towards the 'core'. This is because the outermost surface (or the 'skin') was directly in contact with the spinneret. Consequently, a higher shear flow was induced on the surface of the fibre, which improves the crystallinity and the molecular orientation of the 'skin' structure. However, the magnitude of the shear flow decreases towards the 'core', resulting in an amorphous molecular structure. Therefore, the 'skin' structure will often possess higher tensile modulus, with lower tensile strength and strain-to-failure, and a decreasing tensile modulus towards the core, with a higher tensile strain-to-failure. Hence, failure will first initiate at the skin, which then propagates inwards to the core.

3.5.2 Compressive response

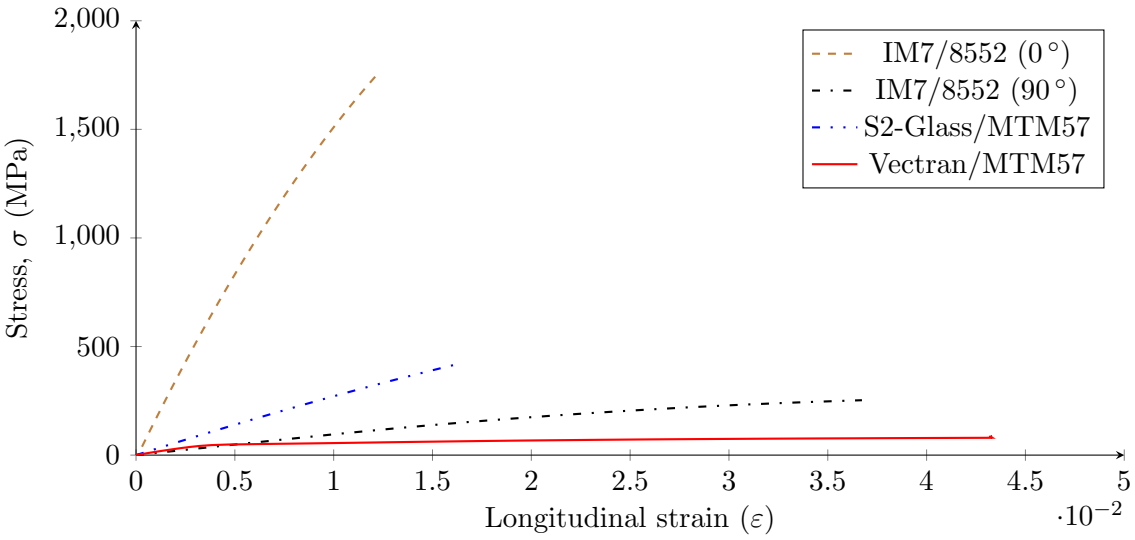


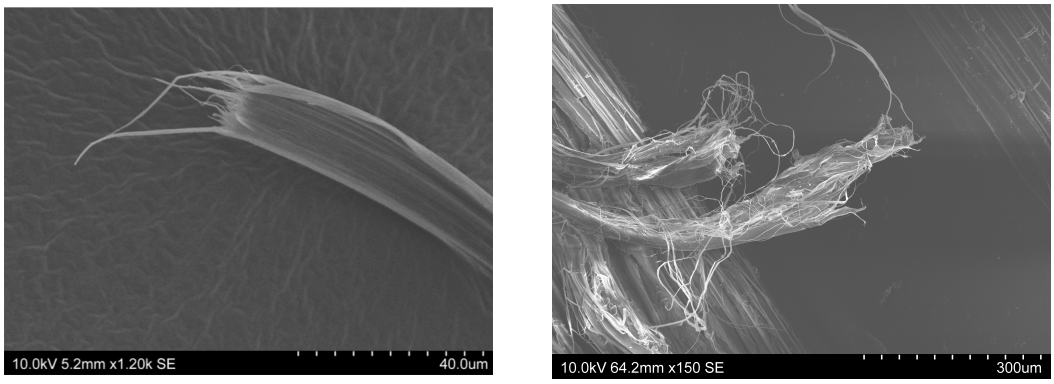
Figure 3.9: Average compressive stress-strain response from each fibre reinforced composite used

Figure 3.9 presents the compressive stress-strain response for IM7/8552, S2-Glass/MTM57, and Vectran/MTM57 composites. A superior compressive behavour can be observed for IM7/8552 laminates, with an average compressive modulus of 165.6 GPa (CV: 1.65%) and an average compressive strength of 1465.6 MPa (CV: 7.11%). For reference, Figure 3.12 presents the longitudinal compressive strength for IM7/8552. In contrast, Vectran/MTM57 laminates exhibited the lowest compressive behaviour, shown in Figure 3.9, with an average compressive strength of 84.1 MPa (CV: 8.7%) and an average compressive modulus of 13.9 GPa (CV: 2.45%).

The superior compressive properties of IM7/8552 can be attributed to its molecular structure, in which the presence of lateral covalent bonds have resulted in a much superior compressive strength than Vectran/MTM57 [149]. This is not the case in Vectran fibres. The weak intermolecular forces which link the chain polymeric structure [149,150] is one of the primary reasons behind the poor compressive performance. In addition, the fibrillar nature of Vectran fibres, shown in Figure 3.10, tends to defibrillate rapidly when placed under compressive loads.

At approximately 38 MPa, the Vectran/MTM57 specimens was observed to yield, beyond which strain-hardening was observed to occur in the stress-strain response, Fig-

ure 3.9. At failure, kink-bands at approximately 45 ° angle were observed to appear in each specimen, shown in Figures 3.11b and 3.11c. Some specimens were observed to delaminate at the middle ply (shown in Figure 3.11c) during kink-band formation. In most cases, kink-bands were observed to be oriented at approximately 45 ° with respect to the loading axis. It must be noted that for Vectran/MTM57, failure was defined where 'crushing' was observed due to kink-band saturation at the gauge region. The compressive strength for Vectran/MTM57 is shown in Figure 3.12.

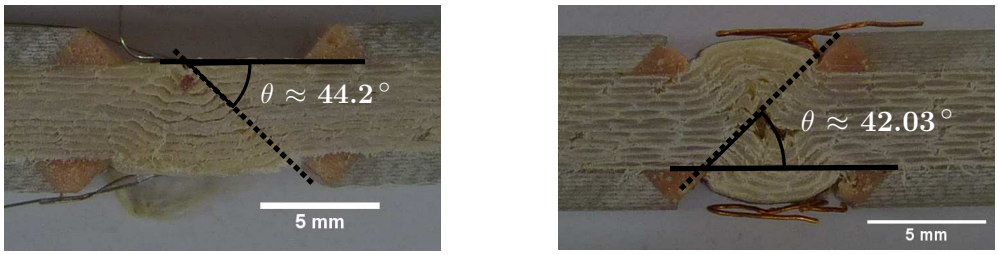


(a) (b)

Figure 3.10: Defibrillation in Vectran (a) Defibrillation in a single fibre under tensile loading [148] (b) Defibrillation in a laminate under ±45 ° in-plane shear loading



(a)



(b) (c)

Figure 3.11: (a) Typical failed Vectran/MTM57 compressive specimens (b) Close up image on the failure region shown in (a) - bottom (c) Close up image on the failure region shown in (a) - top

For IM7/8552 longitudinal laminates, failure was observed to occur near the gauge region (ASTM designation: HAT) with some specimens failing near the tab region (ASTM designation: HIT), shown in Figure 3.13. An almost linear response was exhibited in the stress-strain response, Figure 3.9. The slight non-linearity may be explained by an initial fibre misalignment which promotes shear stress between the fibres, therefore resulting in the deviation from the linear behaviour with increasing stress. The average longitudinal compressive strength was 1465.7 MPa (CV: 7.11%), shown in Figure 3.12. Additionally, the average compressive modulus was computed to be 165.6 GPa (CV: 1.65%).

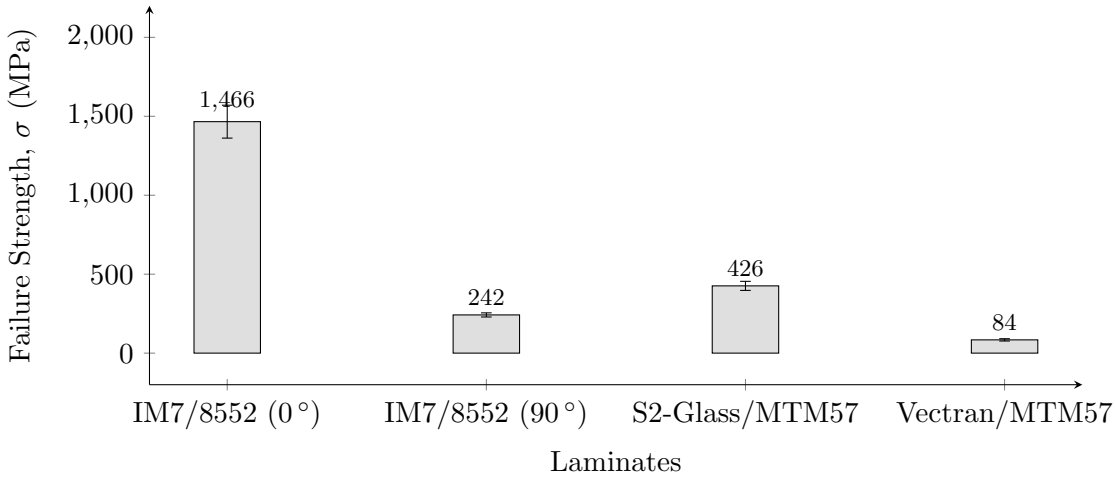


Figure 3.12: Compressive strength for all three composite laminates. Error bars represent the variation of compressive strength between five specimens

Subsequently, the transverse compressive stress-strain response for IM7/8552 was shown in Figure 3.9, exhibiting some non-linearity beyond 1% strain values. This is a typical response usually observed in transverse (matrix) dominated compressive failure, which usually possesses some plastic behaviour [151], hence exhibiting a strain-hardening response prior to failure. The transverse compressive strength for IM7/8552 is reported in Figure 3.12. The average compressive strength and modulus was calculated to be 242 MPa (CV: 5.39%) and 9.6 GPa (CV: 0.45%), respectively. Images of the failed specimens are presented in Figure 3.14, where failure can be seen to occur in the gauge region (ASTM designation: HAT).

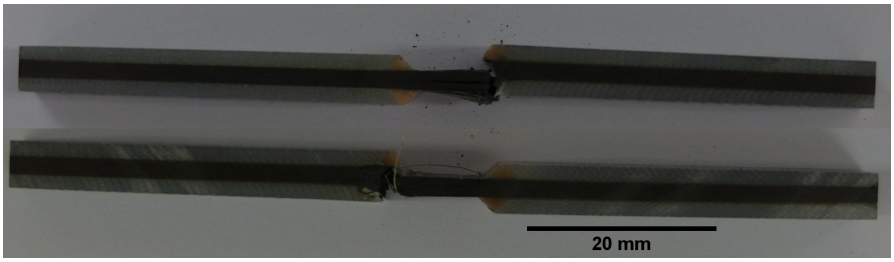
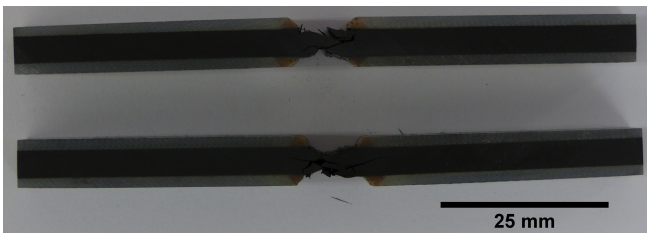
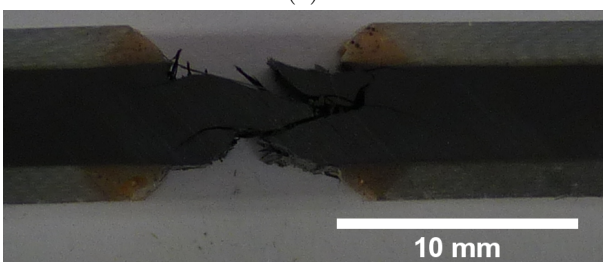


Figure 3.13: Typical failed IM7/8552 longitudinal (0 °) compressive specimens

The compressive strength for S2-Glass/MTM57 for each specimen is reported in Figure 3.12. The average compressive strength was calculated to be 425.6 MPa (CV: 6.75%) whilst the average compressive modulus was 28.2 GPa (CV: 2.12%). All specimens failed near the gauge region (ASTM designation: HAT), shown in Figure 3.15. A linear stress-strain response up to failure was observed for S2-Glass/MTM57, shown in Figure 3.9, exhibiting a common response for brittle fibre based composites. The compressive strength for S2-Glass/MTM57 is shown in Figure 3.12.

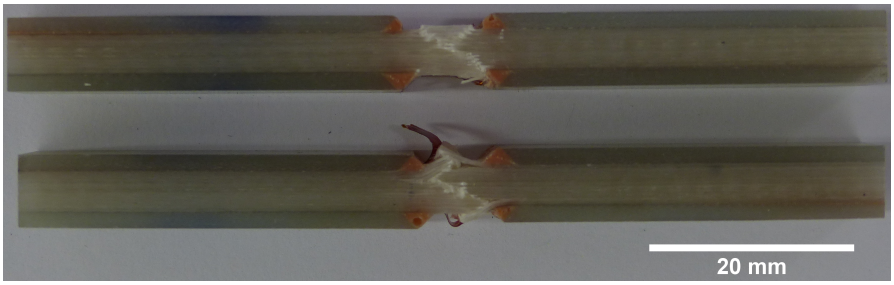


(a)

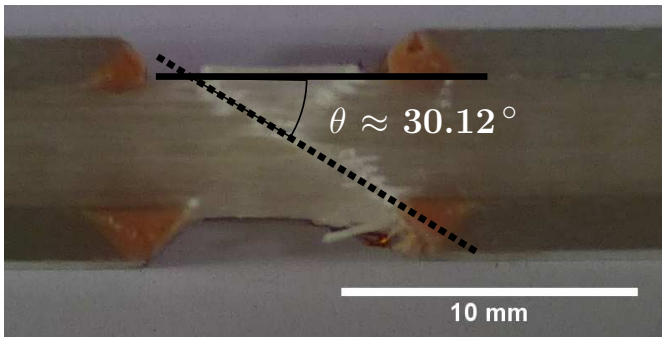


(b)

Figure 3.14: (a) Failed IM7/8552 transverse (90 °) compressive specimens (b) Close up image on the failure region shown in (a) - top



(a)



(b)

Figure 3.15: (a) Failed S2-Glass/MTM57 compressive specimens (b) Close up image on the failure region shown in (a) - top

3.5.3 ±45° In-plane shear response

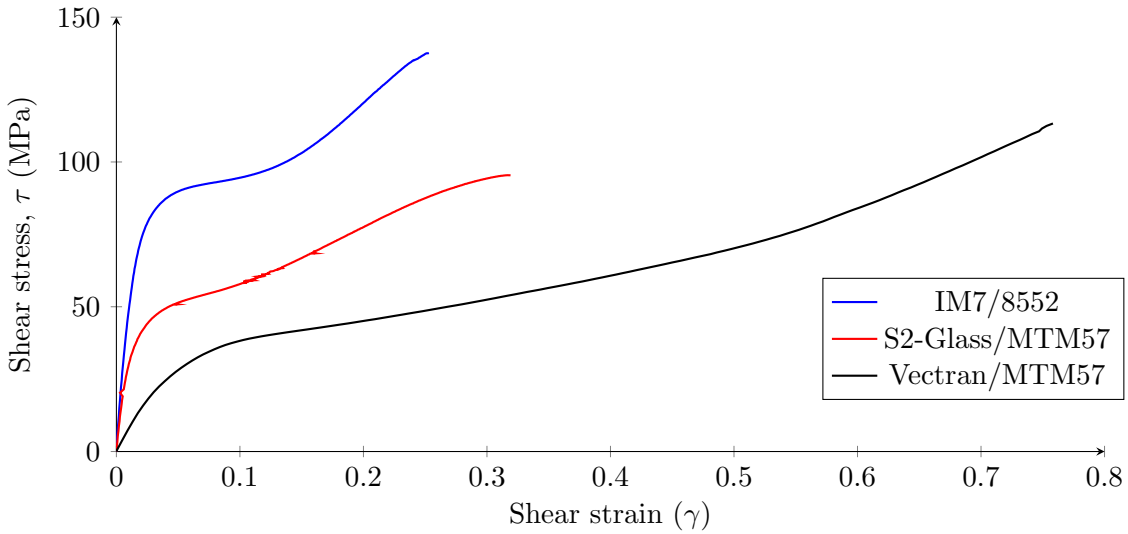


Figure 3.16: Average ±45° in-plane shear response from each fibre reinforced composite

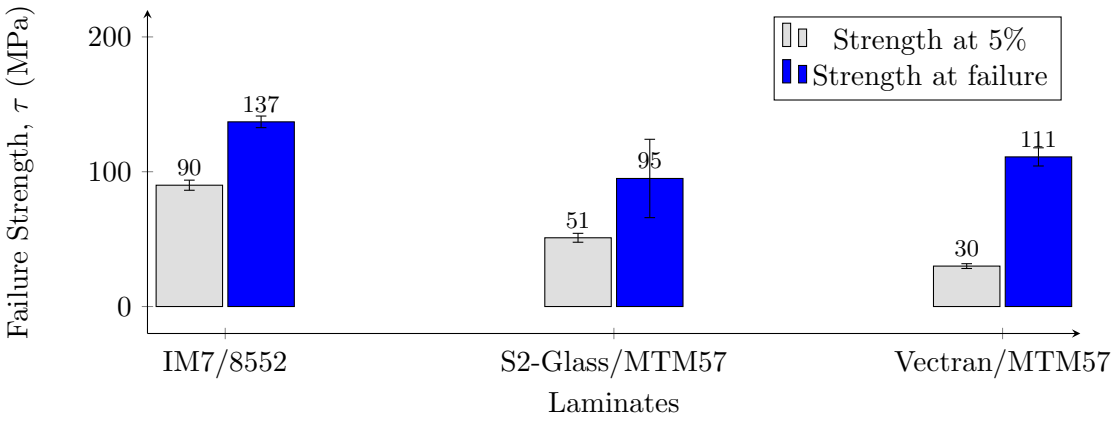
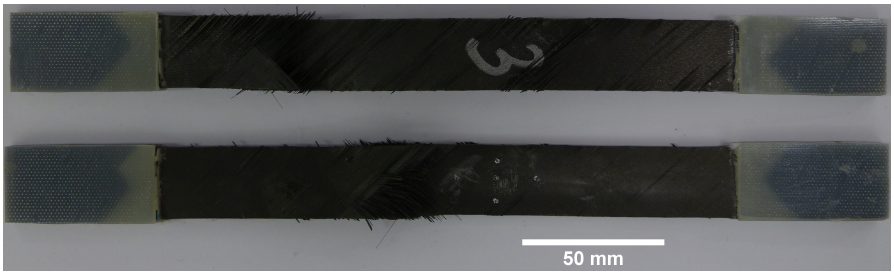
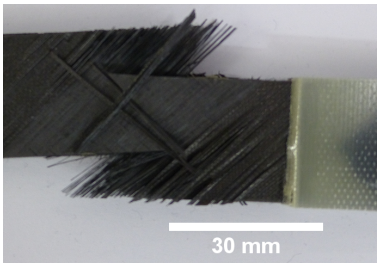


Figure 3.17: ±45 ° In-plane strength for all three composite laminates. Error bars represent the variation of shear strength between five specimens

Figure 3.16 presents the ±45 ° in-plane shear response for IM7/8552, Vectran/MTM57 and S2-Glass/MTM57 composite laminates. The highest shear strength with respect to shear strain was observed for IM7/8552, whilst the lowest was seen for Vectran/MTM57. The shear strength for IM7/8552 is reported in Figure 3.17, with an average shear strength at 5% shear strain calculated to be 90 MPa (CV: 4.17%) and 137.1 MPa (CV: 3.14%) at failure. For Vectran/MTM57, a linear response was observed initially until reaching a shear stress of approximately 23 MPa, beyond which strain-hardening was oberved to occur. The ultimate shear strain was seen to be the highest compared to IM7/8552 and S2-Glass/MTM57, reaching strain values of up to ≈ 75% at failure. The average ±45 ° in-plane shear strength at 5% shear strain was calculated to be 29.6 MPa (CV: 6.03%) and 110.8 MPa (CV: 6.09%) at failure. The shear strength for Vectran/MTM57 is shown in Figure 3.17.



(a)

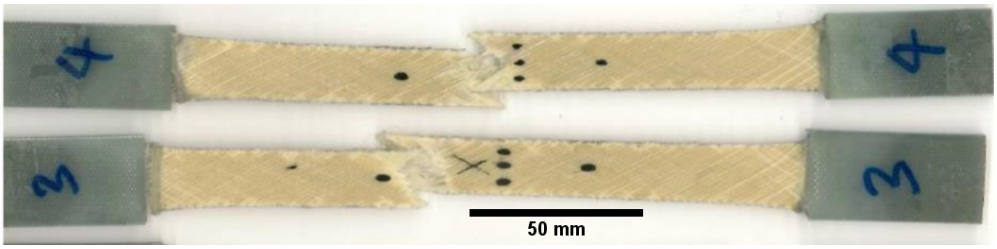


(b)

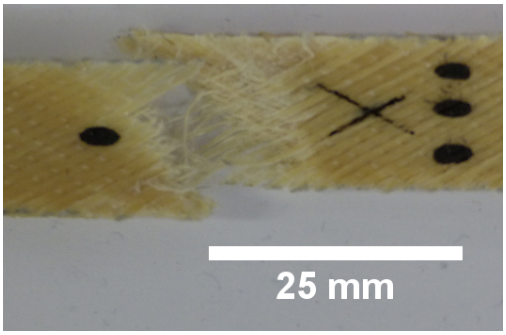
Figure 3.18: (a) Failed $\pm 45^\circ$ in-plane shear IM7/8552 specimens (b) Close up image on the failure region shown in (a) - top

The shear strength for S2-Glass/MTM57 is reported in Figure 3.17, with an average shear strength at 5% shear strain computed to be 51.4 MPa (CV: 6.43%), and at failure to be 95 MPa (CV: 4.35%).

Fibre rotation was observed to occur for all composite laminate used in this study. For S2-Glass/MTM57 and Vectran/MTM57 laminates, a considerable reduction in width was observed prior to failure, whilst minimal change in width was seen for IM7/8552. This may be due to the poor fibre-matrix interfacial properties for S2-Glass/MTM57 and Vectran/MTM57 laminates, compared to IM7/8552. As a consequence, the shear modulus for IM7/8552 was the highest amongst all three composites, calculated to be 5.3 GPa (CV: 3.19%), compared to 3.4 GPa (CV: 12.04%) for S2-Glass/MTM57, and 0.8 GPa (CV: 6.8%) for Vectran/MTM57. All specimens failed around the gauge region (ASTM designation: SGM), shown in Figures 3.18, 3.19, and 3.20, for IM7/8552, Vectran/MTM57, and S2-Glass/MTM57, respectively.



(a)

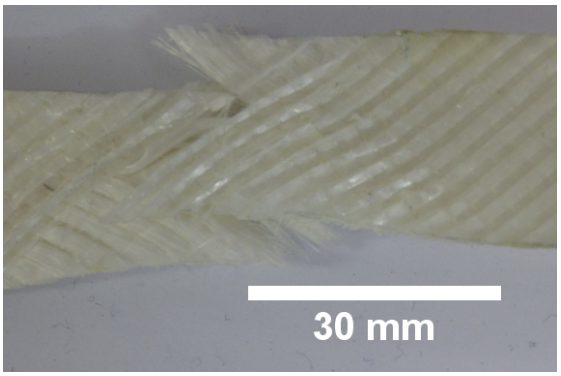


(b)

Figure 3.19: (a) Failed ±45° in-plane shear Vectran/MTM57 specimens (b) Close up image on the failure region in specimen 3



(a)



(b)

Figure 3.20: (a) Failed ±45° in-plane shear S2-Glass/MTM57 specimens (b) Close up image on the failure region in specimen 3

3.6 Summary of the in-plane characterisation for all composite materials

The average measured values of all in-plane properties for all materials are summarised in Table 3.4.

Table 3.4: In-plane material characterisation properties

Mechanical Properties	IM7/8552	S2-Glass/MTM57	Vectran/MTM57
		Modulus	
Tensile 0° (GPa)/C.V. (%)	131.4 (8.29)	28.7 (5.06)	24.2 (1.86)
Tensile 90° (GPa)/C.V. (%)	9.7 (6.5)	28.7 (5.06)	24.2 (1.86)
±45° In-plane shear (GPa)/C.V. (%)	5.3 (3.19)	3.4 (12.04)	0.8 (6.8)
Compression 0° (GPa)/C.V. (%)	165.6 (1.65)	28.2 (2.12)	13.9 (2.45)
Compression 90° (GPa)/C.V. (%)	9.6 (0.45)	28.2 (2.12)	13.9 (2.45)
		Strength	
Tensile 0° (MPa)/C.V. (%)	2681 (4.58)	603.2 (5.18)	780.1 (4.62)
Tensile 90° (MPa)/C.V. (%)	64.1 (8.72)	603.2 (5.18)	780.1 (4.62)
±45° In-plane shear (MPa)[11]/C.V. (%)	90 (4.17)	51.4 (6.43)	29.56 (6.03)
±45° In-plane shear (MPa)[12]/C.V. (%)	137.1 (3.14)	95 (4.35)	110.77 (6.09)
Compression 0° (MPa)/C.V. (%)	1465.7 (7.11)	425.6 (6.75)	84.1 (8.7)
Compression 90° (MPa)/C.V. (%)	242.1 (5.39)	425.6 (6.75)	84.1 (8.7)

3.7 Determination of the fibre volume fraction

3.7.1 Introduction

Two different methods were selected to determine the Fibre Volume Fraction (FVF) for the composites used in this study. In both cases, the optical microscope was employed to capture several images of the laminate cross-section. This was for two reasons. First, the optical microscope was used to measure the number of fibres in a tow for Vec-

[11] Shear strength at 5%
[12] Shear strength at failure

tran/MTM57 and S2-Glass/MTM57. This was to validate the data provided by the manufacturer on the NCF fabrics for Vectran and S2-Glass. Secondly, for IM7/8552, the optical microscope was employed to directly measure the FVF using the optical method [152, 153].

The FVF for S2-Glass/MTM57 and Vectran/MTM57 were then determined using the 'thickness measurement' method proposed by P. T. Curtis [154]. This method was selected since other approaches such as the resin burn off method [155] was not suitable for Vectran. This was due to its low fibre melting temperature, $T_m \approx 330°C$ [143, 145], which is considerably lower compared to the matrix (MTM57) burn-off temperature $> 500°C$ [143]. Furthermore, the 'thickness measurement' method allow for the influence of stitches in the NCF architecture to be excluded.

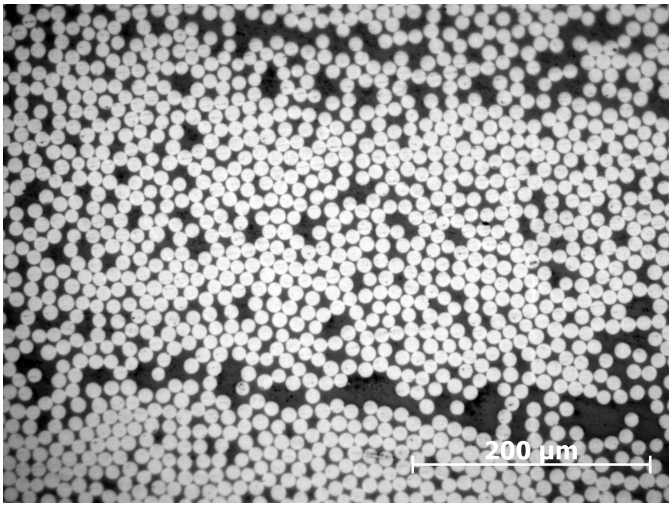
3.7.2 Procedure

For each composite, a 4 mm thick laminate was manufactured and cut into small pieces of 2 cm x 3 cm, before placing it into a small cylindrical pot (radius = 3 cm). A mixed solution of two part resin-hardener were then poured into the pot which was then left overnight to cure. The cured specimens were then polished using a four stage polisher before placing them under an optical microscope. Figure 3.21 presents images from the optical microscope for IM7/8552, S2-Glass/MTM57, and Vectran/MTM57 composites. A Matlab code was written to aid the counting process by marking each counted fibres, therefore ensuring that the fibres were not counted twice. The amount of fibres were then recorded in a separate file for post-processing.

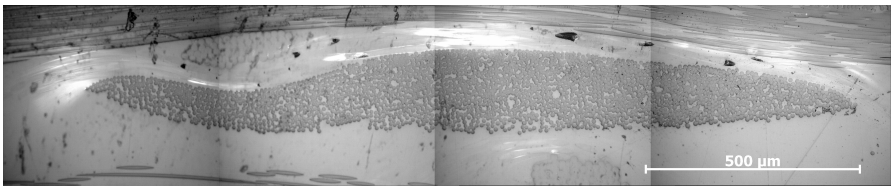
The procedure used in this study follows closely that suggested by Waterbury et al. [152] and Cann et al. [153]. First, several images (similar to Figure 3.21a) were taken at randomly selected areas in the specimen. Next, the number of fibres in each image were counted. Table 3.6 presents the recorded number of fibres in each tow, including the number of tows in an image. Finally, the fibre volume fraction, V_f, for IM7/8552 can be determined using Equation 3.5, given by [153]:

$$V_f = \frac{\pi {d_f}^2 N_f}{4A_i} \tag{3.5}$$

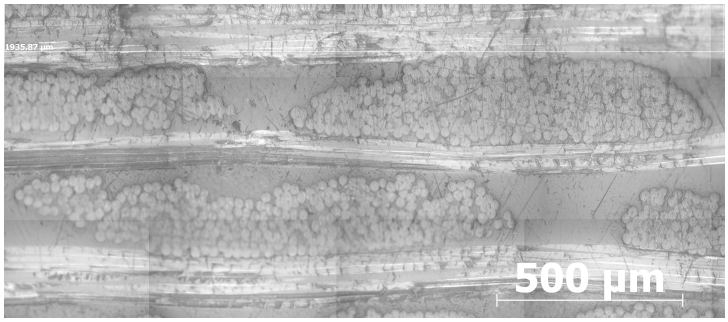
where d_f is the fibre diameter, N_f is the number of fibres in the image, and A_i is the area of the image.



(a)



(b)



(c)

Figure 3.21: Typical optical images of the composite laminates used in FVF determination (a) IM7/8552 (b) S2-Glass/MTM57 (c) Vectran/MTM57

For Vectran/MTM57 and S2-Glass/MTM57, a dry NCF fabric was cut to approximately 10 cm x 10 cm (illustrated in Figure 3.22) and then weighed using a precision balance weighing scale. Next, the yarns in the warp and weft direction, as well as the stitches were carefully isolated, and then weighed on its own. The recorded fabric properties are shown in Table 3.6.

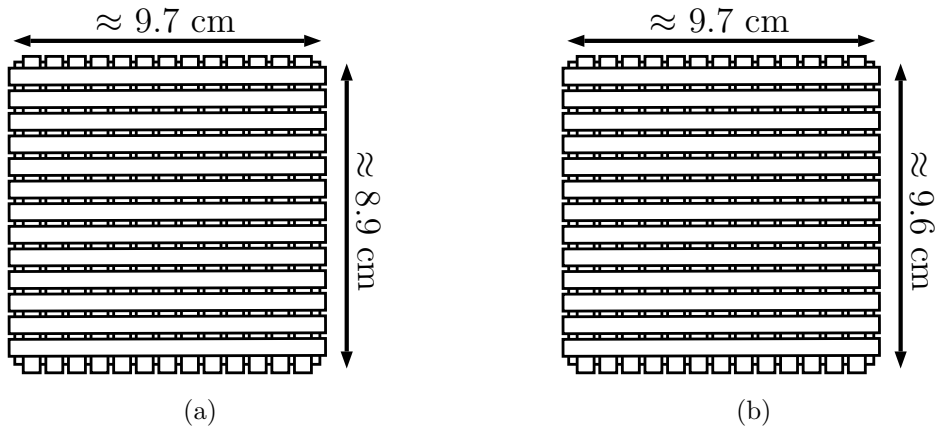


Figure 3.22: Illustration of the cut NCF fabric used for FVF measurement (a) Vectran (b) S2-Glass

The FVF for Vectran/MTM57 and S2-Glass/MTM57 can then be determined using the relationship given by:

$$V_f = \frac{nA_f}{t\rho_f} \tag{3.6}$$

where V_f is the FVF, n is the number of plies in a composite laminate, A_f is the fabric areal weight, t is the thickness of the laminate, and ρ_f is the fibre density. The calculated FVF for all composites are presented in Table 3.7.

Table 3.5: Recorded fabric properties for FVF determination

Material	Areal density (gsm)[13]	Warp weight (g)	Weft weight (g)	Stitch weight (g)
Vectran	315	1.17	1.35	0.20
S2-Glass	340	1.52	1.49	0.14

Table 3.6: Recorded specimen properties for FVF determination

Material	No. of fibres[14]	No. of tows	Fibre diameter (μm)
Vectran	293	149	25.5
S2-Glass	298	148	10

[13]Measured
[14]Number of fibres in a tow (measured)

Table 3.7: Measured FVF for all materials

	IM7/8552	Vectran/MTM57	S2-Glass/MTM57
FVF (%)	58	62	55

3.8 Interlaminar fracture toughness

While the importance of in-plane characterisation is well recognised for many applications such as structural design and Finite Element Method (FEM) modelling, characterising the interlaminar fracture toughness is equally as important. This is due to a number of reasons, mainly:

(i) Delamination toughness - Delamination failure is considered one of the major causes of structural failure. Damage caused by delamination severely weakens the structure, reducing its life expectancy. Therefore, knowledge of delamination toughness is essential in composite structural design;

(ii) FE modelling normally consider delamination by way of specific numerical algorithms such as cohesive elements or cohesive surfaces. Therefore, the obtained interlaminar fracture toughness values can be used as inputs to these algorithms, as well as numerical validation to the experimental observations.

Hence, the Mode I and Mode II Interlaminar Fracture Toughness (IFT) characterisation for composite laminates used in this study were performed to derive the strain energy release rate (G_c). Mixed Mode I and II were not considered due to the time and cost involved for the characterisation.

For Mode I, the most commonly used specimen is the Double Cantilever Beam (DCB), although others exist, such as the Single Edge Notched (SEN), Double Edge Notched (DEN), Wedge Insert Fracture (WIF), Vickers Indentation Crack (VIC), and Surface Cracked (SC), all shown in Figure 3.23.

For Mode II, the Four End Notched Flexure (4ENF) specimen was employed in this study since it has the advantage of generating a constant moment to the specimen in the

region of the crack tip. Other test specimen includes the End Notched Flexure (ENF), and the End Loaded Split (ELS), shown in Figure 3.24.

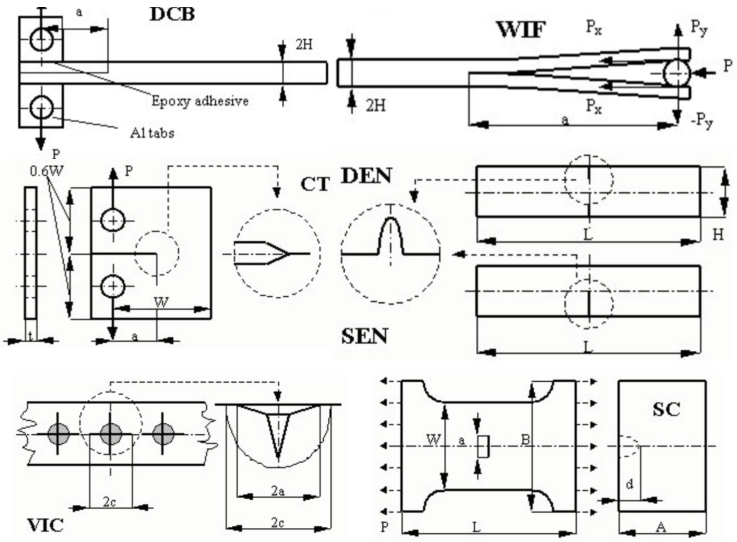


Figure 3.23: Mode I test specimens [156]

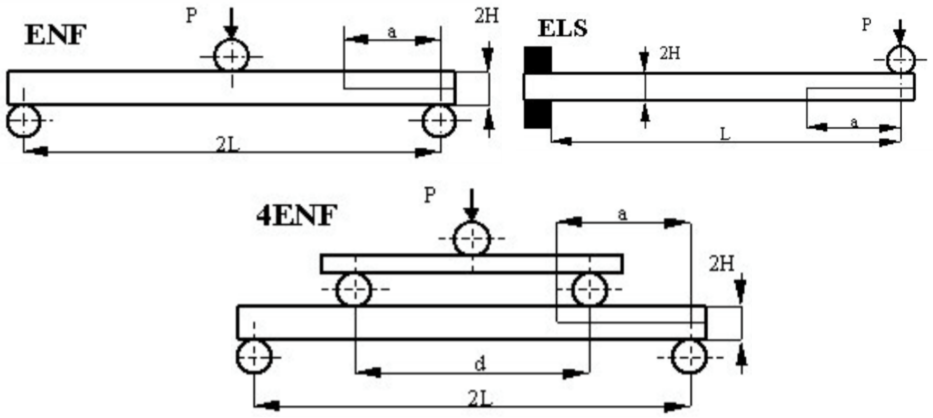


Figure 3.24: Mode II test specimens [156]

However, for IM7/8552, no interlaminar fracture toughness characterisation was performed. This was due to the lack of material available in the department at the time of testing. Furthermore, a large amount of literature was available on the Mode I and II IFT characterisation of IM7/8552 composites. Table 3.8 presents some of the available information on the IFT of IM7/8552.

[15] DCB
[16] 4ENF

Table 3.8: Mode I and II interlaminar fracture toughness for IM7/8552: Available values from the literature

	Mode I (kJ/m^2)[15]	Mode II (kJ/m^2)[16]
Hansen et al. [157]	0.21	1.33
Czabaj et al. [158]	0.22	-
Gutkin et al. [119]	0.26	-
Psarras [159]	0.21	0.61

3.8.1 Data Reduction

Mode I - Double Cantilever Beam (DCB)

At least five specimens were tested, in accordance with the ASTM standard [160] for Mode I IFT testing of composite laminates. The Mode I IFT, G_{Ic}, was then calculated using the Modified Beam Theory (MBT), given by [161]:

$$G_{Ic} = \frac{3P\delta}{2b(a + |\Delta|)} \tag{3.7}$$

where P is the load, δ is the cross-head displacement, a is the crack length, b is the specimen width, and Δ is the x-axis intersection of the cube root compliance $(C/N)^{1/3}$. The MBT method was selected for G_{Ic} calculation due to its conservative approach [161], compared to other methods such as the Compliance Calibration (CC), and Modified Compliance Calibration (MCC).

Mode II - 4 End Notched Flexure (4ENF)

For Mode II, the G_{IIc} can be calculated using Equation 4.6 shown below [162]:

$$G_{IIc} = \frac{P^2}{2b}\frac{\partial C}{\partial a} \tag{3.8}$$

where $\frac{\partial C}{\partial a}$ is the slope obtained from generating a least square fit of the compliance, C, as a function of crack length, a. The compliance is given by:

$$C = -\frac{\delta}{P} \tag{3.9}$$

3.8.2 Manufacturing

All laminates were manufactured using the Resin Film Infusion (RFI) technique, in which resin films (MTM57) were placed between the NCF layers up to the required thickness and Fibre Volume Fraction (FVF). The completed layups were then placed overnight under a vacuum table before curing them in an autoclave.

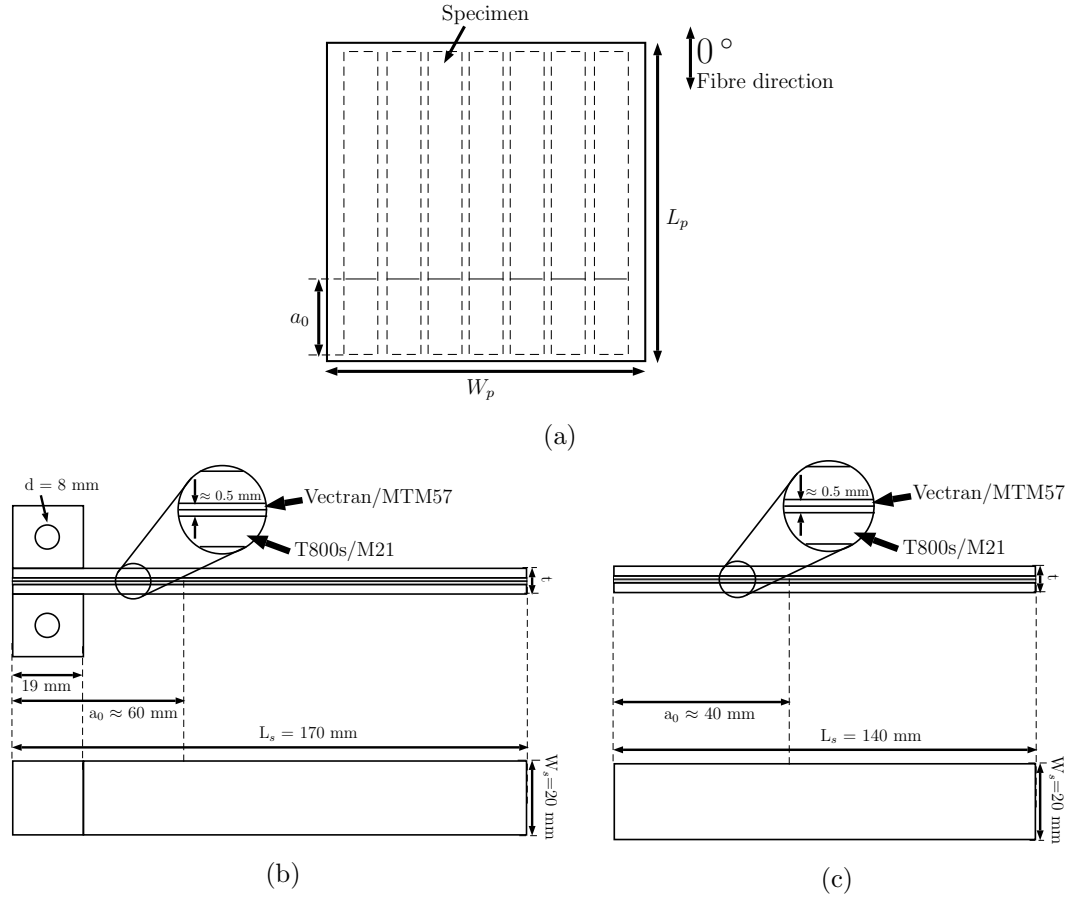


Figure 3.25: Schematic of the Mode I and Mode II specimens (a) Illustration of the plate for Mode I and Mode II specimen (b) DCB (c) 4ENF. For S2-Glass/MTM57, a monolithic sequence is used instead

The nominal plate dimensions for IFT characterisation are shown in Figure 3.25a. Table 3.9 presents the nominal plate and specimen dimensions for each tests. Upon curing, laminates were cut into specific dimensions for each test (shown in Table 3.9) using a water-jet cutter. A schematic of the DCB and 4ENF are shown in Figures 3.25b and 3.25c. Finally, end blocks were placed at the end of each DCB specimens using a two part epoxy-hardener (Araldite 2011) before leaving them overnight in a custom-made

jig to ensure good adhesion.

Table 3.9: Nominal plate and specimen dimensions: IFT characterisation

	S2-Glass/MTM57	Vectran/MTM57[17]
Plate width, W (mm)	300	300
Plate length, L (mm)	300	300
Specimen thickness, t (mm)	5	3.5
Lamination sequence	$[0\,^\circ/90\,^\circ]_{10s}$	$[\{0\,^\circ{}_{18}\}/\{0\,^\circ/90\,^\circ\}]_s$
Specimen flexural Stiffness (GPa)[18]	44	58

On Vectran

Due to the low compressive properties of Vectran (less than 10% of its tensile properties), both Modes I and II specimens require a modification to ensure the specimen did not suffer from any compressive failure during testing. The since Linear Elastic Fracture Mechanics (LEFM) used dictates that in the arms of all specimens remain elastic (i.e. no damage at any part of the specimen except in the delaminated area) [163].

Hence, both DCB and 4ENF specimens will be 'over-wrapped' with CF/Epoxy (T800s/M21) to prevent any damage from occurring in the specimen. A schematic of both hybrid DCB and 4ENF specimens are shown in Figures 3.25b and 3.25c. The cured hybrid specimens are shown in Figure 3.26.

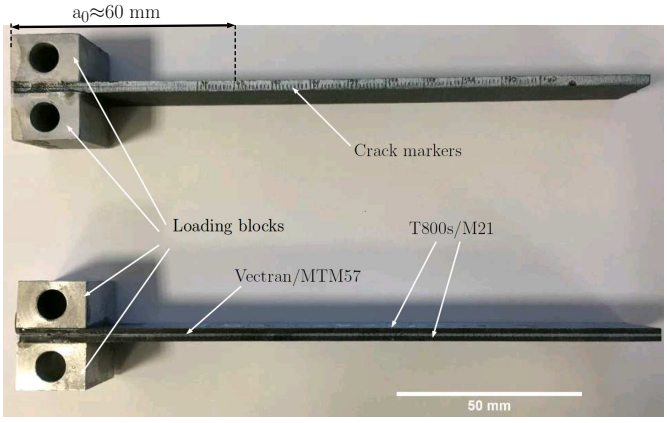


Figure 3.26: Cured T800s/M21/Vectran/MTM57 hybrid specimen

[17] Hybrid T800s/M21/Vectran/MTM57
[18] Calculated using the MBT method

3.8.3 Testing

All IFT testing was performed in-line with the recommended standard for Mode I [160] and Mode II [162]. The loading rate was set to 1 mm/min for Mode I testing and 0.5 mm/min for Mode II testing. The speed was selected not only because it is in the range that was recommended by the standard, but also to ensure a slow crack propagation, allowing for a more accurate data measurement.

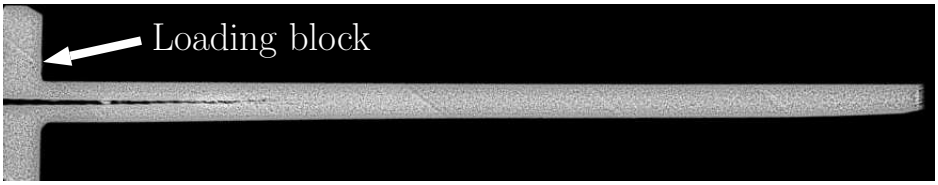
All testing was performed using the Instron 5950 universal testing machine, with a load cell rated to a maximum load of 50 kN. The crack tip was monitored using a Charged-Coupled Device (CCD) camera that displayed an enlarged image in a TV screen. Also, an event marker was used to send a signal to the computer as the crack tip passed through each mark on the side of the specimen. All specimens were pre-cracked up to 5 mm before the actual test. This is to remove any resin-rich area which would result in unusually high initiation values [161].

3.8.4 Results

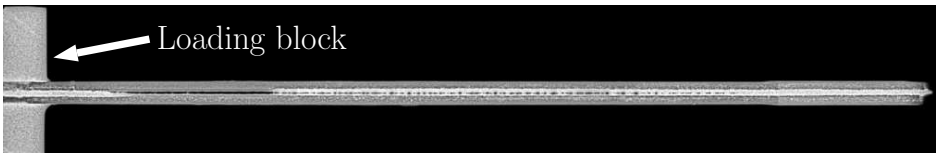
Specimen inspection

All tested specimens were visually inspected for any unwanted plastic deformation to ensure the validity of the test results. In addition, both Vectran/MTM57 and S2-Glass/MTM57 IFT specimens were examined using the radiographic imaging technique for any damage which may not be seen using the naked eye. It should be noted that all specimens were immersed in a penetrant solution (Dibromomethane) to enhance the results of the radiographic images. This is because the low atomic weight of all the elements in the composite material (carbon, oxygen, nitrogen, and hydrogen) means that the resulting radiographic image may not reveal as much defect (if any) in a tested specimen [10].

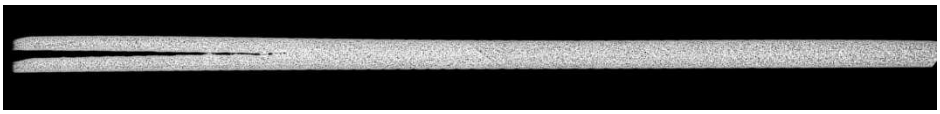
Figures 3.27a to 3.27d present the radiographic images for the DCB and 4ENF Vectran/MTM57 and S2-Glass/MTM57 specimens. No damage can be seen on both arms of the specimen, except in the specimen mid-plane where the crack is intended to propagate. This confirms the reliability of the deduced results using Linear Elastic Fracture Mechanics (LEFM).



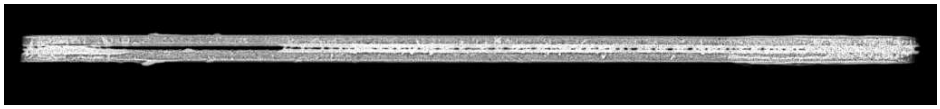
(a) S2-Glass/MTM57 DCB specimen



(b) T800s/M21/Vectran/MTM57 hybrid DCB specimen



(c) S2-Glass/MTM57 4ENF specimen



(d) T800s/M21/Vectran/MTM57 hybrid 4ENF specimen

Figure 3.27: Radiograph images of the failed DCB and 4ENF specimens for S2-Glass/MTM57 and T800s/M21/Vectran/MTM57 hybrid composites

Mode I - S2-Glass/MTM57

The load-displacement response for all five specimens are shown in Figure 3.28, where a clear 'stick-slip' behaviour can be observed. The average initiation and propagation G_{Ic} were calculated to be 1.04 kJ/m^2 and 1.15 kJ/m^2.

The high G_{Ic} observed for S2-Glass/MTM57 specimens is associated with a number of factors. First, the NCF architecture promotes a higher G_{Ic} due to the presence of stitches in the fabric architecture. These stitches act as a crack arrestor, consequently diverting the path of the crack in the direction parallel to the stitches [10]. Therefore, more energy is required to further delaminate the specimen. The presence of stitches in the laminate can be correlated with the 'stick-slip' behaviour seen in Figure 3.28, in which each interval between a load drop is estimated to be approximately 2-3 mm (shown in Figure 3.28), corresponding to the distance between each stitch in the laminate, Figure 3.29.

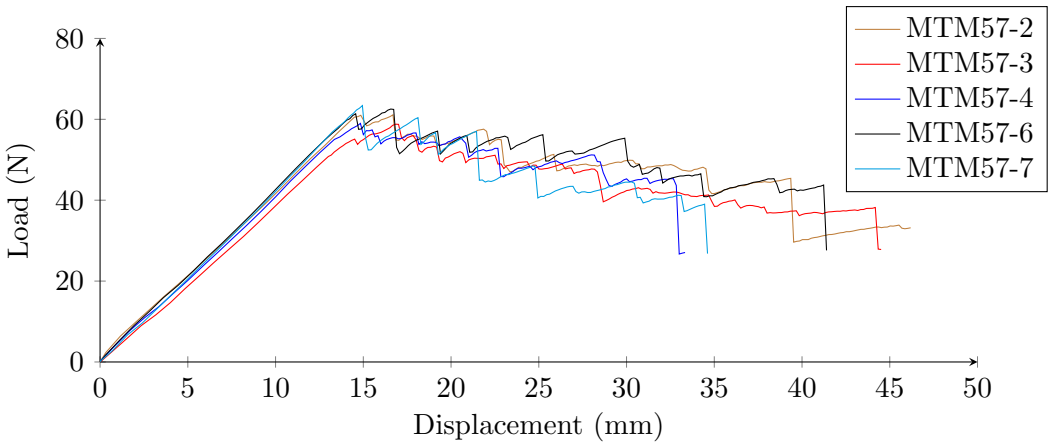


Figure 3.28: Mode I load-displacement response for all five S2-Glass/MTM57 specimens

Figure 3.30 presents the R-curve for S2-Glass/MTM57 laminates, where some scatter can be observed in the initial stage of the test, indicating an unstable crack propagation. As the crack length increases, the R-curve was observed to reach a 'steady-state', confirming a stable crack propagation. This 'two-stage' behaviour can be mainly attributed to the effects of fibre-bridging, which acts as a toughening mechanism to prevent crack growth. Furthermore, the large tensile strain-to-failure of S2-Glass fibres further contributes to the toughening mechanism by enabling a large elastic strain energy absorption. At higher crack lengths, the effects of fibre-bridging were significantly reduced (due to the failure of the bridging fibres), resulting in a 'steady-state' R-curve behaviour.

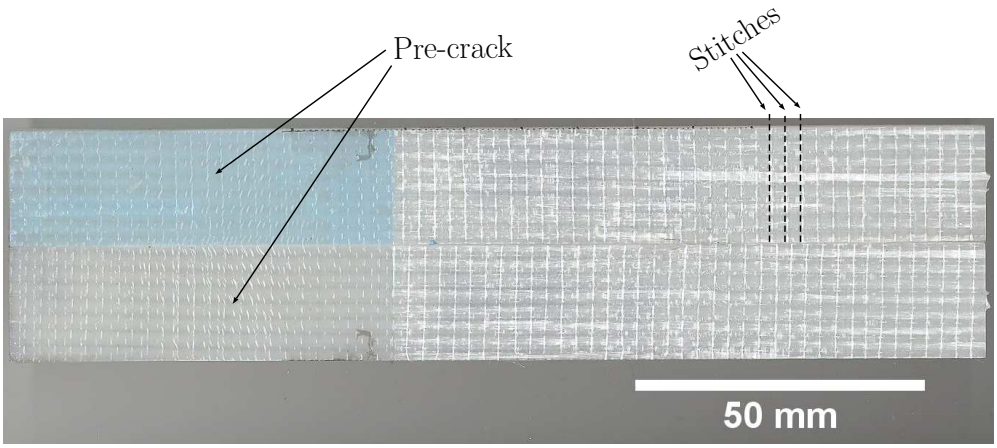


Figure 3.29: Flatbed scan view of the delaminated area of S2-Glass/MTM57

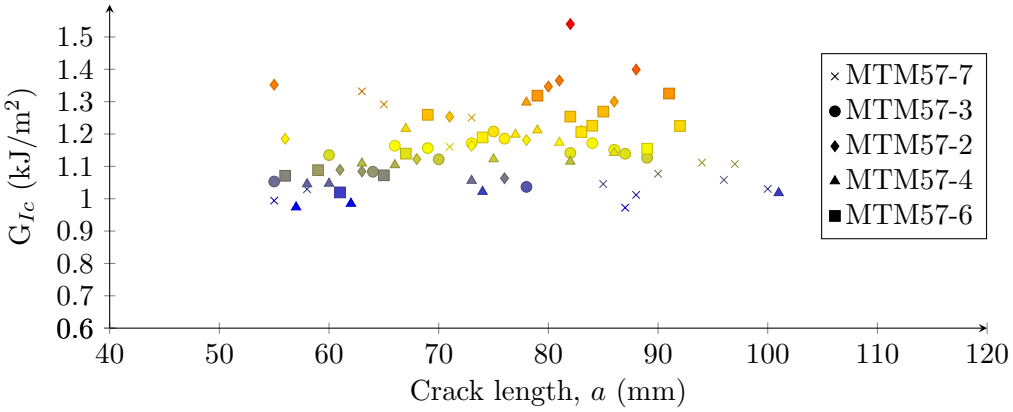


Figure 3.30: Mode I resistance curve for all five S2-Glass/MTM57 specimens

Mode I - Vectran/MTM57

The load-displacement response and R-curve for all five Vectran/MTM57 specimens are shown in Figure 3.31, and 3.32, respectively. The average initiation and propagation G_{Ic} were calculated to be 1.22 kJ/m^2 and 1.41 kJ/m^2, respectively

Concerning the Mode I interlaminar behaviour of Vectran/MTM57, several factors are thought to contribute to the high G_{Ic}. First, the fibrillar nature of the fibre itself (see Figures 3.38a and VectranDCBFibreBridging) promotes extensive fibre-bridging between the top and bottom arms. This is reflected on the R-curve shown in Figure 3.32, where the initial scatter of the R-curve, in particular the first 10-15 mm clearly exhibit a constant rise, until reaching a crack length of approximately 60 mm, where a 'stable-crack' propagation can be observed. This finding is consistent with the results from Briscoe et al. [121] when investigating the interlaminar fracture behaviour of Aramid/Epoxy laminates. In addition, the G_{Ic} values obtained by Briscoe et al. [121] are similar to that obtained in this study, which are in the range of 1-2 kJ/m^2.

Secondly, much like the case of S2-Glass/MTM57, the NCF architecture of the Vectran fabric further contributes to the high G_{Ic} due to the stitches acting as a crack arrestor, which then diverts the path of the crack away from the desired delamination path. Thus, more energy is required to further delaminate the specimen.

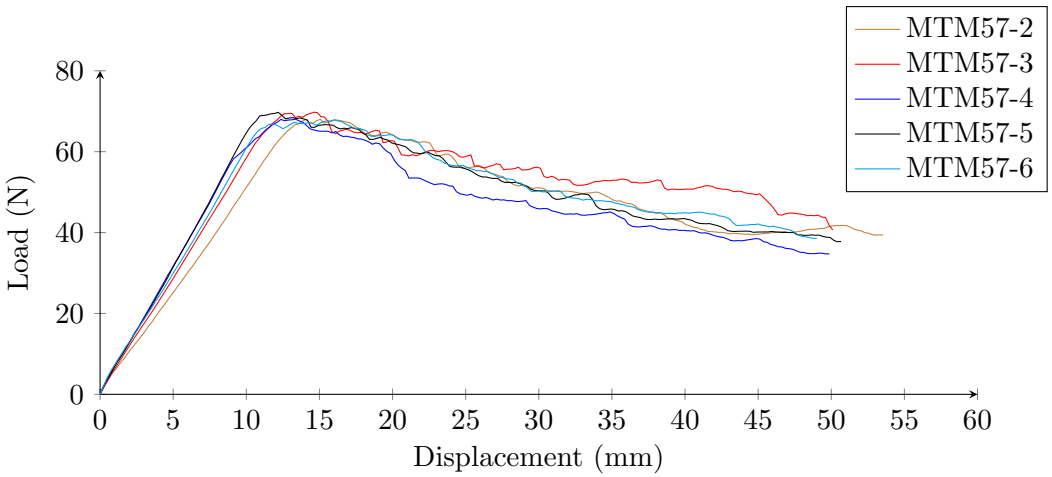


Figure 3.31: Mode I load-displacement response for all five Vectran/MTM57 specimens

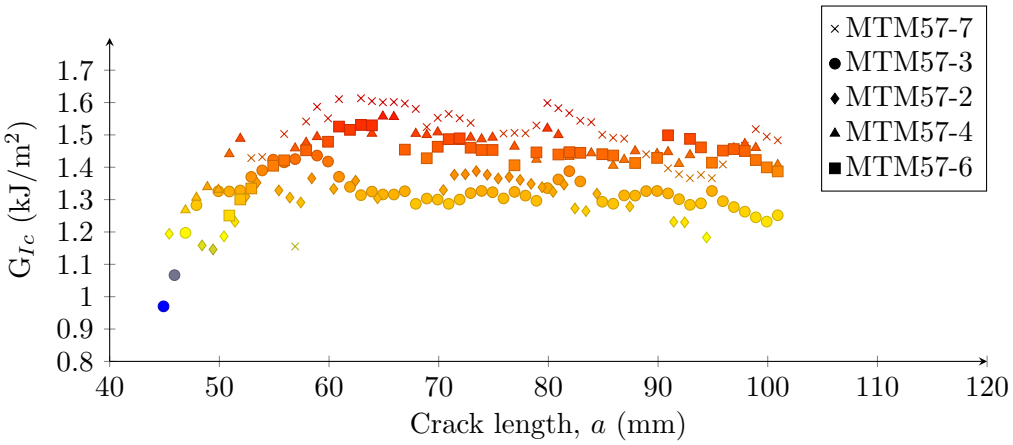


Figure 3.32: Mode I resistance curve for all five Vectran/MTM57 specimens

Mode II - S2-Glass/MTM57

The load-displacement response for all five specimens is shown in Figure 3.33. The average initiation and propagation were calculated to be 1.86 kJ/m^2 and 2.43 kJ/m^2, respectively.

For S2-Glass/MTM57, it can be concluded that the NCF architecture plays a fundamental role contributing to the fracture toughness of the composite. This is due to the presence of stitches, which poses difficulties for the crack to advance. Secondly, the fibre volume fraction of each composite is of particular importance since this can significantly influence the G_{IIc} values. As pointed out by Davies et al. [164], composites with lower fibre volume content (40-45%) generally exhibit a higher G_{IIc} due to crack tip plasticity effects. The resin-rich zone in composites with lower fibre volume content is often larger,

allowing a greater matrix deformation in the composite. Conversely, this effect is less pronounced in composites with higher fibre volume content since the development of shear cracks are often distorted at the fibre-matrix interface. It should be noted that the G_{IIc} found in this study is consistent with that of Davies et al. [164] at similar fibre volume fraction ($\approx 55\%$).

Figure 3.34 presents the R-curve for all five S2-Glass/MTM57 composites. It can be seen that the G_{IIc} increases with increasing crack length, signifying a toughening behaviour in resisting crack growth. This could be due to the presence of fabric stitches as well as the effect of fibre-bridging between the crack faces. Frictional effects could also influence the delamination energy due to the inherent nature of the test. However, its influence is generally small as observed from [161, 162, 165].

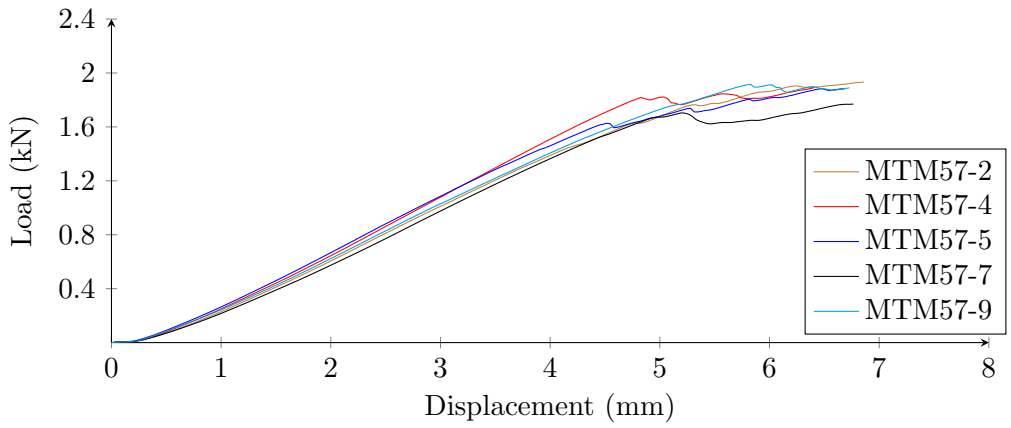


Figure 3.33: Mode II load-displacement response for all five S2-Glass/MTM57 specimens

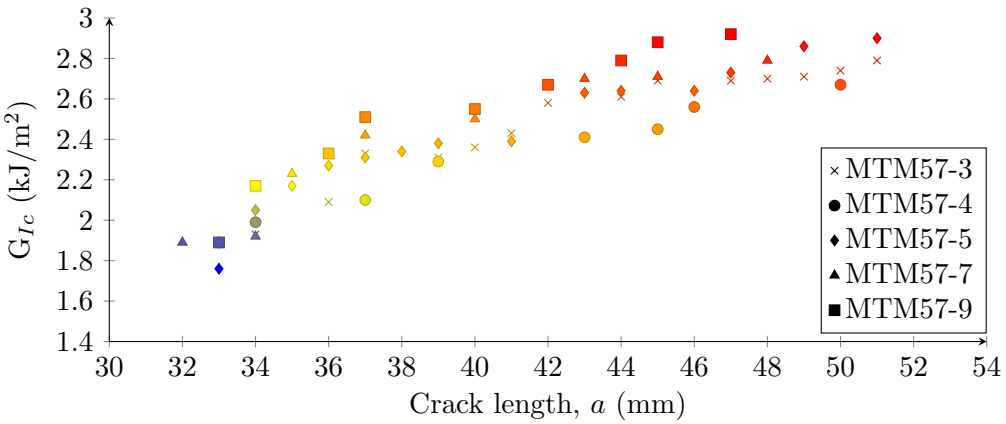


Figure 3.34: Mode II resistance curve for all five S2-Glass/MTM57 specimens

Mode II - Vectran/MTM57

The load-displacement response for all five Vectran/MTM57 specimens is shown in Figure 3.35. The average initiation and propagation G_{IIc} were calculated to be 1.58 kJ/m^2 and 2.41 kJ/m^2, respectively.

Apart from the contribution from the NCF architecture to the high G_{IIc}, the fibrillar nature of Vectran fibres is also concluded to have an important role in the high G_{IIc}. These fibrils often act as a toughening mechanism by way of fibre-bridging between the top and bottom arms of the specimen, preventing the two arms from separating from each other. This is evidenced by the increasing G_{IIc} with increasing crack length, shown in Figure 3.36. Hence, it was concluded that fibre-bridging was the the primary energy absorbing mechanism, apart from the inherent character of the stitches in the NCF architecture which enhances the delamination resistance.

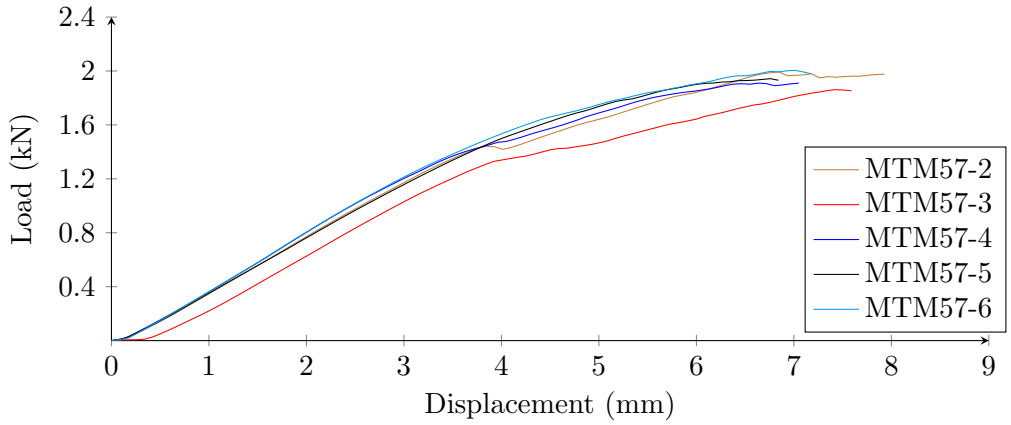


Figure 3.35: Mode II load-displacement response for all five Vectran/MTM57 specimens

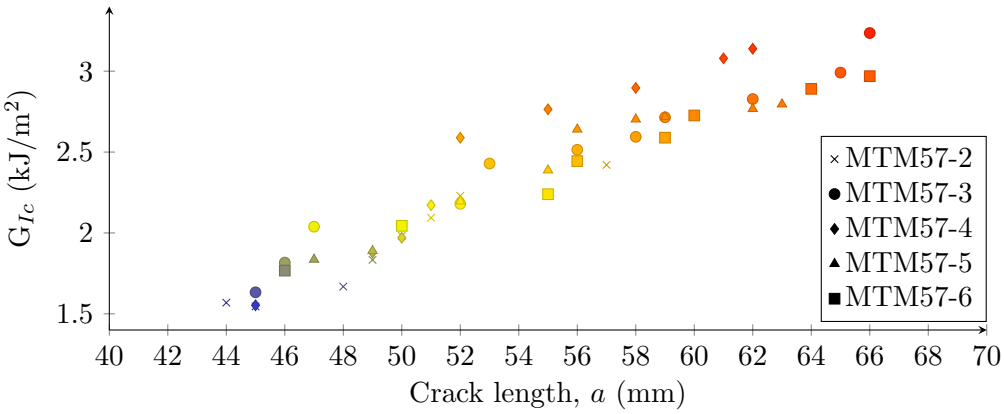
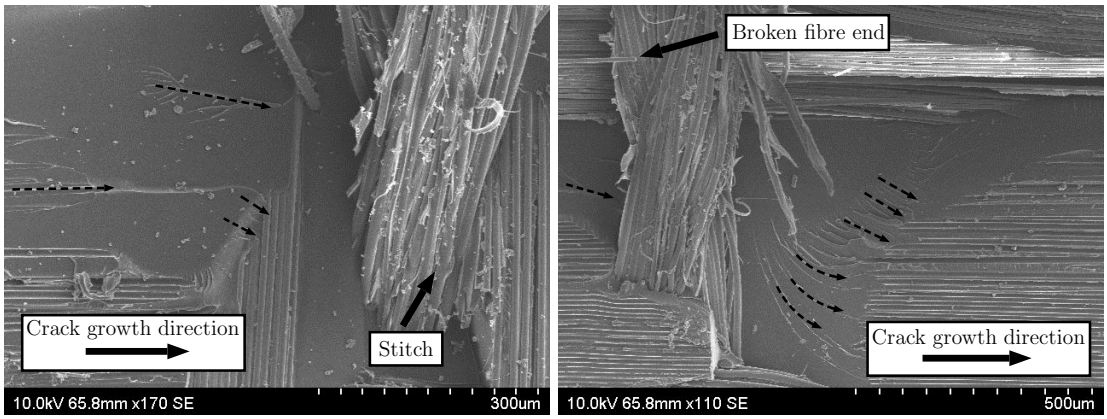


Figure 3.36: Mode II resistance curve for all five Vectran/MTM57 specimens

3.8.5 On Fractography

A fractographic study was undertaken on each material to determine the IFT behaviour under Mode I and Mode II loading. Subsections 3.8.5 to 3.8.5 present results of the fractographic observation on S2-Glass/MTM57 and Vectran/MTM57 following DCB and 4ENF testing. It should be noted that fractographic analyses were only performed on S2-Glass/MTM57 and Vectran/MTM57 since no IFT characterisation was performed on IM7/8552.

Mode I - S2-Glass/MTM57



(a) (b)

Figure 3.37: SEM image on S2-Glass/MTM57 fracture surface showing (a) Crack growth morphology before a stitch (b) Crack growth morphology after the stitch. Note the presence of a broken fibre end due to fibre-bridging. Dotted lines indicate riverlines

Figure 3.37 presents two SEM images of the fracture surface of S2-Glass/MTM57 DCB specimen, showing the distinct riverlines morphology which is often attributed to the Mode I fracture behaviour. These riverlines indicate the movement of the crack, where it can be observed that the crack path was diverted parallel to the stitch, shown in Figure 3.37a. Afterwards, a curved crack path was seen as the crack moves back to its original path, evidenced by the presence of riverlines, shown in Figure 3.37b. This crack path diversion mechanism often result in a greater energy absorption, which contributes to the G_{Ic} of the composite. Finally, the broken fibre end seen in Figure 3.37b is thought to be due to the bridged-fibre failure. As stated before, the effect of fibre-bridging also contributes to the relatively high G_{Ic} of the composite.

Mode I - Vectran/MTM57

For Vectran/MTM57 composite, fractographic observation has revealed several important features which may influence the high G_{Ic} value. Apart from the presence of stitches, which has been discussed in the previous section, the fibrillar nature of Vectran fibres is found to have a substantial effect on G_{Ic}. Figure 3.38 presents four SEM images of a Vectran/MTM57 specimen under Mode I loading. Fibrils can be observed everywhere on the fracture surface, particularly in Figure 3.38a. This implies a high contribution from the fibre-bridging to the G_{Ic} of Vectran/MTM57, consistent with the observation made by Briscoe et al. [121]. This is shown in Figure 3.38d, where extensive fibre-bridging can be seen between the top and bottom arm.

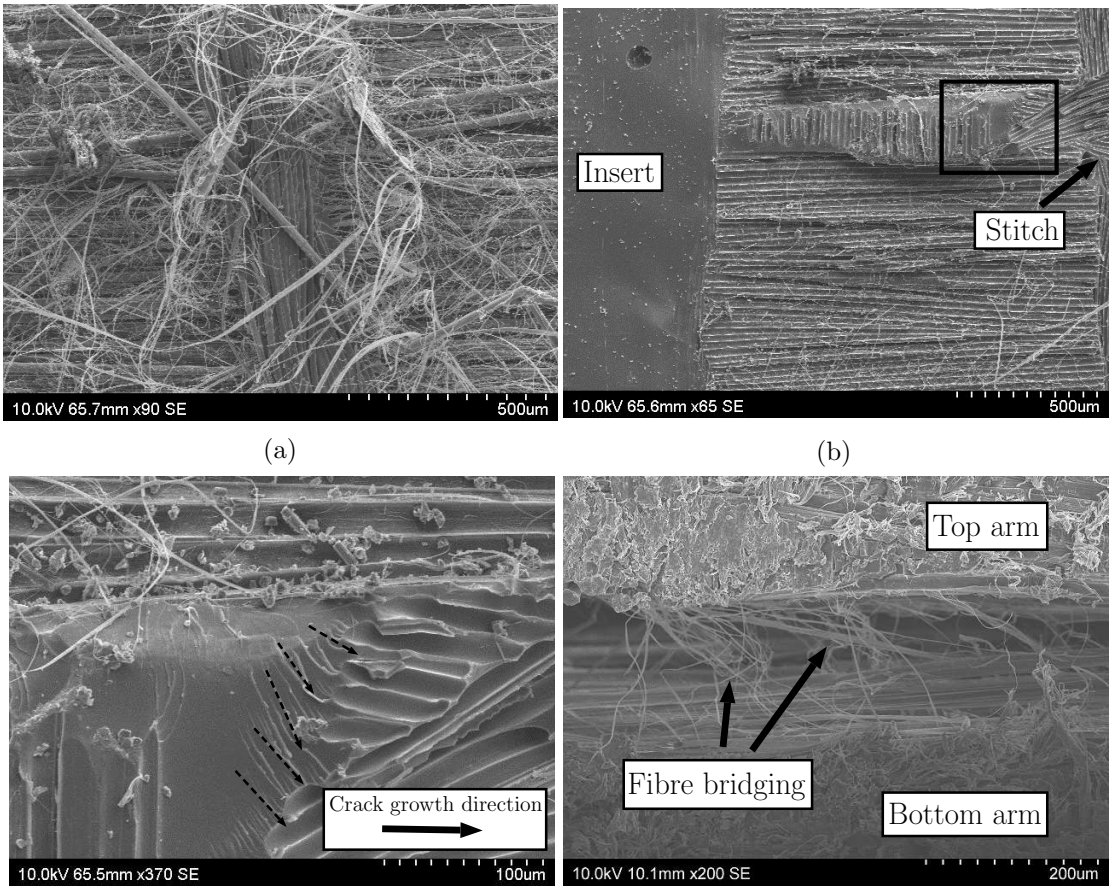


Figure 3.38: SEM images on Vectran/MTM57 fracture surface (a) Fibrils on Vectran/MTM57 fracture surface (b) SEM image around the specimen insert (c) Close up image of the black square in Figure 3.38b. Dashed lines represent riverlines (d) Fibre-bridging seen on Vectran/MTM57 DCB specimen

The poor fibre-matrix interfacial strength between Vectran and the epoxy resin further promotes an increase in delamination toughness, as it often exhibit extensive fibre-matrix debonding [10]. As a result, the degree of fibre-bridging will increase, therefore contributing to the G_{Ic} [121, 166] of the composite.

Mode II - S2-Glass/MTM57

Perhaps one of the most important fractographic features in a Mode II dominated failure are cusps, which appears on the fracture surface as inclined platelets [10]. Depending on factors such as the fibre volume fraction, a larger (or thicker) cusp size may appear [164]. In addition, the morphology of the cusps could also provide an insight on the direction of the crack growth [10]. This is illustrated in Figure 3.39, where cusps which are inclined to the left indicate the opposite (right) shearing direction, and vice versa.

Figure 3.40 shows an SEM image of a S2-Glass/MTM57 specimen following 4ENF testing, where cusps can be seen everywhere on the fracture surface indicating a Mode II dominated failure has occured. The resin-rich site near the stitch promotes a larger cusp size, whilst smaller cusps away from the stitch. The sharp-shaped cusps seen in Figure 3.40 is also an indication of a brittle thermosetting matrix system (MTM57), since in a thermoplastic matrix composite, the cusps is drawn into fibrils by a large amount of ductile drawing [10]. In addition, the increased presence of cusps in between the fibre spacing indicate a relatively low fibre volume fraction, compared to Vectran/MTM57 (Figure 3.41.

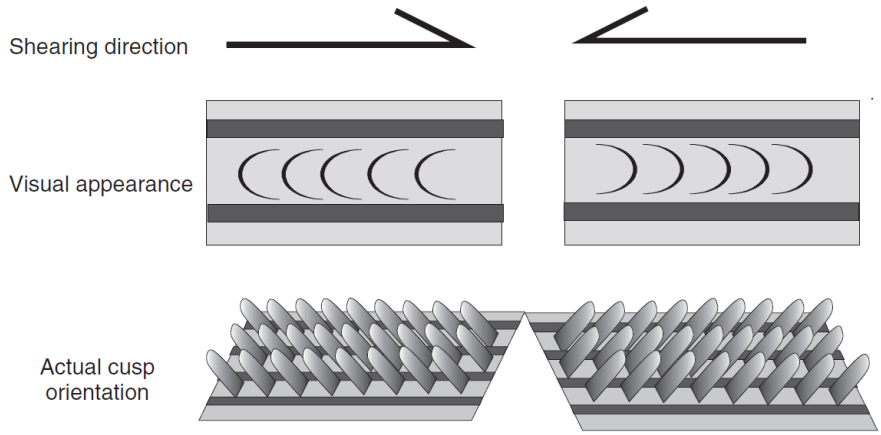


Figure 3.39: Visual appearance of cusps under the Scanning Electron Microscope (SEM) [10]

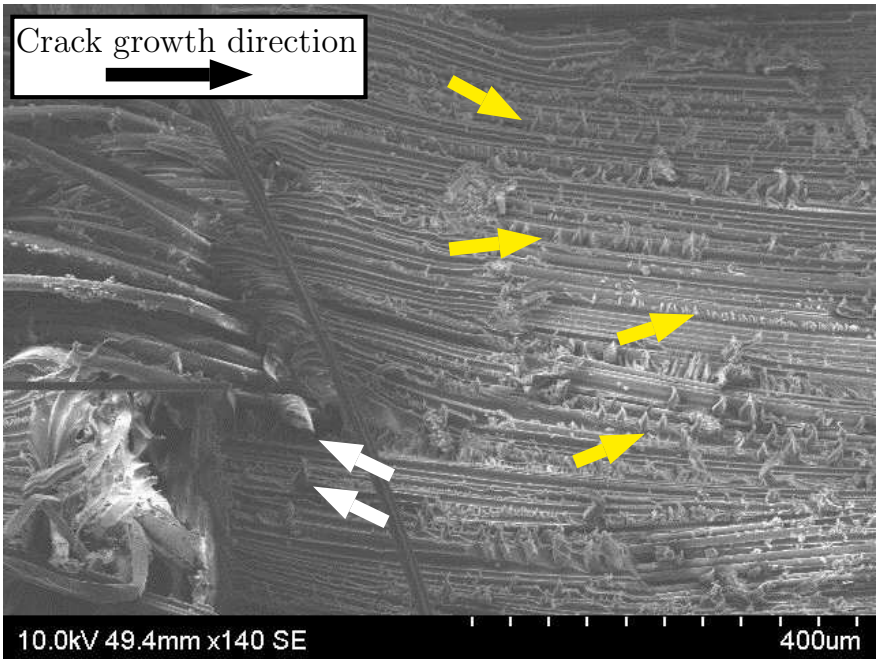


Figure 3.40: Fracture surface of S2-Glass under mode II loading. White arrows indicate large-sized cusps whilst yellow arrows indicate smaller-sized cusps. Crack growth direction is shown in black

Mode II - Vectran/MTM57

Figure 3.41 presents an SEM image of the Mode II fracture surface of Vectran/MTM57. Fibrils can be observed everywhere on the fracture surface, due to the nature of Vectran fibres. The number of cusps observed on the fracture surface of Vectran/MTM57 are lower compared to S2-Glass/MTM57, due to the relatively higher fibre volume fraction of the composite. In addition, the existence of fibrils on the fracture is thought to increase the amount of fibre-bridging in the composite, hence contributing to its G_{IIc}. A similar sharp-shaped cusps were observed on Vectran/MTM57 as in the case of S2-Glass/MTM57, due to the similar resin system used.

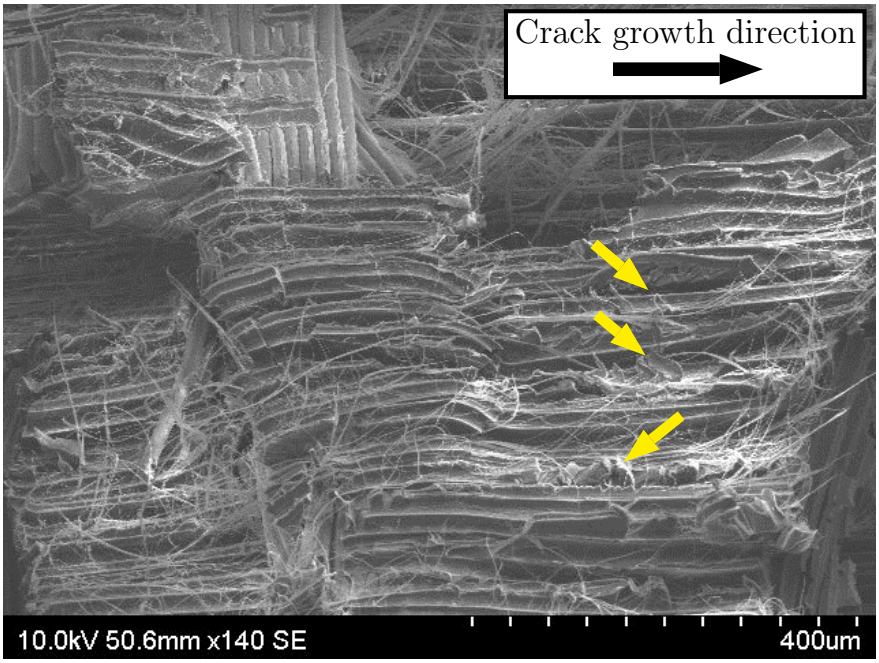


Figure 3.41: Fracture surface of Vectran/MTM57 under Mode II loading. Yellow arrows indicate cusps. Crack growth direction is shown in black

3.9 Summary

This chapter presents the characterisation results for IM7/8552, S2-Glass/MTM57, and Vectran/MTM57 composites. The quasi-static in-plane experimental testing has successfully characterised the material properties of the composites, which can be used as inputs for numerical modelling. In addition, the characterisation activities provide initial insight to the quasi-static in-plane behaviour of each materials, as well as the influence of NCF architecture on S2-Glass/MTM57 and Vectran/MTM57 composites.

Table 3.10: Material properties calculated using the rule of mixtures [58–60, 136, 167]

Material	Strength (MPa)	FVF (%)	Predicted Strength (MPa)	Measured (MPa)	Difference (%)
Vectran	3200	62	1007.22	780.06	22.6
S2-Glass	4890	55	1362.77	603.16	44.26
MTM57	80.1	-	-	-	-

Table 3.10 presents the predicted properties using the rule of mixtures [167]. It can be concluded that the stitches in the NCF composite decrease the in-plane properties by

at least 20% for Vectran/MTM57, and 44% for S2-Glass/MTM57, when compared to the analytical prediction. While the stitches enhance the delamination resistance of both composites, it also promotes resin-rich sites, which may initiate premature failure [10]. For S2-Glass/MTM57, the flaws and defects inherent to GF based composites may also contribute to the large difference when compared to the analytical prediction.

Under Mode I and Mode II IFT testing, superior delamination response was observed for S2-Glass/MTM57 and Vectran/MTM57 composites. The considerable improvement in the delamination resistance was primarily due to the presence of stitches in the NCF architecture as well as the effects of fibre-bridging in the laminate. This is consistent with the findings from previous works performed on composites with an NCF architecture [10, 168]. As stated in section 3.8.4, the stitches act as a crack arrestor, diverting the crack from its original path to become parallel with the stitch direction. Hence, more energy is required to redirect the crack back to its original path to continue delaminating the specimen. For Vectran/MTM57, its fibrillar nature further enhances the interlaminar toughness by way of fibre-bridging between the top and bottom arms. This was confirmed by fractographic observation on the fracture surface of the composite.

Chapter 4

Translaminar Fracture Toughness of Vectran Composite

4.1 Introduction

Often the final failure of composite structures involves fibre fracture, which dissipates the largest amount of energy compared to other damage types. For instance, the amount of energy released from fibre fracture is at least two orders of magnitude larger [69] when compared to matrix cracking or delamination failure. This is due to the occurence of different failure types which contributes to the final translaminar fracture energy, such as fibre pull-out and delamination. To date, research has been focused on characterising the tensile (Mode I) translaminar fracture toughness of CF/Epoxy based composites [69, 169–171]. However, minimal work can be found on other types of composite system, especially polymer based fibre composites. This was largely because of the difficulty in obtaining a reliable fracture toughness result, due to the premature failure in the specimen which invalidate the characterisation test. Figure 4.1 illustrate several failure modes which may occur using a conventional Compact Tension (CT) specimen. The failure modes are: FM1/FM2: local compression, FM3: in-plane shear, FM4: bearing, FM5: shear-out, and FM6: rear buckling.

As mentioned before, superior compressive properties (both stiffness and strength) was observed for IM7/8552 composites. In contrast, the compressive stiffness of S2-

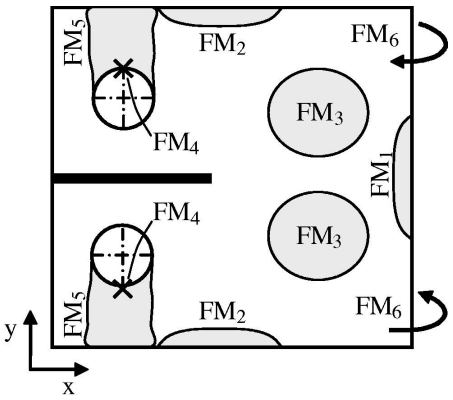


Figure 4.1: Possible failure locations of conventional Compact Tension (CT) specimen [172]

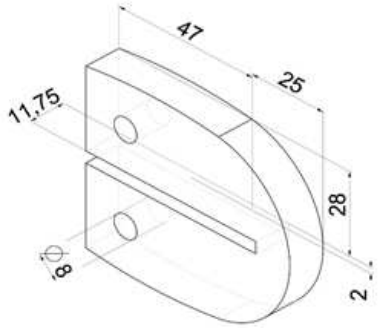
Glass/MTM57 was at least seven times lower than IM7/8552, and more than 10 times lower for Vectran/MTM57. Due to the poor compressive stiffness of both composites, premature specimen failures such as buckling or local compression are expected to occur, before any crack could propagate. Recently, Katafiasz et al. [70] investigated the Mode I translaminar fracture toughness of S2-Glass/MTM57 composite laminates and found the G_{Ic} to be 131.9 kJ/m^2 and 154.2 kJ/m^2 for initiation and propagation, respectively. A modified CT specimen was utilised to mitigate compressive and buckling failure when measuring the G_{Ic} for S2-Glass/MTM57 laminates. In this study, the modified CT specimen proposed by Katafiasz et al. [70] was utilised and further developed to characterise the Mode I translaminar fracture toughness of Vectran/MTM57. In addition, a fractographic study was undertaken to investigate the main energy dissipating mechanism which contributes to the fracture toughness of Vectran/MTM57 composite.

4.2 Specimen design

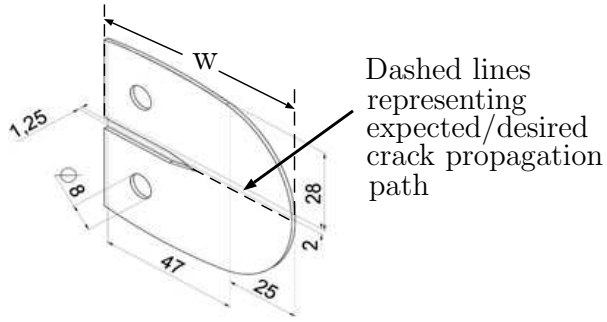
There are many types of specimen configurations which can be used to measure the translaminar fracture toughness of composite materials. These include the Compact Tension (CT), the Extended Compact Tension (ECT), the Single Edge Notched (SEN) and Double Edge Notched (DEN), the Centre Notched Tension (CNT), and finally, the three and four Point Bending (3/4PB) configurations [69]. Perhaps one of the most widely used configurations is the CT specimen [70,169–171,173], to measure the fracture toughness associated with the Mode I tensile (and compressive) translaminar fracture

toughness of composite materials.

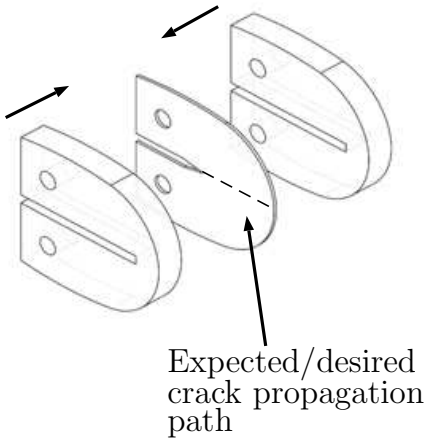
In this research, the CT configuration was selected to measure the Mode I translaminar fracture toughness of Vectran/MTM57. Initial design from Katafiasz et al. [70] was utilised and further developed for use in this research. The design consists of two discrete parts making up the final specimen - the thick part, Figure 4.2a, and the thin part, Figure 4.2b.



(a) Thick part of the CT specimen



(b) Thin part of the CT specimen



(c) Full CT Specimen

Figure 4.2: Schematic of the individual/final parts in the current Compact Tension (CT) specimen design

Due to the poor compressive properties of Vectran fibres, LS-Dyna was utilised to analyse the initial design from Katafiasz et al. [70] for Vectran/MTM57 composite laminate. A detailed discussion in the design development is presented in subsection 4.2.1.

4.2.1 Design development in Finite Element

As shown in Figure 4.2, the design consists of two discrete parts making up the final specimen - the thin and thick parts, Figure 4.2a and 4.2b, respectively. Figure 4.2c shows the exploded view of the final CT specimen, and the crack is expected to grow along the dashed line shown in Figure 4.2b.

The 8-noded thick shell element (single integration point, 6 degrees of freedom) was employed in the FEM analysis. The element type is based on a plane-stress assumption, which considers the transverse shear (through-the-thickness) effect, based on the Mindlin-Reissner plate theory [174]. This element type was chosen since the material model selected (MAT LAMINATED COMPOSITE FABRIC - MAT58 [175]) is based on a plane stress assumption, hence can only be used on shell elements. Initially, only the thin part is modelled in LS-Dyna. However, due to the poor compressive properties of Vectran/MTM57, buckling at the rear specimen was seen even before any crack could propagate, shown in Figure 4.3. Therefore, the thick part was gradually added to improve the compressive properties of the specimen, consequently avoiding any undesirable failure such as compressive or buckling failures. The thick part was added in 1 mm intervals, at both sides of the thin part at each time. The final FEM model, shown in Figure 4.4, consists of 236,156 thick shell elements with six through-the thickness integration points in each element - a total specimen thickness of 23.75 mm for the thick part and 1.5 mm on the thin part. No cohesive elements were included in the model to reduce computational time. A mesh sensitivity study was employed using the CT specimen to be modelled, where the total internal energy was made as a function of the element size. The internal energy was found to converge at an element size of 0.5 mm upon reaching the contact stress of approximately 800 MPa (equivalent to the tensile strength of Vectran/MTM57).

A tiebreak contact criterion was employed in the model (shown in Figure 4.3, which corresponds to the tensile strength of Vectran/MTM57. The tiebreak criterion, or cohesive surface algorithm, is commercially available in LS-Dyna in which users supply the threshold contact strength, and the tiebreak criterion was modelled as discrete linear springs, which would then fail if the failure criterion defined below is met [176]:

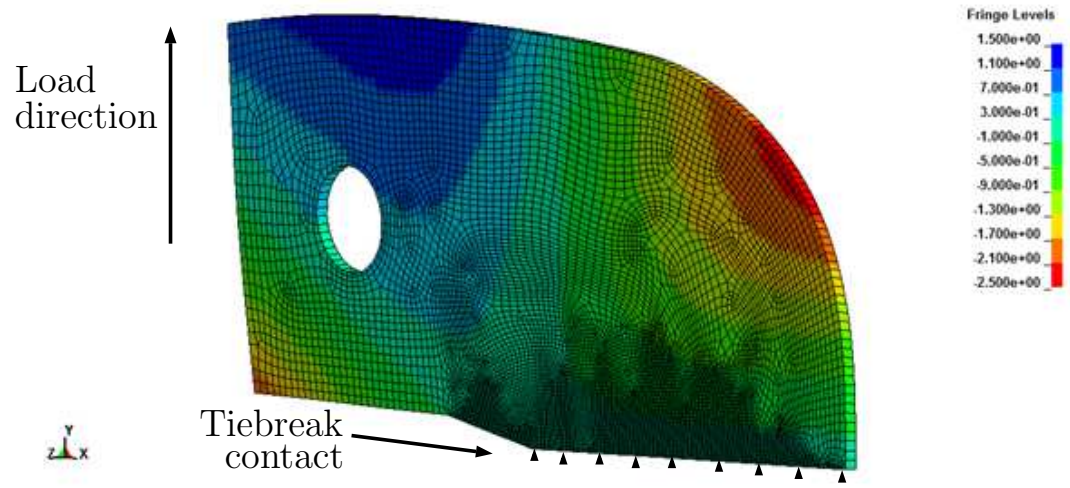
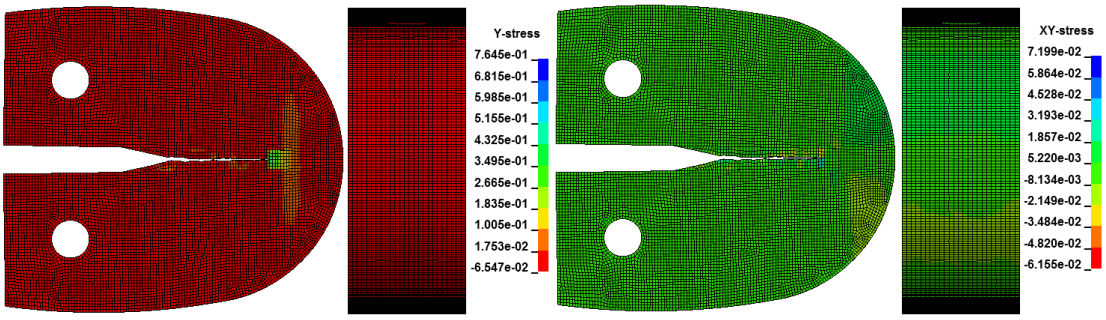


Figure 4.3: CT specimen modelled with LS-Dyna, utilising symmetry. Contours represent the out-of-plane displacement (units in mm). Small dark triangles represent the 'tiebreak' contact used in the simulation

$$\frac{\sigma_n}{NFLS} \geq 1 \tag{4.1}$$

where σ_n is the normal failure stress and $NFLS$ is the normal failure stress (input from the user; in this case, the tensile strength at failure for Vectran/MTM57). Upon failure, the nodes that are initially tied will detach, emulating crack propagation observed experimentally.

The boundary condition that was applied in the simulation was similar to that of the experimental testing, in which the bottom pin is fixed, whilst applying a ramped displacement-time load, to remove any inertial effects. Figure 4.4 shows results of the final FEM design (with dimensions specified in the previous paragraphs), showing contours of tensile, compressive, and $\pm 45\,^\circ$ in-plane shear, at 24 mm crack length, to confirm the absence of irreversible damage on the design.



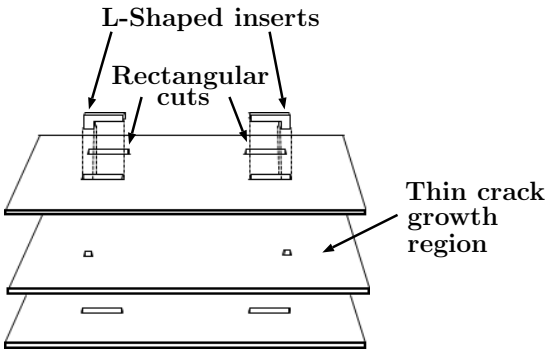
(a) (b)

Figure 4.4: Final FEM results for Vectran/MTM57 CT specimen (a) Tension and compression. Contour represents tensile and compressive strength (b) $\pm 45\,^\circ$ In-plane shear. Contour represent $\pm 45\,^\circ$ in-plane shear strength. All units are in kN/mm^2

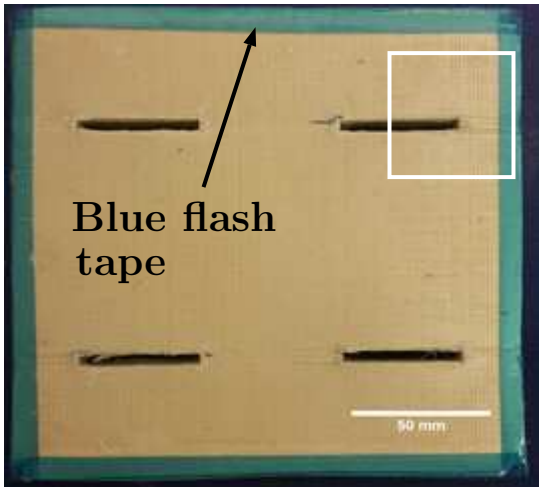
4.2.2 Specimen manufacturing

The Vectran/MTM57 specimens were prepared from 24 sets of three Vectran fabric (stacking sequence: $[(0\,^\circ/90\,^\circ)_3]_{24s}$ with two MTM57 resin film sandwiched in between the fabric layers. The layup was made symmetrical by ensuring both the fabric and the stitches follow the so-called "right and left hand rule". On each set, rectangular cuts were made using a round-tip scalpel, and shown in Figure 4.5a to 4.5c. For the thin crack growth region, two MTM57 resin film were placed in between four plies of Vectran NCF fabric, resulting in a cured thickness of approximately 1.25 $\pm$ 0.1 mm. On each stacked set of Vectran fabric and MTM57 resin films, blue 'flash' tape was placed around the stacked plies, Figure 4.5b, to ensure minimal movement of the Vectran yarns during lay-up and curing. Finally, L-Shaped PTFE inserts were placed into the rectangular 'grooved' section before curing, Figure 4.5d. It should be noted that at each regular intervals (i.e. after completing each set of Vectran/MTM57 lay-up), the lay-up is placed under a vacuum table for at least 5 minutes to remove any excess air pockets, therefore ensuring that the final lay-up (before cure) is not too thick.

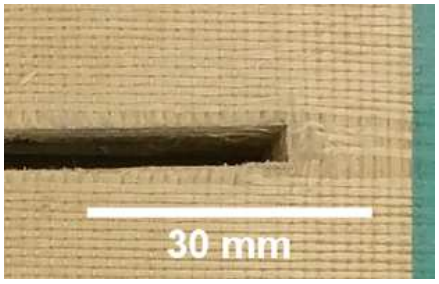
After curing, the laminate was cut into dimensions shown in Figure 4.2. The thin crack growth region was then cut into the final shape as seen in Figure 4.6a using a diamond saw cutter, subsequently removing the PTFE inserts placed earlier. It must be noted that due to the fibrillar nature of Vectran fibres, residual 'floss' were produced when using the diamond coated disc saw. However, it was assumed that the residual



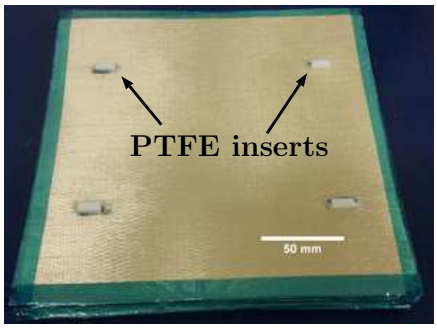
(a) Exploded view on the layup for Vectran/MTM57 CT specimen



(b) Rectangular cuts (grooves) on the uncured laminates



(c) Close up image on white square shown in figure 4.5b



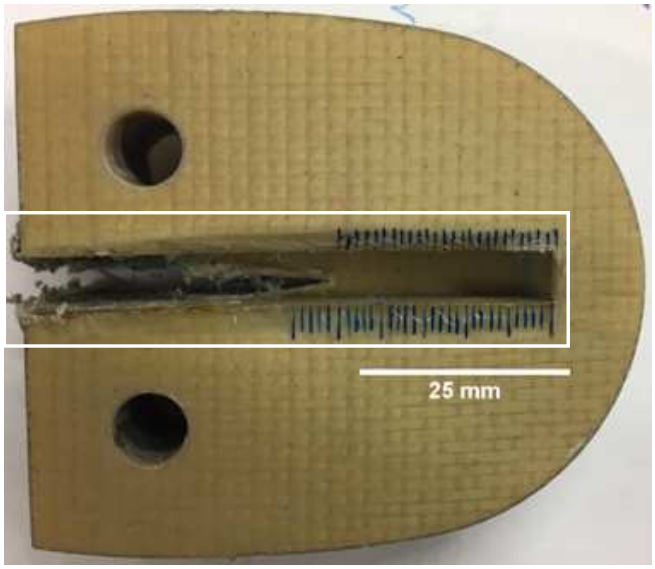
(d) Uncured laminates with PTFE inserts

Figure 4.5: Lay-up process for Vectran/MTM57 CT specimen manufacture

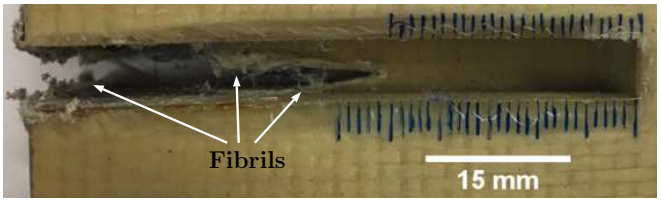
'floss' will not interfere with the G_{Ic} measurement since it was far away from the crack tip.

4.3 Test method and experimental setup

CT tests were performed at room temperature (20 °C) using an Instron universal testing maching (Instron 5969 with a load cell capacity of 50 kN; 0.5% measurement accuracy). Specimens were loaded in tension with a displacement controlled rate of 0.5 mm/min. An Imetrum Optical strain measurement system was employed to measure the machine cross-head displacement as well as a video capture to monitor the crack growth at 10 Hz (10 data points per second). The Microbeam 512 (5,293 Lux at 1 meter, 95 CRI) LED lighting were used to improve visualisation for the video recording.



(a)



(b)

Figure 4.6: (a) Vectran/MTM57 CT specimen used during testing. (b) Close up image from the white square shown in (a). Note the residual floss produced after using the diamond saw cutter

4.4 Data reduction

There are several data reduction methods which are commonly used to obtain the Mode I G_{Ic}. Subsections 4.4.1 to 4.4.4 briefly discuss on some of the most common data reduction method which have been used to derive the Mode I G_{Ic} of the composite material. In this study, the Area Method (AM), the Compliance Calibration (CC) method, and the Modified Compliance Calibration (MCC) method were chosen to calculate the G_{Ic} of Vectran/MTM57.

4.4.1 ASTM E399

The ASTM E399 testing standard [177], valid for isotropic metals, gives the stress intensity factor, K_{Ic}, as:

$$\mathrm{K}_{Ic} = \frac{P_c}{t\sqrt{w}} f(\frac{a}{w}) \tag{4.2}$$

where P_c is the critical load which causes fracture, t is the specimen thickness, w is the width of the specimen, measured from the load line to the right hand edge of the specimen (shown in Figure 4.2b), and $f(\frac{a}{w})$ is a function which relates crack length with the specimen geometry.

4.4.2 Area method

The area method is among the simplest methods in calculating the G_{Ic} and is given by [169]:

$$\mathrm{G}_{Ic} = \frac{1}{2t\Delta a}(P_1 d_2 - P_2 d_1) \tag{4.3}$$

where t is the thickness of the specimen, Δa is the change in the crack length, P_1, P_2, d_1, and d_2 are the loads and displacements observed from the load-displacement response, and is represented in Figure 4.7. Essentially, the G_{Ic} is the area under the shaded curve, excluding the elastic component of the curve (which can be associated with other crack points).

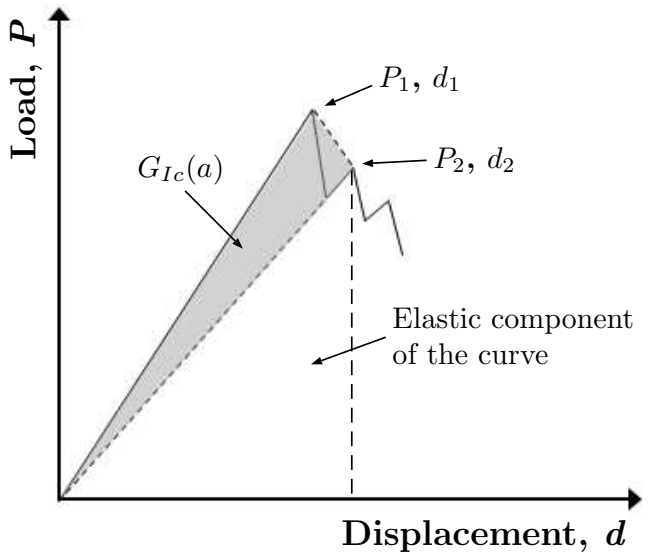


Figure 4.7: The area method

4.4.3 Compliance calibration

The G_{Ic} can also be calculated using the change of compliance, C, with the experimentally obtained crack length, a, given by [169]:

$$G_{Ic} = \frac{P_c^2}{2t}\frac{dC}{da} \tag{4.4}$$

where C is the experimentally observed compliance given by:

$$C = \frac{d_c}{P_c} \tag{4.5}$$

where d_c and P_c are the cross-head and load, respectively, at specific crack lengths. For this study, the experimental C versus a data was plotted in Figure 4.8, and a curve fit with a polynomial function given by:

$$C = (\alpha a + \beta)^{\gamma} \tag{4.6}$$

where α, β, and γ are determined by fitting Equation 4.5 with the experimentally obtained C versus a curve. The G_{Ic} can then be calculated from the following expression [169]:

$$G_{Ic} = \frac{P_c^2}{2t} a\gamma(\alpha a + \beta)^{\gamma-1} \tag{4.7}$$

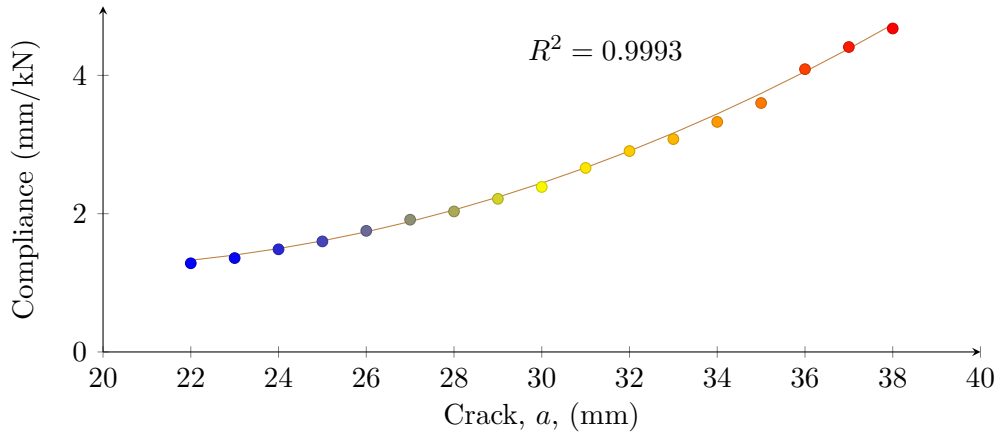


Figure 4.8: Typical compliance versus crack length curve obtained from the CC method

4.4.4 Fibre tensile failure

Determination of the G_{Ic} associated with fibre tensile failure can be derived using a rule of mixture-based relationship which accounts for the fractions of each constituents in the composite. Consider a Representative Unit Cell (RUC) for Vectran/MTM57 shown in Figure 4.9. For a cross-ply laminate, the volume can be computed by:

$$V_c = 0.5 v_f V_f + (1 - v_f - v_s) V_m + (1 - v_f - v_m) V_s \tag{4.8}$$

where v_f and V_f are the fibre volume fraction and fibre volume respectively, v_m and V_m are the matrix volume fraction and matrix volume, respectively, and v_s and V_s are the stitch volume fraction and stitch volume, respectively. By using the ratio of volume between each of the constituents and the whole composite, Equation 4.8 can be extended to include the fracture toughness for each constituent, given by:

$$G^0_{Ic} = \frac{2V_c G^{lam}_{Ic} + V_m G^{mat}_{Ic} + V_s G^{stitch}_{Ic}}{V_f} \tag{4.9}$$

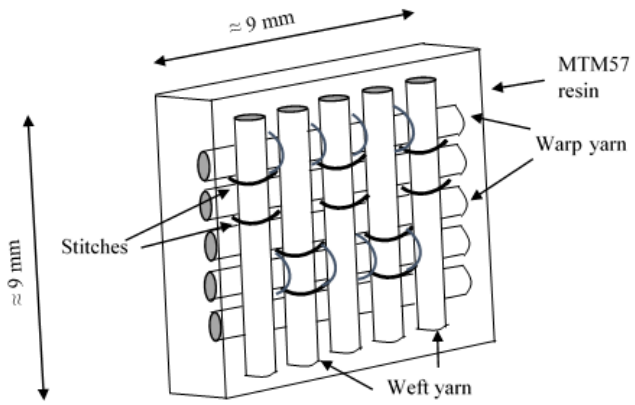


Figure 4.9: Representative unit cell for Vectran/MTM57

Finally, the fracture toughness for the polyester stitches can be determined using the suggestion by Irwin. Consider the relation between the critical stress intensity factor, K_I, and the fracture toughness, given by [163]:

$$G_{Ic} = \frac{K_I^2}{E} \tag{4.10}$$

where E is the fibre tensile stiffness, and K_I is given by:

$$\mathrm{K}_I = \sigma_f \sqrt{\pi a_0} \tag{4.11}$$

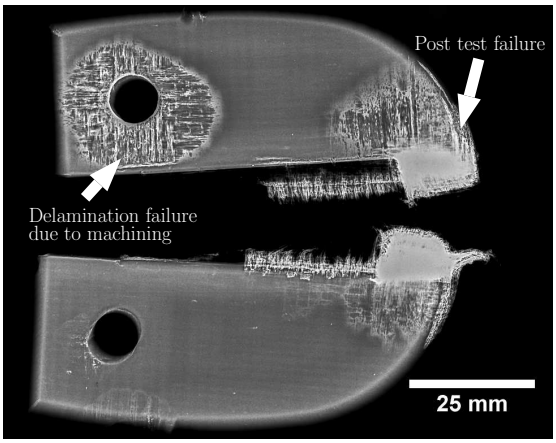
where σ_f is the fracture strength of the fibre, and a_0 is the half crack length. Substituting Equation 4.11 into Equation 4.10. G_{Ic} can be re-written as [178]:

$$\mathrm{G}_{Ic} = \frac{\sigma_f^2 \pi a}{E} \tag{4.12}$$

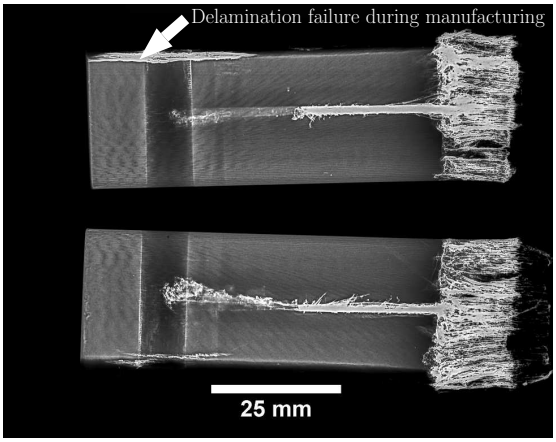
4.5 Results

4.5.1 Specimen inspection

Similar to the case of Interlaminar Fracture Toughness (IFT) specimens (DCB and 4ENF) discussed in subsection 3.8.4, the CT specimens were examined using the radiographic imaging technique to ensure no unwanted plastic deformation outside of the intended crack growth region. Both specimens were immersed in a penetrant solution (Dibromomethane) before radiographic examinations.



(a)



(b)

Figure 4.10: Radiograph images of tested Vectran/MTM57 CT specimen (a) Front view (b) Top view. The delamination failure occured before experimental testing

Figure 4.10 presents the front and top view of damaged Vectran/MTM57 CT specimen. No damage can be observed on the specimen, apart from delamination which occured during the pin-hole drilling of the cured Vectran/MTM57 CT specimen. It should be noted that both arms of the Vectran/MTM57 CT specimen were completely drawn apart after testing, to allow an easier post-test examination, as well as fractographic investigation. This confirms the effective use of the NCT specimen in mitigating unwanted failure modes discussed in section 4.1, especially due to the poor compressive properties of Vectran/MTM57 composite.

4.5.2 Test results

All three CT specimens exhibited a stick-slip fracture growth during testing. The crack growth was recorded for every one mm, up to 15 mm of growth. Figure 4.11 presents a typical load-displacement curve for Vectran/MTM57. Also in Figure 4.11, a typical Mode I load-displacement curve for CFRP was shown for comparison purposes. The elastic compliance, C, was measured directly from the load-displacement curve shown in Figure 4.11. The R-curve obtained from the three different data reduction methods, Area Method, CC, and MCC are shown in Figures 4.12 to 4.14 respectively. The average G_{Ic} obtained using the area method for initiation was 130.64 kJ/m^2 (CV: 7.22%) while the average G_{Ic} obtained for propagation was 259.98 kJ/m^2 (CV: 9.17%). Finally, the average G_{Ic} obtained using the CC method was 142.19 kJ/m^2 (CV: 6.01 %) and 262.68 kJ/m^2 (CV: 9.47 %) respectively for initiation and propagation.

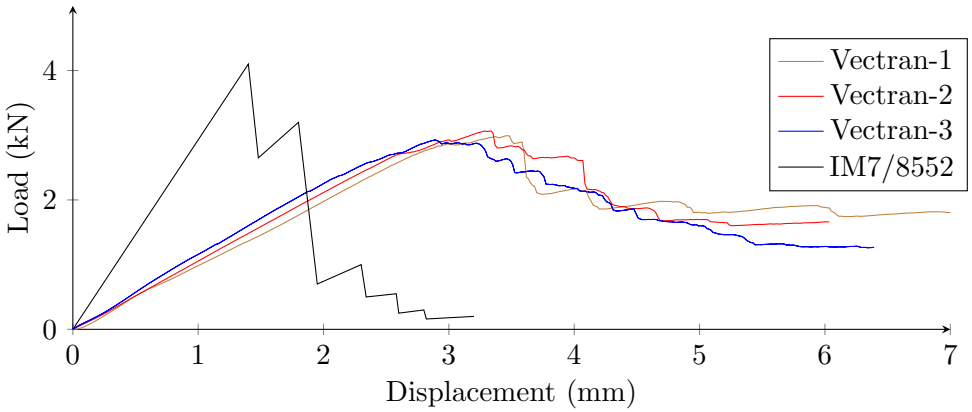


Figure 4.11: Load-displacement response for Vectran/MTM57, including IM7/8552 [169] for comparison purposes

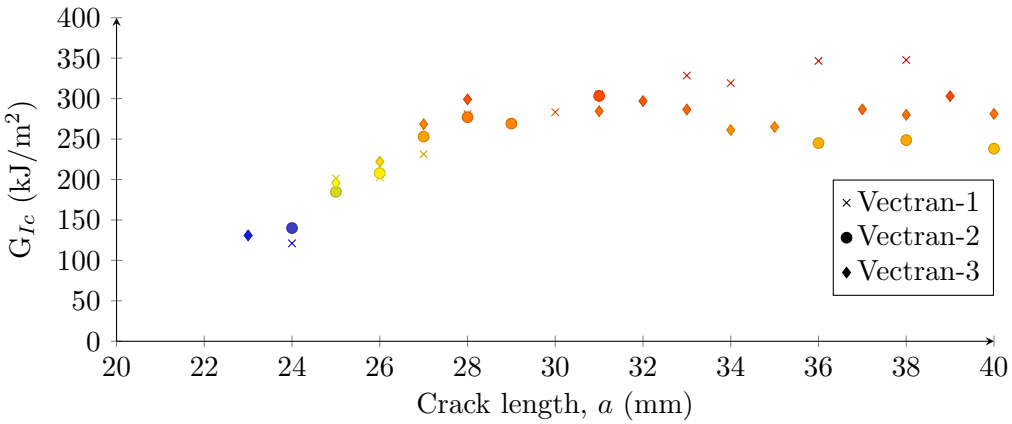


Figure 4.12: R-curve deduced by area method for all three Vectran/MTM57 specimens

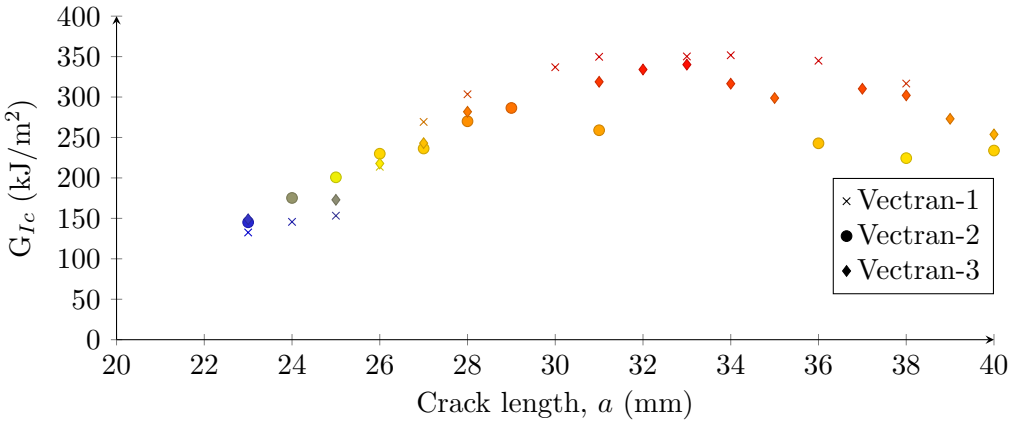


Figure 4.13: R-curve deduced by the CC method for all three Vectran/MTM57 specimens

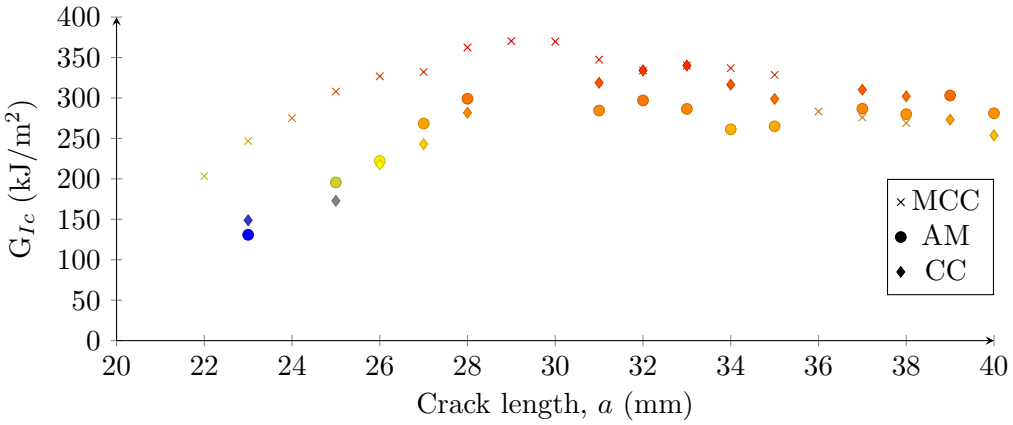


Figure 4.14: R-curve deduced by the MCC method using FEM. Also shown are the representative of AM and CC method for comparison

4.6 Discussions

Fibre dominated failure in a composite material typically involves different failure mechanisms which contribute to the composite fracture energy, G_c. Most authors [167,179,180] agree that fibre pull-out – the case where fibres are 'pulled-out' from its matrix socket [167, 169, 181], contributes largely to the G_c. For polymer based fibre composites, fibre fracture may also have a finite contribution to the G_C. Therefore, it is important to estimate the contribution of each failure mechanisms to the G_C of Vectran/MTM57, hence enabling a comprehensive understanding on the composite fracture behaviour.

The G_c of a composite material can be analytically estimated by considering the energy contribution from different failure mechanisms. This is given by:

$$G_c = G_{id} + G_{po} + G_{ff} \tag{4.13}$$

where G_{id} is the energy associated with interfacial de-bonding, G_{po} is the energy associated with fibre pull-out, and G_{ff} is the energy associated with fibre fracture. The contribution of interfacial debonding to the G_c can also be estimated by considering the interfacial fracture energy, G_{ic} (the energy required for a crack to propagate at the interface between the fibre and the matrix), given by:

$$G_{id} = V_f s G_{ic} \tag{4.14}$$

where V_f is the fibre volume fraction, G_{ic} is the energy associated with fibre-matrix de-bonding, and s is the aspect ratio between the length and radius of the fibre. However, for a continuous fibre, the length may vary, depending on the size of the specimen, as well as the flaws in the fibre which may be determined by performing a Weibull analysis. Therefore, a critical aspect ratio, s^* may be used to represent s, given by [167]:

$$s^* = \frac{\sigma_f^*}{2\tau_i^*} \tag{4.15}$$

where σ_f^* is the fibre fracture strength, and τ_i is the fibre-matrix interfacial strength. The fibre pull-out theory, originally proposed by Kelly et al. [182] takes into account a constant fibre-matrix interfacial shear stress upon fibre-matrix de-bonding, τ_i, and is given by [167]:

$$G_{po} = \frac{{V_f}^2 s r \tau_i}{3} \tag{4.16}$$

where r is the fibre radius. Finally, the estimation of energy contribution from fibre fracture can be made by re-arranging Equation 4.13, which yields:

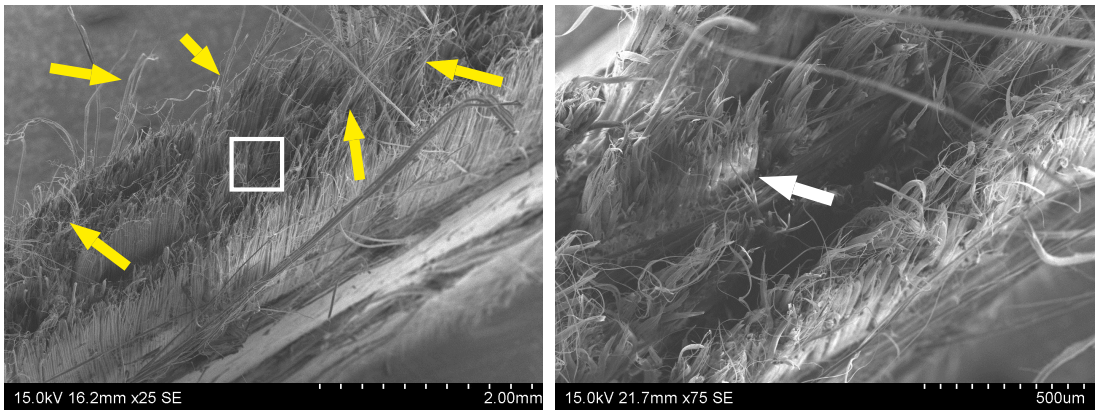
$$G_{ff} = G_c - G_{id} - G_{po} \tag{4.17}$$

Subsections 4.6.1 to 4.6.3 presents the estimated energy contribution from fibre-matrix de-bonding, fibre pull-out, and fibre fracture, including the fractographic study

performed on the fracture surface of Vectran/MTM57 CT specimen.

4.6.1 Fibre-matrix de-bonding

Figure 4.15 presents the fracture surface of Vectran/MTM57 specimen under Scanning Electron Microscope (SEM). Evidence of fibre-matrix de-bonding, Figure 4.15b, can be clearly observed, located at the 0°/90° interface. Therefore, it may be concluded that the initiation of failure begins at the 90° plies, which then propagates inwards towards the adjacent 0° plies, subsequently promoting fibre pull-out.



(a) (b)

Figure 4.15: Evidence of fibre-matrix de-bonding present on the fracture surface of Vectran/MTM57 CT specimen (a) Fracture surface of Vectran/MTM57 showing multiple fibre pull-out with varying lengths indicated by yellow arrrows. (b) Close-up image of the white square in (a) showing fibre-matrix debonding

To estimate the energy contribution from fibre-matrix debonding, consider a crack propagating along a fibre-matrix interface. In order for the crack to continue growing, it has to overcome the G_{ic} associated with the interface. This G_{ic} is difficult to experimentally measure due to the complexity of the interface. Furthermore, Hull [167] argued that the G_{ic} values are in reality not restricted to pure Mode I or II, but rather a mixed-mode condition. Furthermore, the relatively higher Poisson's ratio of polymer fibres such as Kevlar (Poisson's ratio: 0.36 [183]) may promote Mode I debonding due to the fibre's transverse contraction under tensile loads. Recently, Pimenta et al. [179] proposed that the G_{ic} can be related to the Mode II interlaminar G_{IIc}, which can be easily obtained by performing a Four End Notched Flexure (4ENF) or End Loaded Split (ELS) tests (discussed in subsection3.8.4 3), using a scaling factor β, given by:

$$G_{id} = \beta G_{IIc} \tag{4.18}$$

where β can be determined depending on the fibre packing in the Compact Tension (CT) specimen. A square packing [179] is selected for this case since it is better related to the current fibre packing of Vectran/MTM57 CT specimen. Therefore, β is given by:

$$\beta = \frac{1}{1 - 2\sqrt{\frac{V_f}{\pi}} + \sqrt{V_f \pi}} \tag{4.19}$$

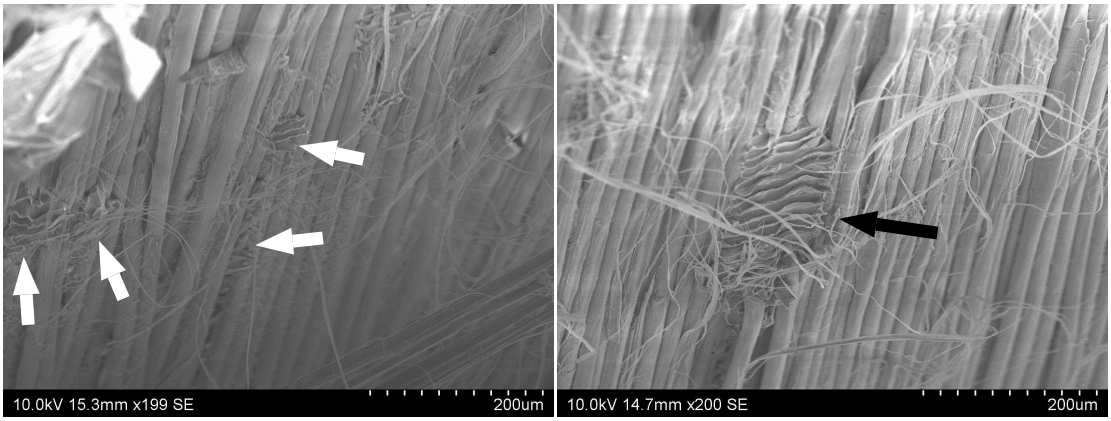
The Mode II Interlaminar Fracture Toughness (IFT) for Vectran/MTM57 has been characterised and discussed in subsection 3.8.4. Therefore, using the relationship proposed by Pimenta et al. [179], the G_{ic} can be estimated to be 1.6 kJ/m^2. However, as argued by Hull [167], the G_{ic} in Equation 4.14 is a mixed-mode I and II condition. Therefore, a lower bound of the G_{ic} can be estimated if the G_{IIc} in Equation 4.18 is substituted with G_{Ic}, yielding G_{ic}= 0.94 kJ/m^2. Hence, using the presented data in Table 4.1, the upper and lower bound G_{id} is calculated to be 16.44 kJ/m^2 and 64.49 kJ/m^2, respectively.

Table 4.1: Some mechanical properties of Vectran/Epoxy composite

τ_i (MPa)	d (μm)	v_f (%)	s*	σ_f (MPa)	G_c (kJ/m^2)	G_{Ic} (kJ/m^2)	G_{IIc} (kJ/m^2)
19.5 [184]	21	62	65.05	2537 [145]	260	1.41	2.41

4.6.2 Fibre pull-out

Potentially the most significant source of fracture energy is due to fibre pull-out, upon initial fibre-matrix debonding. This is inclusive of the contribution of shear (sliding) stress between the fibres and the matrices along the length of the fibre. This is shown in Figure 4.15a, where evidence of fibre pull-out, each with varying lengths, seen everywhere on the fracture surface. In additon, Figures 4.16a and 4.16b present images of shear cusps seen on the fibres, implying a Mode II dominated failure has occurred.



(a) (b)

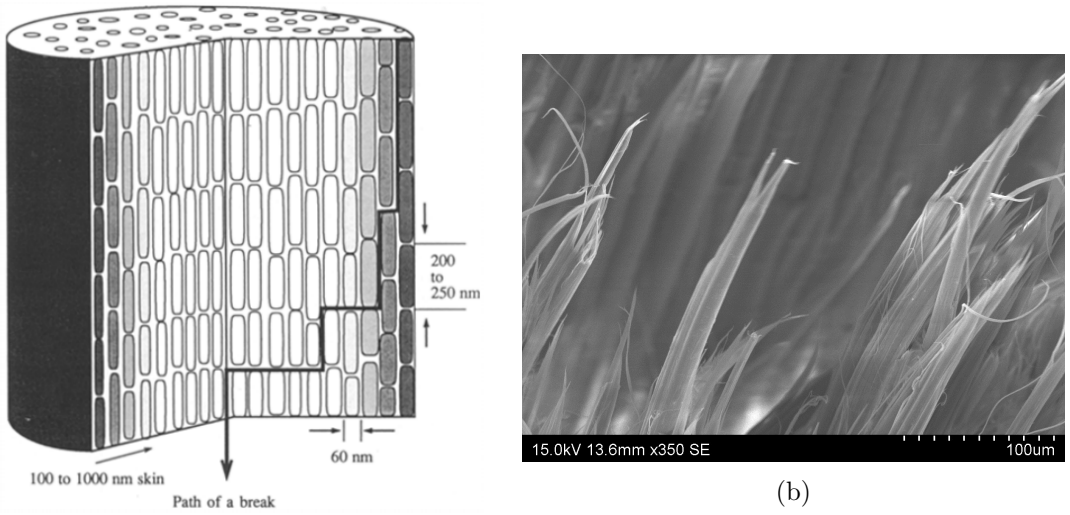
Figure 4.16: Evidence of shear cusps on the fibres (a) multiple cusps seen across the fibre indicated by white arrows (b) Close up image of the shear cusps shown by the black arrow

Analytical estimation of the energy contribution from fibre pull-out can be made using Equation 4.16, by substituting s with s^*. Hence, using information in Table 4.1, the energy related to fibre pull-out is calculated to be 179.06 kJ/m^2. This is a significantly large amount of energy, which account for approximately 70% of the composite fracture toughness.

4.6.3 Vectran fibre failure

Fibre fracture in polymer based fibre composites may account for a finite contribution towards the composite fracture toughness, G_c. A recent study by Porter et al. [178] concluded that the fracture energy contribution from fibre fracture, G_{ff}, for most polymer fibres (including Vectran) is around 1 kJ/m^2. Hull [167] argued that the energy contribution from polymer based composites to the G_c could account for up to a few kJ/m^2 towards the G_c. This is due to the appreciable deformation during tensile loading of the fibre. For Vectran, the energy contribution to the G_c from fibre failure is calculated to be between 16.44 kJ/m^2 and 43.2 kJ/m^2. The calculated values are directly related to the upper and lower bound values for G_{id} in Equation 4.14, due to the mixed-mode dominated failure during fibre-matrix debonding. Additionally, a relatively higher Poisson's ratio may be observed for Vectran fibres (compared to CF and GF), consequently initiating a Mode I dominated fibre-matrix debonding before subsequent fibre failure.

Therefore, assuming a lower bound value for the G_{id} may be appropriate, resulting in a higher G_{ff}. It can also be concluded that the drawing observed on the tip of Vectran fibres, seen in Figure 4.17b, was due to the 'skin-core' structure of Vectran fibres, Figure 4.17a. Failure is thought to initiate in the stiffer 'skin' structure, due to the very high molecular orientation, which then propagates inwards to the 'core'.



(a) (b)

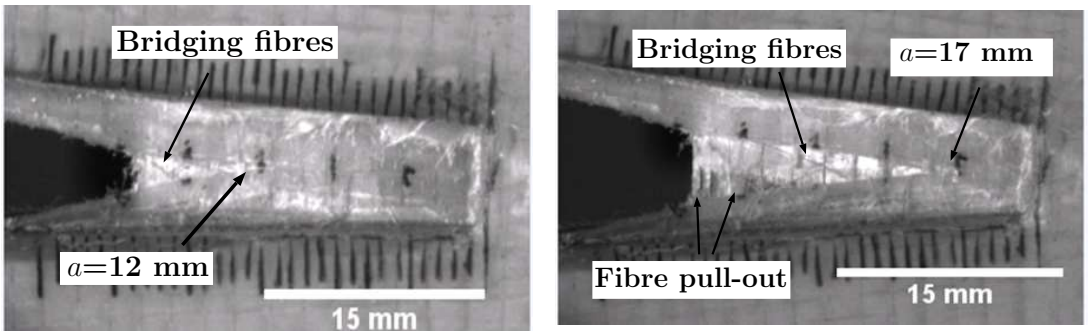
Figure 4.17: (a) Skin-core morphology of Vectran showing the path of failure beginning with failure at the skin which then propagates to the core (b) Close-up image on Vectran fibres

It is also thought the less oriented 'core' region experiences intermolecular friction during molecular chain improvement due to tensile loading [185]. This is a common behaviour of fibres such as Vectran and Dyneema, due to the chain mobility of the polymer molecular structure. The intermolecular friction results in a local temperature increase, followed by a localised failure at the fibre tip. The local temperature increase may have contributed to the failure process of Vectran fibres, resulting in a decrease in the fibre failure strength [148, 185, 186].

4.6.4 Fibre-bridging phenomenon

In the wake of the crack growth, broken embedded fibres are said to be pulled-out from the sockets, leading to a significant amount of energy contribution to the overall fracture energy. This effect is more pronounced when it comes to Vectran fibres. The fibrillar nature of Vectran fibres further promotes fibre-bridging, redistributing the stresses that

were carried by the broken fibres into the composite thus reducing the stress intensity on the crack tip [180].



(a) (b)

Figure 4.18: Fibre-bridging development on Vectran/MTM57 CT specimen (a) a=12 mm: Fibre-bridging phenomenon can be slightly observed (b) a=17 mm: Fibre-bridging phenomenon fully visible, with evidence of fibre pull-off in the wake of the crack

Figure 4.18 shows the development of fibre-bridging phenomenon during crack propagation in Vectran/MTM57 CT specimen. It can be seen that the increase in crack growth gradually reveals the bridging fibres which originates from the adjacent 90 ° plies. The phenomenon can be slightly observed at crack length of approximately 12 mm, Figure 4.18a, and finally fully observable at crack length of 17 mm, Figure 4.18b. Also seen in Figure 4.18b are fibre bundles being pulled out in the wake of the crack tip. These observations seen from Figures 4.18a and 4.18b can be concluded to influence the trend seen in the R-curve, Figures 4.12 and 4.13, in which the R-curve is seen to rise up to crack length of approximately 31 mm, at which the trend is seen to plateau.

4.7 Summary

The research presented in this chapter focused on characterising the translaminar fracture toughness of Vectran/MTM57 composites. Apart from obtaining the G_{Ic} values which is important for numerical modelling, this chapter also aimed to investigate the different failure types which contribute to the G_{Ic}. Existing analytical methods are utilised to estimate the energy associated with the different failure types such as fibre failure and fibre pull-out.

It was found that the relatively high G_{Ic} of Vectran/MTM57 was largely due to fibre pull-out. The fractographic observation performed on the fracture surface clearly revealed pulled-out fibres of varying length, in addition to the evidence of Mode II failure, due to fibre-matrix interfacial sliding during the fibre pull-out proces. Additionally, the energy dissipated from fibre failure may also contribute to the high G_{Ic} obtained for Vectran/MTM57, due to the 'skin-core' nature of Vectran fibres. It is also likely that a local temperature rise may have occured due to the intermolecular friction of the 'core' region, consequently reducing the failure strength of the fibres. Finally, fibre-bridging may also contribute to the G_{Ic} of the composite. This is evidenced by the images from the CCD camera, Figure 4.18, where the development of fibre bridging can be fully observed, in addition to the fibre bundles being pulled-out in the wake of the crack growth.

Chapter 5

The Impact Response of Composite Laminates

5.1 Introduction

The response of composite laminates from transverse impact loading is known to vary with the speed of impact [11, 20]. In Low Velocity Impact (LVI) conditions, boundary effects usually dominate since the impact duration is longer between the laminate and the impactor. Conversely, stress wave effects usually dominate in High Velocity Impact (HVI), since the impact times are usually shorter than LVI. Furthermore, damage patterns observed in the two cases are often different. In LVI, global damage modes may be observed, since large deflections often occur, which depend highly on the shear properties (both in-plane and interlaminar) of the material. Compared to LVI, the type of damage found on HVI laminates are often highly localised at the region of impact

Therefore, characterisation of impact resistance and damage on both impact loading types is crucial before material selection for structural design. In this chapter, the response of all three composite materials to low and high-velocity impact loading is investigated. The type of damage for both low and high-velocity impact is also highlighted and discussed to obtain a detailed understanding of the impactor mass and velocity effects. The extent of delamination for both velocity regimes is studied using ultrasonic C-scan and radiograph images. Finally, where possible, fractographic studies have been

undertaken to understand the influence of the interlaminar toughness on the impact resistance.

5.2 Laminate manufacturing

Three materials were selected to be investigated under impact loading, namely:

1. IM7/8552 - CF/Epoxy;
2. S2-Glass/MTM57 - GF/Epoxy;
3. Vectran/MTM57 - TLCP/Epoxy

For S2-Glass/MTM57 and Vectran/MTM57 laminates, the Resin Film Infusion (RFI) technique was employed, in which the MTM57 resin films were stacked in between the NCF layers. For IM7/8552, each pre-preg ply was stacked up to the required thickness, as shown in Table 5.4. Completed layups were then cured in an autoclave following the cure cycle recommended by each supplier [141, 142]. Finally, the cured laminates were cut into 100 mm x 150 mm specimens (shown in Figure 5.1) as recommended by ASTM [187].

Table 5.1: Laminate and material physical properties

	IM7/8552	S2-Glass/MTM57	Vectran/MTM57
Areal density[1] (g/cm^2)	134	279.67	315.7
Fibre density (g/cm^3)	1.78	2.48	1.41
Fabric thickness (mm)	0.125	0.126	0.224
Laminate thickness (mm)	3.9	3.45	4.3
Resin film thickness (mm)	-	0.268[2]	0.178[3]
Specimen weight (g)	94	90	94
No. of plies/layers	32	14	14
Layup	$[0\,^\circ/90\,^\circ]_{16s}$	$[0\,^\circ/90\,^\circ]_{7s}$	$[0\,^\circ/90\,^\circ]_{7s}$
FVF[4] (%)	60	55	62

[1]This is a combined areal density using the rule of mixture
[2]Corresponds to 319 gsm areal weight
[3]Corresponds to 212 gsm areal weight
[4]Measured using optical method

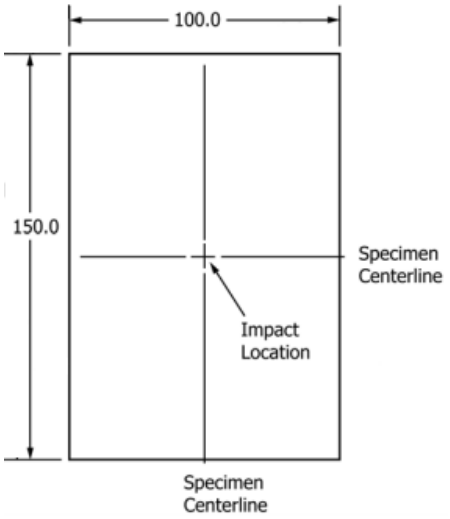


Figure 5.1: Typical impact specimen dimensions [187]

5.3 Experimental procedure

5.3.1 Low Velocity Impact

LVI testing was performed using the CEAST/Instron 9350 instrumented drop tower at three different impact energy level (40 J, 100 J, and 160 J). The energy levels were selected so as to obtain a range of damage from no penetration to full penetration. Specimens were impacted using a steel hemispherical impactor, 16 mm in diameter and 2.4 kg in mass. The impact velocity, V_i, was measured using a photoelectric sensor attached to the drop tower. Upon impact, a reflector which is attached to the impactor rig passes through the sensor hence capturing the impact velocity. A 90 kN load cell (strain gauge based) was attached to the impactor to record the load-time history plots for all materials. The drop tower is fitted with a pneumatically operated anti-rebound system to prevent multiple impacts on the target laminate. Figure 5.2 shows the drop tower used for LVI testing. All laminates are mounted on the ASTM D7136 suggested test fixture [187] before impact.

5.3.2 High Velocity Impact

A 50 mm calibre single stage light gas gun was utilised to perform HVI testing on the aforementioned target laminates. The gas gun has two 10 litre pressure actuators

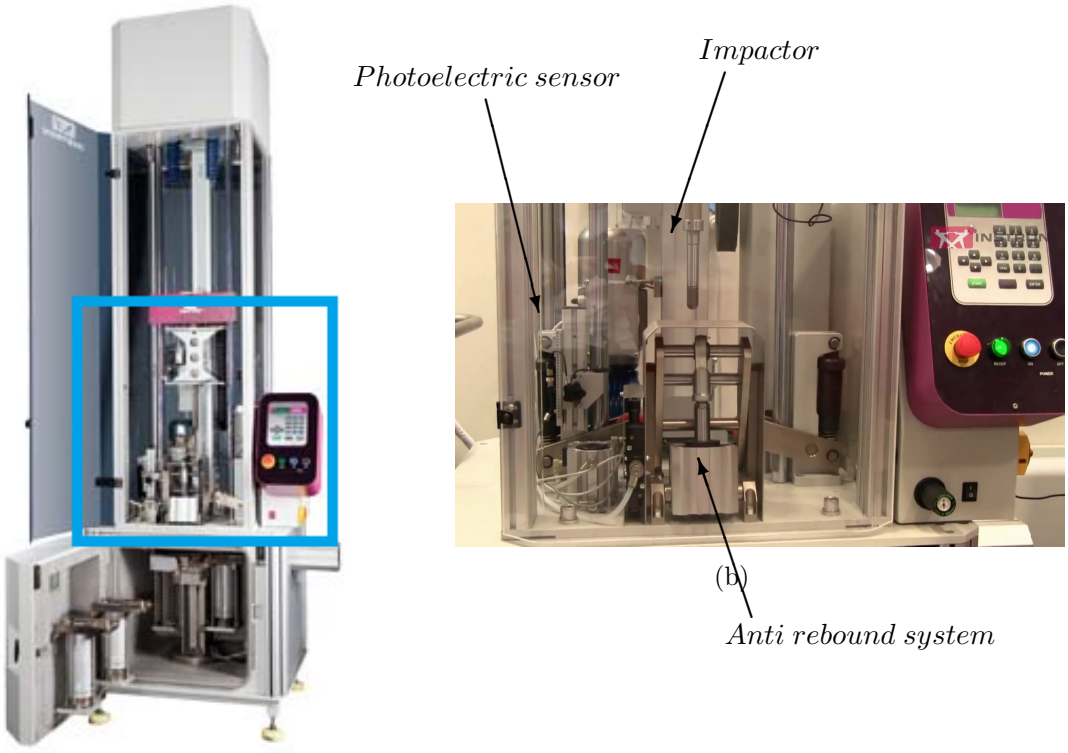


Figure 5.2: (a) Instron 9350 drop tower. Blue square represents close up image in (b)

in which the launch gas can be pressurised up to 330 Bar. The target laminate was supported using braided Kevlar yarns on a custom house-made fixture in the capture tank, which was then closed and a vacuum was drawn (as shown in Figure 5.4). Spherical steel projectiles of approximately 16 mm in diameter and 16.7 g in mass were placed in front of a Polypropylene sabot prior to firing. Upon reaching a vacuum level of 100 mBar, the gas gun was pressurised to the desired pressure and fired.

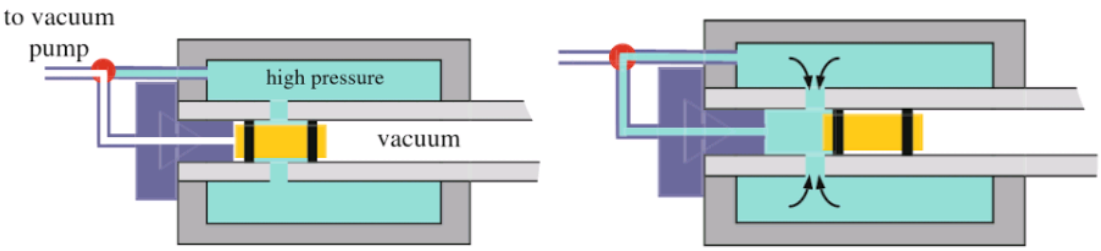


Figure 5.3: Illustration of the 'wrap-around' type breech system employed in the gas gun in this study. (a) Before firing sabot is held in place (b) Upon firing, pressure is released into the main barrel via the annular ports to propel the sabot (and projectile) [188]

The gas gun employs a 'wrap-around' breech [188, 189], shown in Figure 5.3, in which the pressure surrounds the sabot, preventing any unwanted movement before firing. Such a system does not require any burst disks, which is convenient and less expensive to use, as well as ensuring a highly repeatable impact velocity. The annular ports are sealed in between two O-rings which were attached to the sabot, and upon firing, a small amount of gas is supplied at the rear of the sabot, pushing it forward.

The held high pressured gas was then released via the annular ports, driving the sabot (and the projectile) along the 5 m long barrel. The sabot is then arrested at the end of the muzzle via a sabot stripper, leaving the projectile to continue forward until finally impacting the test laminate. The impact and residual velocities were measured using a high-speed video camera (Phantom V25.11), positioned directly to the side of the chamber, focused on the laminate through a window.

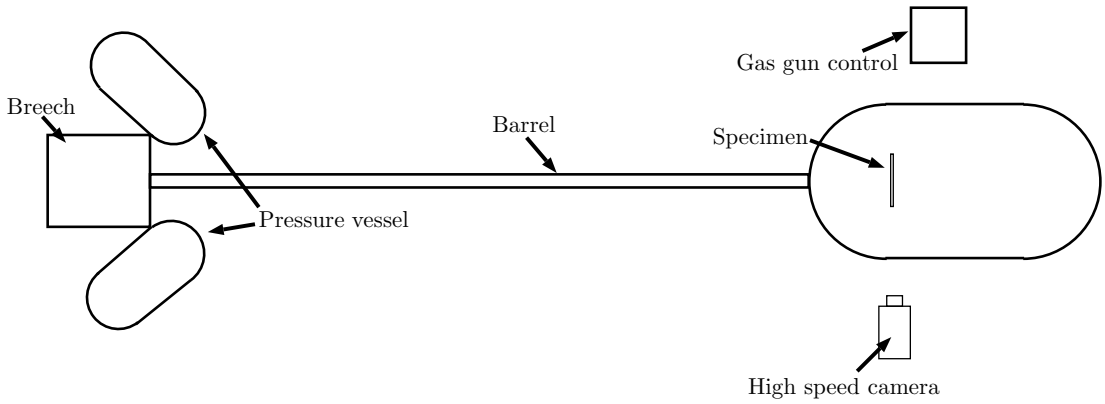


Figure 5.4: HVI testing setup (top view)

Velocity-pressure calibration

Prior to performing any testing on the laminates, the impact velocity must be calibrated with the firing pressure of the gas gun. This is so that the impact velocity to be estimated for each firing pressure, enabling a reliable V_{50} estimation for each test material.

Figure 5.5 shows the calibrated impact velocity and firing pressure. Approximately six shots were fired to obtain a suitable calibration. Note that the calibration was performed using the 16mm steel projectile ($\approx$ 16.7 g) mounted on a Polyethylene sabot ($\approx$ 62 g). It can be observed that the firing velocity increases non-linearly with increasing firing pressure.

The velocity-pressure relationship can also be estimated numerically by using the procedure proposed by Siegel [188, 190]. Siegel showed that a realistic estimate of the muzzle velocity can be obtained by assuming the gas reservoir is an infinitely long tube with the same diameter as the barrel, therefore neglecting the reflection and refraction waves in the gas reservoir. Therefore, the propelling pressure, P can be related to the projectile velocity, v_p, given by:

$$P = P_0 \left[1 - \frac{(\gamma - 1)v_p}{2c_0}\right]^{\frac{2\gamma}{(\gamma-1)}} \tag{5.1}$$

where γ is the adiabatic exponent of the gas (for air, $\gamma = 1.4$), c_0 is the sonic velocity (for air, $c_0 = 343$ m/s at 20 °), v is the velocity of the projectile travelling in the barrel, and P_0 is the initial gas pressure. Equating Equation 5.1 to Newton's second law yields:

$$F = ma = P_0 A_p \left[1 - \frac{(\gamma - 1)v_p}{2c_0}\right]^{\frac{2\gamma}{(\gamma-1)}} \tag{5.2}$$

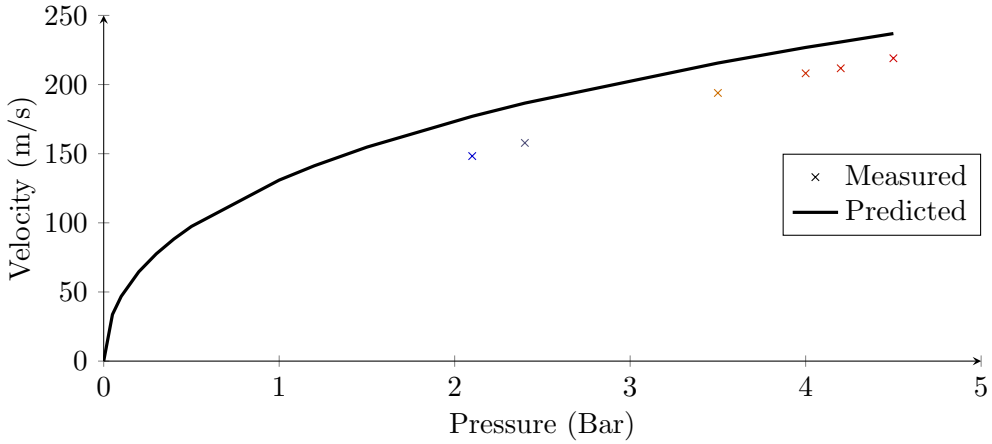


Figure 5.5: Velocity-pressure calibration curve

One can also estimate the velocity by integrating Equation 5.1 [188] yielding:

$$v_p(t) = \frac{2c_0}{\gamma - 1}\left\{1 - \frac{Mc_0}{P_0}\left[1 + \frac{\gamma + 1}{2Mc_0}P_0 t\right]^{-\frac{\gamma-1}{\gamma+1}}\right\} \tag{5.3}$$

where A_p is the projectile cross-sectional area, m_p is the projectile mass, t is the time, and $M = A/m$. Using Equation 5.3, the calculated velocity was plotted against the firing pressure, shown in Figure 5.5. It must be noted that Equation 5.3 is valid up to the end of the muzzle; before the sabot (and projectile) hit the sabot stripper. Consequently,

the experimental projectile velocity was measured after the projectile had exited the sabot stripper. This may explain the overestimation seen in Figure 5.5. Nevertheless, the trend predicted by the numerically calculated velocities showed excellent agreement with the experimentally measured values.

Ballistic limit prediction

At least five tests were performed to identify the V_{50} of each composite material. Determination of V_{50} was made using the bisection method [191] due to the following factors:

(i) The number of available samples was limited;

(ii) This method was deemed most appropriate based on the cost, availability, and reliability [191]

Upon selecting the velocity in which the V_{50} was thought to exist, the laminates were impacted at the average of the velocities at which complete perforation did and did not occur. Initial selection on the impact velocity can be estimated from several existing analytical methods available in the literature [30, 192, 193]. In this PhD, the method proposed by Walker [192] was utilised to approximate the V_{50} for each composite laminate. Table B.1 presents the predicted ballistic limit for the laminates used in this PhD study using the analytical technique proposed by Walker [192]. Appendix 10.2 discusses in detail regarding Walker's approach including the analytical calculations involved.

Finally, the procedure describe was repeated for all laminates. The obtained velocities were then fitted using the Jonas-Lambert model [194] defined as:

$$V_r = \begin{cases} 0 & \text{if } 0 < V_i \leq V_{bl}; \\ \kappa \sqrt[p]{V_i^p - V_{bl}^p}, & \text{if } V_i > V_{bl} \end{cases} \tag{5.4}$$

where V_r is the residual velocity, V_i is the impact velocity, V_{bl} is the ballistic velocity (or V_{50}), κ and p are the Jonas-Lambert parameters. For non-deformable projectiles, the power p is equal to 2 and Equation 5.4 is known as the Recht-Ipson model [195]. In

this work, p=2 since the projectile was not observed to deform. Finally, the parameter κ was assumed between 0.85 and 1 to fit the experimental results.

5.4 Results

5.4.1 Low Velocity Impact

A number of tests were performed under three different impact energies to examine the extent of damage induced on laminates of selected materials, which is:

(i) No penetration: 40 J impact energy;

(ii) Partial penetration: 100 J impact energy;

(iii) Full penetration: 160 J impact energy.

Impacted laminates were then post-processed by way of visual inspection of the impact cross-section, optical microscopy, ultrasonic C-Scan, and radiographic images, enabling a comprehensive investigation of the extent of damage on each material.

40 J impact energy

At 40 J of impact energy, an almost elastic response can be observed for Vectran/MTM57 and S2-Glass/MTM57 laminates, shown in Figures 5.6 to 5.9. This is indicated by an almost perfect bell-shaped curve from the load-time histories for both S2-Glass/MTM57 and Vectran/MTM57 laminates, Figures 5.6 and 5.8, respectively. The average peak load for each laminate was 8.1 kN, 7.4 kN, and 7.9 kN for S2-Glass/MTM57, Vectran/MTM57, and IM7/8552, respectively. The load-deflection histories for both S2-Glass/MTM57 and Vectran/MTM57 laminates display a considerable amount of permanent deflection (the load-deflection curve does unload back directly to the origin). This indicates that both laminates have absorbed a finite amount of energy transferred from the impactor during the impact event.

Figures 5.10 and 5.11 present the load-time and load-deflection histories for IM7/8552. The Delamination Threshold Load (DTL) is identified to be approximately 6 kN, beyond which large oscillations can be observed for the remainder of the impact event.

Each of the impacted IM7/8552 laminates displayed all of the commonly known damage types including matrix cracking, delamination, fibre fracture, and splitting, shown in Figures 5.14a - 5.14b. Matrix cracks (or intralaminar damage) can be seen at a region surrounding the impact site, Figure 5.14b. These cracks are seen to propagate towards the adjacent perpendicular plies, hence initiating delamination between plies, due to the property mismatch [11, 20, 42, 123]. For Vectran/MTM57, initial inspection of the impacted laminates showed minimal deformation, Figures 5.12a and 5.12b, although some permanent deformation can be observed on the front and back face of the plate, Figures 5.43a and 5.43b, respectively. Additionally, some delamination was seen at the point of impact, revealed from radiograph and C-scan images, Figures 5.43c and 5.43d, respectively. Finally, concerning S2-Glass/MTM57 laminates, cross-sectional images taken directly below the point of impact showed matrix and compressive failure, observed from the kink-band morphology close to the laminate front face, Figure 5.13.

It should be noted that the 'ringing' observed in all the load-time/deflection histories (particularly before any failure onset) for IM7/8552, S2-Glass/MTM57 and Vectran/MTM57 was thought to be due to natural frequency of the impactor [187]. In addition, other external factors such as structural vibration of the LVI rig may also influence the severity of the 'ringing'. The wavelength from the load-deflection histories was measured to be 0.8 mm (± 0.2 mm), which was constant across all energy levels (40 J, 100 J, and 160 J) for all composite laminates.

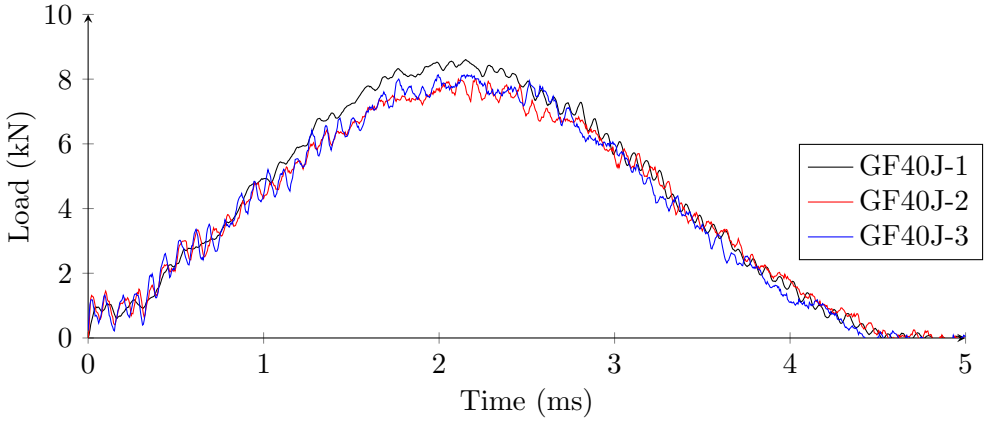


Figure 5.6: Load-time response for 40 J impact loading of all three impacted S2-Glass/MTM57 laminates

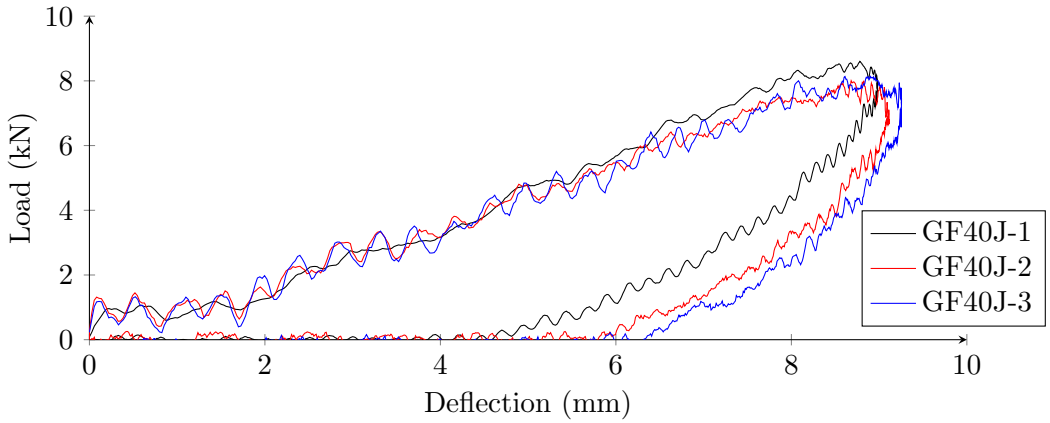


Figure 5.7: Load-deflection response for 40 J impact loading of all three impacted S2-Glass/MTM57 laminates

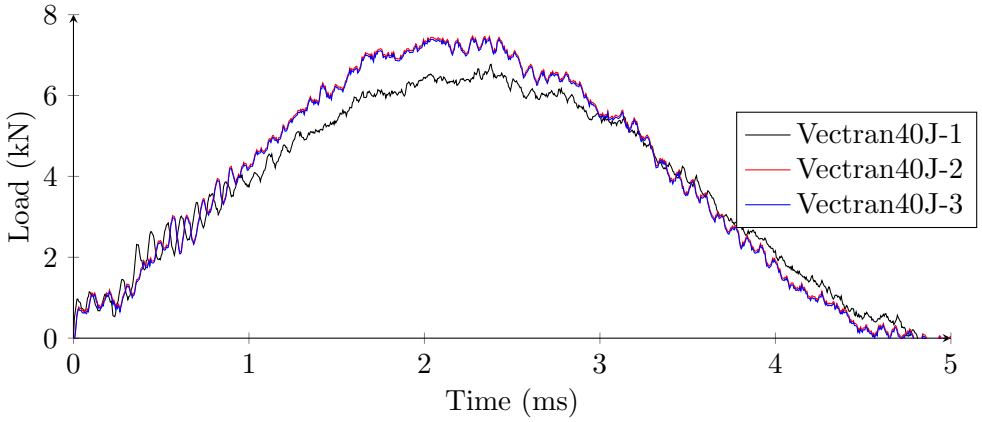


Figure 5.8: Load-time response for 40 J impact loading of all three impacted Vectran/MTM57 laminates

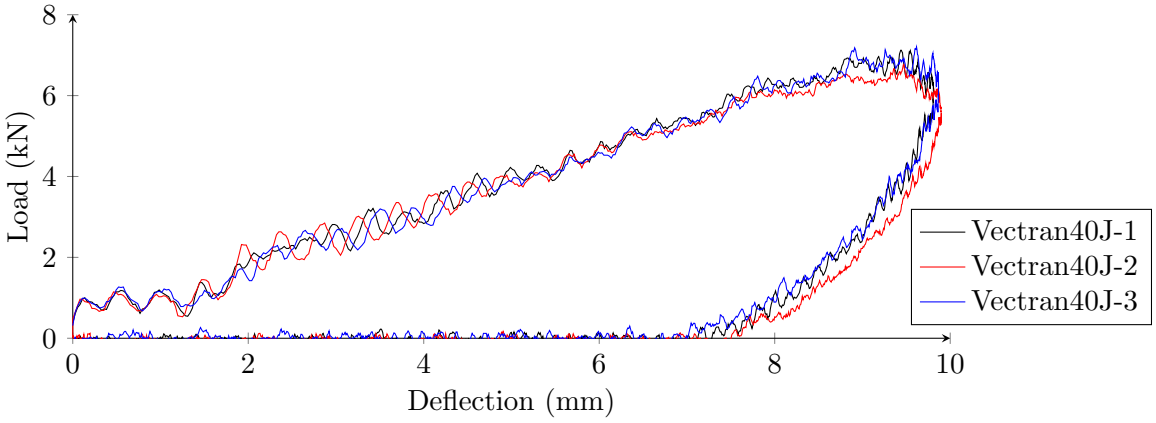


Figure 5.9: Load-deflection response for 40 J impact loading of all three impacted Vectran/MTM57 laminates

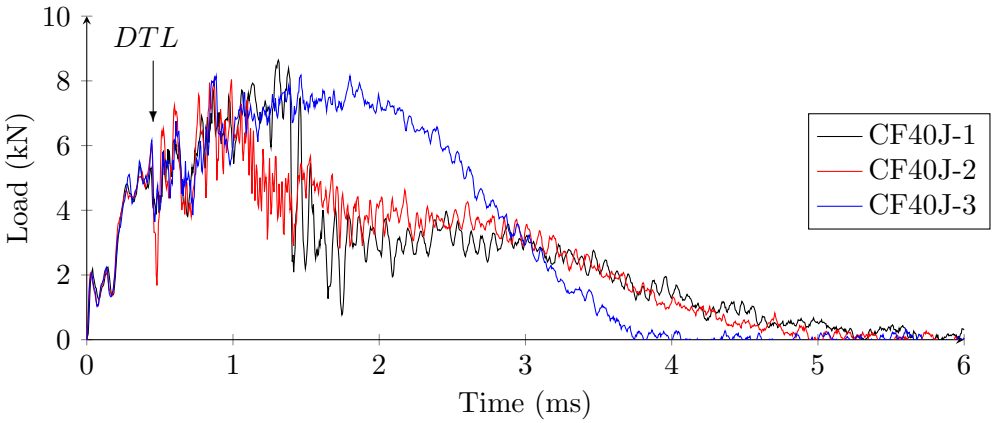


Figure 5.10: Load-time response for 40 J impact loading of all three impacted IM7/8552 laminates. 'DTL' indicates the Delamination Threshold Load

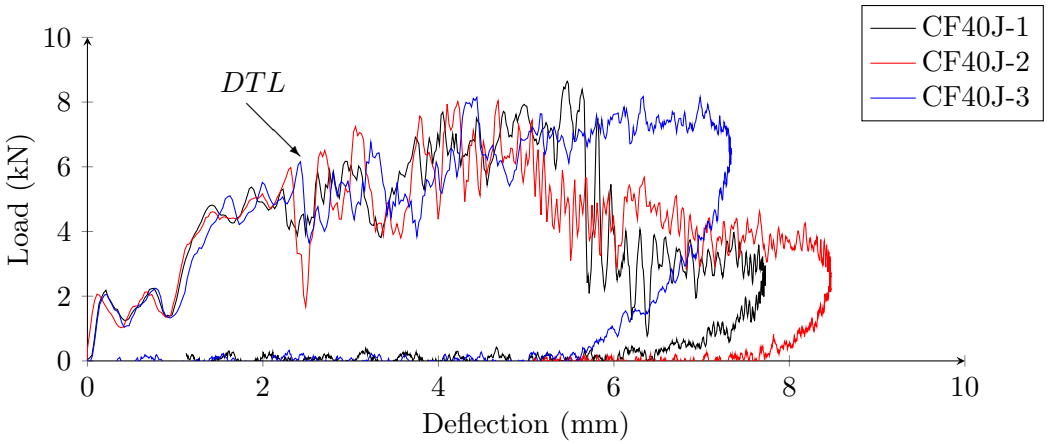
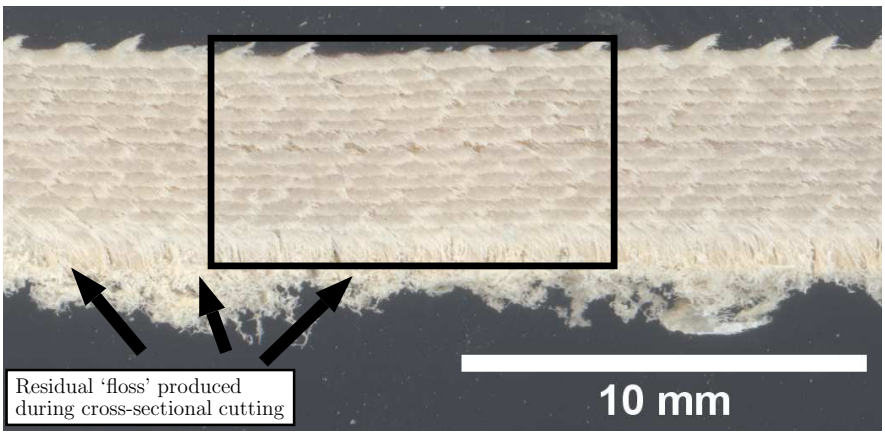
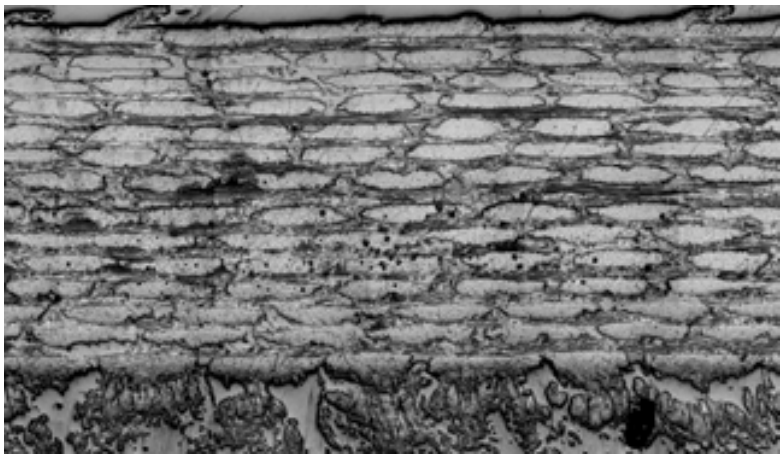


Figure 5.11: Load-deflection response for 40 J impact loading of all three impacted IM7/8552 laminates.'DTL' indicates the Delamination Threshold Load

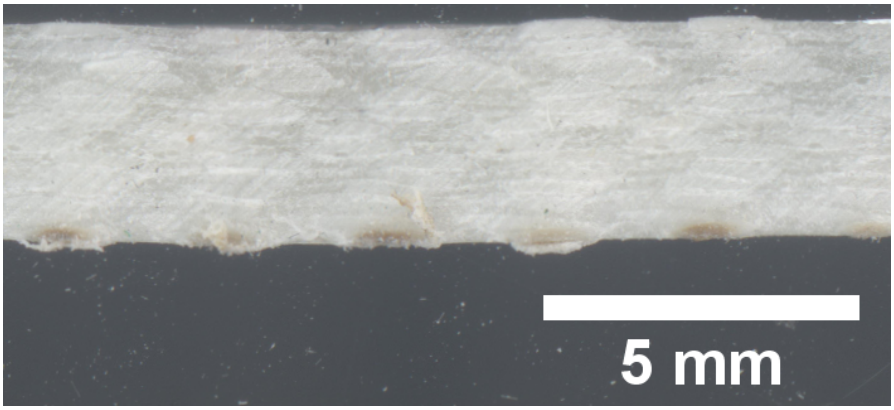


(a)

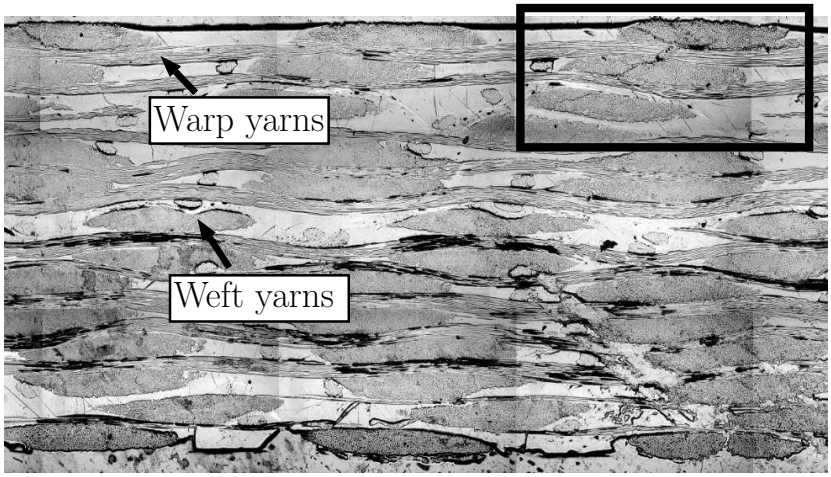


(b)

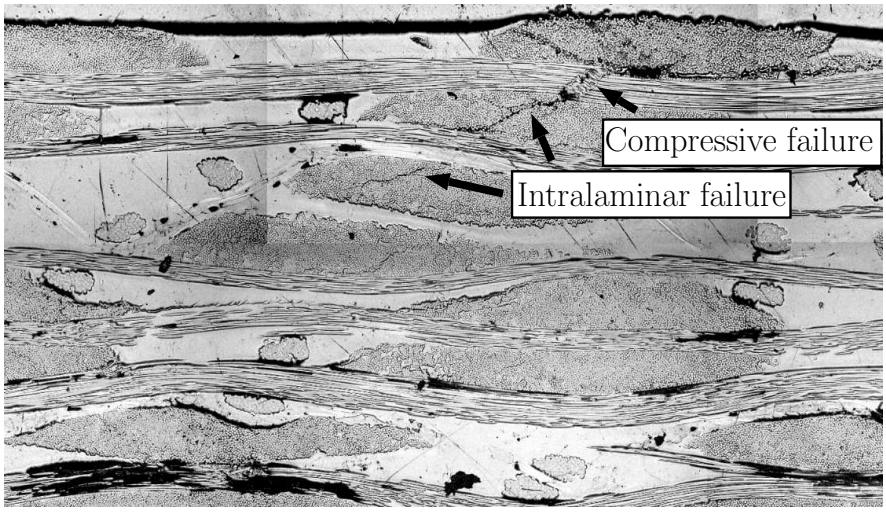
Figure 5.12: (a) Cross-sectional view of Vectran/MTM57 laminate under 40 J impact. (b) Optical micrograph of the black square shown in (a). No observable damage can be seen on the laminate cross-section



(a)

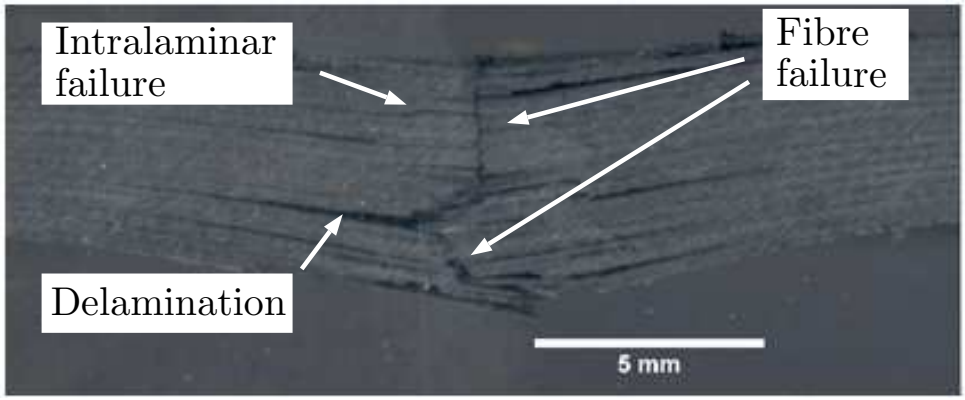


(b)

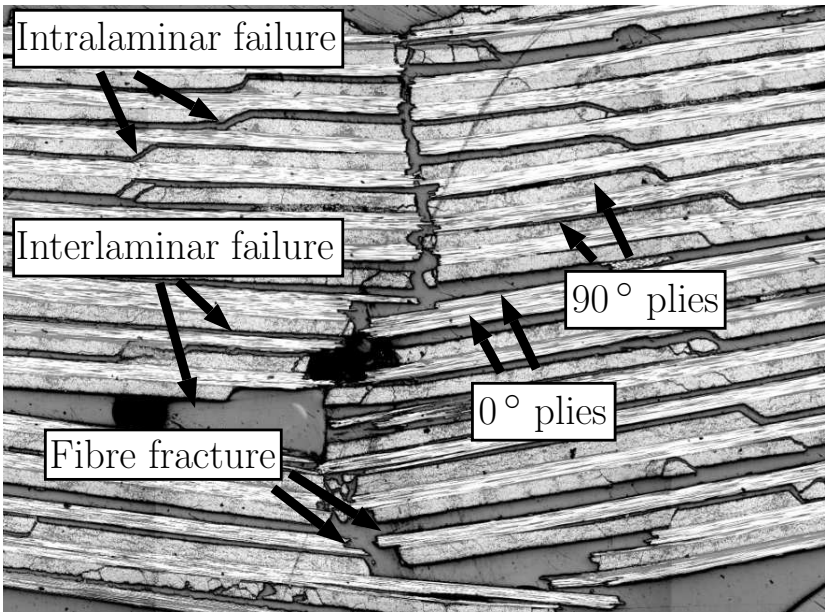


(c)

Figure 5.13: (a) Cross-sectional view of S2-Glass/MTM57 laminate under 40 J impact. (b) Optical micrograph of the black square shown in (a) (c) Close up view of the black square in (b) showing kink-bands and intralaminar damage inidicating compressive and matrix failure



(a)



(b)

Figure 5.14: (a) Cross-sectional view of IM7/8552 laminate under 40 J impact showing multiple damage types (b) Close-up view on the vicinity of impact showing matrix and fibre failure, as well as delamination

100 J impact energy

At 100 J, partial penetration can be observed on Vectran/MTM57 and S2-Glass/MTM57, with full penetration on IM7/8552. Additionally, S2-Glass/MTM57 was seen to absorb the largest amount of energy, quantified as the area under the load-deflection curve, shown in Figure 5.16. The average peak load for each laminate was 12.3 kN, 10.5 kN, and 8.3 kN for S2-Glass/MTM57, Vectran/MTM57, and IM7/8552, respectively.

The DTL may be pointed out clearly for IM7/8552, Figures 5.19 and 5.20, where a

significant drop in the load-time curve can be observed, marking a drop in the whole laminate stiffness and violent oscillations throughout the remainder of the impact event. It should be noted that the magnitude of DTL is comparable to the 40 J loading, indicating a constant DTL throughout all loading energies. Further increase in the load leads to total laminate penetration, followed by a region of pure friction between the laminate and the impactor, denoted by point 'F' in Figure 5.20. A similar peak load was observed in the impact response of IM7/8552 compared to the 40 J case, indicating the maximum load the laminate could withstand. The types of damage were also comparable to the 40 J case, where damage such as intralaminar failure (matrix cracking), delamination, and fibre fracture were all present in the 100 J impact level, Figures 5.23a and 5.23b.

Concerning S2-Glass/MTM57 and Vectran/MTM57 laminates, an increase in the energy absorption was observed for this level of impact. Impactor travel was also markedly higher at around 15 mm, compared to approximately 9 mm for S2-Glass/MTM57 and 10 mm for Vectran/MTM57 under 40 J impact. Damage was also more significant for S2-Glass/MTM57 laminate, where extensive intralaminar failure can be observed throughout the impacted region, including fibre fracture and delamination, shown in Figures 5.21a to 5.21b. For Vectran/MTM57, a larger indentation was observed, with evidence of fibre fracture at the laminate back face, shown in Figure 7.36.

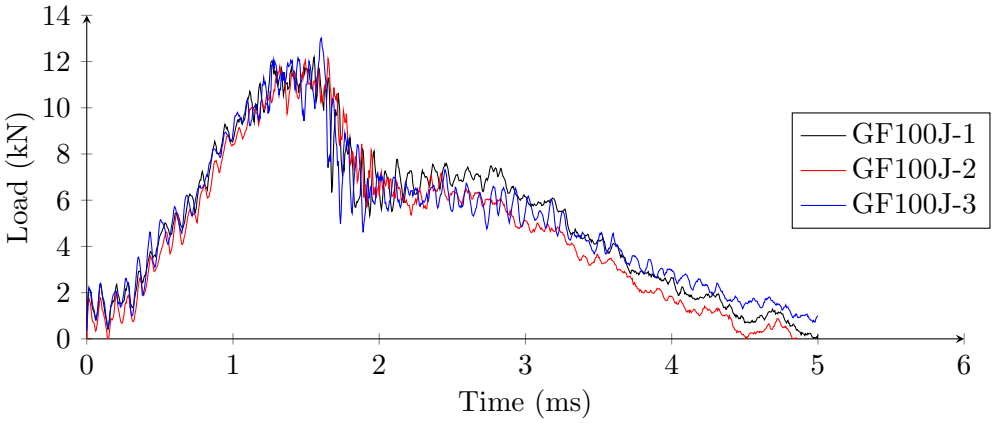


Figure 5.15: Load-time response for 100 J impact loading of all three impacted S2-Glass/MTM57 laminates

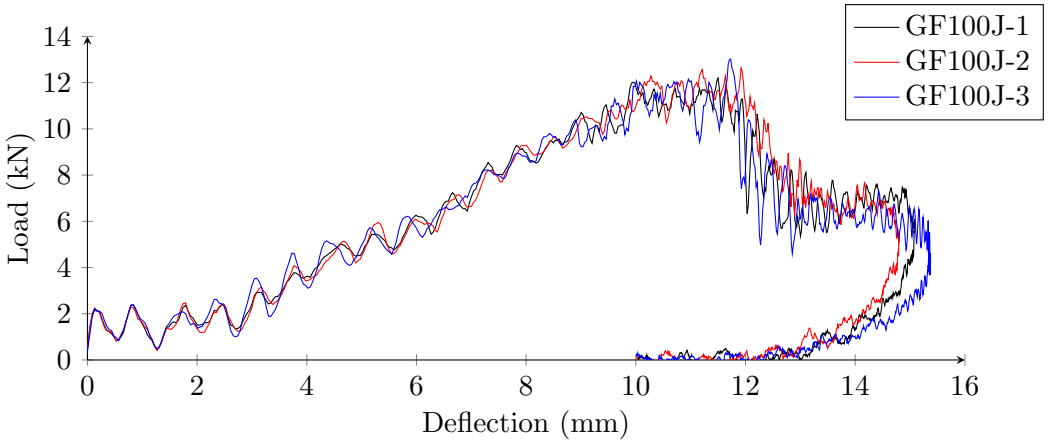


Figure 5.16: Load-deflection response for 100 J impact loading of all three impacted S2-Glass/MTM57 laminates

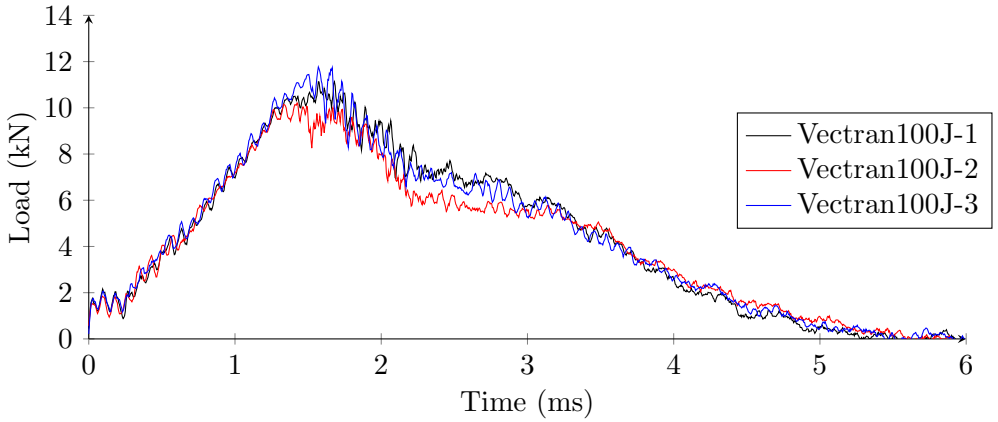


Figure 5.17: Load-time response for 100 J impact loading of all three impacted Vectran/MTM57 laminates

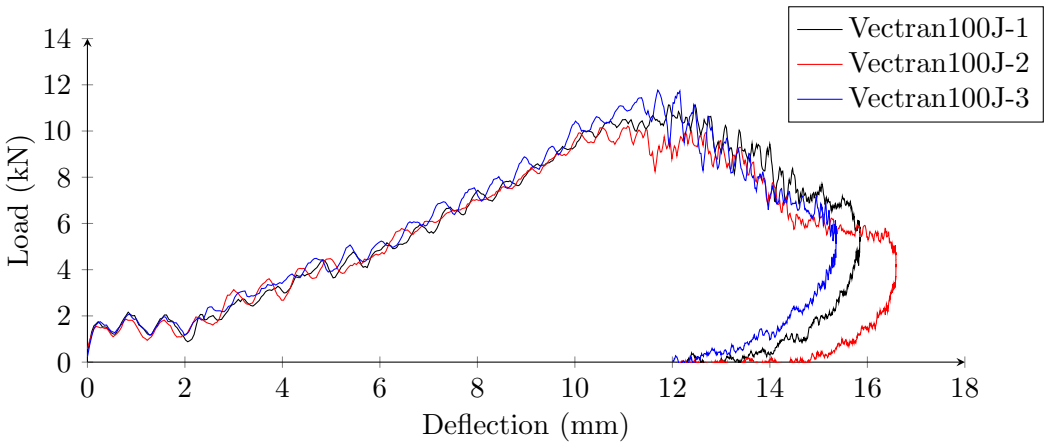


Figure 5.18: Load-deflection response for 100 J impact loading of all three impacted Vectran/MTM57 laminates

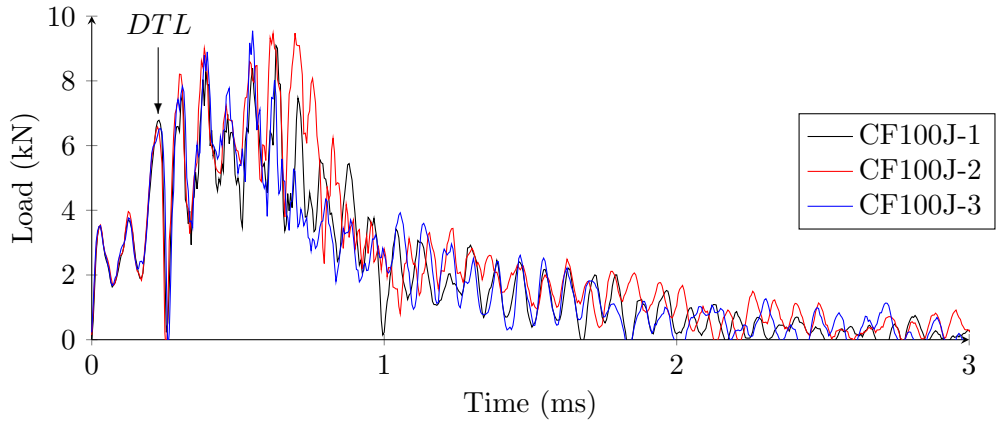


Figure 5.19: Load-time response for 100 J impact loading of all three impacted IM7/8552 laminates

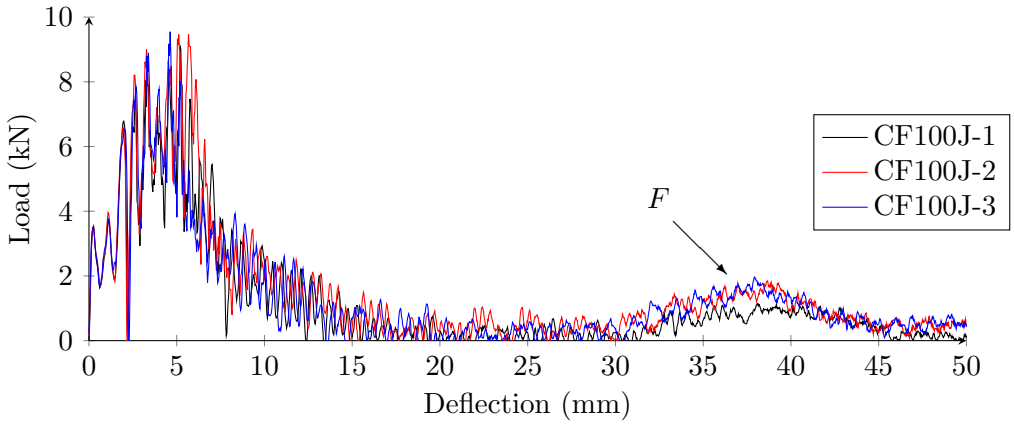
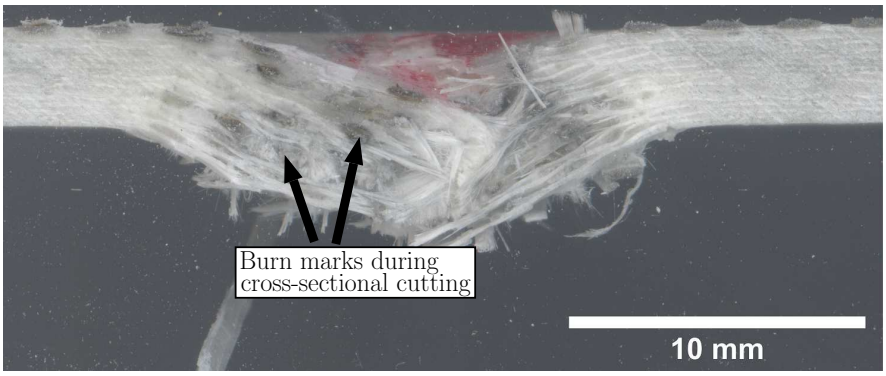
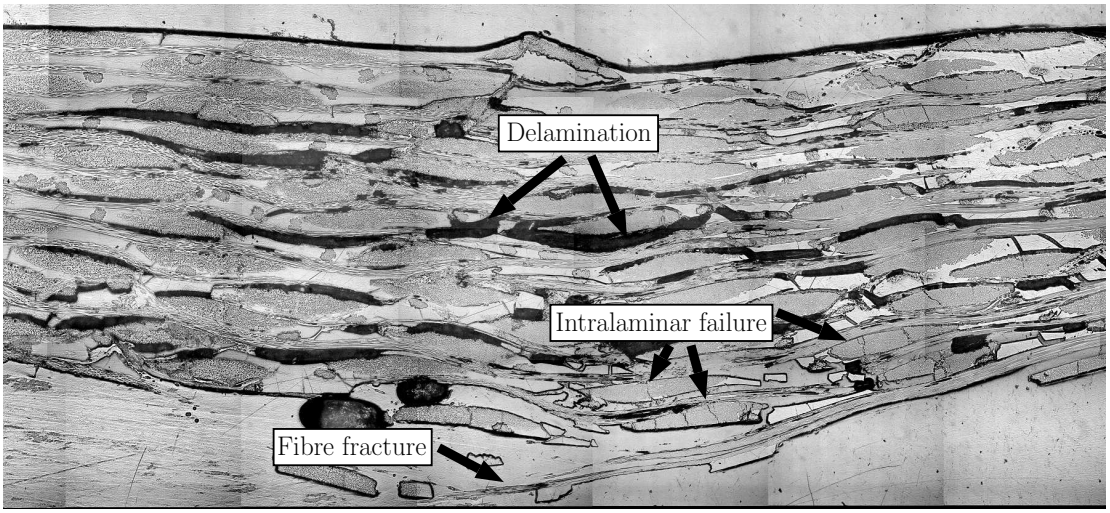


Figure 5.20: Load-deflection response for 100 J impact loading of all three impacted IM7/8552 laminates

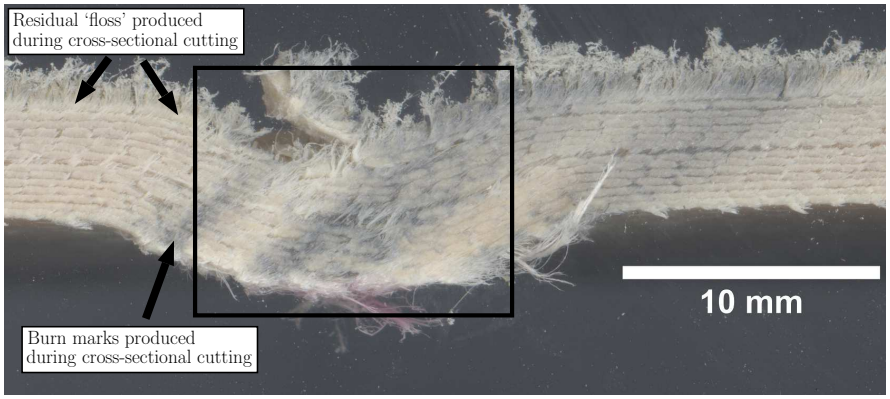


(a)

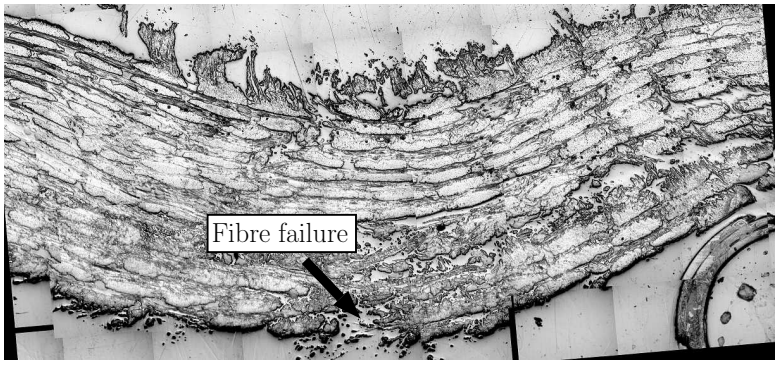


(b)

Figure 5.21: (a) Cross-sectional view of S2-Glass/MTM57 laminate under 100 J impact (b) Close-up view showing intralaminar and fibre failure

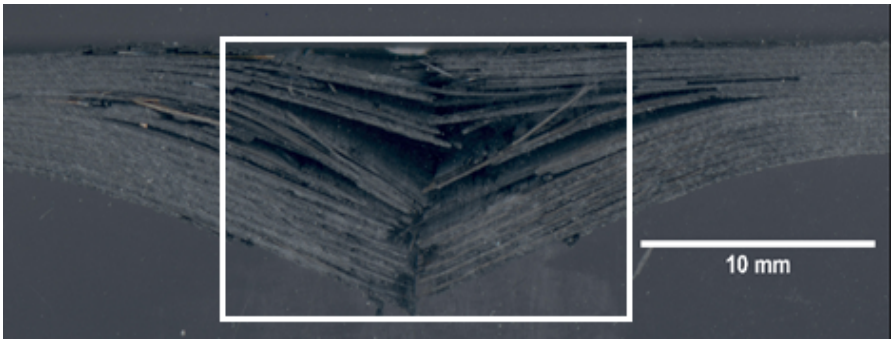


(a)

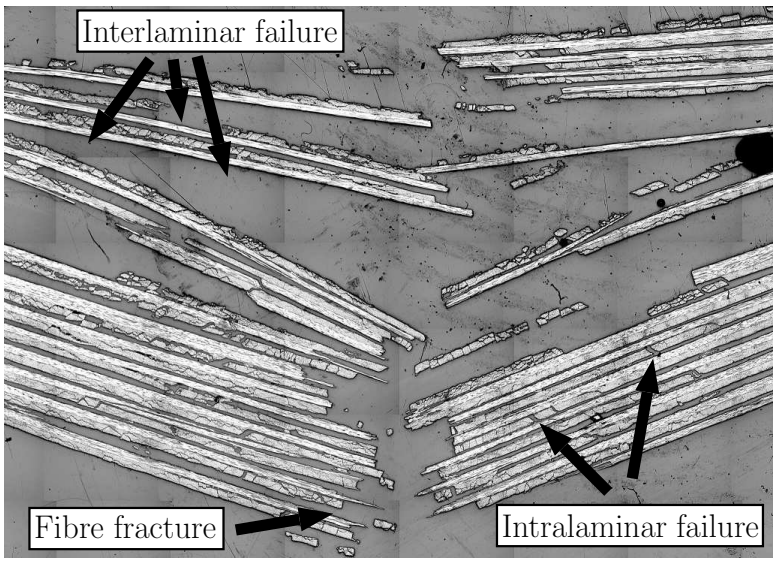


(b)

Figure 5.22: (a) Cross-sectional view of Vectran/MTM57 laminate under 100 J impact showing permanent indentation (b) Optical micrograph of the black square shown in (a)



(a)



(b)

Figure 5.23: (a) Cross-sectional view of IM7/8552 laminate under 100 J impact. (b) Optical micrograph of the white square shown in (a) showing delamination and fibre failure at every ply

160 J impact energy

At 160 J impact energy, all laminates were completely penetrated, with damage localizing at the impact point. This is followed by a region of pure friction between the impactor and the laminate, denoted by point 'F' in the load-time/deflection histories, Figures 5.24 to 5.29. Severe damage can be observed from the laminate cross-section, Figures 5.30 to 5.32, showing all of the commonly known damage types such as matrix cracking, delamination, and fibre failure.

Specifically for S2-Glass/MTM57 and Vectran/MTM57, failure was dominated mainly by transverse shear, resulting in a highly localized failure seen in Figures 5.30 and 5.31; a result of the high impact velocity (hence high energy) inducing a highly localized

event on the laminate. This is also reflected in the load-time/deflection histories for both laminates, Figures 5.24 to 5.27. Both responses showed an increase in the load until reaching the peak force, before unloading with a slope almost symmetrical to the loading part. This could suggest that both laminates experience fibre tensile straining until reaching the maximum, before failing first at the rear of the laminate, which then rapidly progresses upwards (towards the laminate front face). Both laminates also suffered minimal fibre splitting perpendicular to the span of the laminate. No fibre splitting can be observed on the laminate front face. Figures 5.48 and 5.49 shows the top and bottom view of the S2-Glass/MTM57 and Vectran/MTM57 laminates, respectively. Alternatively, Figures 5.30 and 5.31 presents the cross-sectional images of the damaged laminates for S2-Glass/MTM57 and Vectran/MTM57, respectively.

Concerning IM7/8552, the load-time and load-deflection response were highly comparable to the 100 J impact level since in both cases, impactor penetration has occurred. The types of damage present were also similar, displaying intralaminar failure, delamination, and fibre fracture. Finally, the peak load for all laminates were found to be comparable with the 100 J impact case, at 12.62 kN, 12.66 kN, and 8.41 kN for S2-Glass/MTM57, Vectran/MTM57, and IM7/8552, respectively.

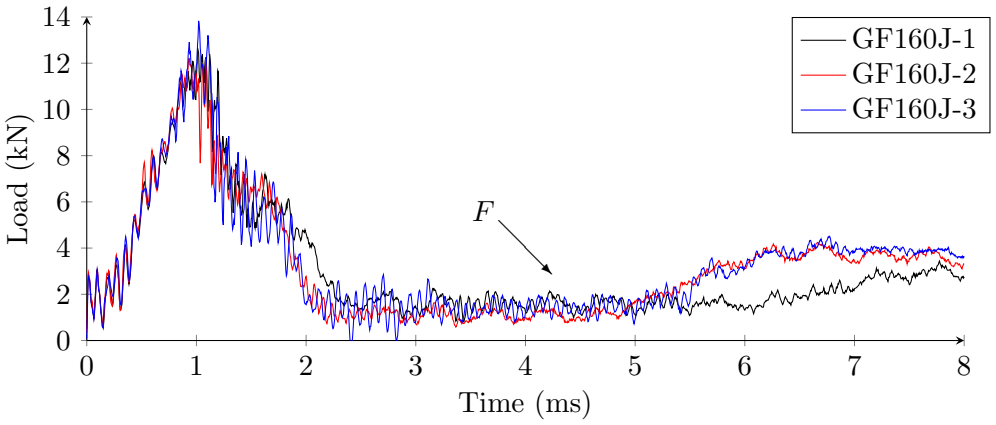


Figure 5.24: Load-time response for 160J impact loading of all three impacted S2-Glass/MTM57 laminates

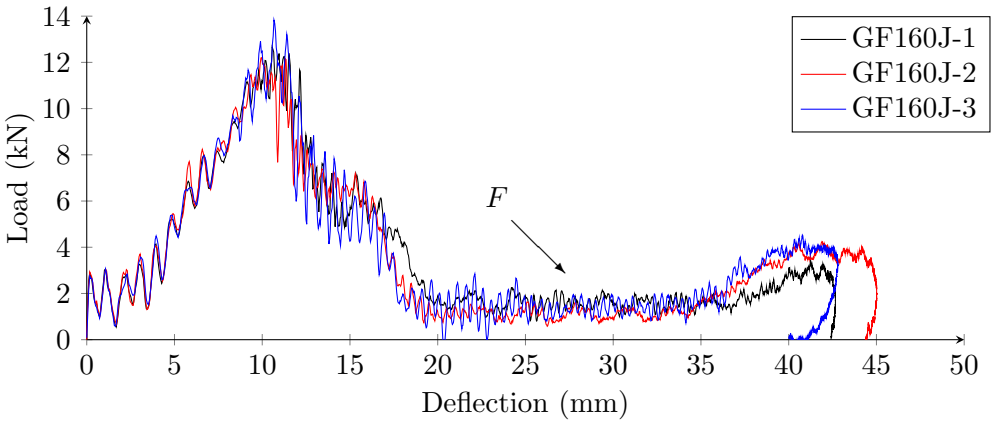


Figure 5.25: Load-deflection response for 160J impact loading of all three impacted S2-Glass/MTM57 laminates

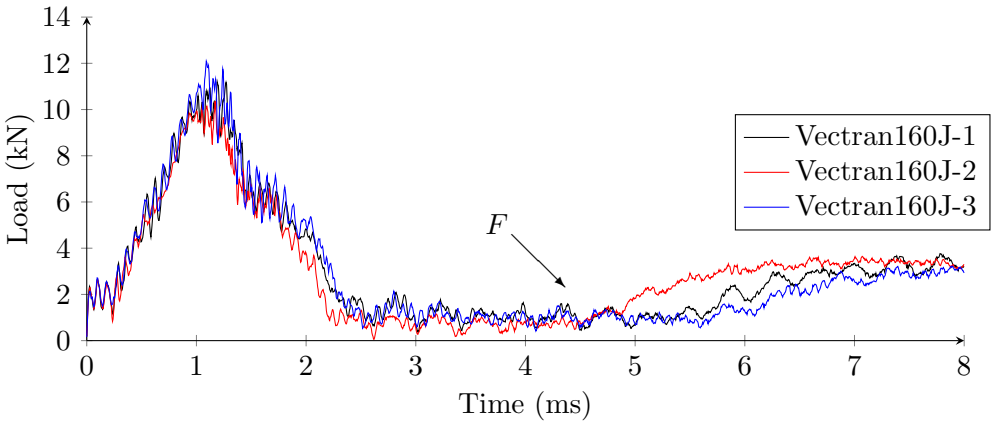


Figure 5.26: Load-time response for 160J impact loading of all three impacted Vectran/MTM57 laminates

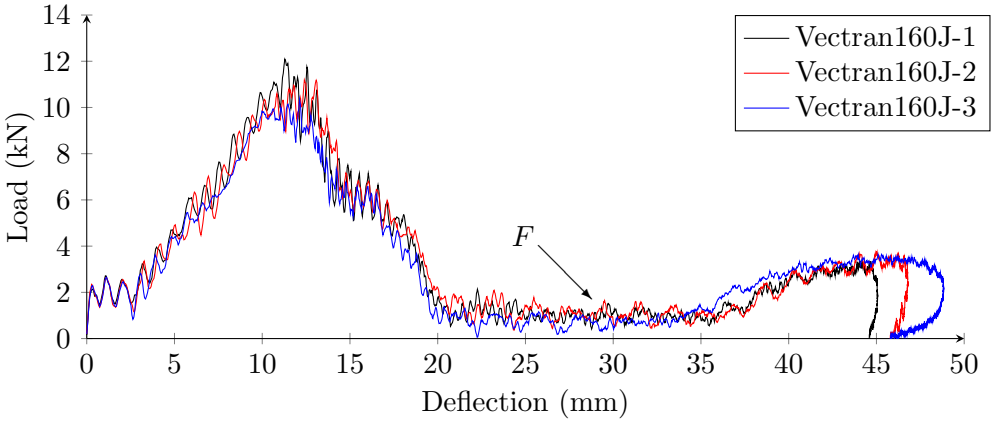


Figure 5.27: Load-deflection response for 160J impact loading of all three impacted Vectran/MTM57 laminates

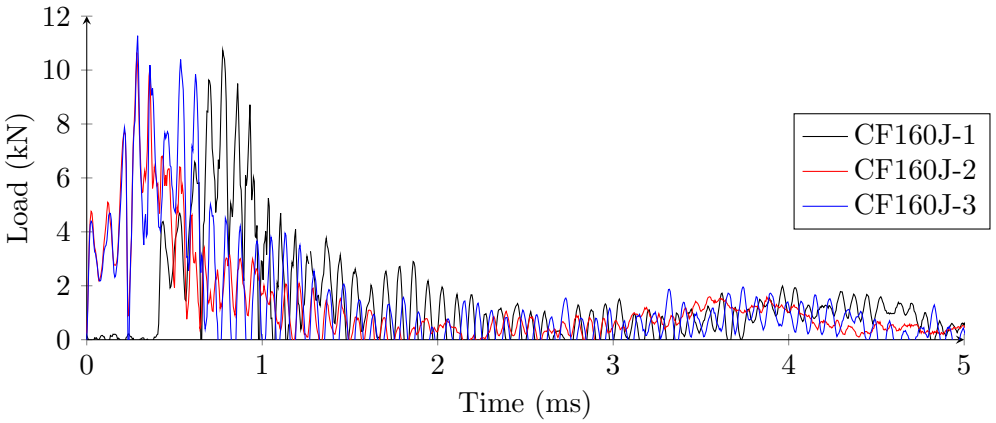


Figure 5.28: Load-time response for 160J impact loading of all three impacted IM7/8552 laminates

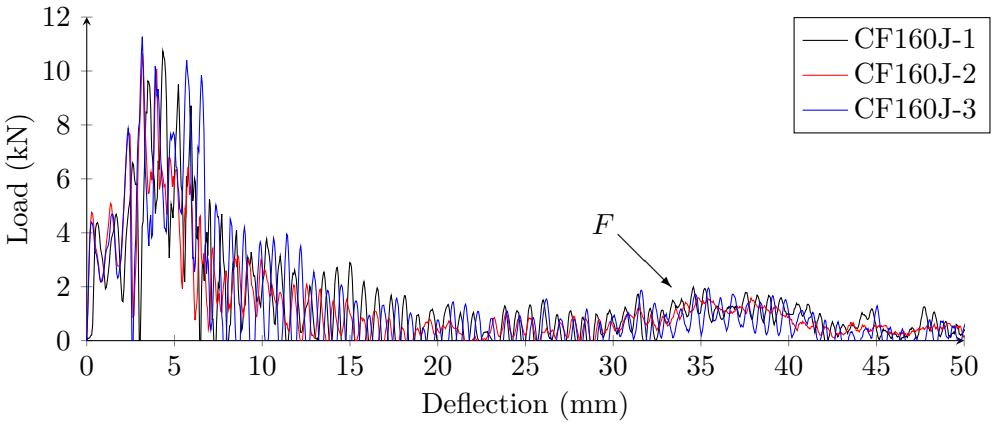
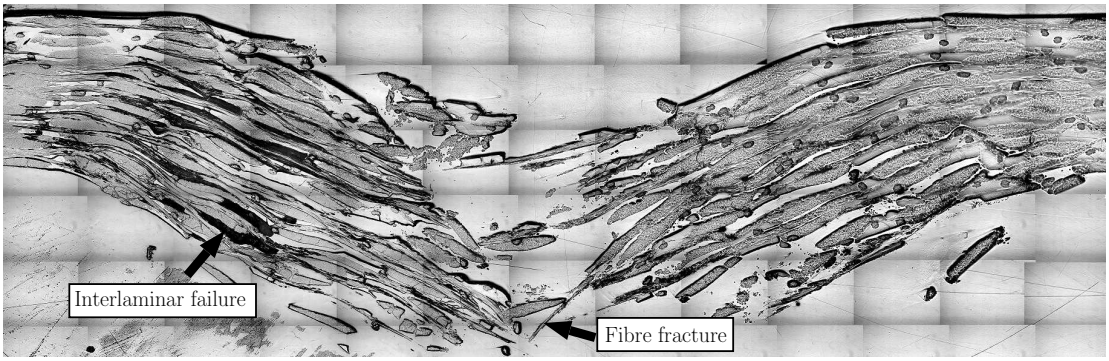


Figure 5.29: Load-deflection response for 160 J impact loading of all three impacted IM7/8552 laminates

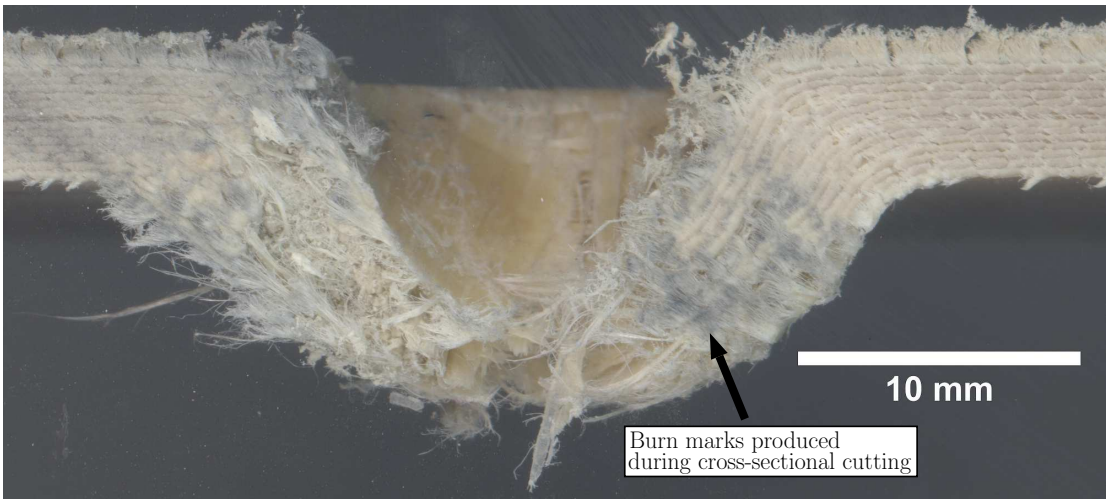


(a)

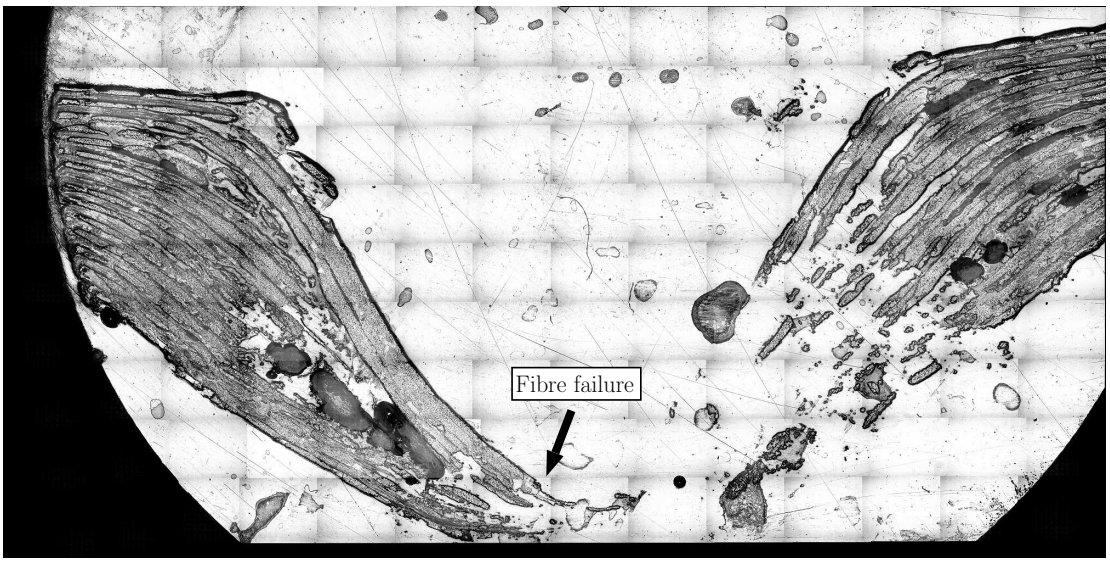


(b)

Figure 5.30: (a) Cross-sectional view of S2-Glass/MTM57 laminate after 160 J impact. (b) Optical micrograph of the black square shown in (a) showing extensive fibre failure at every ply

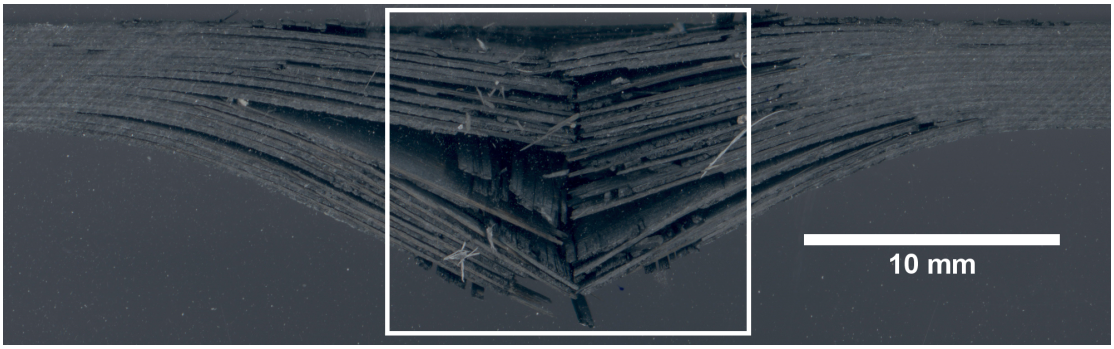


(a)

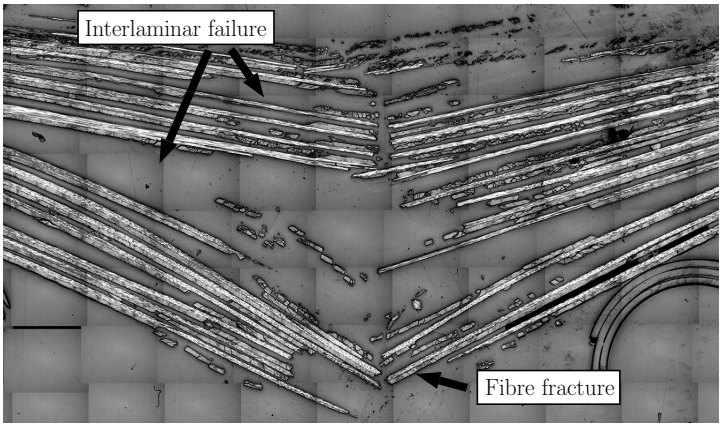


(b)

Figure 5.31: (a) Cross-sectional view of Vectran/MTM57 laminate under 160 J impact. (b) Optical micrograph showing extensive fibre failure at every ply



(a)



(b)

Figure 5.32: (a) Cross-sectional view of IM7/8552 laminate under 160 J impact. (b) Optical micrograph of the white square shown in (a) showing extensive delamination, intralaminar failure, and delamination at every ply

5.4.2 High Velocity Impact

Results

At least five tests were performed to predict the V_{50} for each material. As stated earlier, V_{50} determination was made using the bisection method due to the limited number of samples available. The ballistic curves for all materials are shown in Figure 5.33, where, it can be seen that IM7/8552 has the lowest ballistic performance amongst all three materials used in this study. The V_{50} for IM7/8552 was determined to be 96.67 m/s, approximately 70% lower than Vectran/MTM57 (164.05 m/s). The poor performance of IM7/8552 can be attributed to the inherent characteristic of carbon fibre composite, some of which include a relatively low tensile strain-to-failure compared to the rest of the material used in this study.

Next, considering the ballistic performance for Vectran/MTM57, the V_{50} was calcu-

lated to be approximately 164.05 m/s; the highest V_{50} found among all three materials. This superior ballistic performance of Vectran/MTM57 composites can be attributed to one inherent characteristic of the composite; the low in-plane shear properties (both shear modulus and yield strength) compared to the other two composites, allowing the laminate to absorb more energy by a larger Back Face Deflection (BFD). This is shown in Figure 5.34, in which the BFD is clearly larger if compared to S2-Glass/MTM57, Figure 5.35. Furthermore, the G_c of Vectran/MTM57 is considerably higher than S2-Glass/MTM57 composite (approximately 154.2 kJ/m^2 [70] and 260 kJ/m^2 [68] for S2-Glass/MTM57 and Vectran/MTM57, respectively), enabling the fibre to absorb more energy before failure.

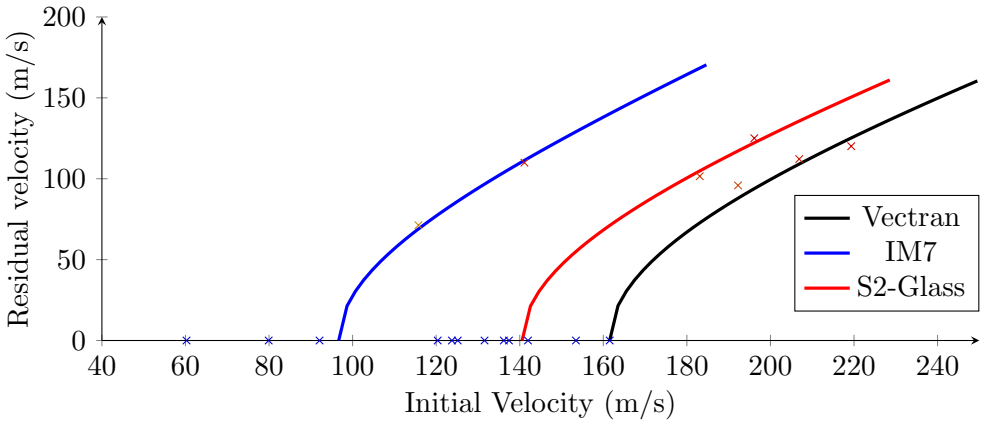
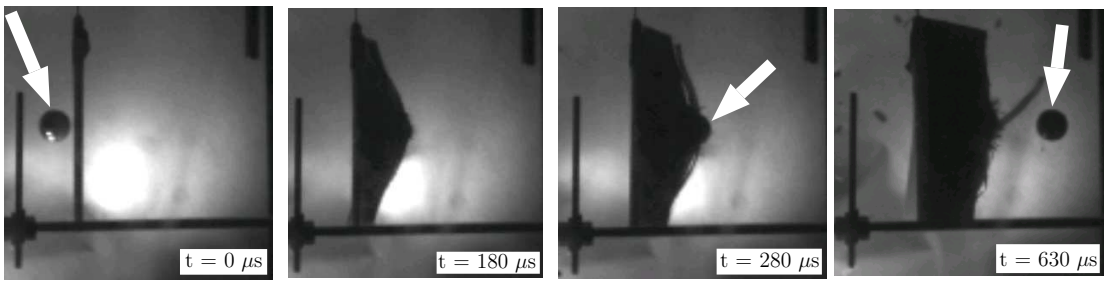


Figure 5.33: Ballistic curve for all three materials used in this study

The ballistic performance of S2-Glass/MTM57 laminates, is considerably better than IM7/8552, although unexpectedly, its performance is slightly inferior to Vectran/MTM57. This is different from the results observed under LVI, in which the performance of S2-Glass/MTM57 is comparable, if not better than Vectran/MTM57. While the tensile strain-to-failure of S2-Glass/MTM57 is higher than Vectran/MTM57 (2.6% for Vectran/MTM57 and 3% for S2-Glass/MTM57), the lower ballistic performance may be attributed to the fibre fracture energy (G_c) of the composite. Further, the inherent flaws which are a common characteristic in glass fibres may further limit the ballistic performance of S2-Glass/MTM57. Finally, the V_{50} for S2-Glass/MTM57 was calculated to be at 140.56 m/s, approximately 20% lower than Vectran/MTM57.

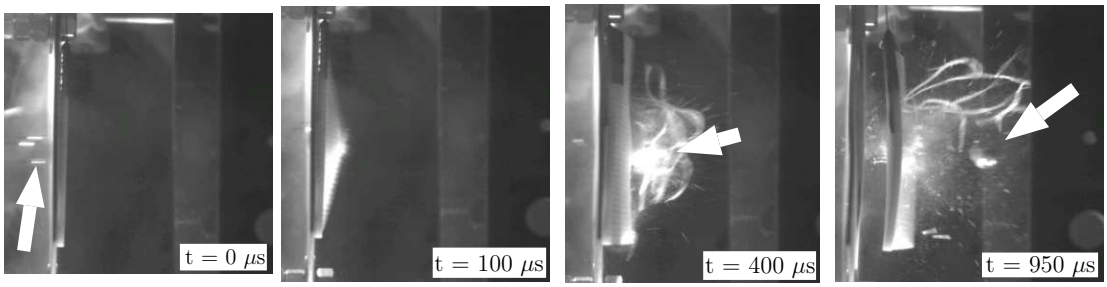
Also shown in Figure 5.36 is a series of montage of the HVI event for IM7/8552.

Note the relatively small BFD compared to the rest of the composite, hence resulting in a poor performing material under dynamic loading.



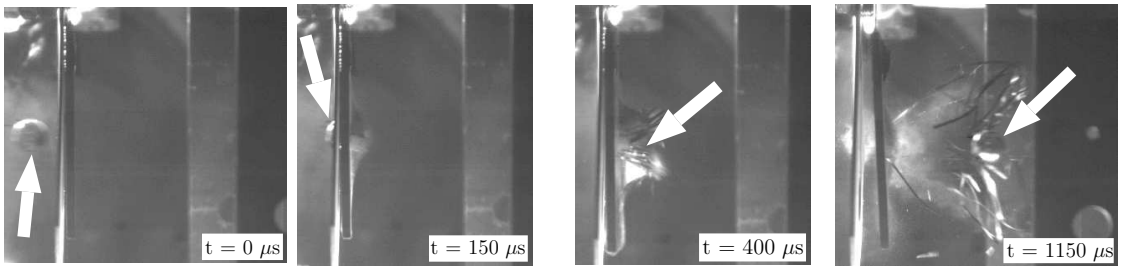
(a) (b) (c) (d)

Figure 5.34: Montage of HVI events on Vectran/MTM57 at 171.2 m/s (a) Before impact (b) During impact (c) Partial penetration (d) penetrated. White arrow indicates projectile



(a) (b) (c) (d)

Figure 5.35: Montage of HVI events on S2-Glass/MTM57 at 183.08 m/s (a) Before impact (b) During impact (c) Partial penetration (d) Penetrated. White arrow indicates projectile



(a) (b) (c) (d)

Figure 5.36: Montage of HVI events on IM7/8552 at 115.75 m/s (a) Before impact (b) During impact (c) Partial penetration (d) Penetrated. White arrow indicates projectile

Damage assessment

Figure 5.37 presents three cross-sectional views of post-impacted S2-Glass/MTM57 laminates under three different impact velocities; 136.19 m/s (below V_{50}), 137.43 m/s (close to V_{50}), and 196.14 m/s (above V_{50}). Here, the progression of damage can be observed, with minimal damage seen when impacted lower than the V_{50}, and severe damage when impacted above the V_{50}. When impacted close to the V_{50} (or above V_{50}), clear delamination can be observed close to the laminate mid-plane extending towards the laminate boundaries. At V_{50}, damage can be observed particularly at the laminate front face, whilst when impacted above the V_{50}, fibre failure can be seen through the laminate thickness indicating penetration has occurred. Again, the composite was observed to delaminate around the laminate mid-plane, in which shear stresses were the highest.

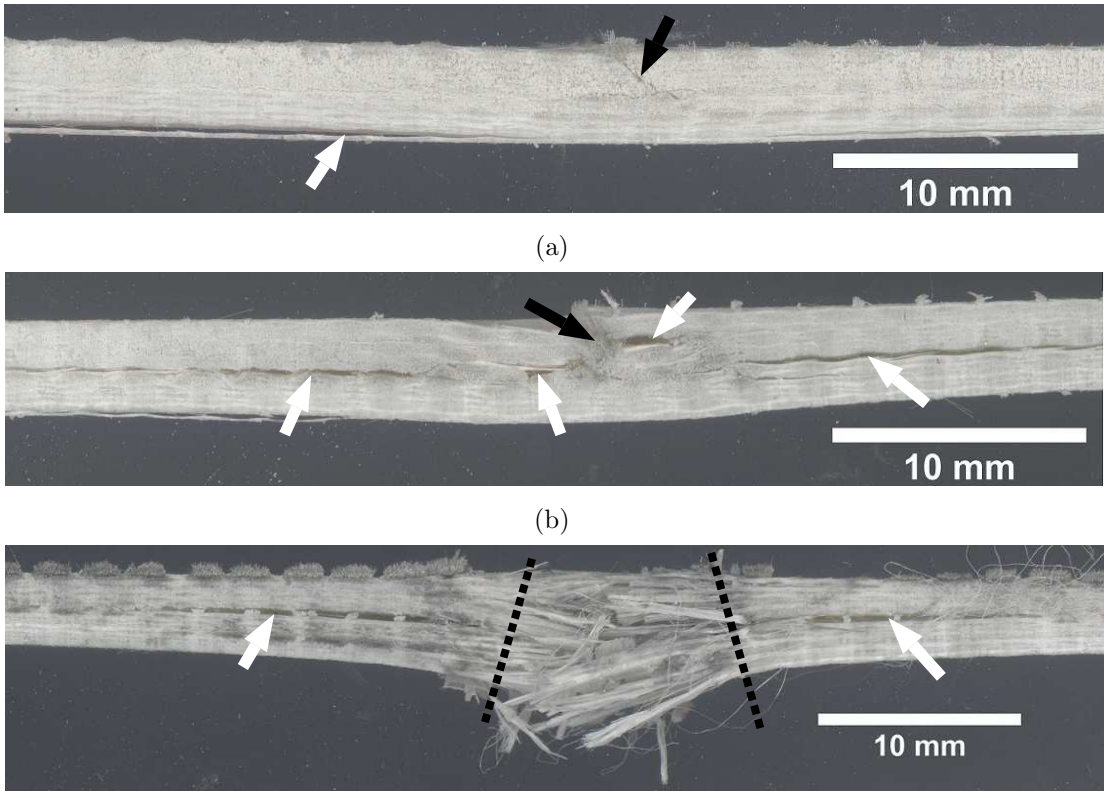
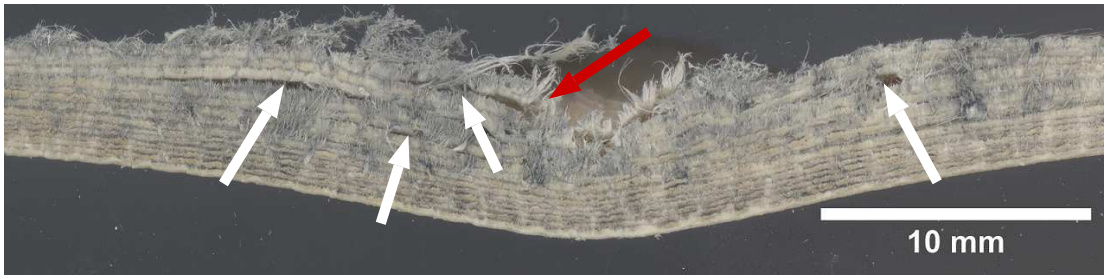


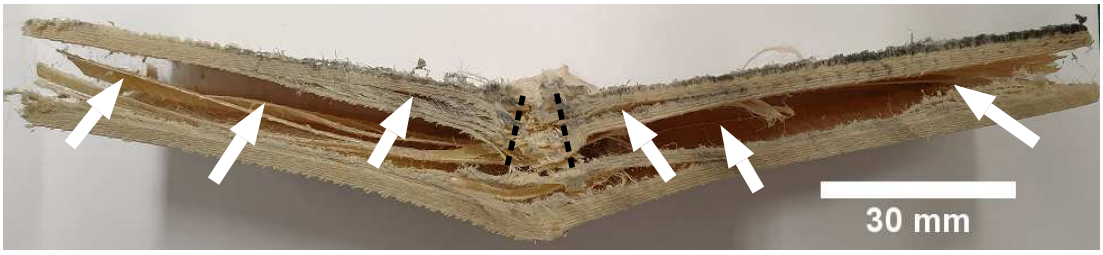
Figure 5.37: Cross-sectional view of S2-Glass/MTM57 under HVI load (a) 136.19 m/s - below V_{50} (b) 137.43 m/s - close to V_{50} (c) 196.14 m/s - above V_{50}. White arrow indicates delamination whilst the black dashed line indicates fibre failure. The black arrow in (a) and (b) shows fibre failure

For Vectran/MTM57, impact velocities which are lower than the V_{50} induce a degree

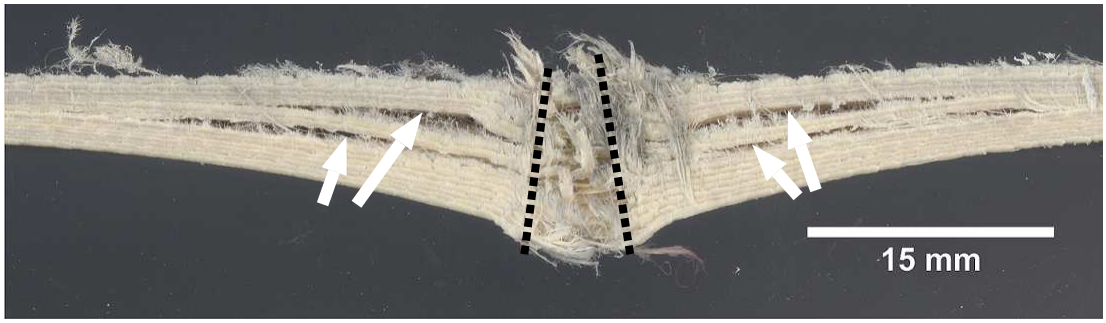
of permanent indentation, with some fibre failure on the laminate front face - Figure 5.38a. Delamination damage can also be seen, extending to the laminate boundaries. Close to the V_{50}, severe delamination can be observed, with an increasing amount of fibre failure through the laminate thickness. At this velocity, the laminate is seen to be split into two halves, indicating a significant amount of energy absorption from delamination. The mechanism of failure under impact loading is comparable to Dyneema composites in which significant delamination can be observed towards the laminate front face up to the laminate mid-plane where shear stresses are highest. This is accompanied by fibre failure initiated from the "indirect tension" mechanism originally proposed by O'Masta et al. [196].



(a)



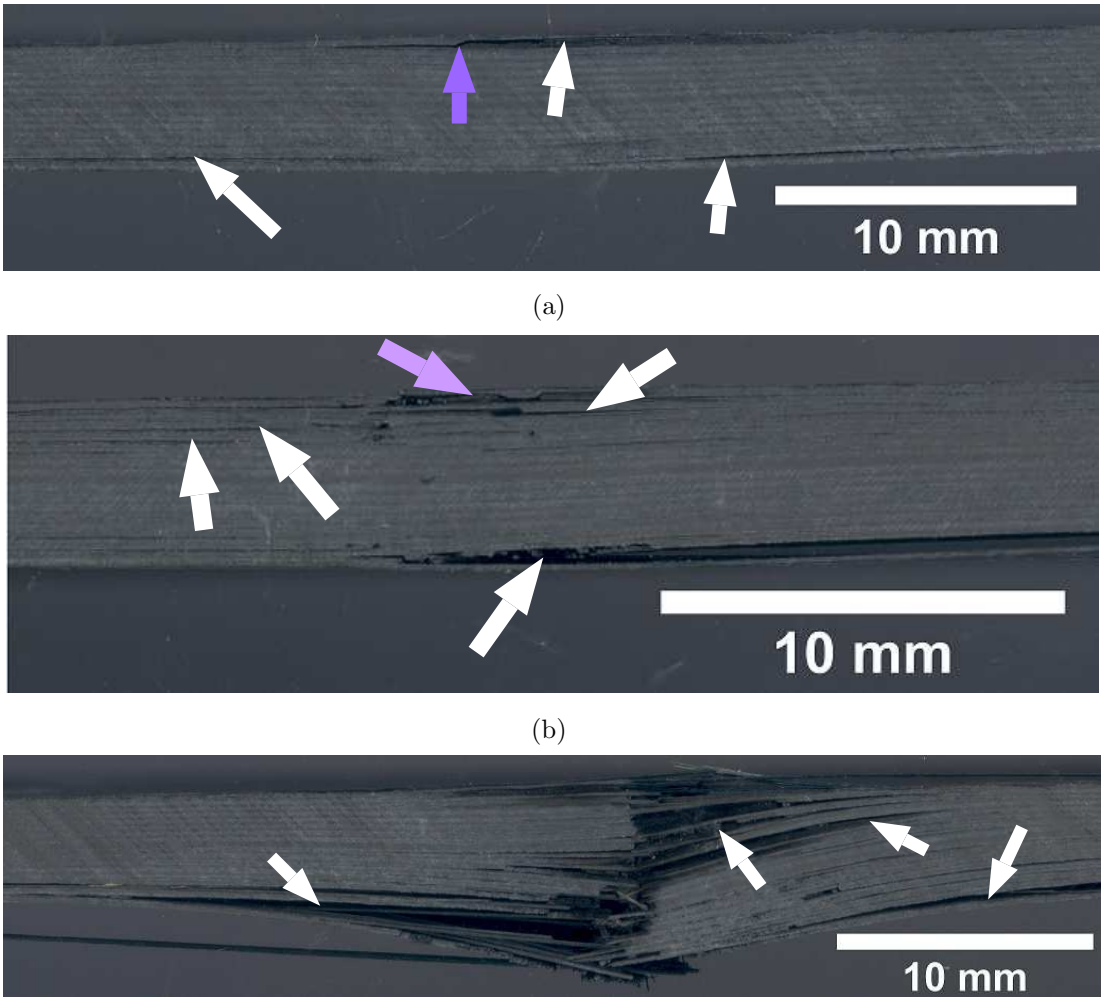
(b)



(c)

Figure 5.38: Cross-sectional view of Vectran/MTM57 under HVI load (a) 152.87 m/s - below V_{50} (b) 165.15 m/s - close to V_{50} (c) 212 m/s - above V_{50}. White arrows indicates delamination, whilst the red arrow indicates fibre failure

Evidence of this is shown in Figure 5.38a, whereby fibre failure is still observed to occur at the laminate front face where compressive stresses were the highest. Finally, at full penetration, multiple delaminations can be observed extending to the laminate boundaries, with fibre failure occuring at each ply.



(a)

(b)

(c)

Figure 5.39: Cross-sectional view of IM7/8552 under HVI load (a) 60.25 m/s - below V_{50} (b) 79.91 m/s - close to V_{50} (c) 115.75 m/s - above V_{50}. White arrows indicates delamination, whilst the blue arrow indicates intralaminar failure

Lastly, Figure 5.53 presents cross-sectional images of IM7/8552 laminates at three different projectile penetration level. When impacted below the V_{50}, minimal damage can be observed on the laminate, Figure 5.39a, although some delamination can be seen on the front and back face of the laminate. Close to the V_{50}, multiple delaminations were observed to be present, with the back face being the most severe. Lastly, above the V_{50},

extensive delaminations can be seen, with increasing severity towards the laminate back face. Fibre failure can be seen to be present in every ply, displaying a clear penetration path - Figure 5.39c.

5.4.3 On delamination

In general, impact-induced delamination damage is always a mixed-mode dominated failure which is inclined towards Mode II, particularly for LVI events. This is due to the nature of LVI events, in which flexural deformation dominates throughout the whole impact duration. In contrast, mixed-mode interlaminar failure inclined towards Mode I can usually be observed in HVI loading. For HVI loading, stress wave effects usually dominate, inducing Mode I delamination in between plies. This is particularly true for polymer-based fibre composites such as Dyneema HB26, in which it was found that the Mode II delaminations were observed closer to the impact site and the laminate mid-plane, whilst away from the impact site, the Mode I component increases [197]. A similar response is observed to occur for Vectran/MTM57 laminates, due to the laminate's low shear strength resulting in an increase in flexural response upon impact. An example of this is shown in Figure 5.40, in which the presence of multiple delaminations through the laminate thickness can be observed. Delaminations can also be seen extending towards the laminate boundary, with the largest degree of delamination observed closer to the laminate mid-plane.

As stated earlier, under LVI loading, Mode II dominated delamination can be expected. This is shown in Figure 5.41, illustrating a typical fracture surface seen on IM7/8552 under LVI loading. Note the presence of moderately formed shear cusps around the fracture surface indicating a Mode II (shear) failure has occurred. Additionally, a small presence of riverlines was observed, suggesting that a Mode I (opening) failure has taken place.

For IM7/8552, delamination can be clearly observed under LVI loading in all three energy levels. At the lowest energy level (40 J), delamination can be observed on almost all of the plies, with increasing severity towards the rear of the laminate. Peanut-shaped delamination can be observed along the fibres, forming an almost rhombus shape, shown

in Figure 5.44, consistent with the findings of previous researchers [11, 12, 20, 123].

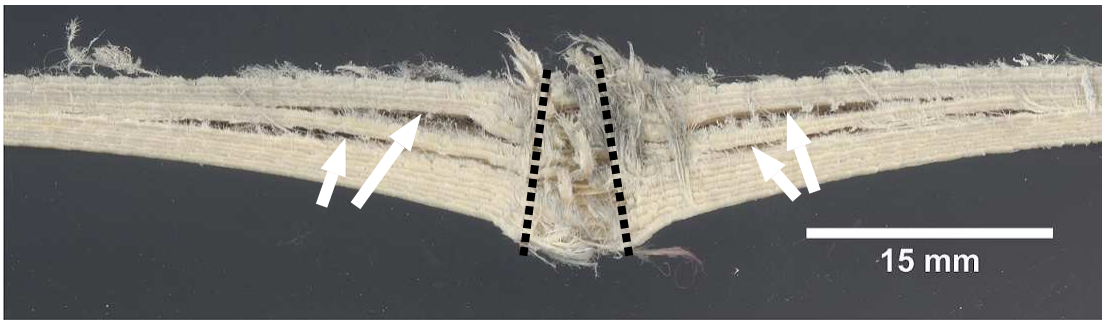


Figure 5.40: Cross-sectional view of an impacted Vectran/MTM57 laminate (≈ 210 m/s) under HVI loading. Note the multiple delamination extending towards the laminate boundary (shown with white arrows). Dashed lines represents penetration path

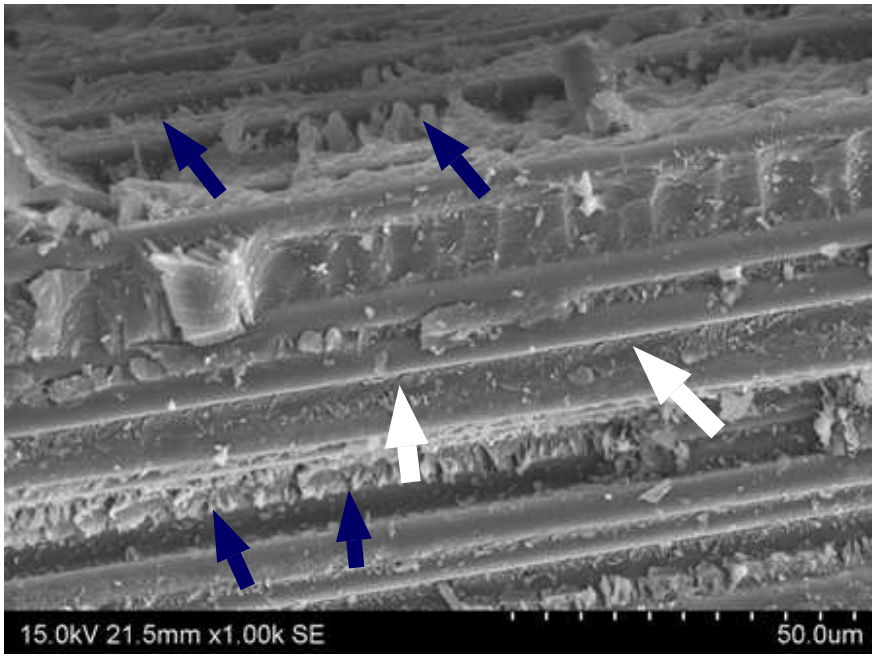


Figure 5.41: Typical fracture surface of IM7/8552 under low velocity impact loading. Blue arrows indicate shear cusps whilst white arrows indicate riverlines

It can also be concluded that the largest area of delamination between the plies is towards the rear of the laminate, whilst the smallest towards the front. This is because the laminate was subjected to a flexural load, which induces high tensile stresses leading to a failure initiating from the rear. Upon failure, the area of delamination, particularly towards the back face further propagates under Mode I, which extends towards the laminate boundaries. As the velocity is increased, the average delamination area is

observed to increase, Figures 5.47 and 5.50, up to the point of the highest energy level - shown in Table 5.2. This may be due to relatively high impact velocity (hence inducing a localized impact), resulting in the saturation of damage at both energy levels.

Table 5.2: Average measured delamination area. Units are in mm^2

Material	40 J	100 J	160 J	HVI	G_{Ic} (kJ/m^2)	G_{IIc} (kJ/m^2)
IM7/8552	1227	1677	1645	2366 [5]	0.21	0.61
S2-Glass/MTM57	140	173	186	4118 [6]	1.15	2.43
Vectran/MTM57	162	272	303	2092 [6]	1.41	2.41

While pronounced delamination are observed with IM7/8552, little to no delamination can be seen for S2-Glass/MTM57 in all energy levels under LVI loading, shown in Figures 5.42, 5.45, and 5.48d for 40 J, 100 J, and 160 J, respectively. The cross-sectional images under 100 J and 160 J, Figures 5.21 and 5.30, showed minimal delamination between plies at the impact location. For Vectran/MTM57 laminates under LVI, C-scan images (Figures 5.43d, 5.46d, and 7.42d for 40 J, 100 J, and 160 J energy levels, respectively) reveal some delamination in the vicinity of impact. However, not at the severity of the case of IM7/8552 which may be due to several possible reasons. First, the enhancement of delamination resistance in NCF composites is particularly pronounced, due to the presence of stitches on each fabric ply. This is shown in Table 5.2, where the G_{Ic} and G_{IIc} of both S2-Glass/MTM57 and Vectran/MTM57 are considerably higher compared to IM7/8552. Secondly, it is thought that the effects of fibre-bridging may influence the delamination toughness of the composite, which is a common phenomenon in fibre reinforced composites. The inherent characteristics of a dry fabric often promotes fibre misalignment, which further encourage fibre nesting resulting in an increase in fibre-bridging. Thirdly, the relatively large tensile strain-to-failure of both S2-Glass and Vectran fibres further impede delamination propagation by absorbing a large amount of elastic strain energy. In all cases, the delamination area was observed to increase with increasing impact energy, shown in Table 5.2

The DTL, calculated from the equation proposed by Davies and Robinson [27] are

[5] Corresponds to energy level of approximately 70 J ($\approx$ 92 m/s impact velocity)
[6] Corresponds to energy level of approximately 240 J ($\approx$ 170 m/s impact velocity)

presented in Table 5.3. Interestingly, the model closely predicts the DTL for IM7/8552. However, this is not the case for Vectran/MTM57 and S2-Glass/MTM57 laminates. This large discrepancy could be due to a number of reasons. First, the model depends on the flexural stiffness of the composite. Whilst the calculated flexural stiffness may be reliable for S2-Glass/MTM57, this may not be the case for Vectran/MTM57. The low compressive properties, both stiffness and strength, suggest that the flexural stiffness is driven by tensile strain. Secondly, the Poisson's ratio for both laminates was significantly lower than IM7/8552, due to the fabric architecture of S2-Glass/MTM57 and Vectran/MTM57, compared to IM7/8552.

Table 5.3: Delamination Threshold Load: Measured and calculated

Material	Measured (kN)[7]	Calculated (kN)
IM7/8552	5.78	6.11
S2-Glass/MTM57	N/A	4.96
Vectran/MTM57	N/A	7.25

Under HVI loading, a more severe delamination damage can be observed on all laminates, due to the dominance of the through-thickness stress waves, promoting extensive delamination which extends towards the laminate boundaries. For Vectran/MTM57, delamination is observed to be most severe when impacted close to its V_{50}, Figure 5.38b. Figures 5.52c and 5.52d presents the radiograph and C-scan images, respectively for Vectran/MTM57 impacted close to its V_{50}. It can be observed that delamination is most severe close to the laminate mid-plane, where the laminate split into two halves. Furthermore, the flexural response of the laminate under HVI loading may greatly contribute to the extent of delamination of Vectran/MTM57 laminates. The laminate flexural response upon impact promotes maximum out-of-plane shear at its mid-plane, hence initiating Mode II interlaminar failure, which explains the severity of delamination at the laminate's mid-plane. Extensive delamination can also be seen close to the laminate mid-plane for the penetrated case, Figure 5.40, which confirms the flexural contribution towards delamination propagation.

[7] Averaged between three specimens

The flexural deformation is also thought to contribute towards the delamination growth on S2-Glass/MTM57 laminates. The cross-sectional images shown in Figure 5.37 highlighted the presence of delamination, clearly observable at the laminate mid-plane, extending towards the laminate boundaries. This can also be seen in the radiograph and C-scan images, Figures 5.51c and 5.51d, showing the extent of delamination on the laminate.

Finally for IM7/8552, an increase in delamination area can be observed when compared to the LVI case. This may be due to the greater amount energy dissipation under HVI loading, hence promoting a more extensive delamination if compared to the LVI case. However, contribution from flexural deformation is not thought to be as significant for IM7/8552, if compared to Vectran/MTM57 and S2-Glass/MTM57 laminates. This is due to the relatively higher laminate flexural stiffness, if compared to Vectran/MTM57 and S2-Glass/MTM57 laminates, hence resulting in the smallest BFD, seen in Figure 5.36.

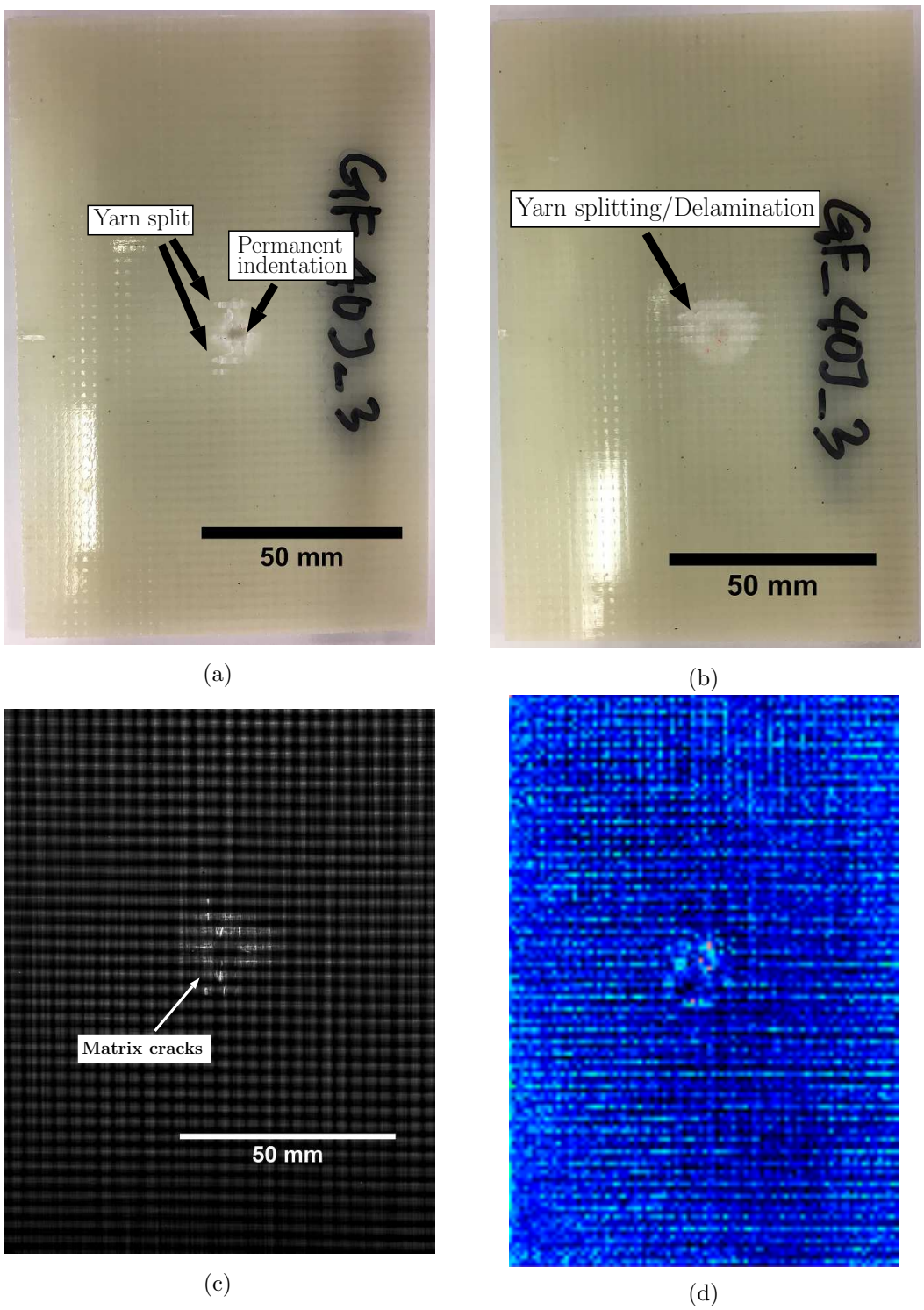
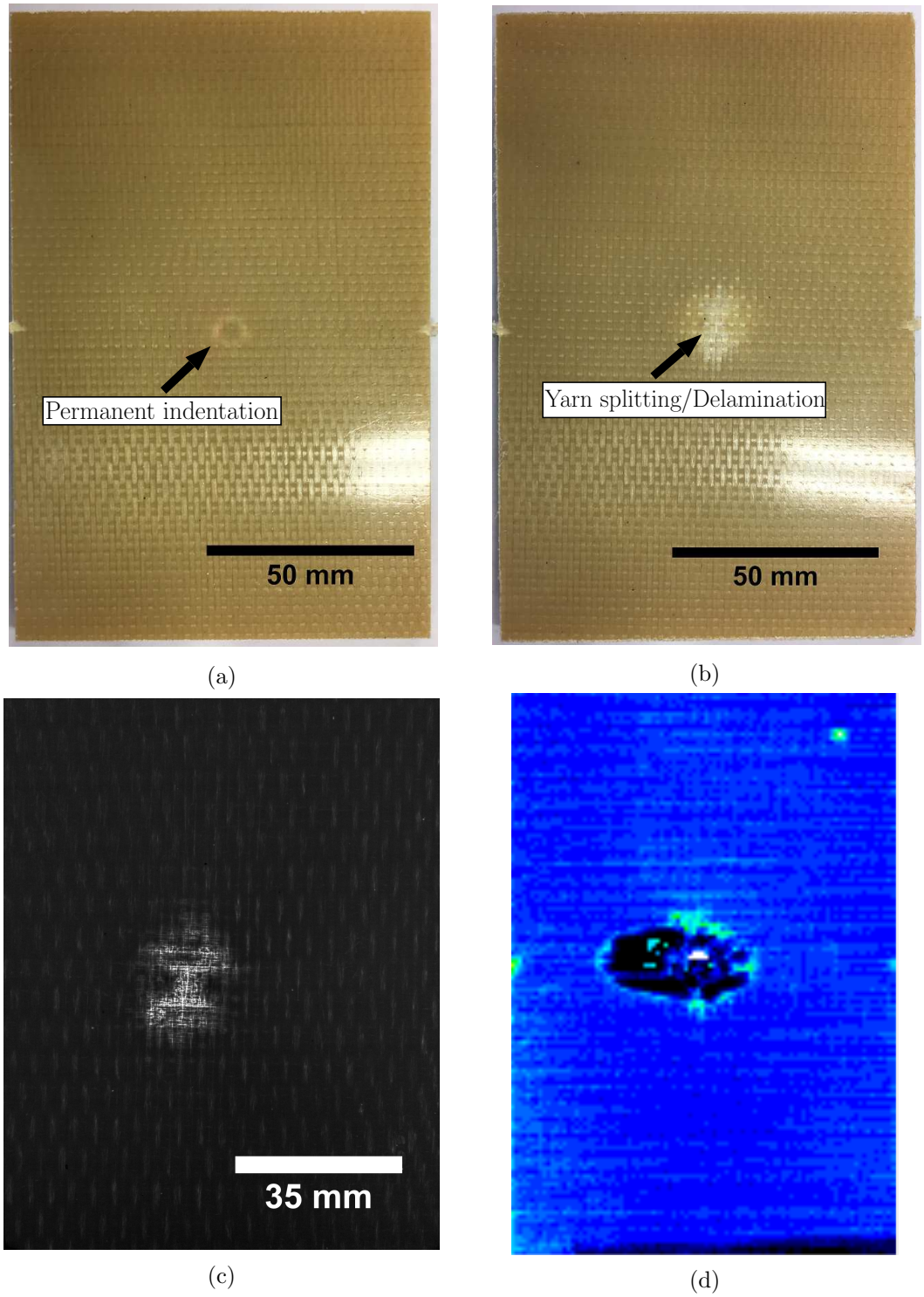


Figure 5.42: Damaged S2-Glass/MTM57 specimen under 40 J of impact load (a) Front face (b) Back face (c) Radiograph image of the specimen showing matrix cracks (d) Specimen under ultrasonic C-scan



(a) (b)

(c) (d)

Figure 5.43: Damaged Vectran/MTM57 specimen under 40 J of impact load (a) Front face (b) Back face (c) Radiograph image of the specimen showing matrix cracks (d) Specimen under ultrasonic C-scan

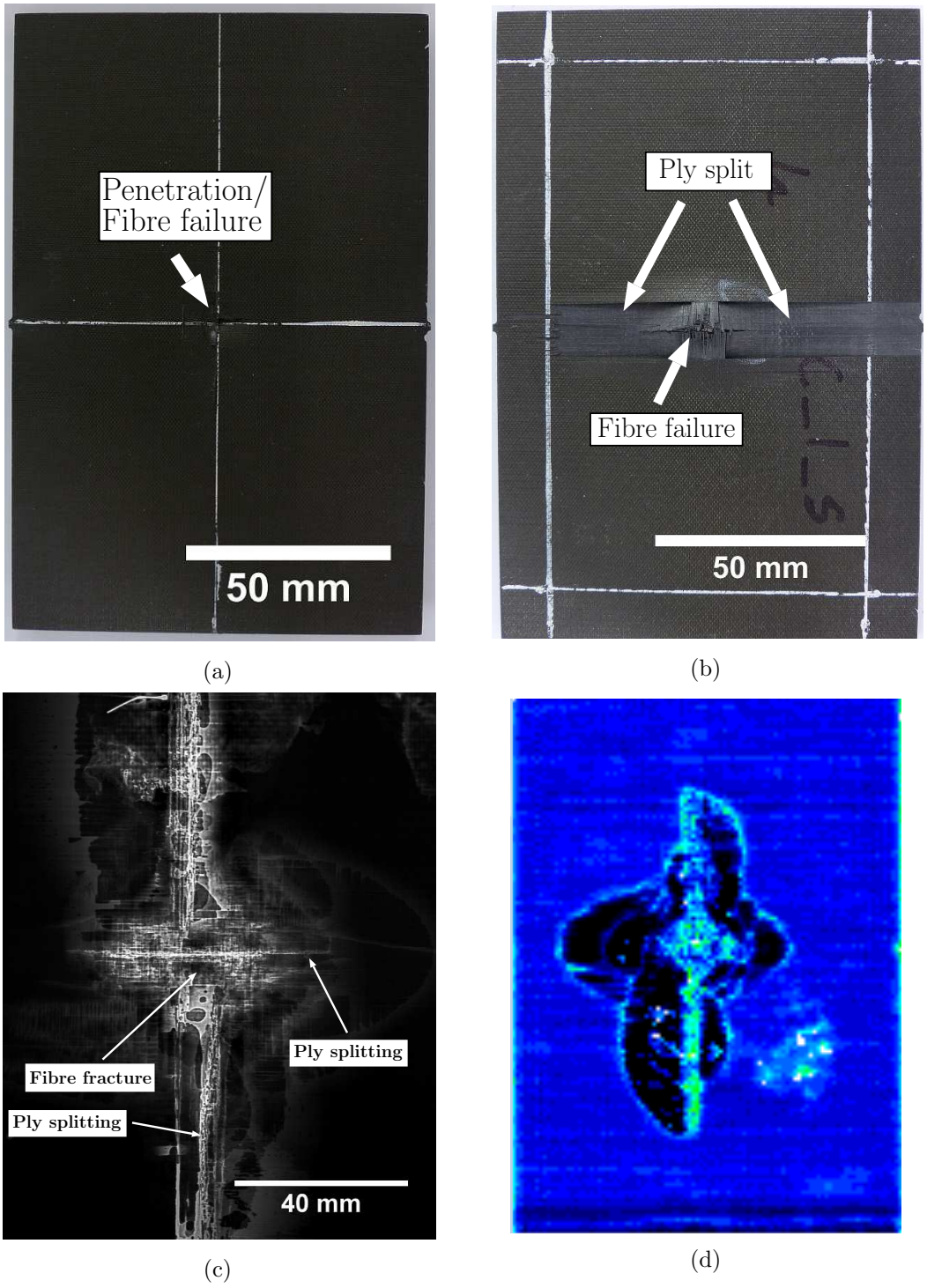


Figure 5.44: Damaged IM7/8552 specimen under 40 J of impact load (a) Front face (b) Back face (c) Radiograph image of the specimen showing matrix cracks (d) Specimen under ultrasonic C-scan

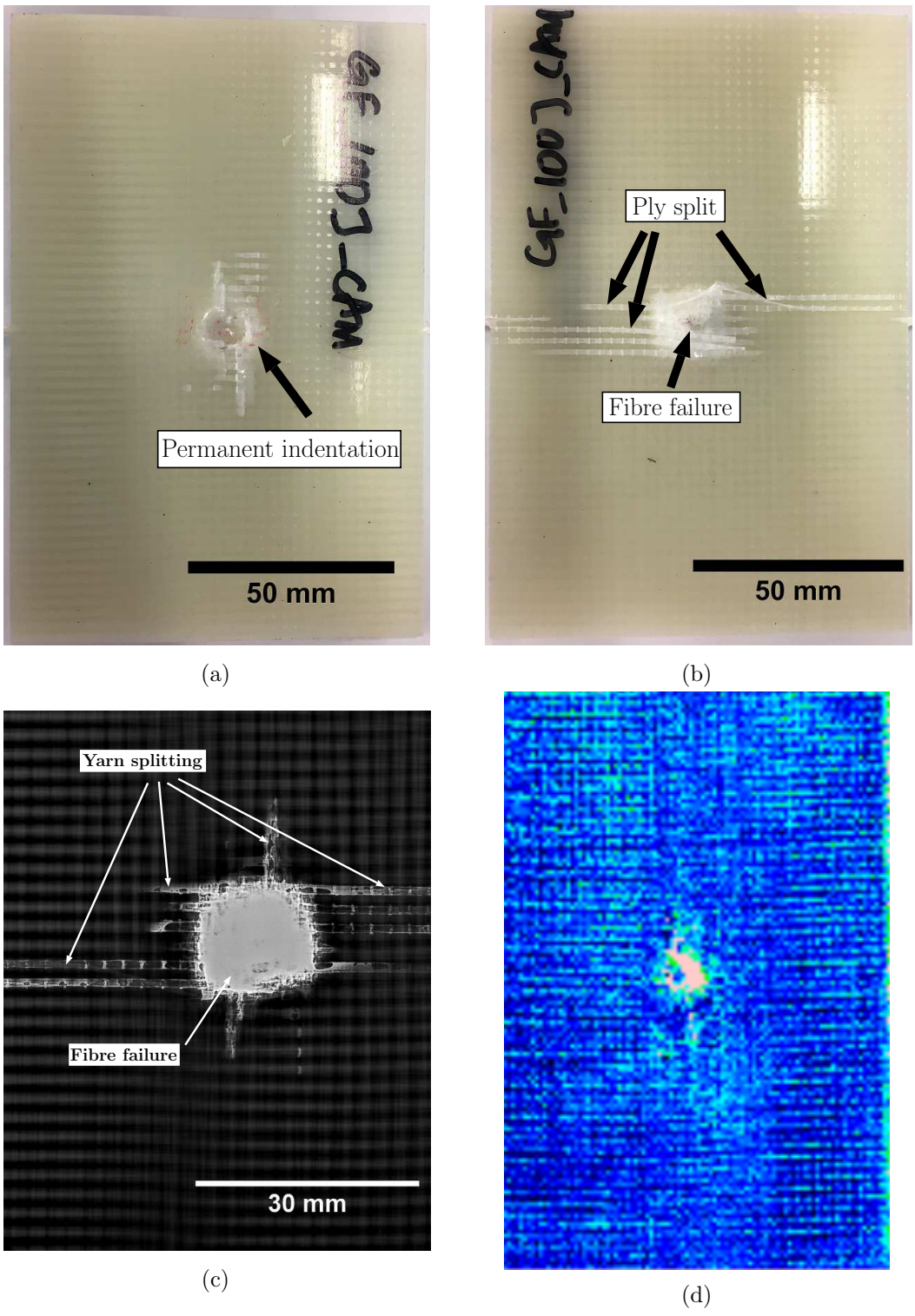


Figure 5.45: Damaged S2-Glass/MTM57 specimen under 100 J of impact load (a) Front face (b) Back face (c) Radiograph image of the specimen showing matrix cracks (d) Specimen under ultrasonic C-scan

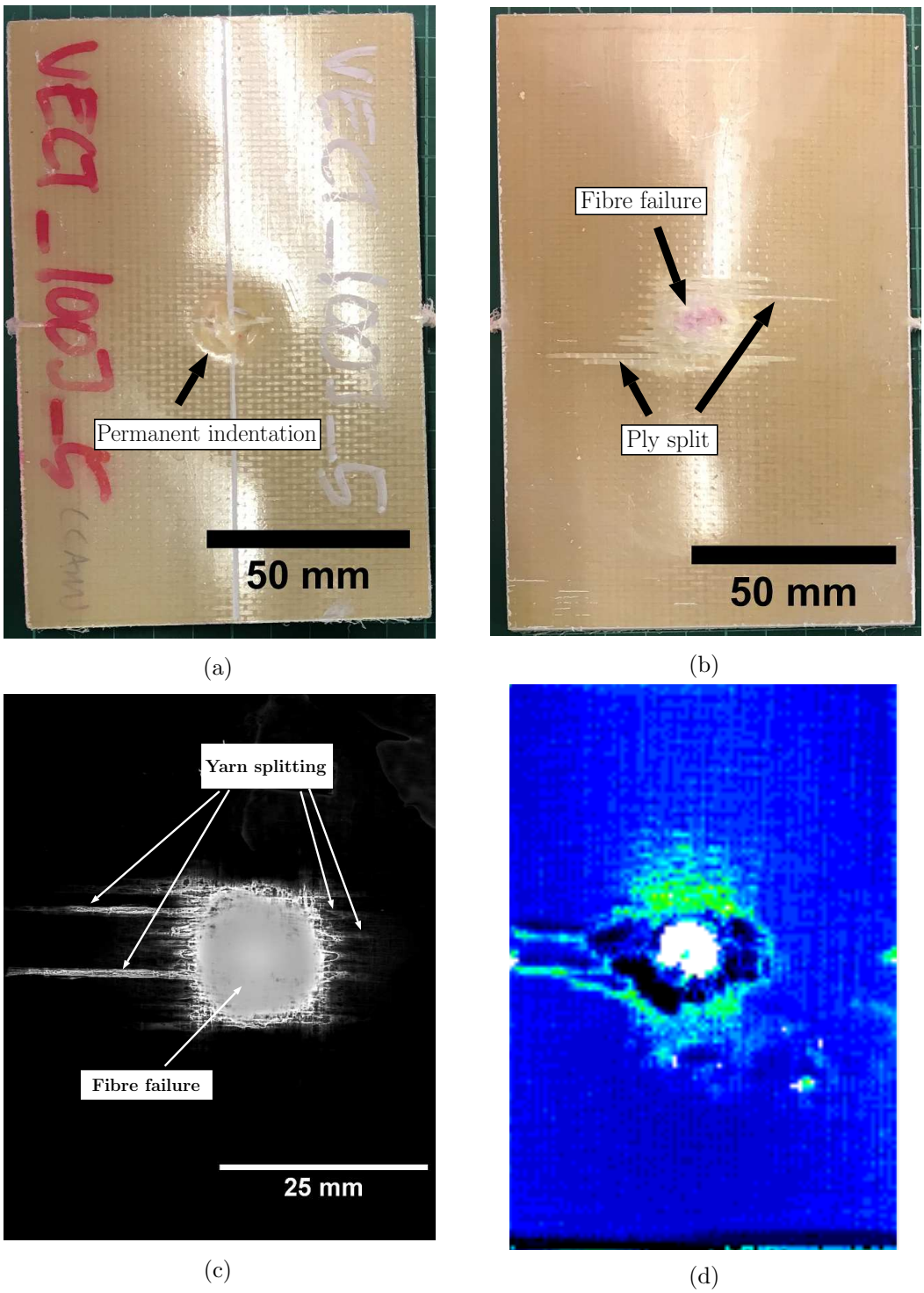


Figure 5.46: Damaged Vectran/MTM57 specimen under 100 J of impact load (a) Front face (b) Back face (c) Radiograph image of the specimen showing matrix cracks (d) Specimen under ultrasonic C-scan

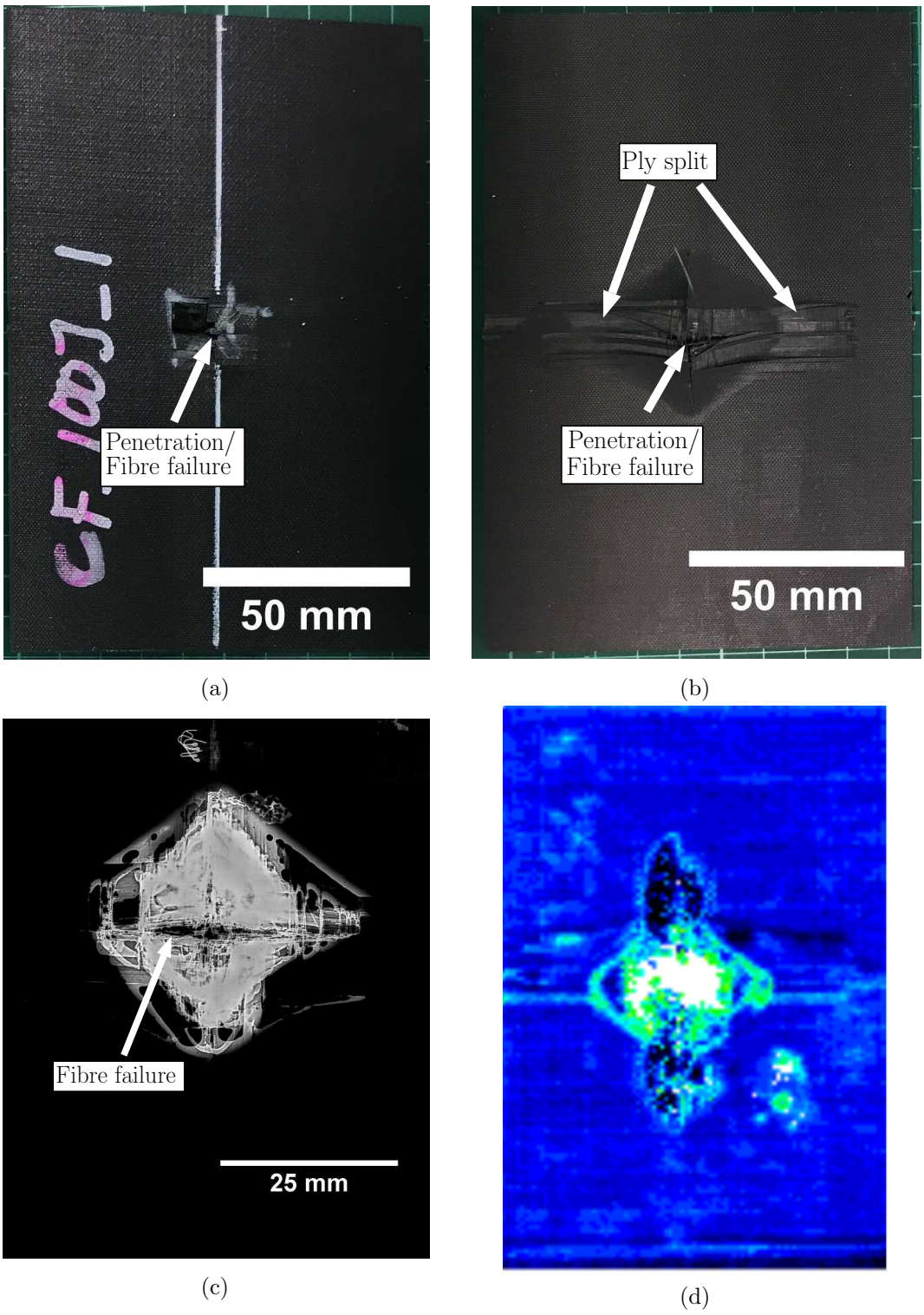
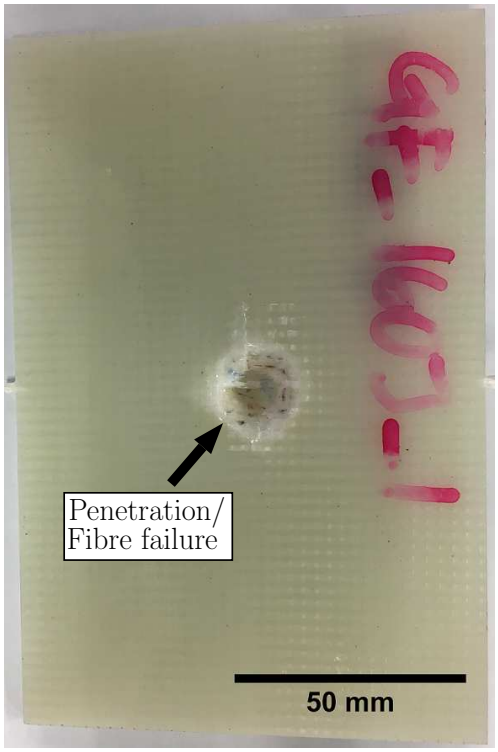
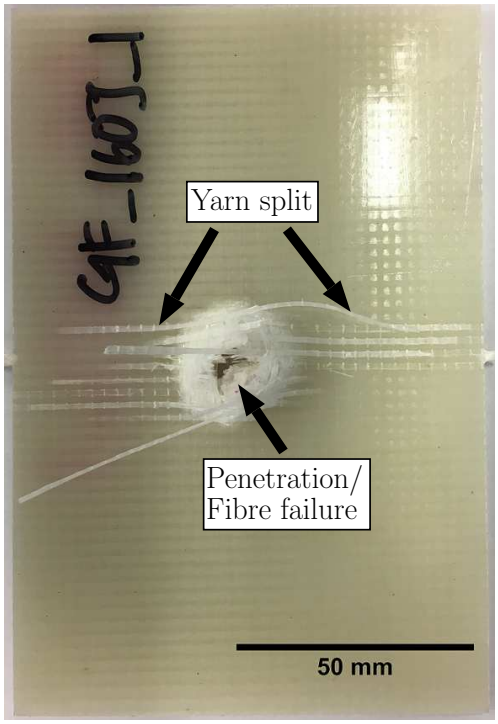


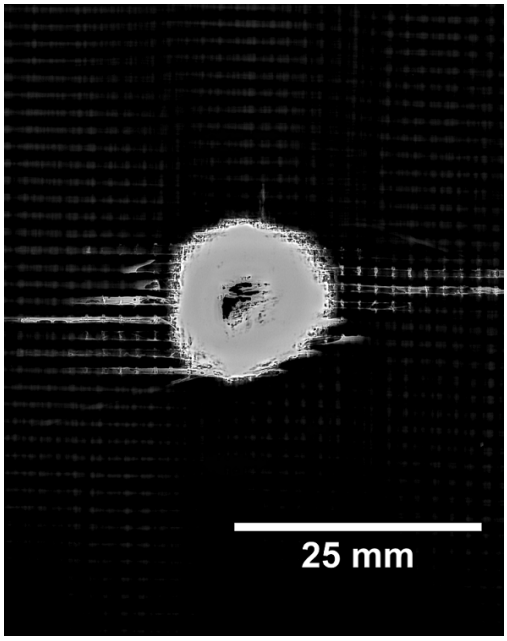
Figure 5.47: Damaged IM7/8552 specimen under 100 J of impact load (a) Front face (b) Back face (c) Radiograph image of the specimen showing matrix cracks (d) Specimen under ultrasonic C-scan



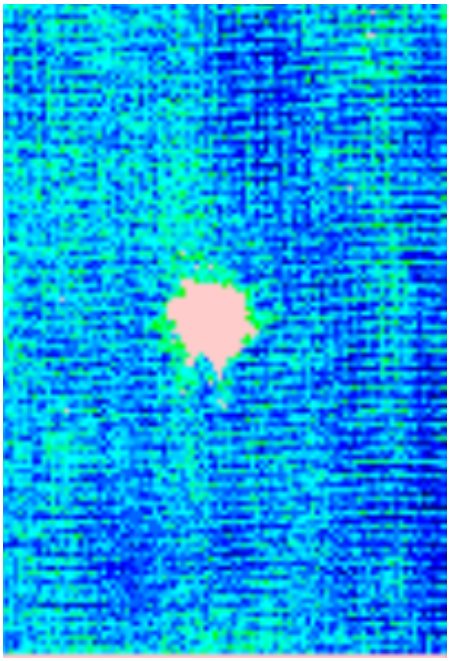
(a)



(b)

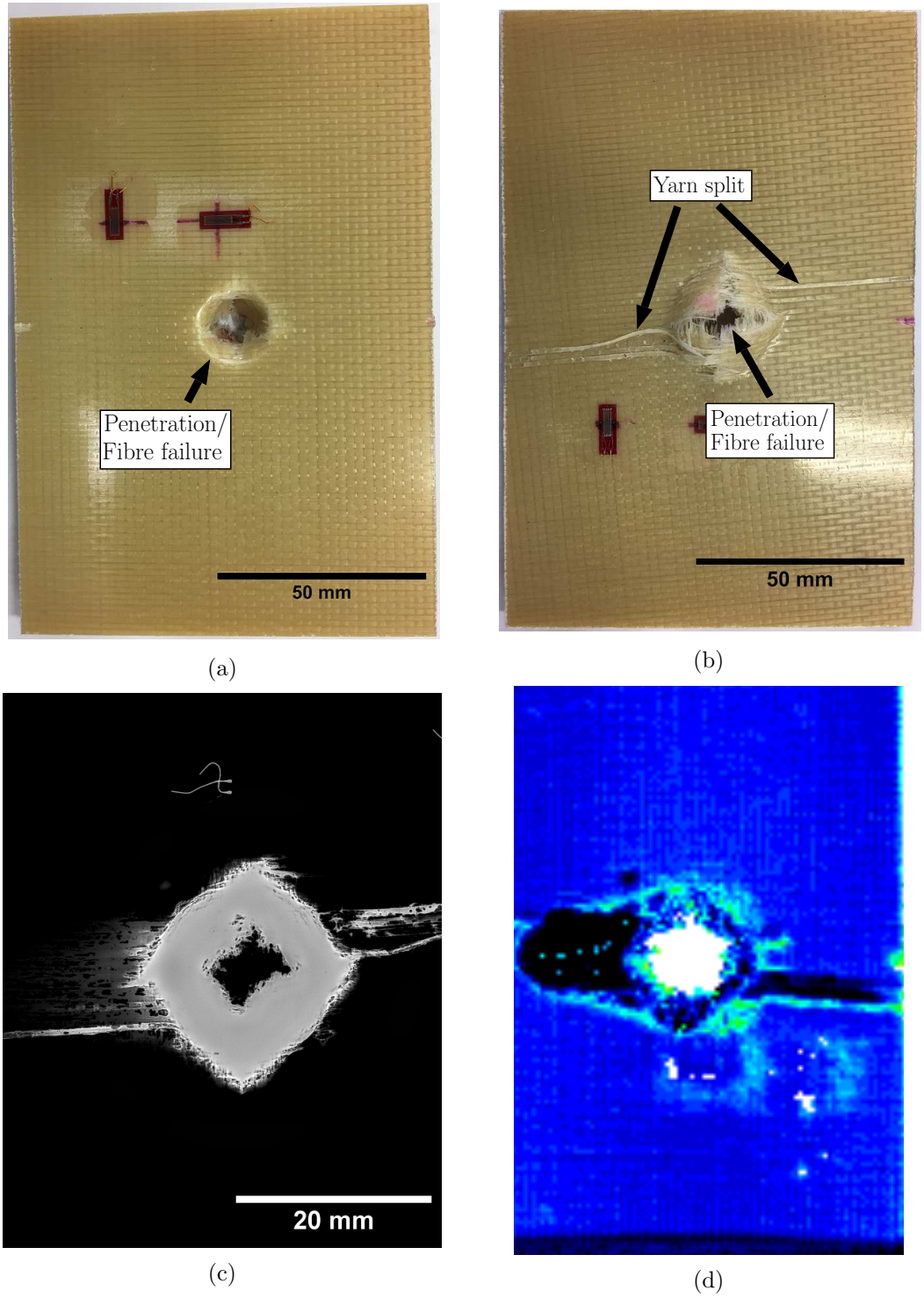


(c)



(d)

Figure 5.48: Damaged S2-Glass/MTM57 specimen under 160J of impact load (a) Front face (b) Back face (c) Radiograph image of the specimen showing matrix cracks (d) Specimen under ultrasonic C-scan



(a) (b)

(c) (d)

Figure 5.49: Damaged Vectran/MTM57 specimen under 160J of impact load (a) Front face (b) Back face (c) Radiograph image of the specimen showing matrix cracks (d) Specimen under ultrasonic C-scan

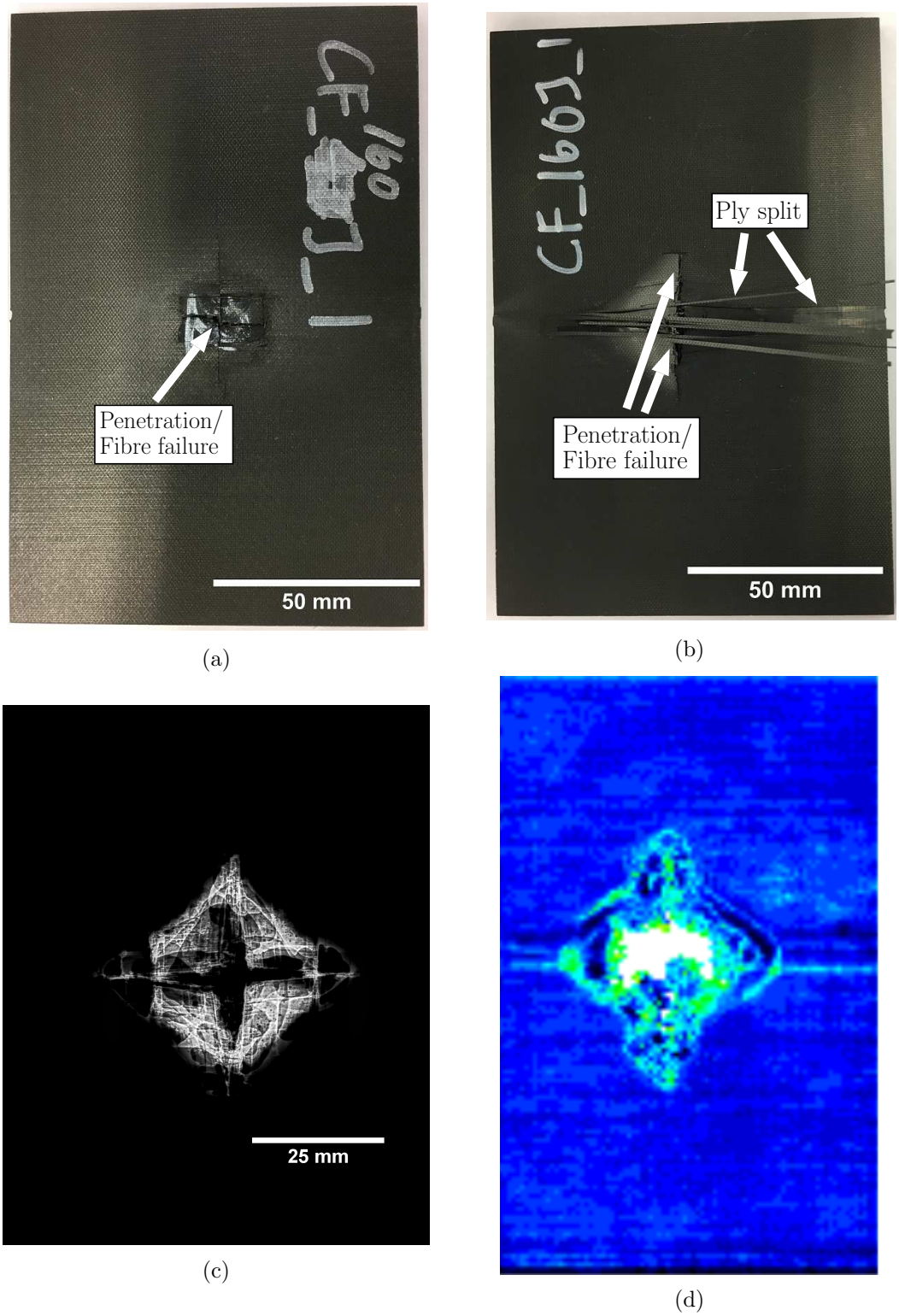
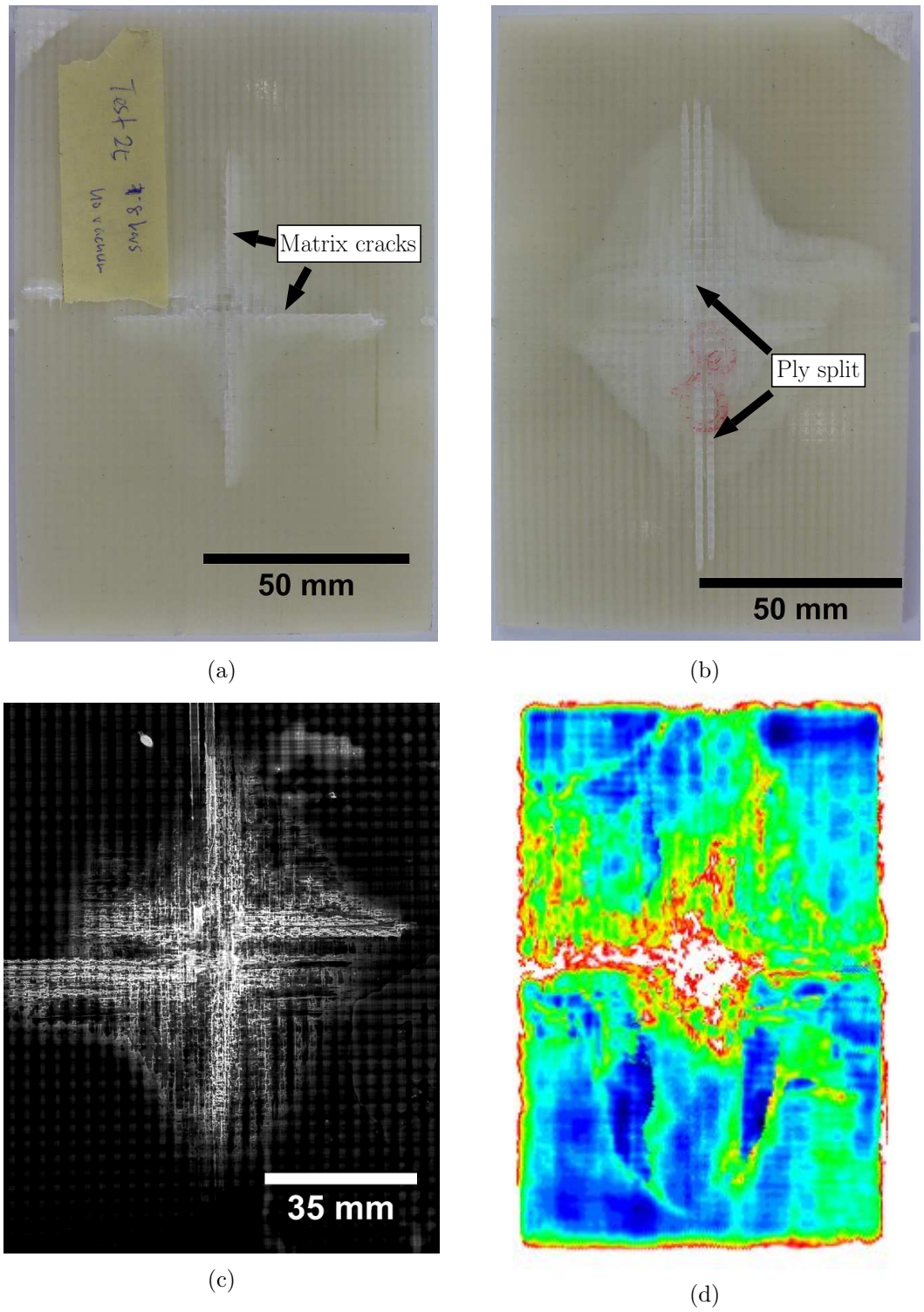


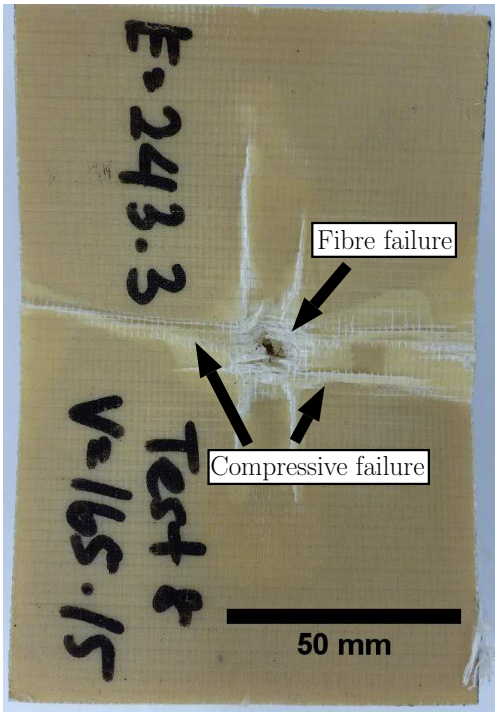
Figure 5.50: Damaged IM7/8552 specimen under 160J of impact load (a) Front face (b) Back face (c) Radiograph image of the specimen showing matrix cracks (d) Specimen under ultrasonic C-scan



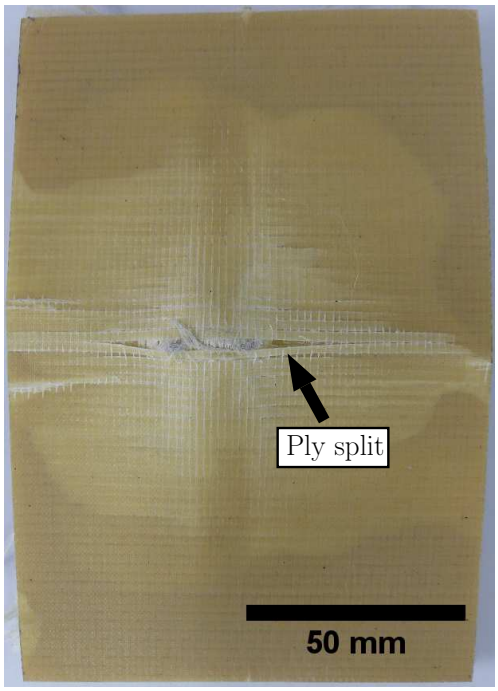
(a) (b)

(c) (d)

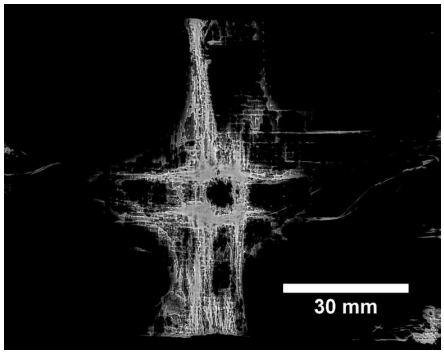
Figure 5.51: Damaged S2-Glass/MTM57 specimen under HVI loading close to V_{50} (a) Front face (b) Back face (c) Radiograph image of the specimen showing matrix cracks (d) Specimen under ultrasonic C-scan



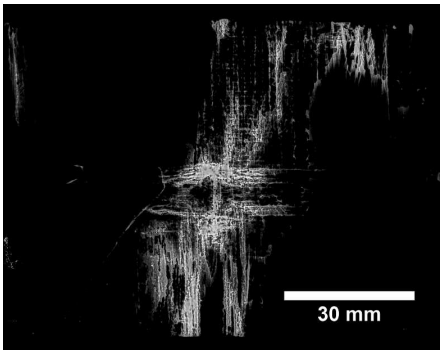
(a)



(b)

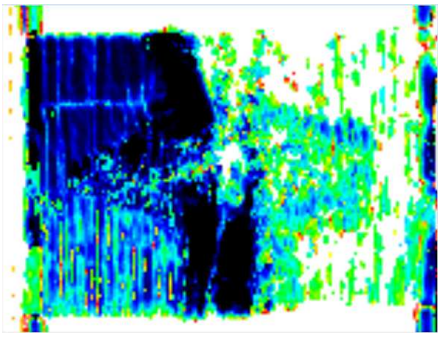


Front

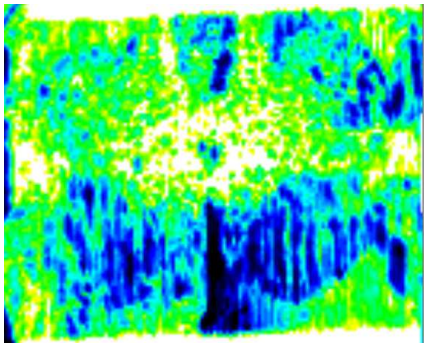


Back

(c)



Front



Back

(d)

Figure 5.52: Damaged Vectran/MTM57 specimen under HVI loading close to V_{50}. Note that the specimen was split into two halves (a) Front face (b) Back face (c) Radiograph image of the specimen showing damage on the front and back face (d) Specimen under ultrasonic C-scan showing delamination on the front and back face

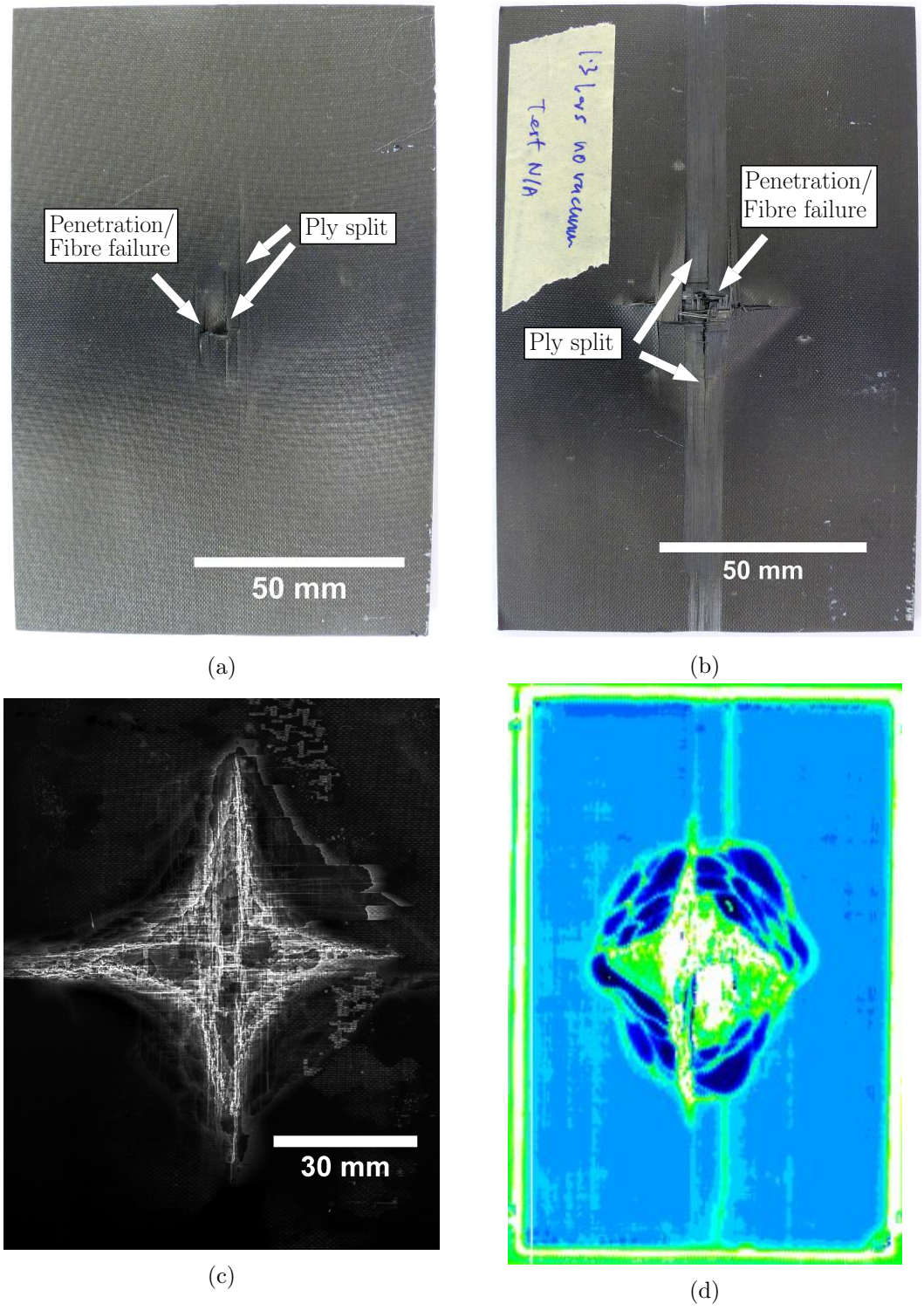


Figure 5.53: Damaged IM7/8552 specimen under HVI loading close to V_{50} (a) Front face (b) Back face (c) Radiograph image of the specimen showing matrix cracks (d) Specimen under ultrasonic C-scan

5.5 Discussions

5.5.1 Energy absorption

Figure 5.54 presents the average normalized energy absorption (energy per unit weight) for all laminates under LVI, whilst Figure 5.55 shows the normalized energy absorption for all laminates under HVI loading. In general, it can be concluded that IM7/8552 performed poorly in both LVI and HVI events. Under LVI, full penetration was observed for the 100 J and 160 J energy levels, whereas partial penetration was observed for the 40 J impact case. The inherent characteristics of IM7/8552, possessing relatively lower tensile strain-to-failure compared to the other two composites was one of the main reasons limiting the laminate performance under both impact events. The relatively lower interlaminar fracture toughness of IM7/8552 further exacerbate its already poor impact performance. Moreover, its relatively high shear properties result in a stiffer laminate, eliminating the possibilities of further energy absorption by way of flexural deformation. The flexural stiffness for all composite laminates is presented in Table 5.4, where IM7/8552 is seen to have the highest flexural stiffness, compared to S2-Glass/MTM57 and Vectran/MTM57. This further reinforces the assumption made earlier, where the high flexural stiffness is thought to limit the energy absorption transferred from the impactor.

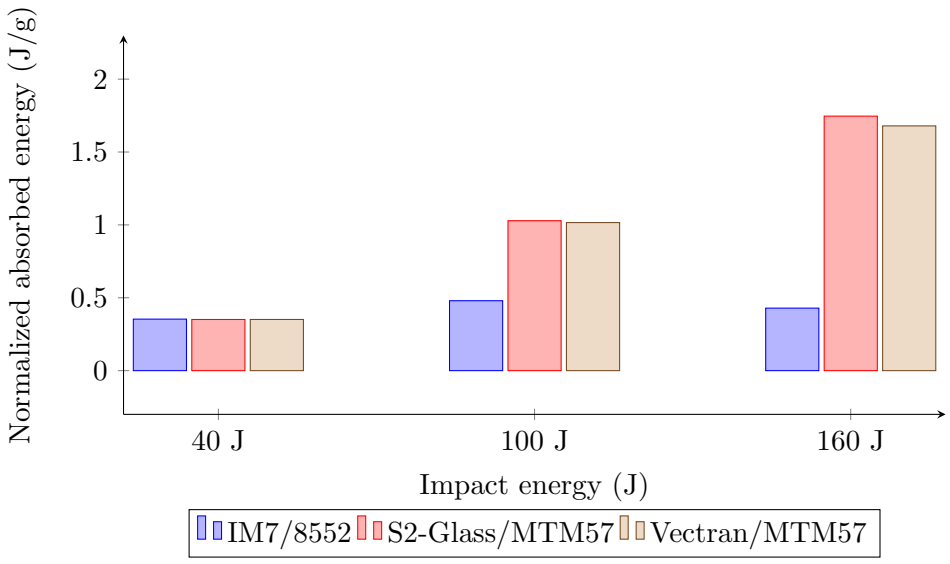


Figure 5.54: Average normalized absorption per unit weight for all laminates under LVI loading

Therefore, a few conclusion can be drawn from the impact behaviour of IM7/8552. First, the tensile strain-to-failure of composite laminates largely contributes to its impact performance, in which it allows a greater elastic strain energy absorption before failure. This is reflected by the superior impact performance of S2-Glass/MTM57 laminates, having the largest tensile strain-to-failure, shown in Table 5.4. Secondly, flexural stiffness is also an important property since a composite with a low flexural stiffness often performs better under impact loading. This is because the low flexural stiffness enables the composite to deform further resulting in a greater energy absorption from the impact event. Moreover, a low $\pm 45^\circ$ in-plane shear property (both stiffness and strength) further promotes the flexural deformation, resulting in the so-called 'pull-in' effect often observed in Dyneema composites. While the 'pull-in' effect was not visually observed on the composites in this study, it must be noted that the shear strength of Dyneema composites is often less than 10 MPa [16, 63, 91]. However, the lowest shear strength obtained in this study is of Vectran/MTM57, which is approximately 30 MPa. Perhaps this could also explain the superior performance of Vectran/MTM57 compared to S2-Glass/MTM57 and IM7/8552 under HVI loading, apart from having a comparable tensile strain-to-failure with S2-Glass/MTM57.

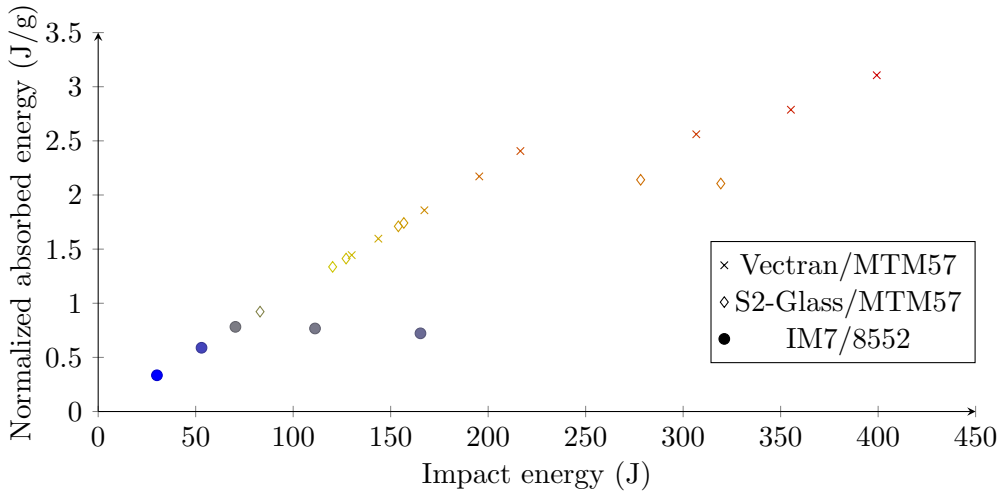


Figure 5.55: Average normalized energy absorption per unit weight for all laminates under HVI loading

Finally, it can also be observed that the FVF of S2-Glass/MTM57 is the lowest when compared to IM7/8552 and Vectran/MTM57, which could suggest its slight inferior performance under HVI loading, when compared to Vectran/MTM57. As the fibres

in a composite laminate carry the load, thus an increase in the number of fibres may contribute to an increase in the impact performance. In addition, these fibres disperse the longitudinal and transverse stress waves which were generated during projectile impact, preventing large strains from developing at the impact point [198]. The fibre pull-out energy is also the lowest compared to IM7/8552 and Vectran/MTM57, due to the relatively lower FVF. This is because the energy associated with fibre pull-out is the biggest contributor in the fracture toughness of composite laminates [167]. A large fibre pull-out energy often indicate a high composite fracture toughness, consequently resulting in a superior impact performance. Therefore, a higher FVF may be beneficial in improving the impact performance of composite laminates. However, its effect should not be as significant as the tensile strain-to-failure.

Table 5.4: Relevant mechanical properties for all the composites used

Properties	IM7/8552	S2-Glass/MTM57	Vectran/MTM57
Flexural stiffness (GPa)[8]	64.05	36.29	21.95
FVF (%)	58	55	62
No. of fibres in each tow[9]	-	300	300
Weight (g)[10]	94	90	94
Cuniff velocity (m/s)	721.65	634.05	616.12
Tensile strain-to-failure (%)	1.4	2.6	2.8
$\pm 45^\circ$ in-plane shear strength (MPa)	90.01	51.38	29.56
G_{Ic} (kJ/m^2)	147.2 [169]	154.2 [70]	260 [68]
σ_f (MPa)	5654 [58]	4890 [60]	2537 [145]
G_{po} (kJ/m^2)	143.47[11]	96.14 [12]	179.06

[8] Calculated using simple beam theory
[9] Data provided by the manufacturer
[10] Referenced against 4 mm thick IM7/8552
[11] Estimated using AKSA A-42 CF/epoxy interfacial shear strength value (τ_i=28 MPa) [199]
[12] Estimated using E-glass/epoxy interfacial shear strength value (τ_i=57 MPa) [200]

5.5.2 Damage types

The impacted laminates demonstrates all of the known damage types normally seen within composites under impact loading, such as intralaminar (matrix cracking) failure, delamination, fibre failure, as well as ply-splitting. For Vectran/MTM57, significant permanent indentation can be observed on partially/un-penetrated laminates, which is not observed in the other composite materials used in this study. This may be attributed to the poor transverse shear properties of Vectran/MTM57 laminates, apart from the inherent nature of polymeric resin which always display some form of plastic deformation [151]. Furthermore, the transverse compressive properties of Vectran fibres were also suggested to exhibit some form of irreversible deformation, owing to its fibrillar structure [201, 202].

For IM7/8552 and S2-Glass/MTM57, matrix cracking was observed on all LVI energy levels. For IM7/8552, the matrix failure can be seen to extend to the adjacent 90 ° plies, therefore initiating the so-called "delamination migration" phenomenon often seen in UD based composite laminates. This phenomenon can also be observed in S2-Glass/MTM57 laminates, with matrix failures propagating across the fibre tow and then migrating to the adjacent tows, initiating delamination in the interface between the 0 ° and 90 ° layers. However, due to the existence of the stitches in the S2-Glass/MTM57 fabric plies, the propagation of delamination was impeded whereas in the IM7/8552 plies, no stitches were present, hence resulting in a larger delamination damage propagating to the laminate boundaries.

Under HVI, superior performance was observed for Vectran/MTM57 laminates if compared to the other materials. BFD was observed to be the largest for Vectran/MTM57, absorbing further energy hence resulting in a superior ballistic performance. Extensive ply-splitting was observed for all laminates prior to penetration, signifying the so-called "indirect tension" first observed by O'Masta et al. [196], due to the localised flexural deformation upon impact. Upon impact, plies at the laminate back face experiences a high tensile stress which eventually causes ply-splitting across the laminate back face, even before the projectile starts to penetrate the composite. Similar observation was also observed on Vectran/MTM57. Finally, all damage types including matrix cracking,

delamination, fibre fracture, and ply-splitting can be observed for IM7/8552, even at the lowest impact energy in both loading cases (LVI and HVI). This signifies poor impact performance compared to the other materials used in this study.

5.5.3 Delamination

The extent of delamination damage in both LVI and HVI loading for all laminates were observed to vary, particularly between IM7/8552 and the two other materials used in this study. This variation was primarily due to the composite architecture, IM7/8552 possesses a UD based architecture whilst S2-Glass/MTM57 and Vectran/MTM57 was based on NCF. In general, it is known that the NCF architecture will enhance the composite's delamination resistance due to the existence of stitches in the fabric. These stitches, as mentioned before, will impede the propagation of crack, greatly supressing the extent of delamination. Table 5.4 presents the Interlaminar Fracture Toughness (IFT) properties for IM7/8552, S2-Glass/MTM57, and Vectran/MTM57, where it can be observed that both S2-Glass/MTM57 and Vectran/MTM57 possesses a large IFT properties when compared to IM7/8552. As a result, delamination can be clearly observed in IM7/8552 laminates, with the extent of delamination considerably larger compared to S2-Glass/MTM57 and Vectran/MTM57. Additionally, toughening mechanism such as fibre-bridging further enhances the delamination resistance of S2-Glass/MTM57 and Vectran/MTM57.

However, while delamination was suppressed for S2-Glass/MTM57 and Vectran/MTM57 under LVI loading, under HVI, delamination damage was observed to be significantly greater. Under LVI, the laminate's response was mainly from flexure, whilst under HVI, stress wave effects usually dominates. The influence of fabric architecture in enhancing delamination resistance can no longer be observed due to the greater energy dissipation in HVI loading. In HVI events, delamination can be visually observed from the cross-sectional images particularly at the laminate mid-plane, where in-plane shear stresses is the highest. This is particularly true for Vectran/MTM57, where its in-plane shear properties, both stiffness and strength, is the lowest amongst all three laminates. The low flexural stiffness further enable a greater flexural deformation, resulting in a larger

delamination damage, extending to the laminate boundaries. The cross-sectional images shown in Figure 5.38 reveal that the laminate was split into two halves when impacted at its V_{50}, confirming the dominance in flexure under HVI impact.

5.6 Summary

In this chapter, the impact performance of IM7/8552, S2-Glass/MTM57, and Vectran/MTM57 composites were investigated under LVI and HVI loadings. Under LVI loading, each laminate was subjected to three different energy levels (40 J, 100 J, and 160 J) to obtain a range of impact-induced damage, namely no penetration, partial penetration, and full penetration. It was found that IM7/8552 was the worst performing composite under LVI, whilst a superior performance was observed for S2-Glass/MTM57. The NCF architecture of S2-Glass/MTM57 and Vectran/MTM57 laminates were observed to considerably surpress delamination, resulting in a significantly reduced delamination area when compared to IM7/8552. All of the commonly observed impact-induced damage types such as matrix cracking, delamination, permanent indentation, and fibre failure were present in the IM7/8552, S2-Glass/MTM57, and Vectran/MTM57 composites. Damage was most severe for IM7/8552, with delamination observed at almost every ply under all energy levels. For Vectran/MTM57, permanent indentation was seen to be the primary damage type for non-penetrating energy levels, whilst extensive matrix cracks and fibre fracture was observed for IM7/8552 and S2-Glass/MTM57 laminates. At the 160 J energy level, all laminates were completely penetrated, showing all of the known damage types under impact loads.

Superior impact performance was observed for Vetran/MTM57 laminates under HVI loading, whilst IM7/8552 was found to be the poorest. Extensive delamination damage was found for both S2-Glass/MTM57 and Vectran/MTM57 laminate, extending to the laminate boundaries, particularly at velocities close and above their V_{50}. In the case of Vectran/MTM57, the laminate was observed to split into two halves at projectile impact velocities close to its V_{50}. The energy absorption for Vectran/MTM57 laminates were concluded to be the largest, mainly due to its low $\pm 45^\circ$ in-plane shear properties (both stiffness and strength), consequently resulting in the largest Back Face Deflection

(BFD), when compared to S2-Glass/MTM57 and IM7/8552 laminates.

Chapter 6

An Energy-Based Damage Model for Vectran Composite

6.1 Introduction

Due to the increasing popularity of composite materials in many industries such as aerospace and defence, reliable design tools must be developed to exploit the full potential of fibre composite materials. This can only be done if the design takes into account specific composite properties such as the strain energy release rates (G_c), therefore avoiding over-engineered solutions, taking advantage of the stiffness to weight ratio of the composite laminates.

To date, many FEM models have been proposed on composite materials for structural design. In general, several modelling strategies have been suggested to predict failure of laminated composites subjected to static or dynamic loads [81, 85, 88, 98, 100, 203]. However, the proposed FEM models were usually tailored to brittle fibre composites, such as CF and GF, which behaves linearly up to failure, and does not take into account the compressive behaviour of high performance fibre composites, such as Vectran and Aramids. Due to the increasing use of high performance fibres, a new formulation is required to address its behaviour to represent accurate stress-strain relations, as well as correct dynamic response due to impact loading. In this section, an energy-based FEM model is proposed to represent the behaviour of Vectran/epoxy composite. The

constitutive model will be specific to plane stress assumptions, which considers zero through-thickness stresses, and constant transverse shear stresses according to the Classical Laminate Theory (CLT). The work presented here is an extension of the proposed FEM model by Iannucci et al. [88, 204, 205] which has been modified to capture the non-linearity observed in the stress-strain relations of Vectran/MTM57 laminated composites. The constitutive equations have been implemented into the LS-Dyna explicit FEM code as a User-defined Material model (UMAT), using an incremental Lagrangian approach.

6.2 Vectran fibres

It is well established that Vectran fibres (commonly known as a type of Thermotropic Liquid Crystal Polymers, TLCP) possess the so-called 'skin-core' structure [146, 147], which determines the mechanical performance of the fibre. Differences in the processing conditions (i.e. draw ratio, temperature, etc.) will result in a change in the fibre structure, often manifesting into a different 'skin-core' ratio (i.e. the thickness of the 'skin' would increase or decrease), hence altering the mechanical properties of the fibre. For instance, a thicker 'skin' would result in an increase in the fibre tensile modulus, and a decrease in the tensile strength and failure strain. In general, the 'skin' structure is often identified by a smooth surface, often with a highly oriented crystalline domain. Moving in towards the 'core', the molecular structure was found to be less oriented, physically seen as fibrils in the fibre.

Failure under tensile loading would often initiate from the skin, moving inwards before finally fracturing in the tip of the core, shown schematically in Figure 4.17a [166]. An entirely different response will be observed under compressive loads. The fibrillar structure of the core which is suggested to be made up of packings of micro-fibrils [146, 147], schematically shown in Figure 6.1 - de-fibrillate almost immediately when placed under compressive loads [75, 150]. Section 6.3 presents the proposed constitutive equations to represent the behaviour of Vectran fibre based composites.

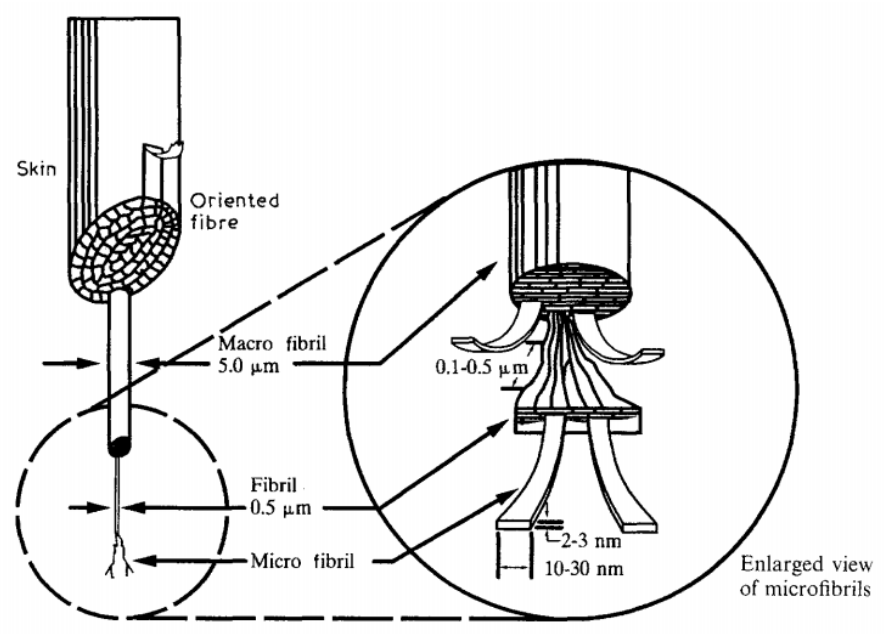


Figure 6.1: The three-tier model established for TLCP fibres [147]

6.3 Governing equations

6.3.1 Effective stress-strain relationship

The principle of strain equivalence, which is derived from the work of Kachanov and Rabotnov [79, 206], stating: "a damaged volume of material under the nominal stress shows the same stress-strain response as a comparable undamaged volume under the effective stress", $\overline{\sigma}$, and is defined as:

$$\overline{\sigma} = \frac{\sigma}{(1-d)} \tag{6.1}$$

where d=0 represents a virgin intact material and d=1 represents a fully damaged material. The damaged modulus of elasticity, E, can be related to the isotropic damage variable as:

$$E = E_0(1-d) \tag{6.2}$$

Using the framework defined in Equations 6.20 and 6.2, damage can be extended into the stress-strain relationship of Vectran composite. Therefore, *five* different damage

variables have been incorporated into the stress-strain relationship at the ply level, defined as:

(i) d_1: damage associated with the **tensile** fibre failure in the **warp** direction;

(ii) d_2: damage associated with the **tensile** fibre failure in the **weft** direction;

(iii) d_3: damage associated with **in-plane shear** failure;

(iv) d_4: damage associated with the **compressive** fibre failure in the **warp** direction;

(v) d_5: damage associated with the **compressive** fibre failure in the **weft** direction;

Material degradation, or damage propagation, would occur as soon as the composite reaches the point of damage onset (d=0), in which the stiffness will be degraded until reaching full damage (d=1). Since the proposed FEM model will be based on a woven architecture, damage onset will be the same in both warp and weft directions for tensile and compressive failure modes. Therefore, the maximum stress criterion was chosen to predict the onset of damage, given by:

$$\begin{cases} \dfrac{\sigma}{X_T} = 1, & \text{for tensile damage, } d_1,\ d_2; \\ \dfrac{\sigma}{X_C} = 1, & \text{for compressive damage, } d_4,\ d_5 \end{cases} \tag{6.3}$$

where X is the respective strength for both tensile, T, and compression, C. The propagation of damage is modelled separately for tension and compression. However, since both tension and compression shares the same stiffness, both damage variables for warp and weft directions can be combined, yielding:

$$\begin{cases} E_{11} = (1 - d_x)E_{11}^0, & \text{for damage in warp direction;} \\ E_{22} = (1 - d_y)E_{22}^0, & \text{for damage in weft direction} \end{cases} \tag{6.4}$$

where E_{11}^0 and E_{22}^0 are the initial stiffness in the warp and weft directions, respectively, and $(1 - d_x)$ is defined as:

$$(1 - d_x) = (1 - d_1)(1 - d_4) \tag{6.5}$$

and $(1 - d_y)$ to be:

$$(1 - d_y) = (1 - d_2)(1 - d_5) \tag{6.6}$$

For in-plane shear, the stiffness-damage relationship is defined simply as:

$$G_{12} = (1 - d_3)G_{12}^0 \tag{6.7}$$

Finally, for equality, the Poisson's ratio must also be reduced in the similar manner as the stiffness, defined as:

$$\nu_{12} = (1 - d_x)\nu_{12}^0 \tag{6.8}$$

and the minor Poisson's ratio is given by:

$$\nu_{21} = (1 - d_y)\nu_{21}^0 \tag{6.9}$$

where the following relationship between Poisson's ratio and stiffness is given by:

$$\frac{\nu_{12}}{E_{11}} = \frac{\nu_{21}}{E_{22}} \tag{6.10}$$

6.3.2 Stress-strain-damage relationship

The plane stress orthotropic elastic matrix can be defined as:

$$\varepsilon = \mathbf{C}\sigma \tag{6.11}$$

where $\mathbf{C}$ is a fourth rank stiffness tensor given by:

$$\begin{bmatrix} \frac{1}{E_{11}^0} & -\frac{\nu_{21}}{E_{22}^0} & 0 \\ -\frac{\nu_{11}}{E_{21}^0} & -\frac{1}{E_{22}^0} & 0 \\ 0 & 0 & \frac{1}{G_{12}^0} \end{bmatrix}$$

Inverting the stiffness tensor, and including damage variables, the stress-strain-damage relationship can be re-written as:

$$\begin{bmatrix} \sigma_{11} \\ \sigma_{22} \\ \tau_{12} \end{bmatrix} = \frac{1}{N} \begin{bmatrix} (1-d_x)E_{11}^0 & (1-d_x)(1-d_y)\nu_{21}^0 E_{11}^0 & 0 \\ (1-d_y)(1-d_x)\nu_{12}^0 E_{22}^0 & (1-d_y)E_{22}^0 & 0 \\ 0 & 0 & N(1-d_3)G_{12}^0 \end{bmatrix} \begin{bmatrix} \varepsilon_{11} \\ \varepsilon_{22} \\ \gamma_{12} \end{bmatrix}$$

where N is given by:

$$N = 1 - (1-d_x)(1-d_y)\nu_{12}\nu_{21} > 0 \tag{6.12}$$

For Vectran/MTM57 laminates, the stress-strain relationship is slightly modified to represent the non-linear behaviour seen in the tensile stress-strain response. The general stress-strain relationship is given by:

$$\sigma_{11} = E_{11}^0(\varepsilon_{11}^N + \varepsilon_{11}^M) \tag{6.13}$$

and

$$\sigma_{22} = E_{22}^0(\varepsilon_{22}^N + \varepsilon_{22}^M) \tag{6.14}$$

where E^0 is the secant modulus, N and M ($1 < N$,$M < 2$) are constants which can be found by least square fitting of the tensile stress-strain curve. One could consider defining two (or more) stiffness variable to represent the stiffness of the 'skin' and the 'core'. However, a further simplification was made to reduce the complexity of Equation 6.13. In damage terms, Equation 6.13 becomes:

$$\overline{\sigma}_{11} = E_{11}^0(1-d_x)(\varepsilon_{11}^N + \varepsilon_{11}^M) \tag{6.15}$$

and similarly for 6.14:

$$\overline{\sigma}_{22} = E_{22}^0(1-d_y)(\varepsilon_{22}^N + \varepsilon_{22}^M) \tag{6.16}$$

Therefore, the new stress-strain-damage relationship for Vectran/MTM57 can be re-written as:

$$\begin{bmatrix}\sigma_{11}\\ \sigma_{22}\\ \tau_{12}\end{bmatrix} = \frac{1}{N}\begin{bmatrix}(1-d_x)E_{11}^0 & (1-d_x)(1-d_y)\nu_{21}^0 E_{11}^0 & 0\\ (1-d_y)(1-d_x)\nu_{22}^0 E_{21}^0 & (1-d_y)E_{22}^0 & 0\\ 0 & 0 & N(1-d_3)G_{12}^0\end{bmatrix}\begin{bmatrix}\varepsilon_{11}^N+\varepsilon_{11}^M\\ \varepsilon_{22}^N+\varepsilon_{22}^M\\ \gamma_{12}\end{bmatrix}$$

Equation 6.16 can also be re-written in an incremental form, given by:

$$\Delta\sigma_{22} = (N\varepsilon_{22}^{N-1} + M\varepsilon_{22}^{M-1})(1-d_2)E_{22}^0\Delta\varepsilon_{22} + (\varepsilon_{22}^N + \varepsilon_{22}^M)\Delta E_{22}^0 \tag{6.17}$$

where ΔE^0 is defined as:

$$\Delta E_{22} = -E_{22}^0\Delta d_2 \tag{6.18}$$

therefore Equation 6.17 can be re-written as:

$$\Delta\sigma_{22} = E_{22}^0\big[(N\varepsilon_{22}^{N-1} + M\varepsilon_{22}^{M-1})(1-d_2)\Delta\varepsilon_{22} - \beta(\varepsilon_{22}^N + \varepsilon_{22}^M)\Delta d_2\big] \tag{6.19}$$

where the β term defines irreversible (permanent) strain, ε_p, from any unloading point during damage propagation. $\beta = 1$ will result in an unloading straight back to the origin, whilst β >1 results in positve irreversible strain, illustrated in Figure 6.2. For instance, upon reaching the initiation strain at point A, damage will propagate which would result in a linear degradation of the stiffness. For β=1, any unloading beyond point A will result in an unloading straight back to the origin (point O), using the 'damaged' stiffnes as the unloading slope. However, with β >1, the degradation slope (the slope beyond point A) would be increased due to the positive β term, hence resulting in a positive irreversible strain, OF. The choice of the β term in this study was made by trial and error, to accomodate the permanent strain observed in the load-displacement histories under LVI loading.

Any reloading after the initial unloading beyond point A will follow the original slope ('damaged' stiffness) in which the original unloading was made (i.e. slope OB for β=1 and slope FD for β >1). Upon reaching the original unloading point (i.e point B for β=1 and point D for β >1), damage will continue to propagate until reaching

zero stress. It must be noted that any unloading upon damage initiation (beyond point A) will stop damage from propagating. This is also true for reloading after the initial unloading, until reaching the point where the original unloading was made (i.e point B for β=1 and point D for β >1).

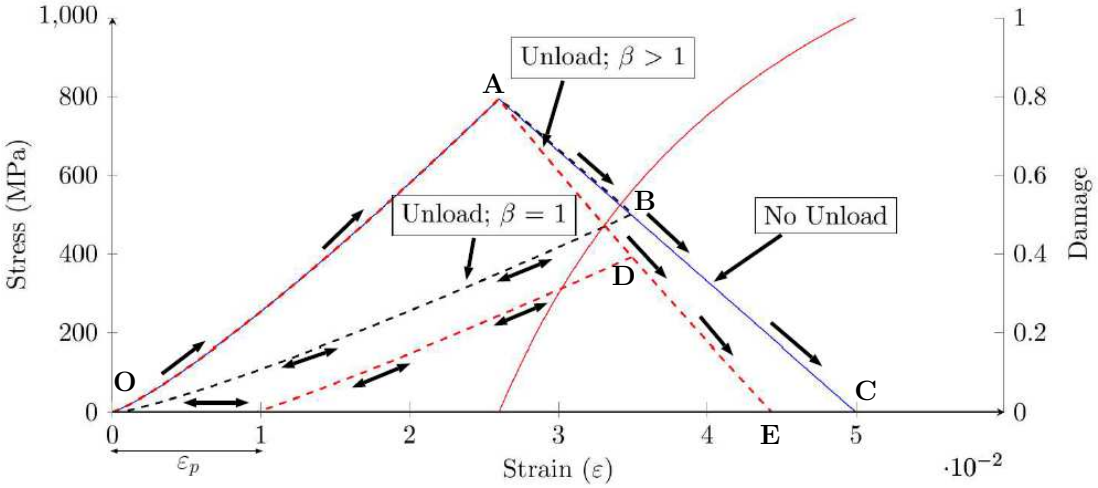


Figure 6.2: Direct stress component with unloading

6.3.3 Damage propagation

Tensile and compressive direct stresses

As mentioned earlier, damage propagation follows a linear softening curve, in which the stress is degraded as a function of strain. For simplification, Poisson's coupling is neglected prior to damage initiation. For both tensile and compressive component, damage propagation is defined as:

$$d_i = 1 - \bar{A}\left[\frac{\varepsilon_{max,i} - \varepsilon_{ii}}{\varepsilon_{ii}^N + \varepsilon_{ii}^M}\right] \tag{6.20}$$

where i=1,2 and $\bar{A}$ is a constant given by:

$$\bar{A} = \left[\frac{\varepsilon_{0,i}^N + \varepsilon_{0,i}^M}{\varepsilon_{max,i} - \varepsilon_{0,i}}\right] \tag{6.21}$$

where $\varepsilon_{max,i}$ is the strain at zero stress (full damage), $\varepsilon_{0,i}^N$ and $\varepsilon_{0,i}^M$ are the initiation strain, and ε_{ii} is the current strain. Equation 6.20 can also be written in an incremental form, which has been implemented in LS-Dyna, given by:

$$\Delta d_i = \left[\frac{1}{\varepsilon_{ii}^N + \varepsilon_{ii}^M} + \frac{(\varepsilon_{max,i} - \varepsilon_{ii})(N\varepsilon_{ii}^{N-1} + M\varepsilon_{ii}^{M-1})}{(\varepsilon_{ii}^N + \varepsilon_{ii}^M)^2} \right] \overline{A} \Delta\varepsilon_{ii} \tag{6.22}$$

Computing the strain at final failure, $\varepsilon_{max,i}$ will require the strain energy release rate, G_C to be known in the appropriate modes of failure. For instance, under tensile loading, the G_C is related to the tensile fibre failure, which defines the area under the stress-strain curve, shown in Figure 6.3, consequently obtaining the value for $\varepsilon_{max,i}$. G_C is a fracture mechanics property which can be experimentally obtained by performing some well-known fracture mechanics characterisation such as the Compact Tension (CT) or Compact Compression (CC) test. The fracture and damage mechanics coupling utilised in this study will be discussed in detail in subsection 6.3.4.

The strain energy consumed during material failure is a volumetric energy, and it is generally known as the area under the stress-strain curve. Since fracture mechanics considers the energy per unit area, kJ/m^2, another length parameter has to be introduced, defined as:

$$V \int_0^{\varepsilon} \sigma d\varepsilon = l_c A \int_0^{\varepsilon} \sigma d\varepsilon = G_C A \tag{6.23}$$

where l_c is the characteristic element length describing the finite element mesh, σ is the failure strength, and A is the fracture cross-sectional area. Therefore, the size of l_c can vary with the element size. This inherently alleviates the mesh dependency of the finite element model, since the energy under the curve must equal to the G_C to prevent any spurious energy dissipation. Equation 6.23 is also the basis of the crack smearing approach which will be discussed in subsection 6.3.4.. Figure 6.3 presents the failure envelope for Vectran/MTM57 tensile and compressive direct stresses.

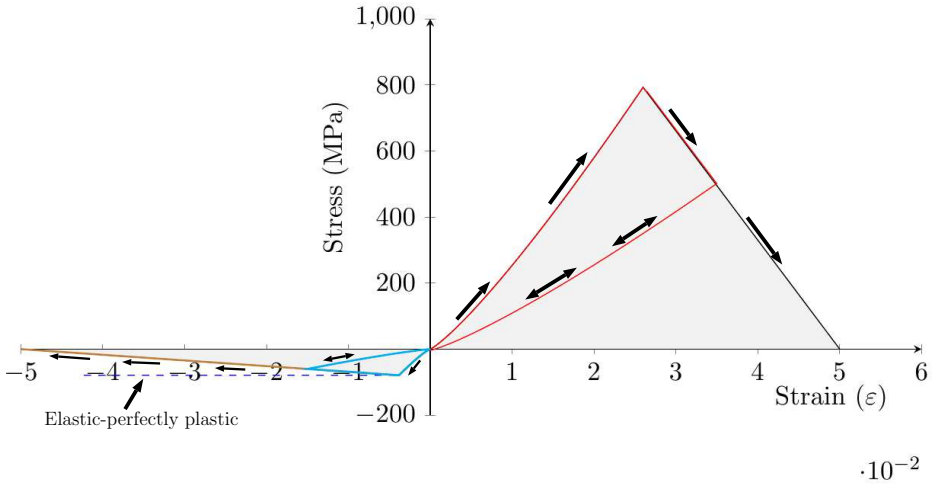


Figure 6.3: Failure envelope for tensile and compressive direct stresses. Shaded area represents G_c. Also shown is the elastic-perfectly plastic assumption under compressive loading

Residual strength for compressive failure

For Vectran fibres (or laminates), the compressive strength is generally governed by the fibre, irrespective of the matrix compressive strength. This implies that the compressive strength of Vectran laminates will be considerably lower compared to its tensile strength, even if its matrix strength is higher than the fibre's strength. This is due to the fibrillar nature of the fibre, which de-fibrillate almost immediately when placed under a compressive load [146, 147, 149].

It was also observed that when Vectran/Epoxy laminates were placed under uniaxial compressive loads, the laminate will exhibit a strain-hardening response, which allows the laminate to carry a further load with increasing strain. This is shown in Figure 6.4, where it can be seen that non-linearity begins at approximately 40 MPa (ε= 0.021%). Upon passing its yield strength, the fibres will start to buckle, seen as micro-kinks at the fibre level [149]. Strain-softening begins until approximately 80 MPa (ε = 4.3%) when finally the specimen was observed to be 'crushing'.

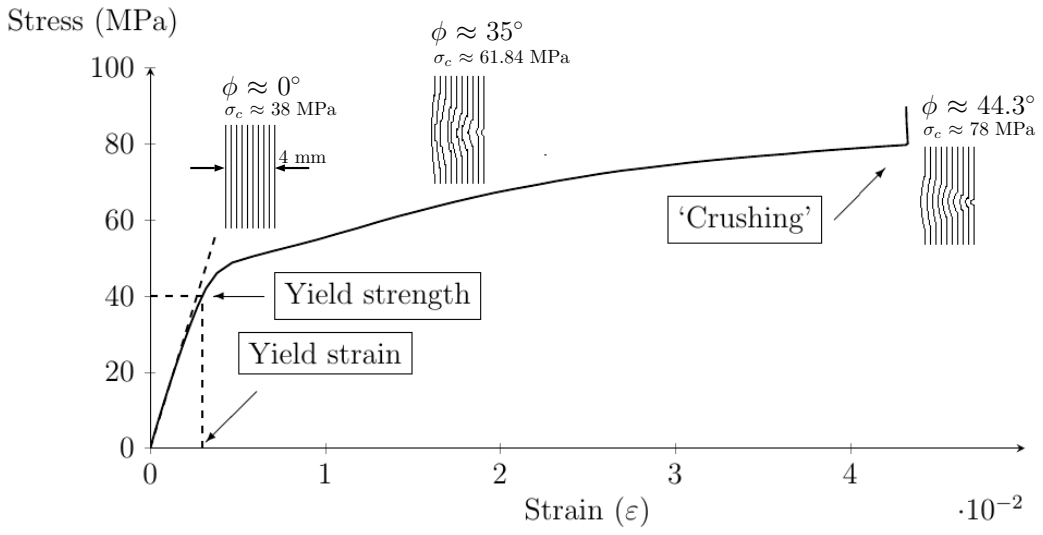


Figure 6.4: Typical experimental compressive response for Vectran/MTM57 laminates. ϕ represents the kink-band angle

It is common for brittle fibre – brittle matrix system such as CF/Epoxy and GF/Epoxy laminates that the residual compressive strength is estimated from the matrix compressive strength, which is considerably lower than the fibre compressive strength. However, for Vectran/Epoxy laminates, the residual compressive strength is taken as the ultimate strength before 'crushing' (≈80 MPa in this case). Therefore, upon reaching the maximum compressive strength of the laminate, no degradation of the compressive strength is being made, emulating an elastic-perfectly plastic response. Although this assumption could be seen as an over-simplification of the experimentally observed behaviour, it is assumed that the compressive response is significantly lower than its tensile component. Furthermore, if one were to fully capture the composite experimental response, such as the kink-band effects, 3D-stresses is required which would necessitate a full 3D formulation. Several researchers have proposed a method to predict the kink-band formation for polymer fibres, especially the ones which possesses 'skin-core' structure [207, 208]. The formulation was derived based on the assumption that the 'skin-core' structure was made of layers, with each layer connected with a spring (through-the-thickness), as well as frictional effects between each layer. Also, a separate spring is assigned to govern the kink-band formation when the 'damaged' layers start to rotate.

In-plane shear

A simple approach in modelling the in-plane shear response, including the non-linear component typically observed in many in-plane shear test, was implemented in LS-Dyna. The model was based on a 'piece-wise' approach with an exponential function to predict the non-linear response. A linear softening follows upon reaching the ultimate shear strength until zero stress. For shear strain below the yield strain, γ_{12}^0, a linear shear stress-shear strain relationship is proposed, given by:

$$\tau_{12} = \alpha G_{12}^0 \gamma_{12} \tag{6.24}$$

where G_{12}^0 is the initial shear modulus obtained from standard laboratory testing, τ_{12} is the shear stress, and α relates to the shear strain-rate enhancement case defined by a sigmoid relation initially proposed by Iannucci et al. [88, 204, 205] given by:

$$\alpha = 2 - e^{\frac{-\dot{\gamma}}{\kappa}} \tag{6.25}$$

where κ is a material parameter defining the shear strain-rate, $\dot{\gamma}$, with respect to the magnitude of enhancement. The effect of strain-rate on the shear stress-strain response will be discussed in subsection 6.3.3.

Following this, the shear stress-shear strain response follows an exponential function, given by:

$$\tau_{12} = ae^{b\gamma} + ce^{d\gamma} \tag{6.26}$$

where a, b, c, and d can be found by performing a least square fit on the non-linear component of the shear stress-shear strain curve. Finally, upon reaching the ultimate shear strength (damage onset), a linear degradation is proposed, given by:

$$\tau_{12} = \frac{\tau_{12}^u}{\gamma_{12}^{max} - \gamma_{12}^u}(\gamma_{12}^{max} - \gamma_{12}) \tag{6.27}$$

where τ_{12}^u is the ultimate shear strength, σ_{12}^{max} is the maximum shear strength (damage = 1), and γ_{12}^u is the ultimate shear strain. The maximum shear strain, γ_{max} can be

obtained by using fracture mechanics, which will be discussed in subsection 6.3.4. This can be estimated from the Mode II interlaminar fracture test [209], in the absence of Mode II intralaminar energy, shown by the area under the shaded curve in Figure 6.6. Writing as a function of damage, Equation 6.28 is given by:

$$d_3 = 1 - \bar{C}\frac{\gamma_{12}^{max} - \gamma_{12}}{\gamma_{12}} \tag{6.28}$$

where the constant $\bar{C}$ is given by:

$$\bar{C} = \frac{\tau_{12}^0}{G_{12}^0(\gamma_{12}^{max} - \gamma_{12}^0)} \tag{6.29}$$

Finally, converting equation 6.28 into an incremental form yields:

$$\Delta d_3 = \alpha\bar{C}\frac{\gamma_{12}^{max}}{\gamma_{12}^2}\Delta\gamma_{12} \tag{6.30}$$

Equation 6.30 has been implemented into the explicit LS-Dyna code, and its response is shown in Figure 6.6.

Unloading behaviour

Experimental evidence of the in-plane shear unloading behaviour for Vectran/MTM57 shows a similar unloading stiffness with the initial modulus. This is shown in Figure 6.5, where the unloading stiffness is nearly constant with strain range between 0 to 3, and a slight increase in shear stiffness with further increase in strain. Therefore, loading and unloading stiffness is assumed to be similar to the initial stiffness, G_{12}^0. The total strain can be additively decomposed into the elastic and inelastic strain, given by:

$$\gamma_{12}^t = \gamma_{12}^e + \gamma_{12}^i \tag{6.31}$$

where γ_{12}^e is the elastic (recoverable) strain, and γ_{12}^i is the inelastic (permanent) strain. This is schematically shown in Figure 6.5, where unloading from point A will result in a residual permanent shear strain OB. The magnitude of permanent shear strain will increase with increasing strain – unloading from point C yields a permanent strain with magnitude OE. Upon passing the ultimate shear strain, γ_{12}^u, stress will be degraded

with a negative stiffness, defined in the previous section. Any unloading beyond this point will follow the damaged stiffness, defined as:

$$\bar{G} = \gamma_{12}^{0}(1 - d_3) \tag{6.32}$$

It must be noted that unloading from any point before damage initiation will utilise the initial shear stiffness, G_{12}^{0}, consistent with the results obtained experimentally. Additionally, a similar response will be observed the model is loaded in a negative direction, Figure 6.3.

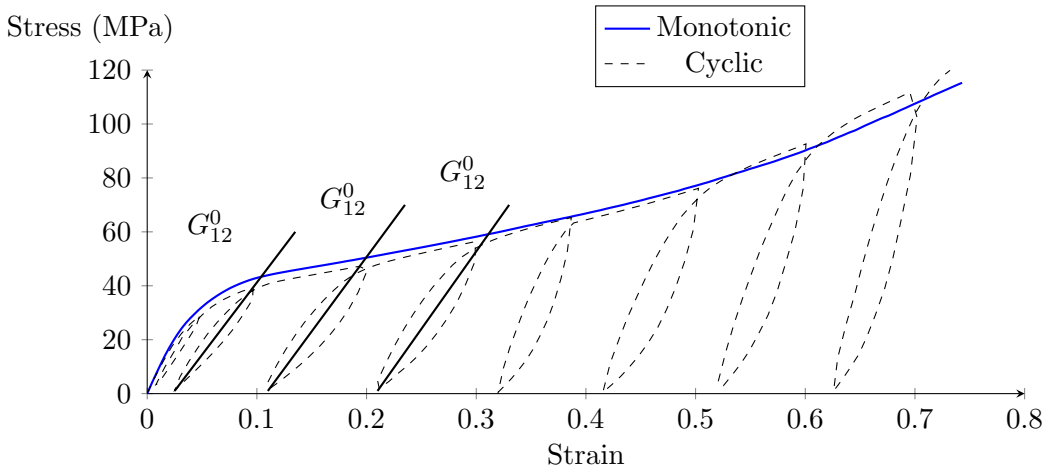


Figure 6.5: Cyclic and monotonic ±45 ° in-plane shear response for Vectran/MTM57

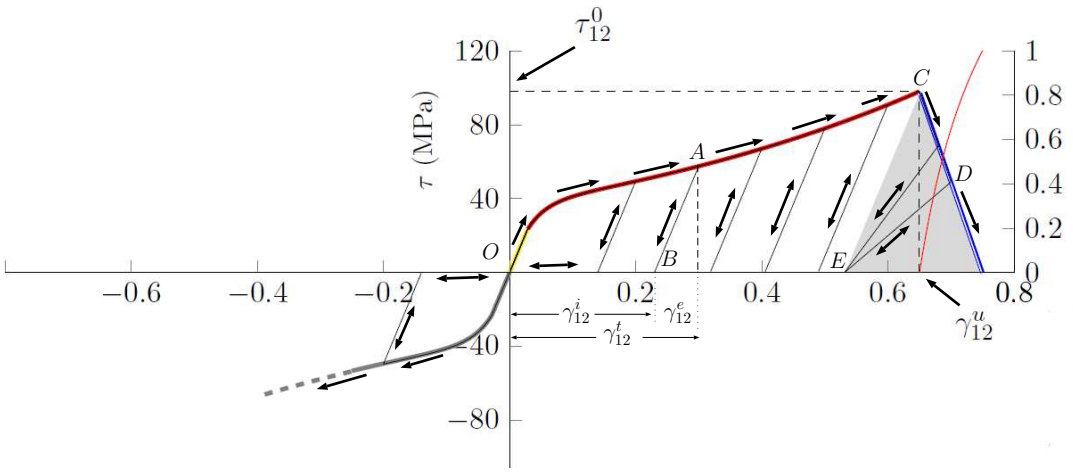


Figure 6.6: ±45 ° in-plane shear response including the loading and unloading behahavior shown in black. Initial phase is shown in yellow, strain-hardening phase in red, and linear degradation in blue. Shaded area highlights G_c

Strain-rate dependency

The strain-rate dependency of the in-plane shear component of Vectran/MTM57 is implemented by using the enhancement factor originally proposed by Iannucci et al. [88] given by:

$$\alpha_{rate} = 2 - e^{-\frac{\dot{\gamma}_{12}}{\kappa}} \tag{6.33}$$

where κ is a material parameter defining the shear rate at which enhancement is applied. In general, the overall shear strength and modulus were improved with increasing strain-rate. Figure 6.7 illustrates the effect of strain-rate enhancement of the $\pm 45\,^{\circ}$ in-plane shear response of Vectran/MTM57. Subsequently, Figure 6.8 presents the sigmoid relation implemented in the UMAT to define the shear strain-rate, in which it can be seen that the enhancement will always asymptote to a factor of 2 after reaching a strain-rate of 100/s and above.

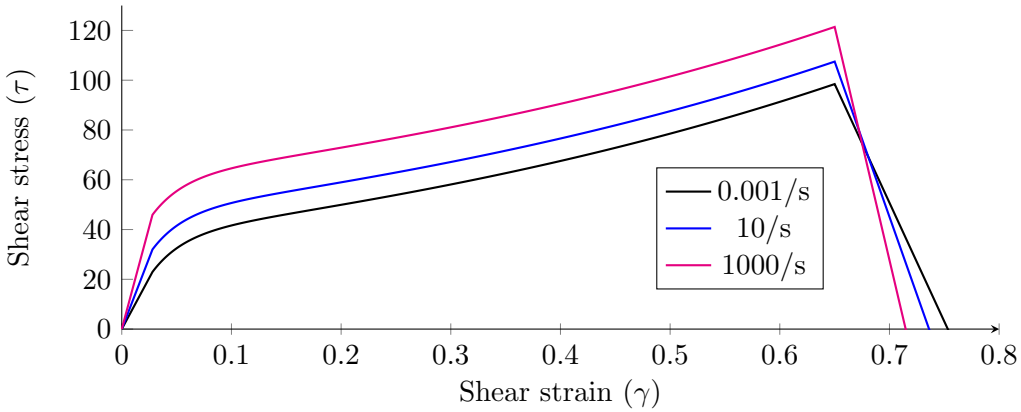


Figure 6.7: Effects of strain-rate enhancement of Vectran/MTM57 $\pm 45\,^{\circ}$ in-plane shear behaviour

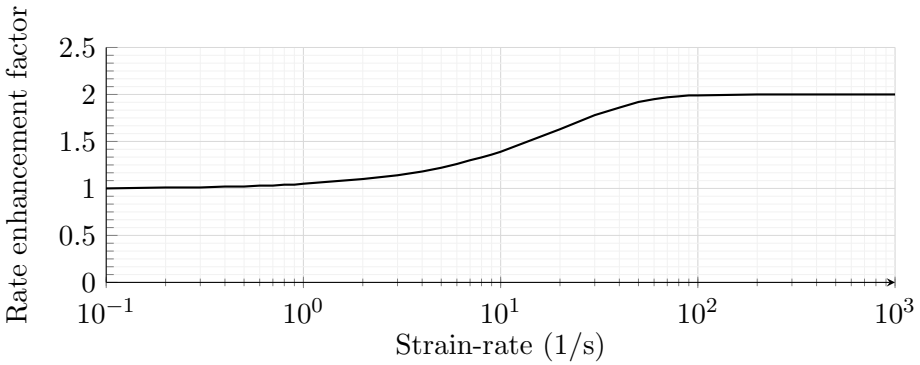
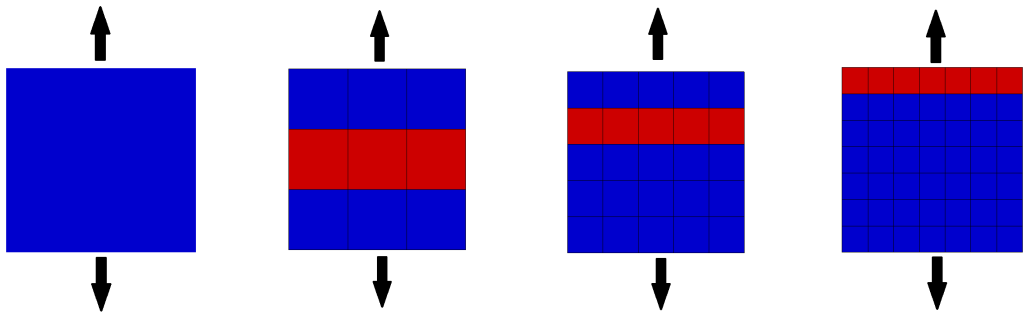


Figure 6.8: Sigmoid relation to define the shear strain-rate enhancement

6.3.4 Mesh dependency

To alleviate mesh dependency, a smeared crack formulation was used. This method was originally proposed by Bažant et al. [93], and was utilised by many researchers [88, 95, 98, 203–205] to reduce the mesh size dependency on the FE model. Therefore, the mesh dependency was verified by performing several simulations utilising a square specimen of 1 mm^2 loaded in tension. The specimen was discretised into several mesh sizes - one element, 3^2 elements, 5^2 elements, and 7^2 elements. Figure 6.9 shows the predicted failure for each mesh discretization cases. As expected, failure always occurred in a band perpendicular to the loading direction. No artifice or outside trigger were used to initiate failure in any location. As a result, the load-displacement curves, shown in Figure 6.10 were independent of any mesh sizes.



(a) One element (b) 3^2 elements (c) 5^2 elements (d) 7^2 elements

Figure 6.9: Square specimens loaded in tension with different mesh densities. Failed elements are highlighted in red

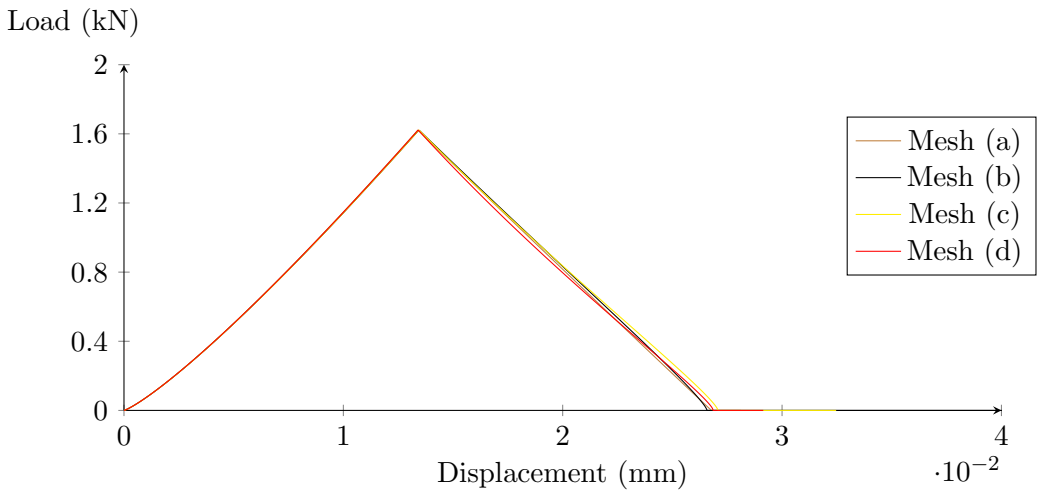


Figure 6.10: Load-displacement response of specimens with different mesh densities loaded in tension

In spite of the mesh independence, it must be noted that the current approach is only suitable for a quadrilateral structured mesh type. In addition, the current approach requires the crack growth direction to be parallel with one edge of the finite element, which is not always the case in a multi-directional composite. This is because upon failure, crack will propagate in a direction perpendicular to the relevant failure mode. For instance, fibre failure will result in a crack perpendicular to the orientation of the fibre, with the characteristic element length, l_c being in the fibre's direction. Without a specific algorithm to calculate a unique l_c, arbitrary damage propagation may occur yielding a discontinuous band, as seen in Figure 6.11.

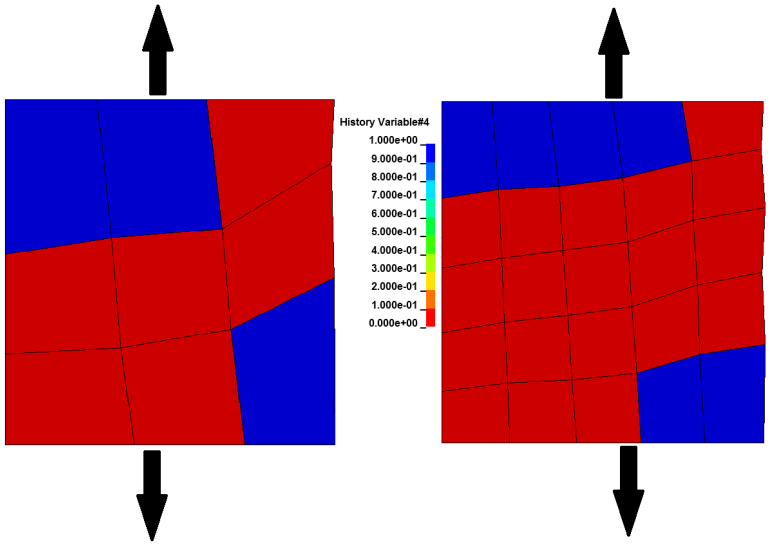


Figure 6.11: Unstructured mesh with different mesh densities (a) 3^2 (b) 5^2

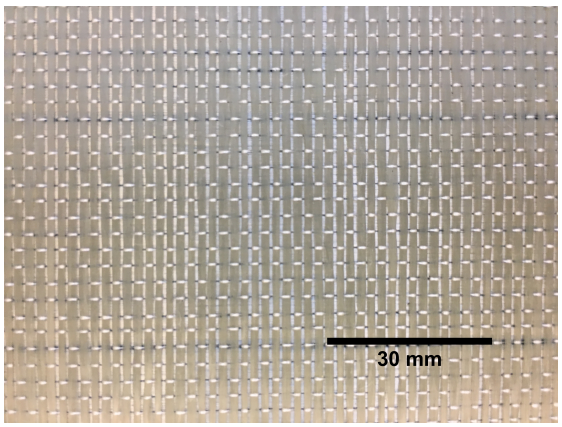
While the characteristic length in the model was taken as the average of each computed element length in LS-Dyna, one could observe the crack-band 'discontinuity' upon damage onset and growth due to the non-similar element area. This is a considerable limitation which requires the need for a specific algorithm for l_c calculation. However, although this may present a problem for a complex composite laminate possessing different mesh sizes, the current approach is adequate for the current study due to the simple laminate shape. Furthermore, the ply orientation utilised in this study was restricted to a $0°/90°$ (cross-ply) direction, ensuring that crack popagation will always be perpendicular to one edge of the finite element.

6.4 Model validation

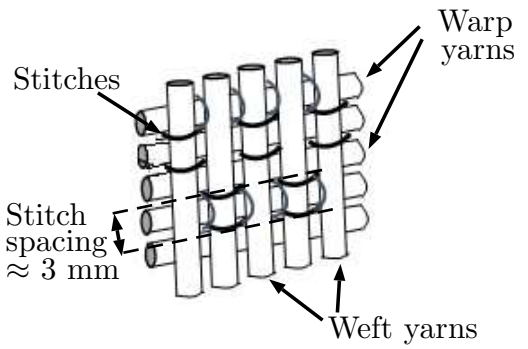
The proposed plane stress damage model described in the previous subsections has been implemented into the explicit LS-Dyna code for thin and thick shell formulations. The next subsections will present results of the in-plane modelling of standard coupon specimens for tension, compression, and $\pm 45\,^{\circ}$ in-plane shear. Finally, results from the FEM modelling will be compared with the in-plane experiments, therefore enabling an appropriate validation of the UMAT model. Appendix C presents a flowchart of the implemented UMAT in LS-Dyna

6.4.1 Model set-up

The mechanical properties used in the FEM model are summarised in Table 6.1, whilst the modelling constants in Table 6.2. Engineering properties (both in-plane and fracture toughness) were obtained by performing quasi-static mechanical characterisation on the NCF laminate, shown in Figure 6.12. All mechanical properties are defined in terms of an updated engineering stress and strain.



(a)



(b)

Figure 6.12: Vectran NCF used in this study (a) NCF fabric (b) Schematic of the RUC

Subsequently, one end of the specimen was constrained against translation along and across the specimen, whilst the other end was subjected to a ramped velocity boundary condition. The ratio between internal and kinetic energy was kept below 0.1% to ensure quasi-static conditions.

It must be noted that in all cases of the quasi-static in-plane modelling, no cohesive

algorithm was used. This is because the modelling is mainly being performed to validate the stress-strain response of the UMAT. However, cohesive algorithm was utilised using cohesive surfaces in modelling the impact response of the composite which is discussed in detail in subsection 7.2.3.

Table 6.1: Mechanical properties used in the FEM analysis

Mechanical properties	NCF Vectran/MTM57
$E_x = E_y$	31.2 GPa
$\sigma_x = \sigma_y$	811 MPa
$\nu_{12} = \nu_{21}$	0.05
G_{12}	0.82 GPa
τ_{12}	23 MPa
G_{Ic}	260 kJ/m^2

Table 6.2: Modelling constants

Constants	NCF Vectran/MTM57
$N = M$	1.196622
σ_{ult}	80 MPa
τ_{ult}	98 MPa
γ_{ult}	65%
γ_{max}	75%
a	34.34 MPa
b	1.519 MPa
c	-38.71 MPa
d	-33.56 MPa

6.4.2 Tension

A tensile FEM model was created with specimen dimensions defined as 250 mm x 25 mm x 2 mm (L x W x t) utilising the four-noded quadrilateral thin shell elements. The total number of elements was 6250, with 6 through-the-thickness integration points in each element, corresponding to 6 Vectran NCF plies. 5 damage variables were assigned to each integration point - corresponding to the damage variables described in subsection 6.3.1.

Figure 6.15 shows the FEM prediction on the tensile stress-strain curve for Vectran/MTM57. Also shown in Figure 6.15 is the experimentally obtained stress-strain curve from the quasi-static tensile tensile testing of Vectran/MTM57. Good agreement

can be seen between the experimental and FE predictions with similar ultimate stress and strain values obtained.

Figure 6.13 shows the predicted failure in the FEM model. As expected, failure occurs close to the constrained end of the specimen, where the stress concentration was highest. Damage initiates at the side of the specimen, progressing to the centre of the specimen finally failed when all integration points in the damage band have failed. In contrast, Figure 6.14 presents the failed Vectran/MTM57 specimen, in which it can be observed that failure does not occur at the end of the specimen if compared to the FEM prediction. This is because failure initiates at the weakest point in the specimen (due to voids or stress concentration in resin rich areas etc.), which then propagate perpendicular to the loading direction.

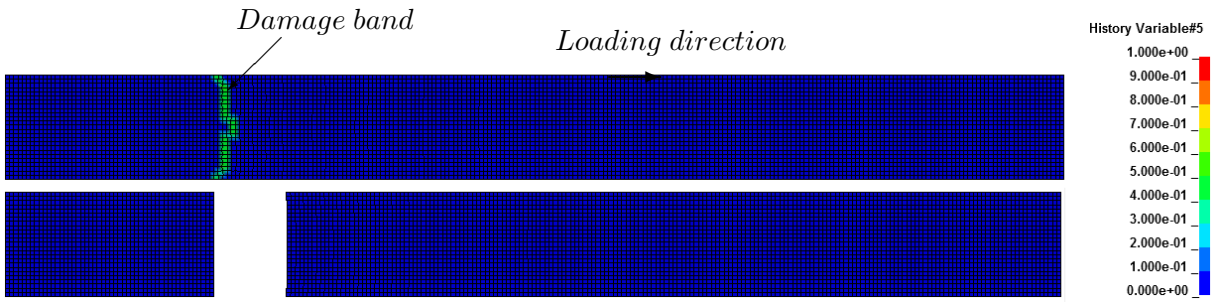


Figure 6.13: Progression of damage in the FEM model (top) damage band in the FEM model prior to final failure (bottom) final failure



Figure 6.14: Failed Vectran/MTM57 specimen under quasi-static tensile loading

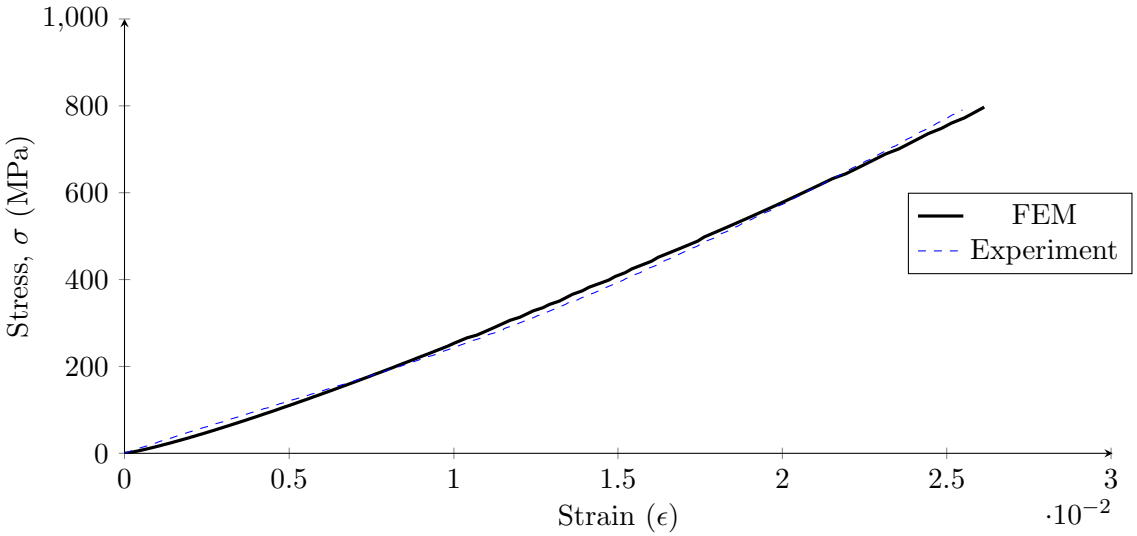


Figure 6.15: FE prediction on the tensile stress-strain response for Vectran/MTM57

6.4.3 Compression

For compression, an FEM model with specimen dimensions defined as 90 mm x 10 mm x 4 mm (L x W x t) was created using 900 four-noded quadrilateral thin shell elements. 12 through-the-thickness integration points were assigned in each element, corresponding to 12 Vectran NCF plies. Similar to the tensile modelling, 5 damage variables were assigned to each integration points enabling a comprehensive investigation of damage in each integration points.

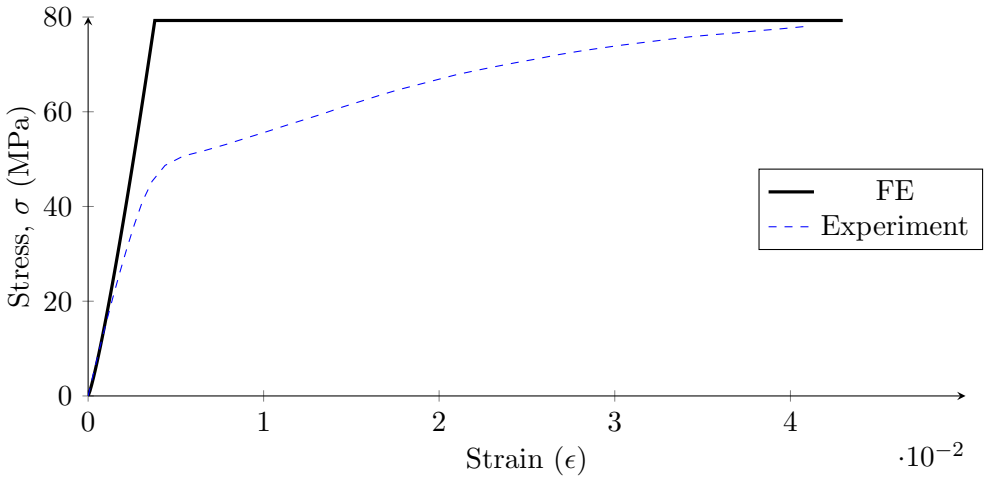
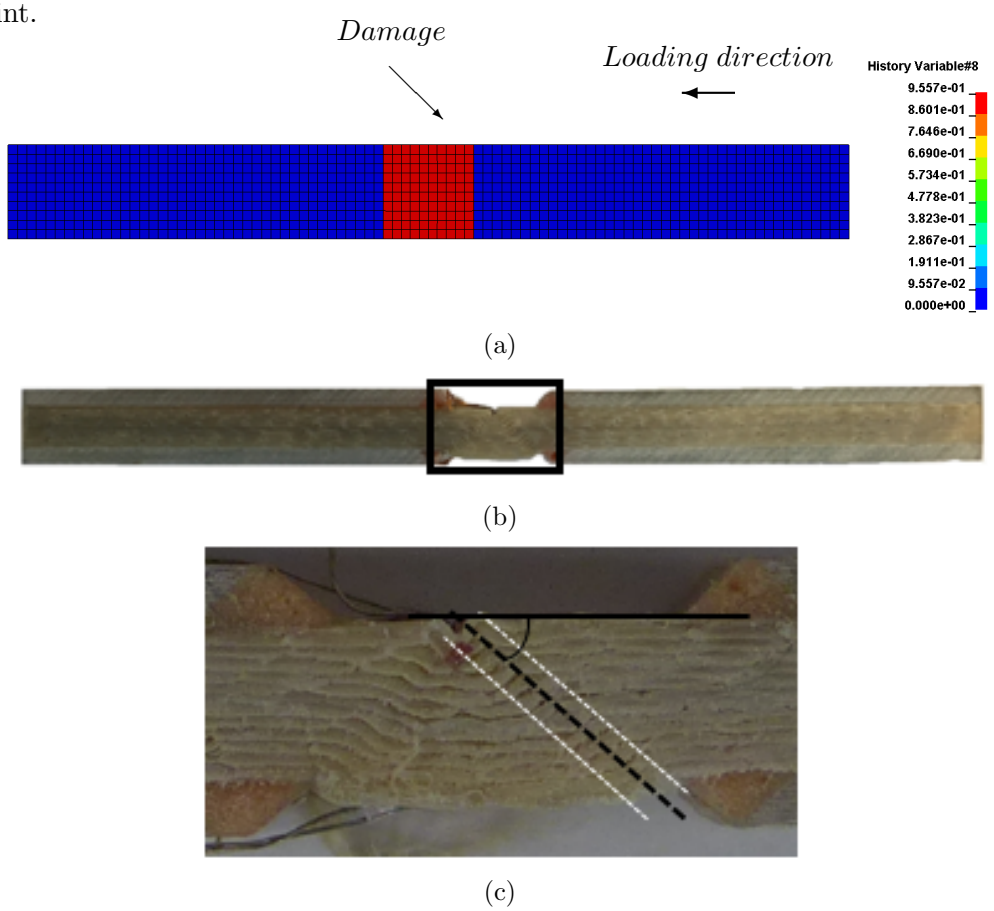


Figure 6.16: FEM prediction on the compressive stress versus strain response for Vectran/MTM57

Figure 6.16 shows the stress-strain response of the FEM model under compressive

loading. Also shown in Figure 6.16 is the experimental stress-strain curve for comparison purposes.

Next, Figure 6.17a presents the graphical illustration of the FEM model under compressive loading. As seen from Figure 6.17a, damage saturates in the gauge region, similar to the experimental observations. If incompressibility is imposed (which is the case shown in Figure 6.17a), damage will not propagate further as a result of the constraint.



(a)

(b)

(c)

Figure 6.17: Vectran/MTM57 under quasi-static compression loading (a) FEM prediction on the damaged region (b) Failed Vectran/MTM57 specimen (c) Close-up image of the black square in (b) showing the kink-bands

6.4.4 $\pm 45^\circ$ In-plane shear

For $\pm 45^\circ$ in-plane shear, an FEM model with dimensions similar to the experimental specimen was created (250 mm x 25 mm x 2 mm) using 6250 four-noded quadrilateral thin shell elements. Six through-the-thickness integration points were assigned in each element, corresponding to the 6 Vectran NCF plies ised in the experiment.

The predicted shear stress-shear strain response is shown in Figure 6.18, along with the experimentally obtained results. Excellent agreement can be observed between the FEM prediction and the experiment, up to the ultimate shear stress ($\approx$ 98 MPa).

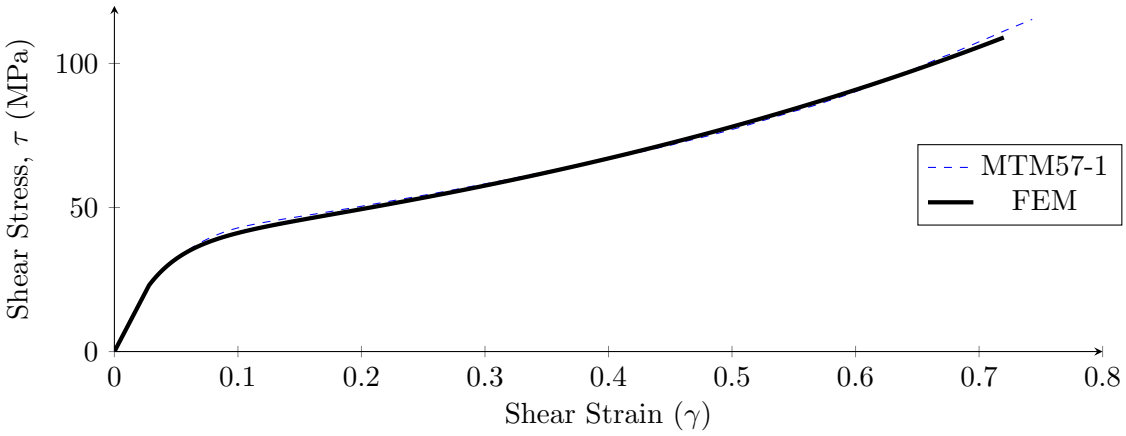
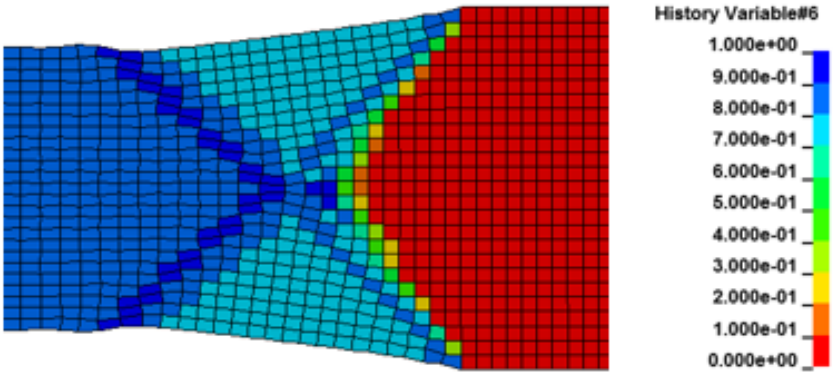


Figure 6.18: Shear stress versus shear strain curve for Vectran/MTM57

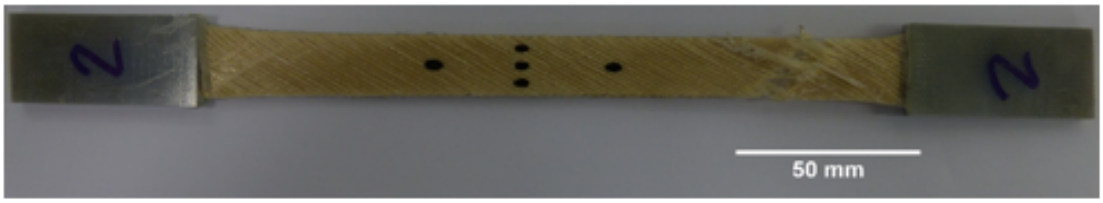
Figure 6.18 shows the FEM prediction for the $\pm 45^\circ$ in-plane shear stress-strain behaviour, in which an excellent agreement can be observed between the experimental response. Consequently, Figure 6.19 presents a comparison between the experimental and FEM specimens. At first glance, a similar 'necking' behaviour can be observed between the FEM model and the experimental specimen. However, the 'necking' observed around the gauge region in the experimental specimen was due to fibre rotation (i.e. scissoring effect), upon passing it's 'yield' strength. In the FE model, 'necking' was due to the element co-rotational formulation (Belytschko-Lin-Tsay shell [174]), since the element local direction (fibre direction) was kept at a constant 90° relative to each other throughout the analysis. It was verified on a single element as well as coupon tests that the longitudinal and transverse strain in the $\pm 45^\circ$ in-plane shear were in good agreement with the experimental results for shear strains of up to 20%. shown in Figure 6.20.



(a)



(b)



(c)

Figure 6.19: Vectran/MTM57 under quasi-static ±45 ° in-plane shear loading (a) FEM prediction on the damaged region (b) Close-up image of the black square in (a) showing the damage bands (c) Experimental specimen

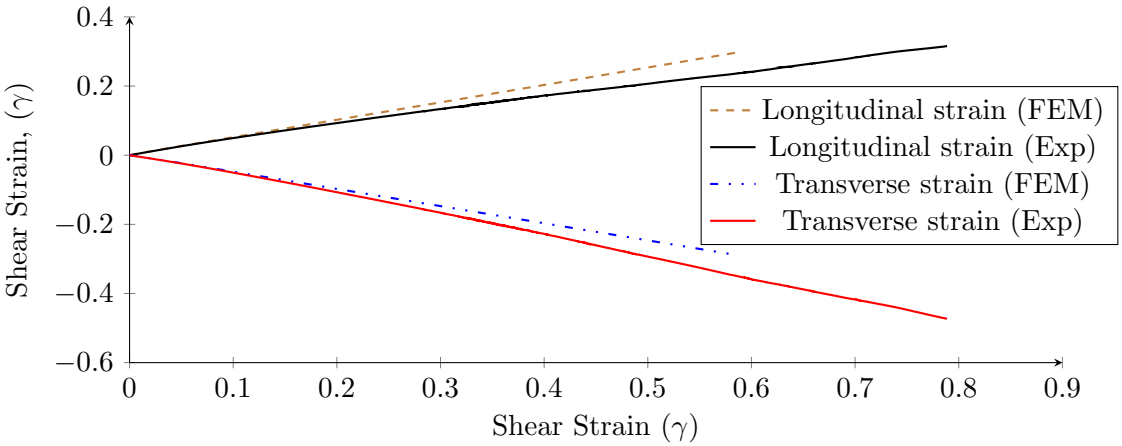


Figure 6.20: Comparison between experimental and FEM predicted longitudinal and transverse shear strain component versus total shear strain

6.5 Discussions

6.5.1 Tensile behaviour

Behaviour under tensile loading showed excellent agreement with the experimental results, whereby both stress-strain response and damage pattern were closely predicted using minimal inputs. This is important since it allows users to use the UMAT with minimal experimental information which can be obtained from standard quasi-static in-plane tests. In spite of this, the physically based two (or three) tier model could be implemented to enable a more comprehensive analysis to be performed to capture the micro-mechanics of failure in Vectran fibre based composites.

6.5.2 Compressive behaviour

Due to the plane stress formulation implemented in the UMAT, it is inherently assumed that the through-thickness stresses are a constant which was defined using a 'penalty' approach utilizing a linear spring for both through-thickness direct (σ_3) and shear (τ_{13}, τ_{23}) stresses. This places severe restriction in capturing the through-thickness effects of the laminate. In the case of compressive failure, the distinct kink-bands observed in the through-thickness direction (Figure 6.17c) cannot be predicted using the current UMAT framework since it requires additional constitutive formulation to describe the particular response. This could be represented using the approach proposed by Wadee et al. [207,208], in which the kink-band phenomenon was described using explicit constitutive relations, including band width growth following kink-band growth saturation.

6.5.3 $\pm 45^\circ$ In-plane shear

Under in-plane shear loading, extensive 'necking' is observed on Vectran/MTM57 due to the extensive fibre-rotation phenomenon which occurs progressively with increasing load. This effect was not explicitly captured since it requires a specific formulation which links the rotating angle with the shear stress/strain. As mentioned before, the necking observed in the FEM prediction was due to the element formulation, which uses a co-rotational formulation at the local (element) level. In spite of this, excellent agreement can be observed between the experimental and numerical results, although the

input required for the in-plane shear behaviour is more involved (at least four additional constants are required to obtain the optimal correlation).

6.5.4 Mesh dependency

Although mesh dependency has been alleviated with the smeared formulation approach, it should be noted that the volume of the damaged material is still meshed dependent, thus a mesh sensitivity study should be performed to capture the correct stress gradient in every discretized continuum. While no additional algorithm was developed to accommodate the use of non-structured meshes in this formulation, it was found that the model works well when using a structured quadrilateral mesh. Furthermore, due to the simple laminate dimensions used in this research, no complex meshing techniques were required. Hence the current formulation is found to be adequate in simulating the experimental response. However, it may beneficial in the future to modify this numerical model therefore enabling the use of a non-structured mesh in a more complex FEM analysis.

6.6 Summary

This chapter presents the development of a plane-stress constitutive model for Vectran fibre based composites. The proposed numerical model is found to be able to predict the response of Vectran/MTM57 with a considerable accuracy despite several drawbacks which are inherent under plane stress assumptions. The FEM prediction of the composite stress-strain response showed very good agreement with the experimental results, apart from the compressive component, in which the strain-hardening effect could be addressed using kink-band models in a full 3D formulation. The use of a single tensile modulus has resulted in a good correlation with the tensile stress-strain response, although this could be further enhanced by using two (or more) non-linear springs, as well as a dashpot to better represent the 'skin-core' structure. In addition, the effects of fibre rotation in the $\pm 45^\circ$ in-plane shear loading could be explicitly represented in the composite shear stress-strain response in order to fully capture the non-linear $\pm 45^\circ$ in-plane shear behaviour.

Chapter 7

Modelling the impact response of composite laminates

7.1 Introduction

The wide use of composite materials in many fields such as aerospace and automotive demands a deeper understanding of their behaviour. Such an understanding can be used to design more reliable and safer structures using robust computational algorithms, such as those based on the Finite Element Method (FEM).

In this Chapter, results from the FEM modelling are presented and compared with the low and high velocity impact testing of IM7/8552, S2-Glass/MTM57, and Vectran/MTM57. An energy based damage model available in LS-Dyna (MAT262) was utilised to model the behaviour of IM7/8552 and S2-Glass/MTM57, whilst the developed User MATerial model (UMAT) was used for Vectran/MTM57. The accuracy of both material models was assessed in terms of energy absorption under LVI and HVI loadings. The predicted damage and failure were also compared with the experimental observations on the damaged laminate. In addition, the accuracy and reliability of the used cohesive algorithm (cohesive surface) in the PhD study was investigated, particularly for S2-Glass/MTM57 and Vectran/MTM57 due to the NCF architecture as well as the fibre-bridging influence in the composite.

7.2 FEM model set-up

7.2.1 Element type and boundary conditions

A simplified representation of the Low Velocity Impact (LVI) condition was made in the FEM modelling. Four layers of stacked 8-noded thick shell elements (single integration point, six degrees of freedom) were utilised to model the 100 mm x 150 mm composite plate, with each connected using a cohesive algorithm (explained in subsection 7.2.3) to represent the delamination behaviour. Similar to the experiment, the 16 mm diameter steel hemispherical impactor and the 110 mm x 160 mm steel backplate to represent the composite plate support was modelled using solid elements. A total of 60000 thick shell elements and 13760 solid elements were used in this model. Figure 7.1 shows the FEM model setup for LVI condition.

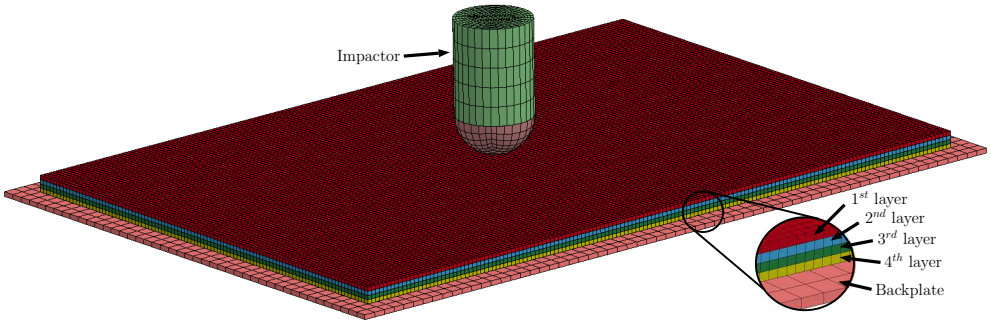


Figure 7.1: FEM model used in the low velocity impact case

The impactor was constrained in all directions, except the vertical (z-axis), following the experimental boundary conditions. A full constraint was applied on the backplate, whilst no constraint was given to the composite plate. The composite plate was fixed on the backplate, and a contact algorithm (CONTACT AUTOMATIC SURFACE TO SURFACE) was used between the two parts to model their interactions. The contact algorithm utilises linear springs, with the stiffness of each spring calculated based on the bulk modulus of each connected parts (composite plate and impactor/composite plate and backplate).

Under High Velocity Impact (HVI) condition, no backplate (as in the case of LVI modelling) was utilised. This is because the composite plate was supported using braided Kevlar yarns on a custom house-made fixture in the experiment. The 16 mm diameter

steel spherical projectile for HVI loading was modelled using solid elements. A total of 60000 thick shell elements and 3584 solid elements were utilised in the HVI modelling.

7.2.2 Material models

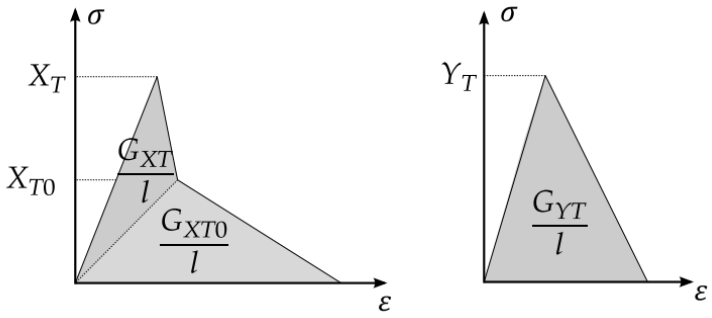
MAT ELASTIC was chosen to represent the behaviour of the impactor and backplate, while MAT LAMINATED FRACTURE DAIMLER CAMANHO (MAT262) was selected to represent the behaviour of IM7/8552 and S2-Glass/MTM57. The former material model is based on an hypoelastic formulation, suitable for modelling elastic isotropic materials such as steel. For the latter, the formulation is based on an energy-based damage mechanics material model, utilising fracture mechanics to represent material failure. A tri-linear initiation-propagation law was established for the tensile and compressive fibre failure, Figure 7.2a, and a bi-linear law was defined for failure in the transverse direction for both tensile and compressive failure modes, Figure 7.2b. Information for the energy input can be found by performing standard fracture mechanics-based laboratory tests such as Compact Tension/Compression or Four Point Bending (4PB). Finally, for Vectran/MTM57, a vectorized user-defined material model (UMAT 41v) was utilised. The material model uses a plane stress formulation which is described in Chapter 6 to represent the behaviour of Vectran/MTM57 composite material.

Both material model formulations, (MAT262 and UMAT 41v), utilise the smeared crack approach in alleviating the mesh dependency. However, the calculation for the characteristic element length, l_c, in MAT262 is slightly different from the approach described in subsection. While l_c is taken as the smallest element length in the UMAT, MAT262 calculates l_c from a purely geometrical approach which utilises information from the nodal connectivity, discussed in section 2.3 of Chapter 2.

Inputs for the in-plane material properties are shown in Table 3.4 whilst for the fracture energies are given in Table 7.1.

Table 7.1: Fracture toughness inputs for composite materials used in this study

Composite system	G_{Ic}[1] (kJ/m^2)	G_{Ic}[2] (kJ/m^2)	G_{Ic}[3] (kJ/m^2)	G_{Ic}[4] (kJ/m^2)
IM7/8552	133.33 [171]	47.5 [171]	0.21 [159]	0.61 [159]
S2-Glass/MTM57	154.2 [70]	154.2 [70]	1.15	2.43
Vectran/MTM57	262.68 [68]	262.68	262.68	262.68



(a) (b)

Figure 7.2: (a) Trilinear law to represent tensile and compressive fibre failure (b) Bilinear law to represent tensile and compressive failure in the transverse (matrix) direction. l represent the characteristic element length [175]

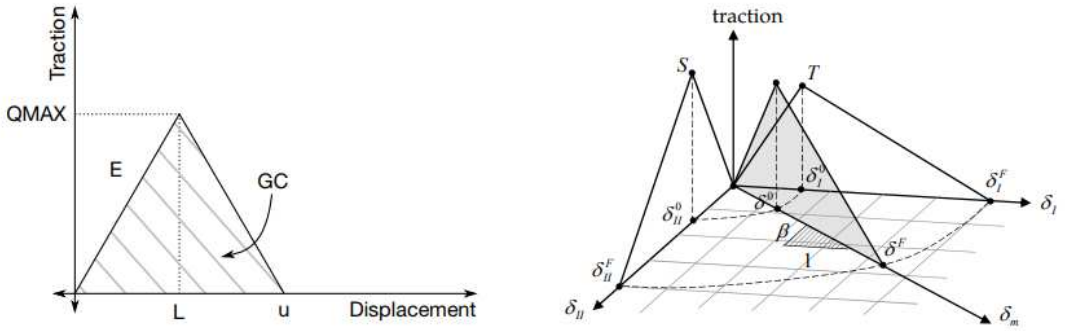
7.2.3 Cohesive algorithm

The delamination behaviour for each laminated composite used in the study was modelled using the commercially available cohesive algorithm in LS-Dyna. There are two types of cohesive algorithm commonly used to predict delamination damage by way of the Cohesive Zone Method (CZM). These are the cohesive surface and the cohesive element approach. In this study, the cohesive surface approach was utilised as no additional element was needed to model the interlaminar behaviour. The approach utilises a tiebreak contact formulation (CONTACT AUTOMATIC ONE WAY SURFACE TO SURFACE TIEBREAK: OPTION 9) to 'tie' the nodes of the part in contact using linear springs on each node. The behaviour of each spring is constituted by a bi-linear

[1]Fracture energy for tensile fibre failure, taken from a Mode I translaminar fracture toughnesss test
[2]Fracture energy for compressive fibre failure, taken from a Mode I translaminar fracture toughnesss test
[3]Fracture energy for transverse (matrix) tensile failure, taken from a Mode I interlaminar fracture toughness test
[4]Fracture energy for transverse (matrix) compressive failure, taken from a Mode II interlaminar fracture toughness test

initiation-propagation law, based on fracture mechanics. The area under the curve (Figure 7.3) represents the strain energy release rate (G_C) for Mode I and II, and β in Figure 7.3 is the 'mode-mixity' which defines the ratio of Mode I and II in a mixed-mode delamination case. Table 7.2 presents the inputs used in the cohesive algorithm.

For the interaction between the composite plate and the backplate, and the composite plate with the impactor, CONTACT AUTOMATIC SURFACE TO SURFACE type was employed. This type of contact utilises a penalty stiffness based on linear springs between the two parts. The penalty (spring) stiffness is calculated based on the bulk modulus of the two parts (composite plate and backplate).



(a) (b)

Figure 7.3: Contact algorithm for interlaminar properties (a) Bi-linear initiation-propagation law (b) Mixed-mode I and II iinitiation-propagation law [175]

Table 7.2: Inputs for delamination prediction

Input type	IM7/8552	S2-Glass/MTM57	Vectran/MTM57
Peak traction, normal (MPa)	60	60	60
Peak traction, shear (MPa)	120	120	120
G_{Ic} (kJ/m^2)	0.21	1.15	1.41
G_{IIc} (kJ/m^2)	0.61	2.43	2.41

7.2.4 Mesh sensitivity study

Although both MAT 262 and UMAT utilises the smeared crack formulation to alleviate mesh dependency, careful selection of mesh sizes must be made to ensure the convergence of results. This is due to the mesh dependency on the volume of damaged material, which is a common problem with many FE formulations [95]. For this, a mesh sensitivity study

was performed on the two material models used in this study.

First, results from the mesh sensitivity study for UMAT is discussed. Figure 7.4 and Figure 7.5 presents the load-time and load-deflection histories, respectively, for Vectran/MTM57 under 40 J of LVI loading using three different mesh sizes. Results from the FE predictions were observed to converge as the mesh was further refined, resulting in a closer agreement with the experimental results. This is similar to the load-displacement response, where it can be observed that the irreversible strain was larger (closer to the experimental result), with a decrease in mesh size. Note the difference between the FE predictions on the impactor deflection and the experimental results. This will be discussed in subsection 7.3.1.

Secondly, the results for MAT262 are considered. Figures 7.6 and 7.13 presents the load-time and load-deflection histories, respectively, for IM7/8552 under 40 J of LVI loading using three different mesh sizes. It can be observed that a considerable difference in the load-time and load-deflection response was indicated with a change in mesh size. Whilst the initial (elastic) response was nearly identical between all three mesh sizes, results tend to diverge as the mesh size increases.

Further FEM analysis using MAT262 employed a mesh size of 1 mm since the results are the most comparable when compared to the experimental observations. Also, the computational cost is not as excessive (approximately 4 hours of running time on a local PC for each analysis), which is a critical aspect in a FEM analysis.

Mesh biasing was not applied since the characteristic element length, l_c, was manually entered in the model before the analysis. Therefore, the same l_c may not be applicable for the different mesh sizes due to biasing. Hence, it is desirable to use a uniform mesh size throughout the analysis.

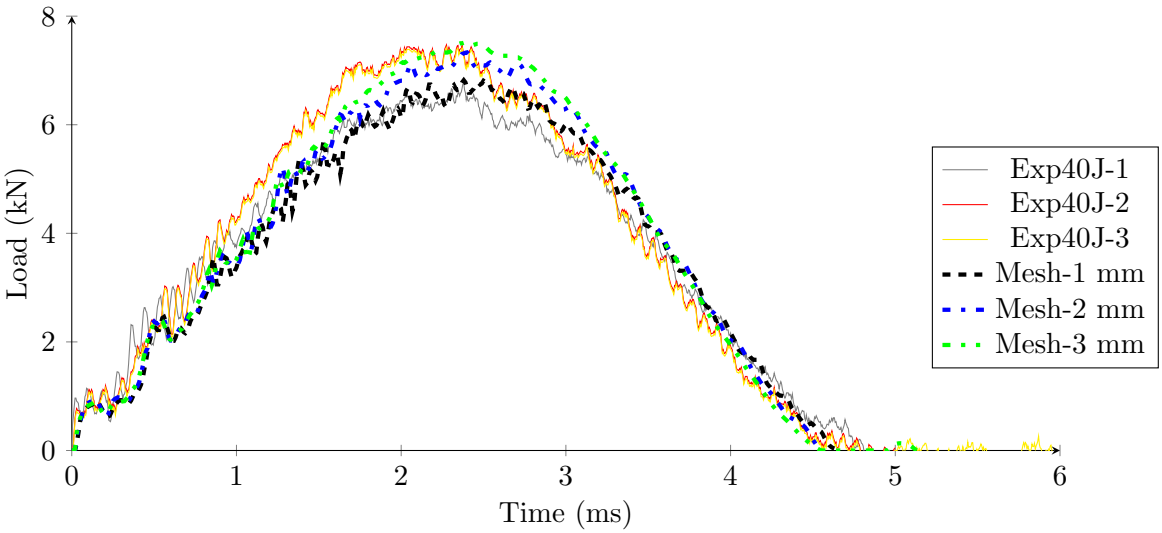


Figure 7.4: Load-time curve for 40 J impact loading of Vectran/MTM57 using three different mesh sizes

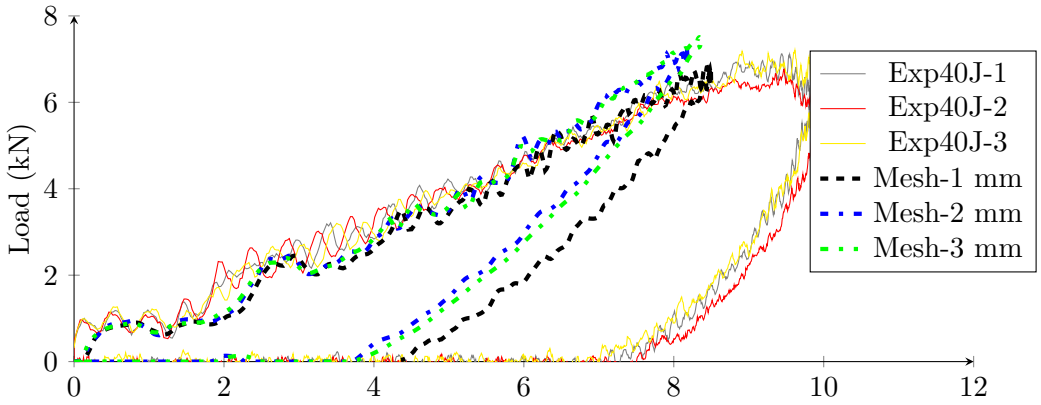


Figure 7.5: Load-deflection response for 40 J impact loading of Vectran/MTM57 using three different mesh sizes

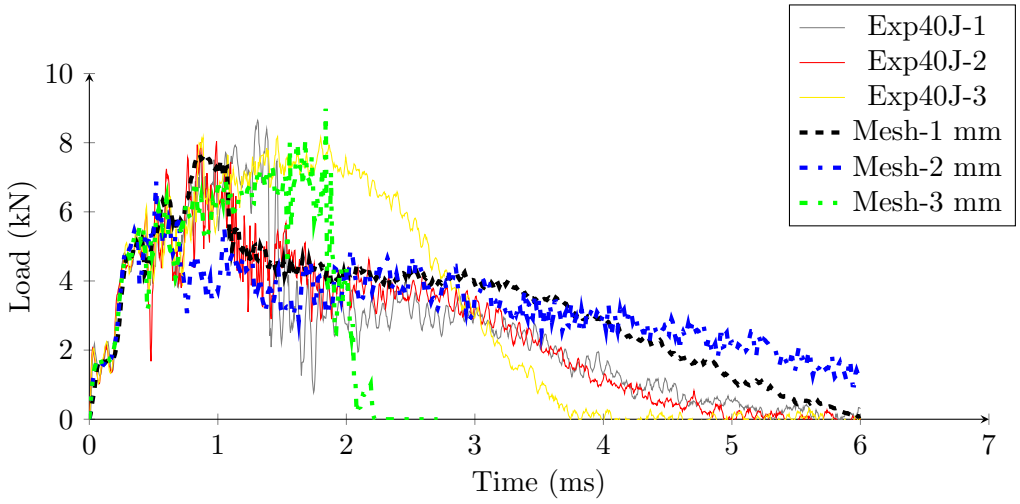


Figure 7.6: Load-time response for 40 J impact loading of IM7/8552 using three different mesh sizes

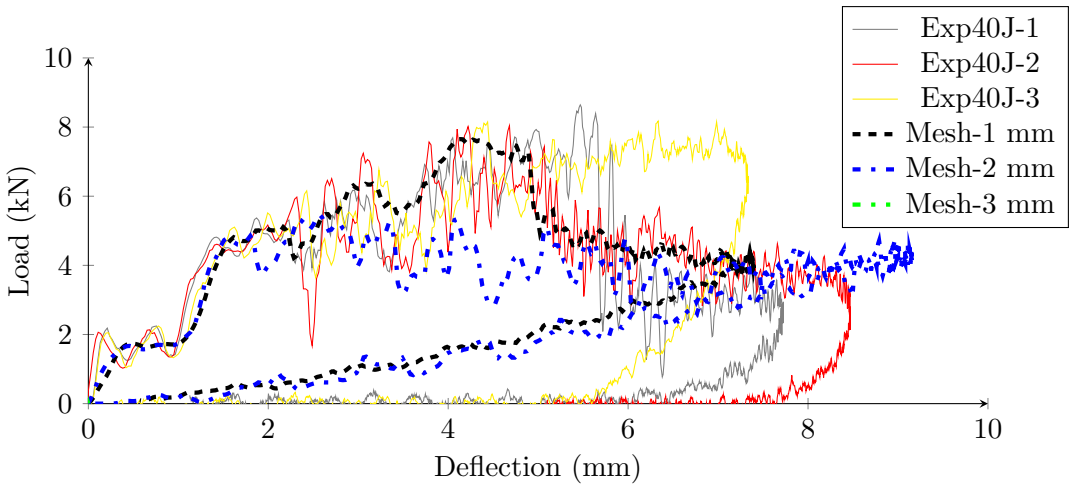


Figure 7.7: Load-deflection response for 40J impact loading of IM7/8552 using three different mesh sizes

7.2.5 Delamination sensitivity analysis

While the objective in performing a mesh sensitivity study is clear, it is also important to investigate the effects of the cohesive algorithm in the FE model. In the current FE analysis, the model was discretised into four separate layers, each representing a specific number of plies with respect to the experimental laminate. Each ply is represented by a through-thickness integration point, with the orientation adjusted according to the ply orientation. Three cohesive surfaces were placed in between the four layers, Figure 7.8, with each layer having two cohesive surface segments to represent the 'master' and 'slave' surface.

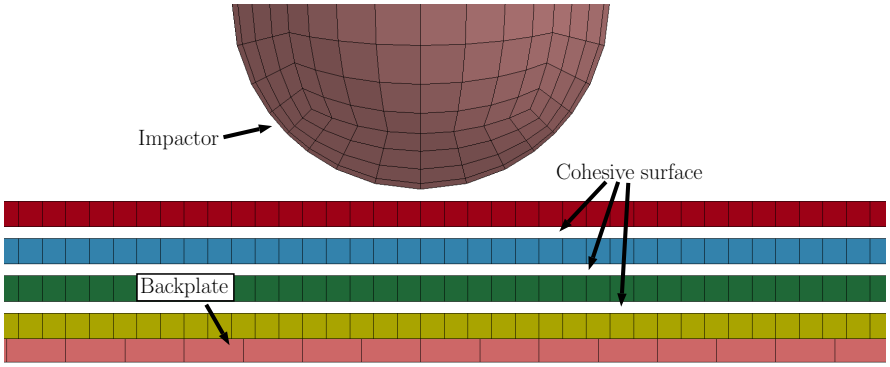


Figure 7.8: Side view of the FE model. Note that the distance between each layers are slightly increased to illustrate the placement of each cohesive surface

While the post-damage oscillations can be seen to reduce with an increase in the

number of cohesive layers used in the model, no significant difference can be observed in the load-time response, Figure 7.9. This is also shown by the contour of FE delamination prediction, Figure 7.10, exhibiting no considerable difference with respect to the number of cohesive layers. More importantly, this highlights that under LVI loading, delamination damage is not the primary source of energy absorption, partly due to the enhanced interlaminar properties of Vectran/MTM57 laminate, consistent with the experimental observation.

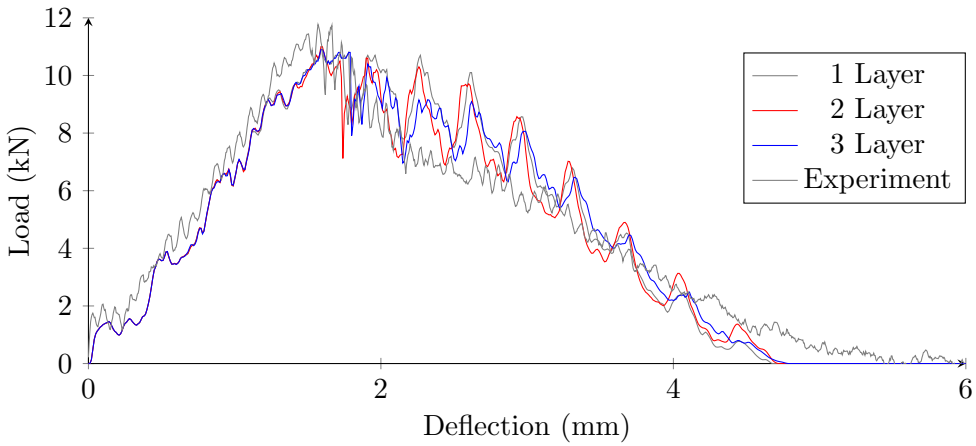


Figure 7.9: Load-time response for 100 J impact loading of Vectran/MTM57 with varying layer of cohesive surface

However, the use of three cohesive surface resulted in a greater dispersion of energy from delamination damage. This is shown in Figure 7.11, where each layer is seen to have delaminated. Moreover, while the influence of delamination may not be significant under LVI, substantial delamination damage can be seen under HVI impact. Therefore, the use of three cohesive layers in HVI modelling may be beneficial due to the greater energy absorption, hence predicting a more accurate result.

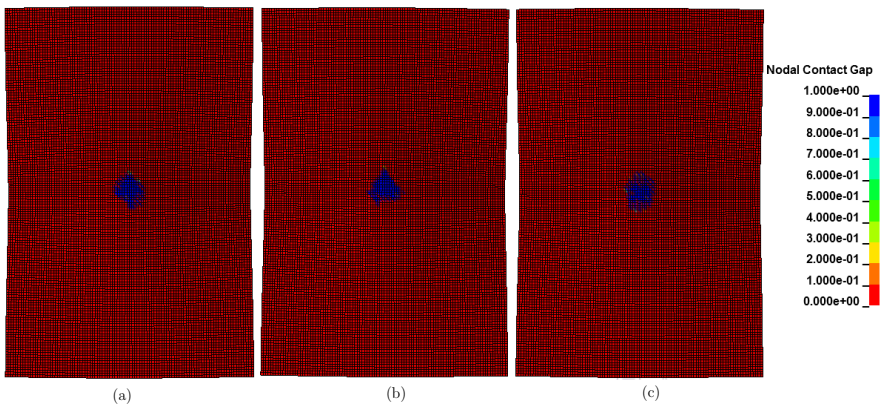


Figure 7.10: FEM prediction on the delamination damage under 100 J loading at the middle layer (a) One cohesive layer (b) Two cohesive layer (c) Three cohesive layer

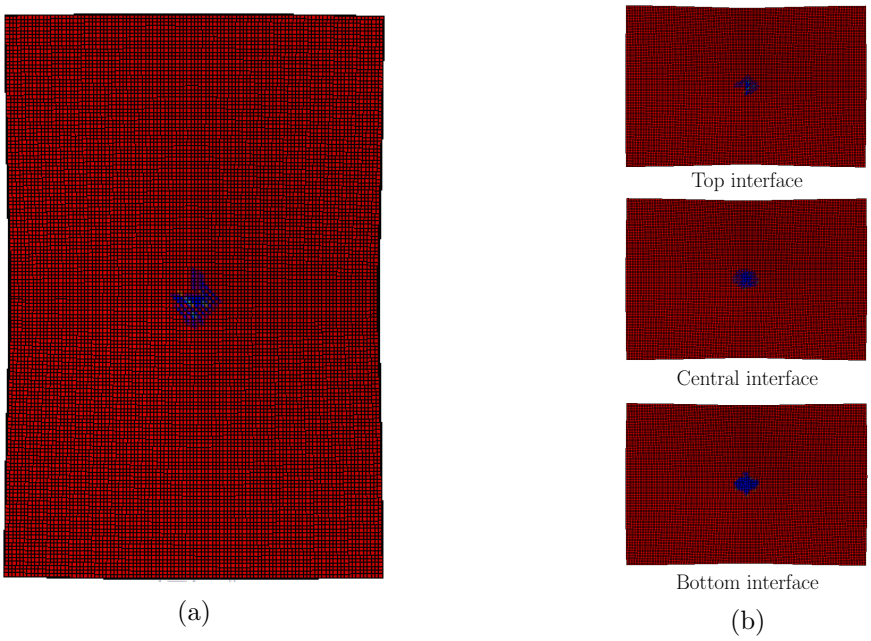


Figure 7.11: FEM prediction of delamination under 100 J LVI loading using three cohesive surfaces (a) Average envelope (b) Individual interface

7.3 Results

7.3.1 Low velocity impact

IM7/8552

In general, all the FEM predictions under all three energy levels (40 J, 100 J, and 160 J) displayed a good correlation with the experimental results. However, a number of issues were found during the FE analyses. First, MAT262 does not consider any definition

of residual strain in the material formulation, hence resulting in an unloading curve returning to the origin upon load removal. This can be seen in the 40 J impact case, where the load-displacement response, Figure 7.13, unloads to the origin towards the end of the simulation.

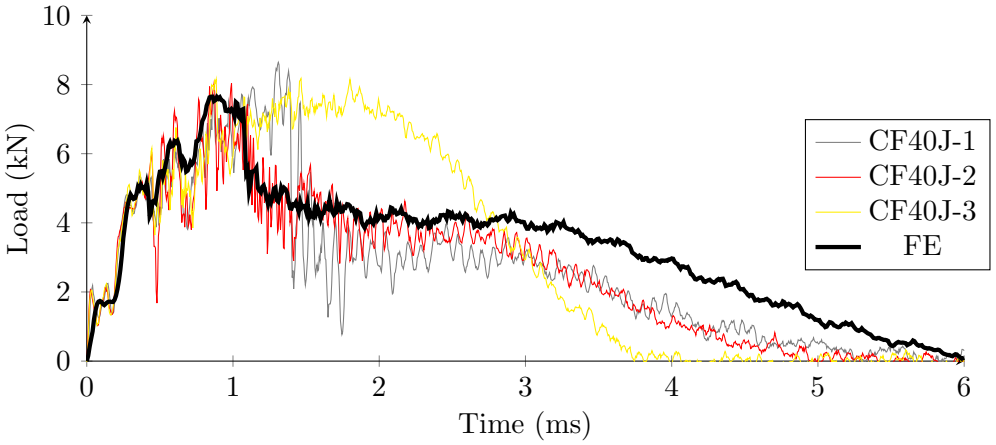


Figure 7.12: FEM prediction of the load-time response for 40 J impact loading on IM7/8552 and compared with three experimental results

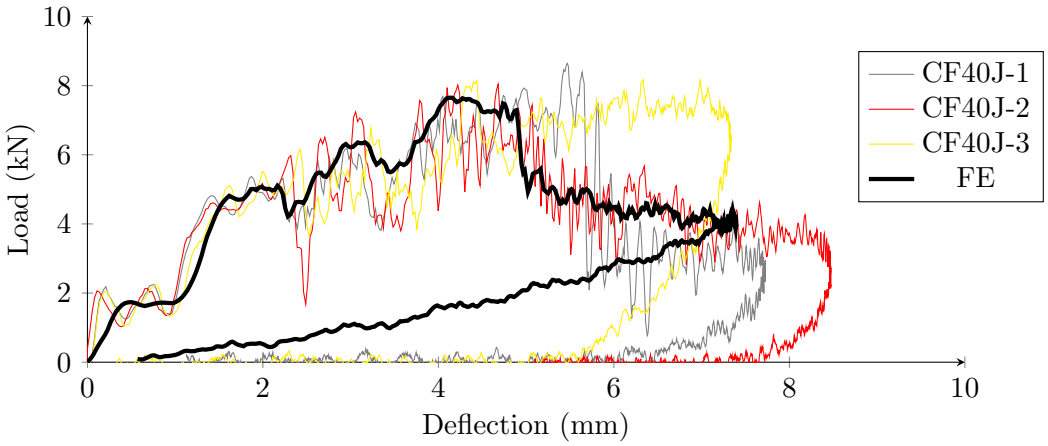


Figure 7.13: FEM prediction of the load-deflection response for 40 J impact loading on IM7/8552 and compared with three experimental results

Large oscillations can also be observed in the experimental load-time and load-displacement histories under all energy levels. These oscillations were thought to be due to the natural frequency of the impactor, in addition to other external forces such as vibrations from the LVI rig. These effects were not included in the FE model, which may result in the relatively smooth response observed in the FEM predicted load-time and load-deflection histories.

Under the 100 J and 160 J energy levels, a better correlation can be observed between the FEM model and the experimental results, shown in Figures 7.19 to 7.17. This is largely due to the fact that in both cases, complete penetration has occured. Examination of the predicted delaminations indicate the FE prediction slightly underestimating the experimental results by approximately 20%. This is thought to be due to the bi-linear formulation of the cohesive algorithm, which may be too simplistic and does not explicitly consider the failure mechanism under interlaminar failures, such as the fibre-bridging effect. In spite of this, the typical rhombus shape normally observed for UD cross-ply laminates under impact loading was well predicted by the FEM model at each impact energy level, shown in Figures 7.18c, 7.19c, and 7.20c, for 40 J, 100 J, and 160 J LVI energies, respectively.

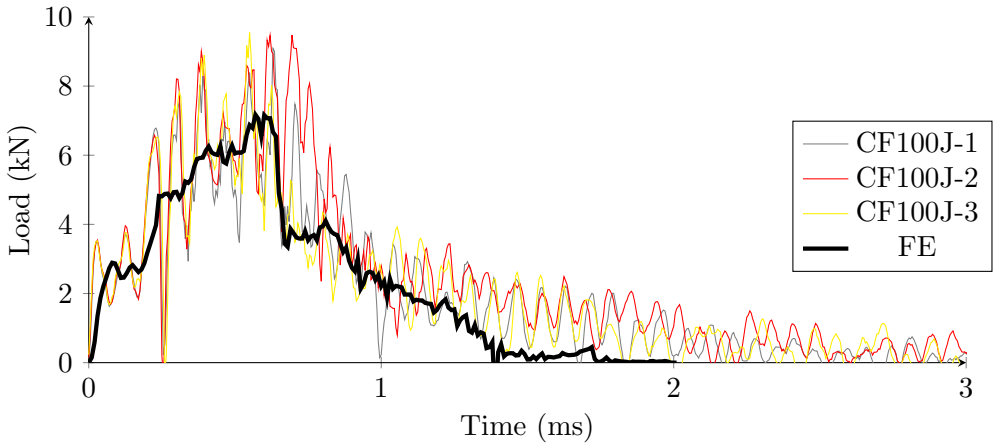


Figure 7.14: FEM prediction of the load-time response for 100 J impact loading on IM7/8552 and compared with three experimental results

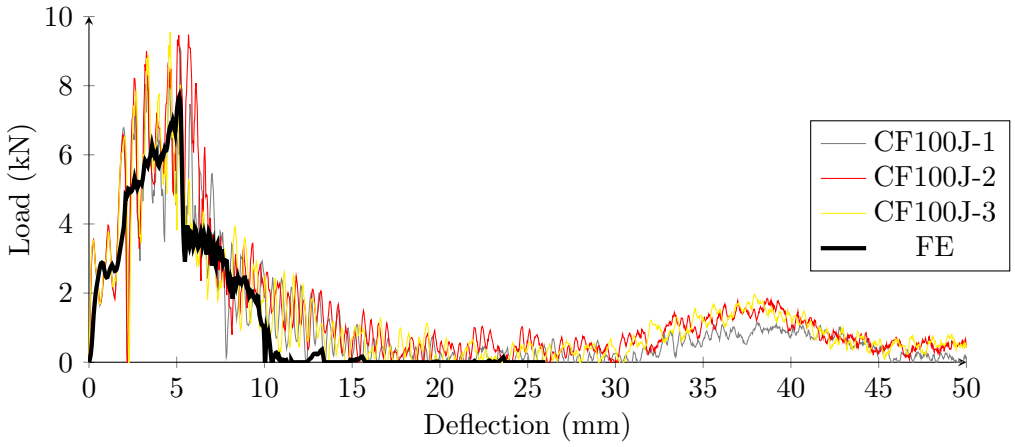


Figure 7.15: FEM prediction of the load-deflection response for 100 J impact loading on IM7/8552 and compared with three experimental results

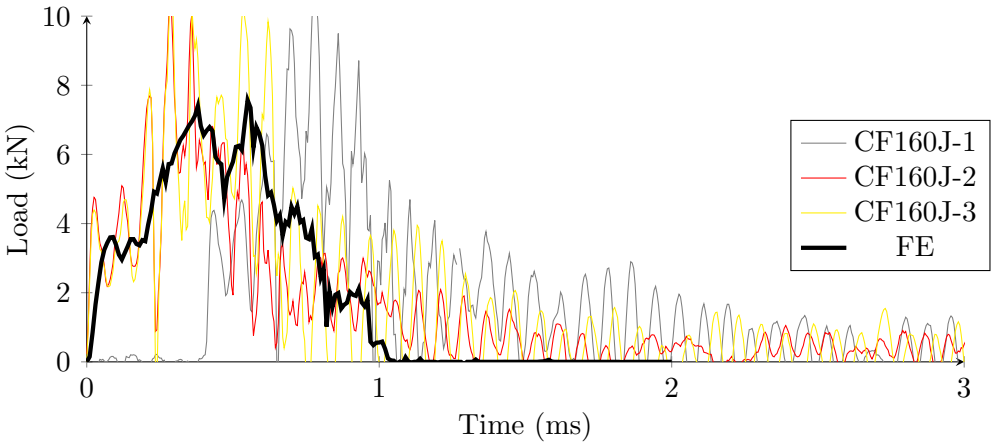


Figure 7.16: FEM prediction of the load-time response for 160J impact loading on IM7/8552 and compared with three experimental results

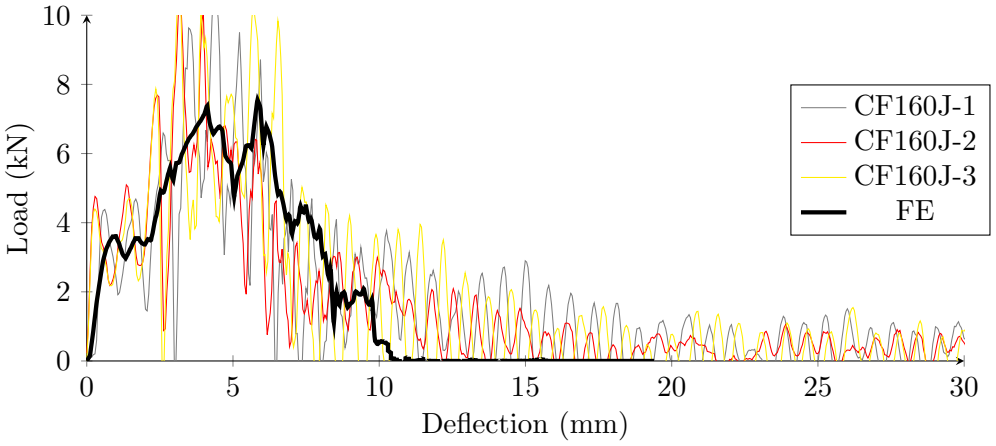
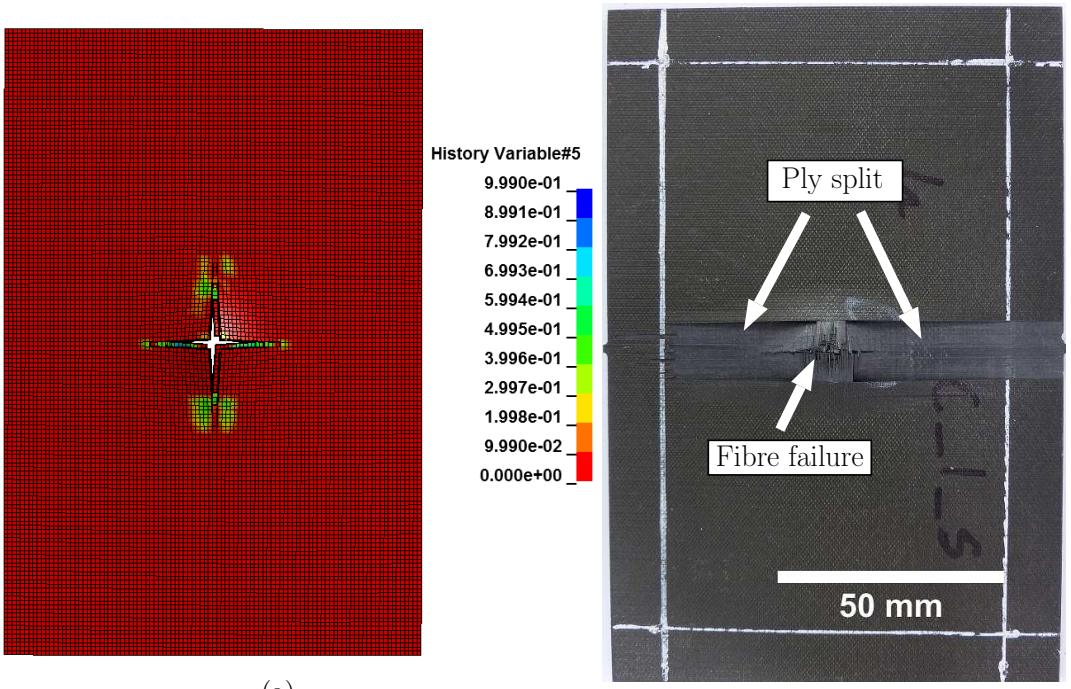
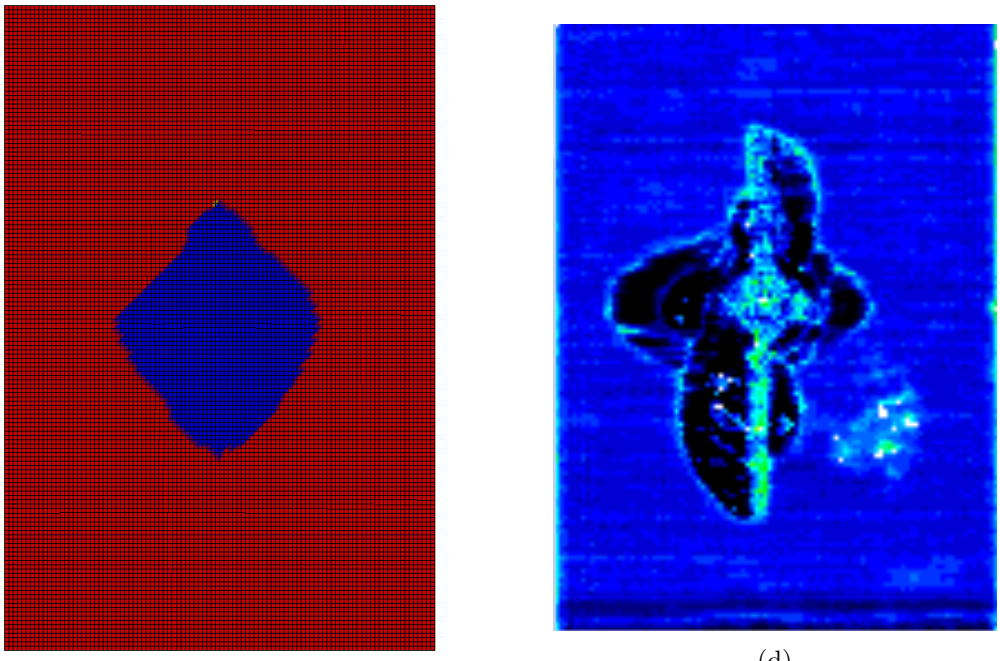


Figure 7.17: FEM prediction of the load-deflection response for 160J impact loading on IM7/8552 and compared with three experimental results

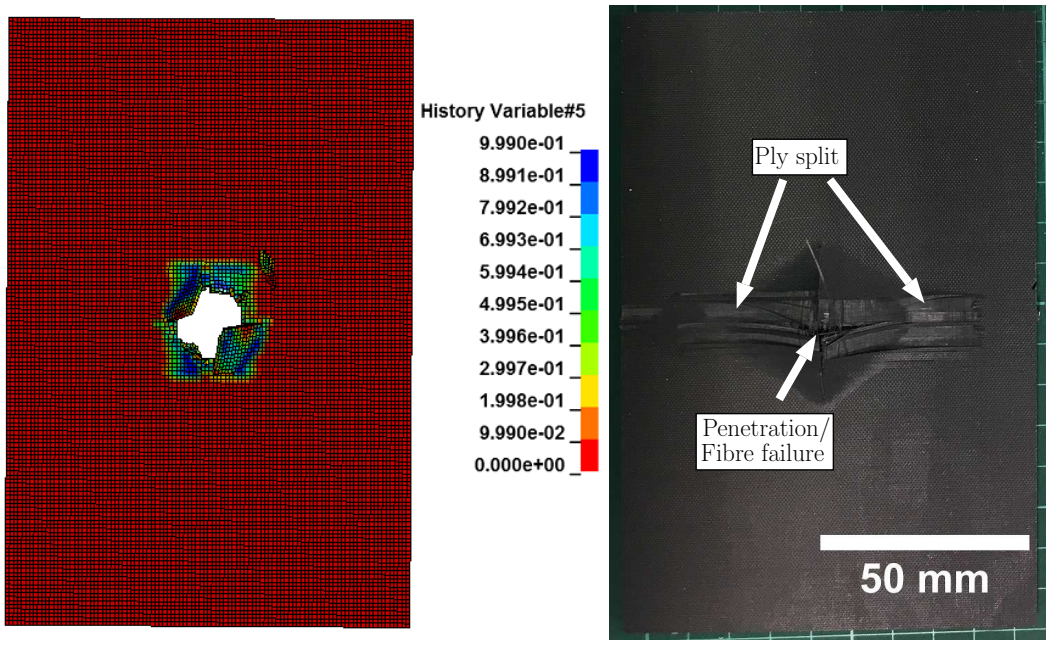


(a) (b)

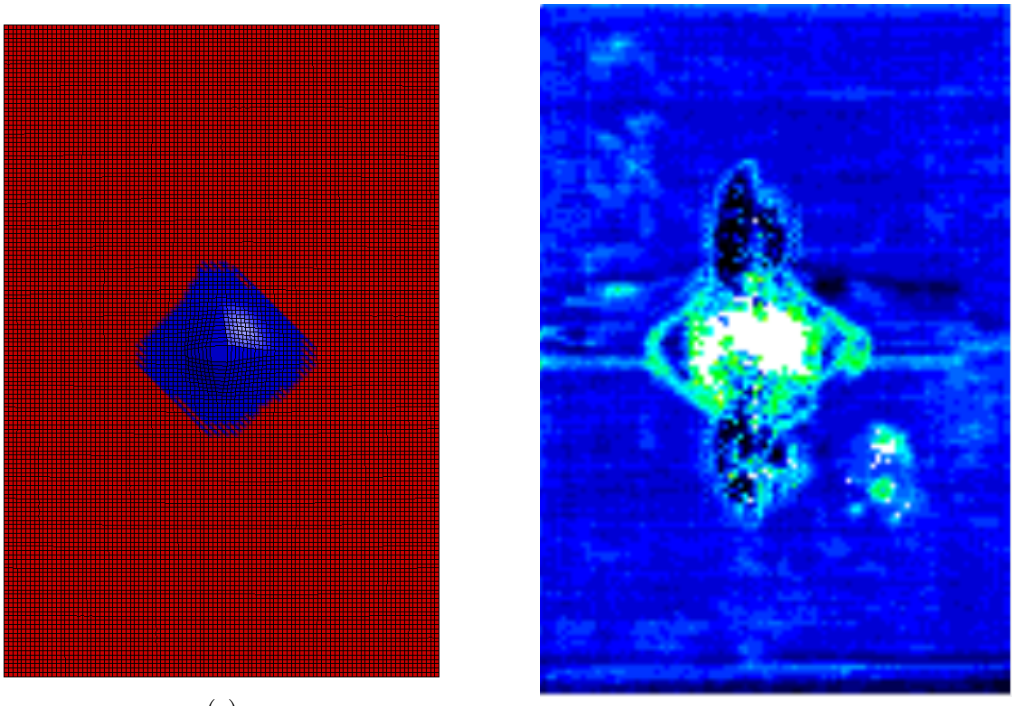


(c) (d)

Figure 7.18: Comparison of experimental and simulation results for 40 J impact load on IM7/8552 (a) FEM prediction of damage on the laminate back face. Contours showing the damage associated with tensile fibre failure (b) Experimental back face damage (c) FEM prediction on delamination damage (d) C-scan results

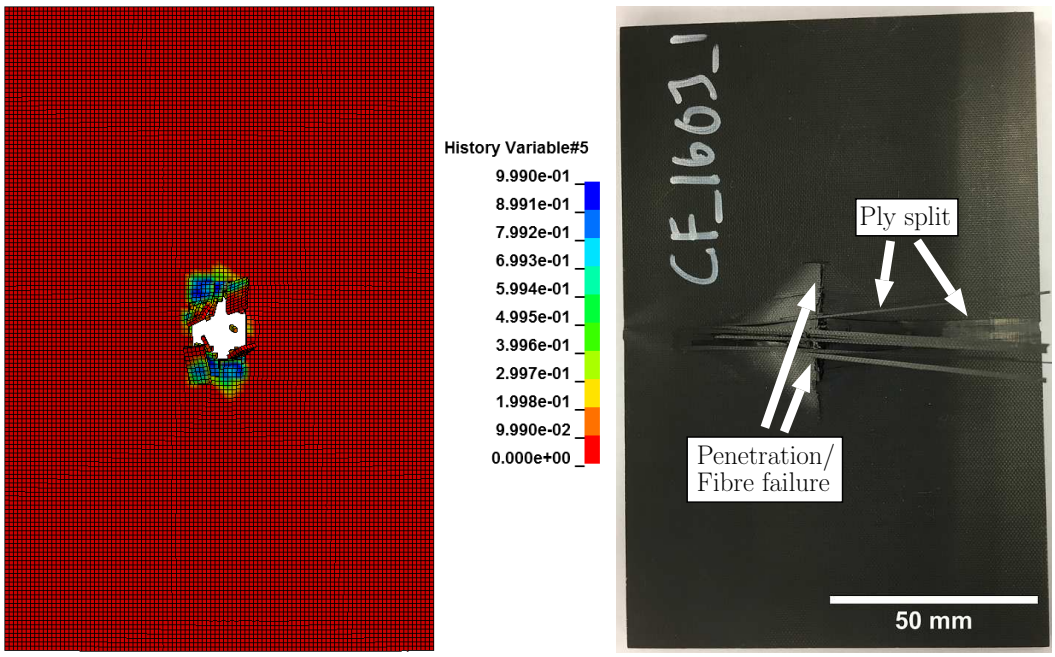


(a) (b)

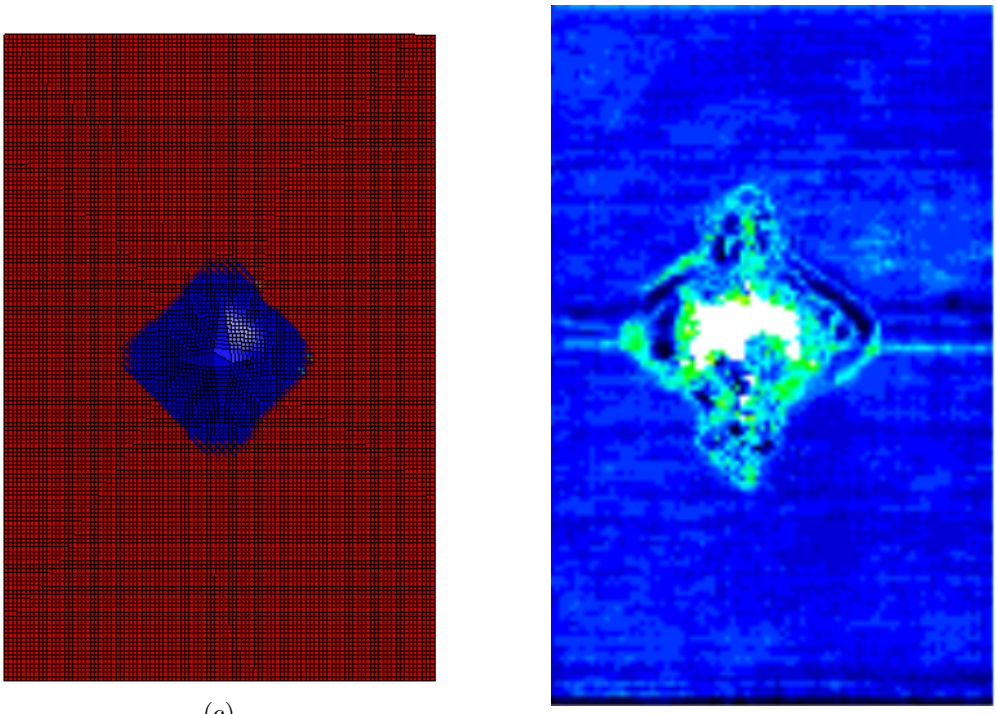


(c) (d)

Figure 7.19: Comparison of experimental and simulation results for 100 J impact load on IM7/8552 (a) FEM prediction of damage on the laminate back face. Contours showing the damage associated with tensile fibre failure (b) Experimental back face damage (c) FEM prediction on delamination damage (d) C-scan results



(a) (b)



(c) (d)

Figure 7.20: Comparison of experimental and simulation results for 160J impact load on IM7/8552 (a) FEM prediction of damage on the laminate back face. Contours showing the damage associated with tensile fibre failure (b) Experimental back face damage (c) FEM prediction on delamination damage (d) C-scan results

S2-Glass/MTM57

There were several issues identified during the numerical modelling of S2-Glass/MTM57 composites. First, although the load-time history under 40 J of LVI loading is in good agreement with the experimental results, Figure7.21, a significant underestimation was observed in the load-deflection history, Figure 7.22. This is largely due to the absence of a permanent strain definition in the formulation of MAT 262 (such as the β term in the developed UMAT), particulary in the tensile and compressive failure modes. Secondly, it should be noted that in the case of S2-Glass/MTM57, the experimentally measured material properties were converted to UD architecture (from NCF composite) using Classical Lamination Theory (CLT) since the formulation established in MAT262 was developed for UD architecture only, thus adding more difficulty in correlating the FEM model with the experimental results.

Under 40 J of impact energy, it was found that the FEM model underestimated the impactor travel (deflection) by approximately 1 mm (measured from the load-deflection response, Figure 7.22, resulting in significant underestimation in terms of the impact energy absorption. For the 100 J of energy level, the FEM prediction resulted in a premature failure, resulting in a sharp load drop at approximately 11 kN of load. This is in contrast with the experimental observations, where failure is observed to occur at approximately 12 kN of load. Furthermore, the experimental observation showed a short 'plateau' region (denoted by point 'R' in Figures 7.23, 7.25 and 7.26) after the load drop, signifying a further energy absorption from the laminate. This is similar to the 160 J of impact energy level, although in this case, the peak load is accurately predicted by the FEM model. The resistance to penetration may be attributed to the NCF architecture which is not explicitly accounted for in the FEM model.

Concerning delamination, it was found that the FEM model predicted no delamination damage has occured in the laminate (shown in Figures 7.27 to), mainly due to the high interlaminar properties of S2-Glass/MTM57 (G_{Ic} and G_{IIc}) used in the numerical model. However, it was found that little to no delamination damage can be observed in the experimental results, due to the enhancement of the NCF architecture.

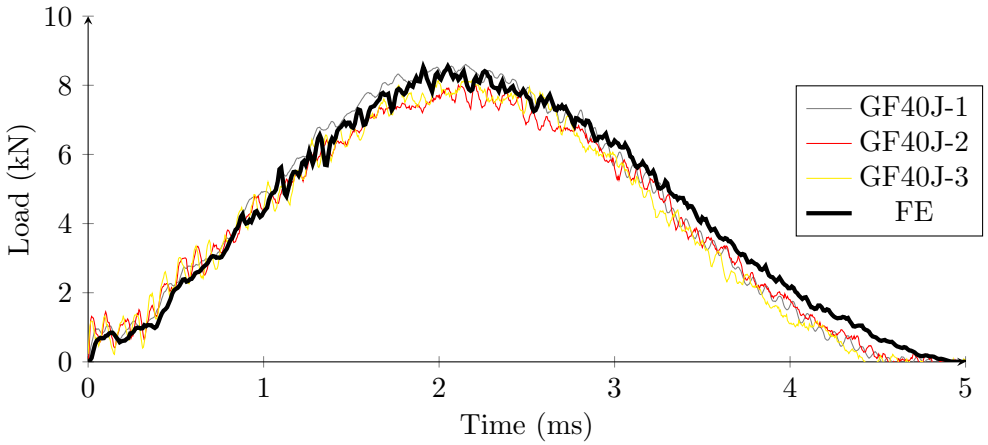


Figure 7.21: FEM prediction of the load-time response for 40 J impact loading on S2-Glass/MTM57 and compared with three experimental results

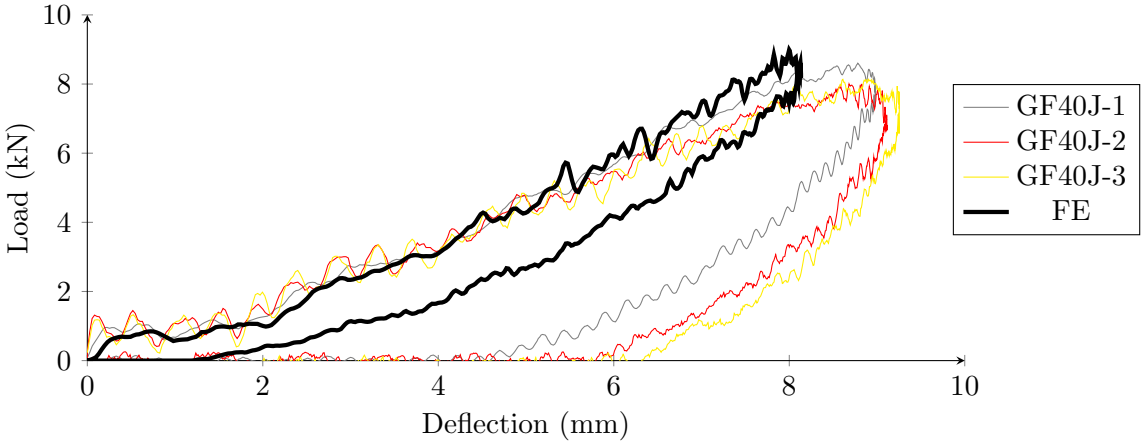


Figure 7.22: FEM prediction of the load-deflection response for 40 J impact loading on S2-Glass/MTM57 and compared with three experimental results

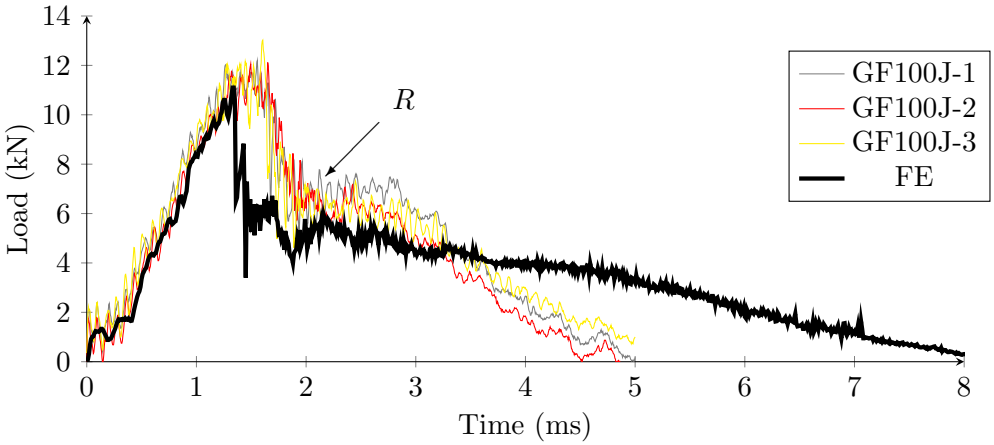


Figure 7.23: FEM prediction of the load-time response for 100 J impact loading on S2-Glass/MTM57 and compared with three experimental results

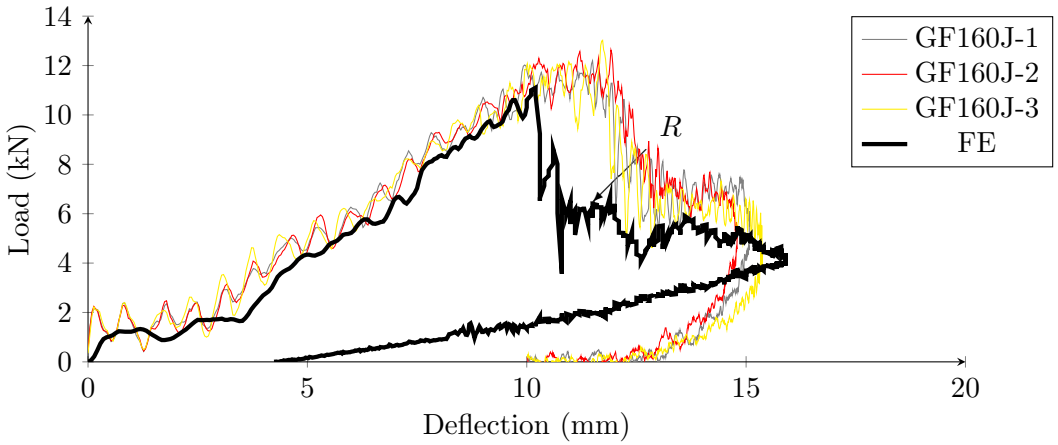


Figure 7.24: FEM prediction of the load-deflection response for 100 J impact loading on S2-Glass/MTM57 and compared with three experimental results

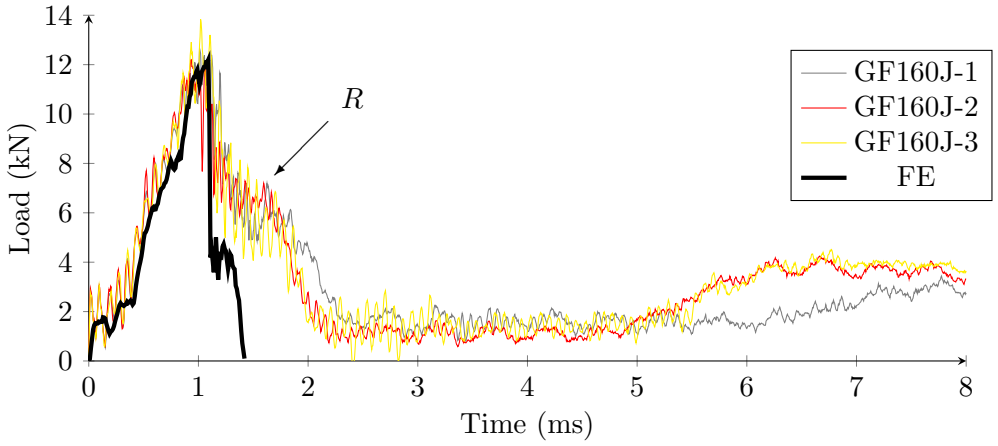


Figure 7.25: FEM prediction of the load-time response for 160J impact loading on S2-Glass/MTM57 and compared with three experimental results

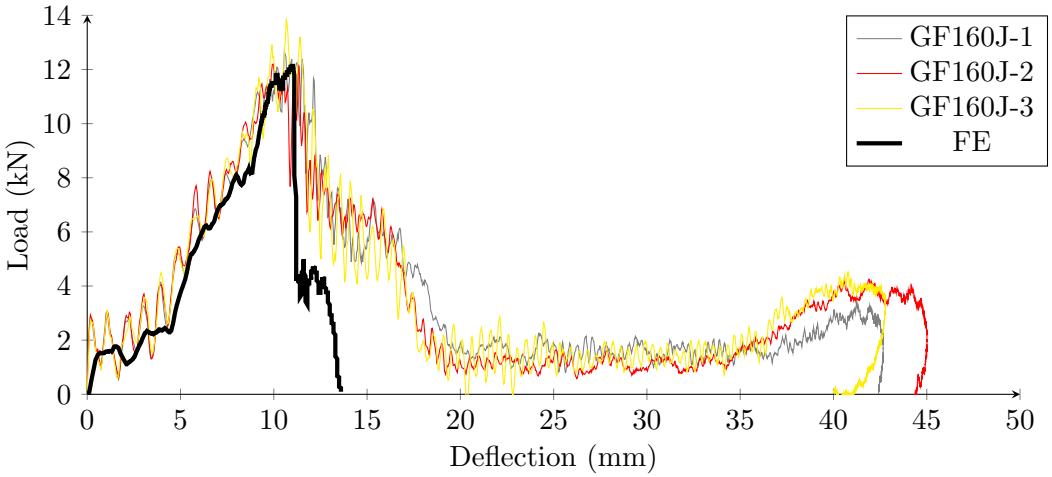


Figure 7.26: FEM prediction of the load-deflection response for 160J impact loading on S2-Glass/MTM57 and compared with three experimental results

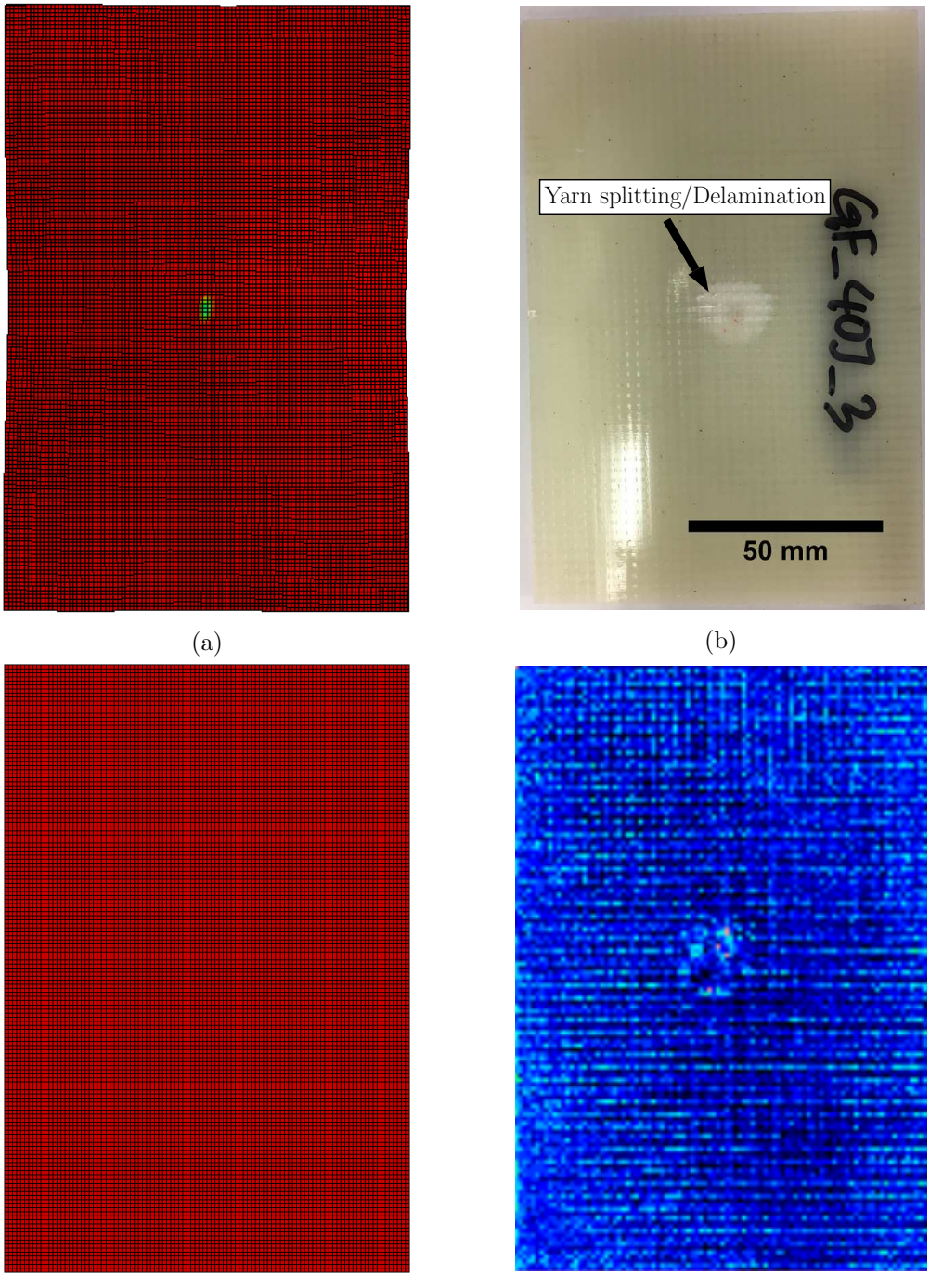


Figure 7.27: Comparison of the simulation and experimental results for 40 J impact load on S2-Glass/MTM57 (a) FEM prediction of damage on the laminate back face (b) Experimental back face damage (c) FEM prediction on delamination damage (d) C-scan results

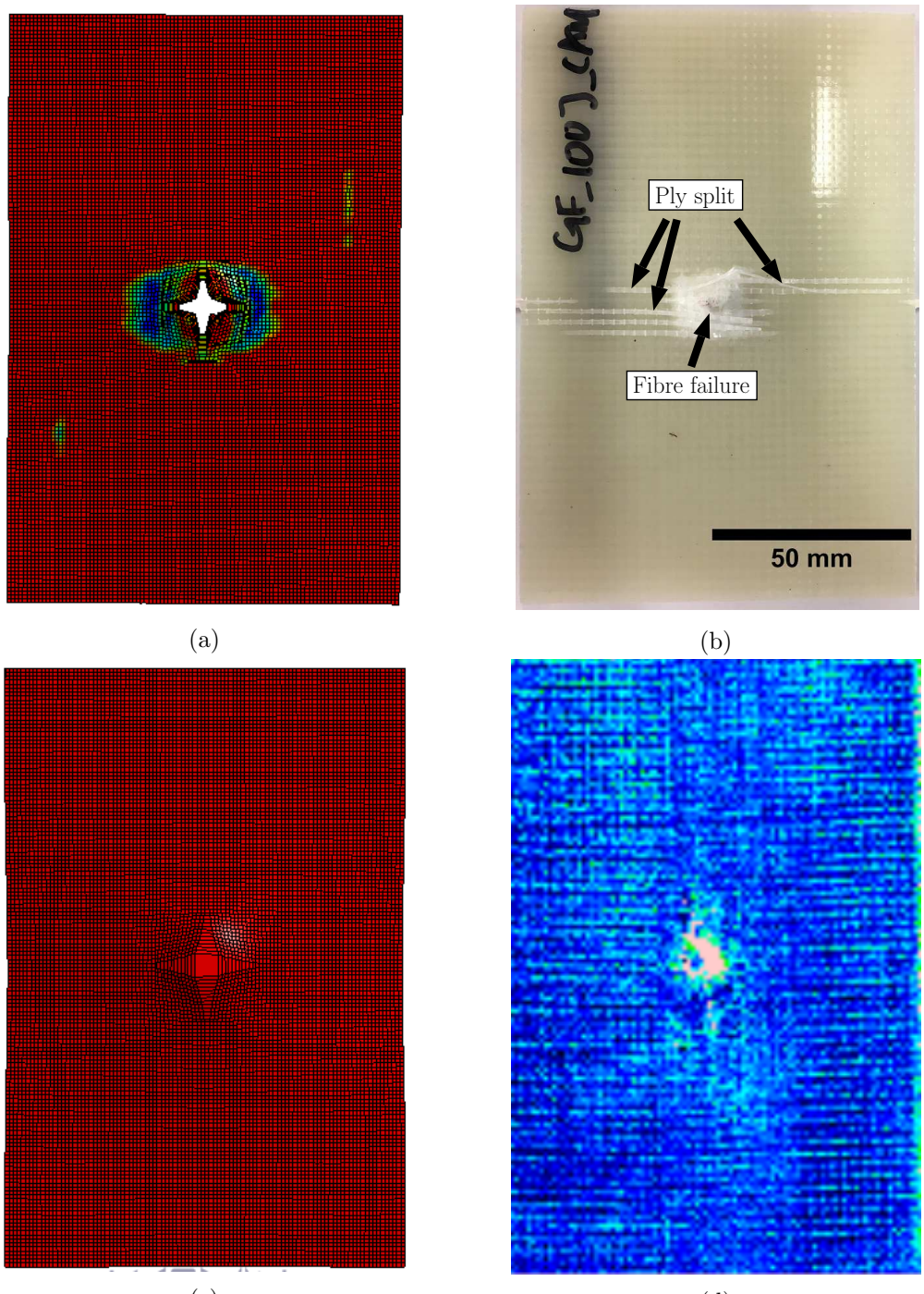


Figure 7.28: Comparison of the simulation and experimental results for 100 J impact load on S2-Glass/MTM57 (a) FEM prediction of damage on the laminate back face (b) Experimental back face damage (c) FEM prediction on delamination damage (d) C-scan results

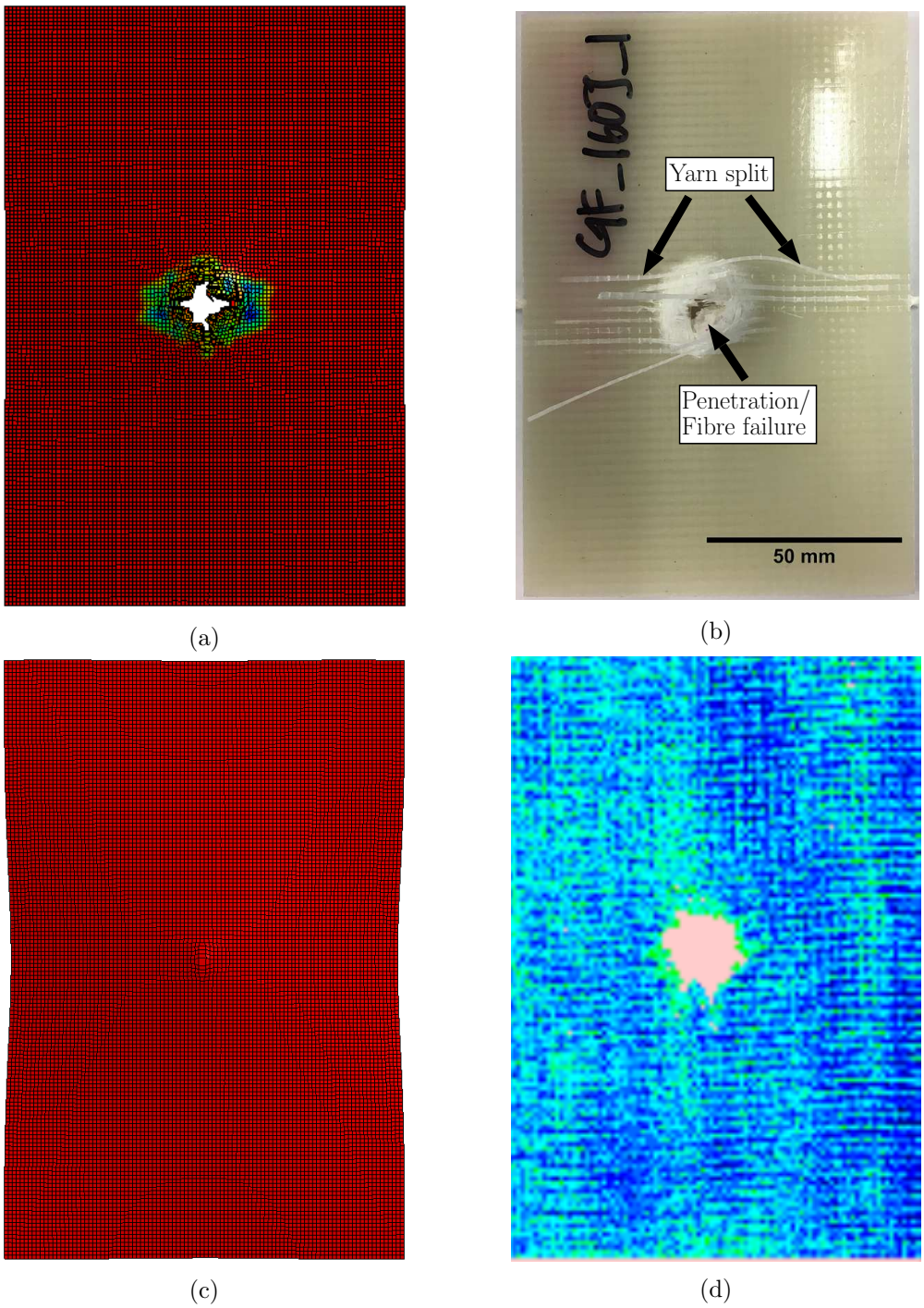


Figure 7.29: Comparison of the simulation and experimental results for 160J impact load on S2-Glass/MTM57 (a) FEM prediction of damage on the laminate back face (b) Experimental back face damage (c) FEM prediction on delamination damage (d) C-scan results

Vectran/MTM57

The load-time and load-deflection histories are presented in Figures 7.30 and 7.31, respectively for Vectran/MTM57 laminates under a 40 J impact load. The predicted load-time response, correlates well with the experimental results, although a slight overestimation on the peak load can be observed. An underestimation of the permanent through-thickness deformation can be seen in the load-deflection history, shown in Figure 7.31, by approximately 2-3 mm, hence leading to an underestimation of the energy absorbed by the FEM model in the 40 J impact event.

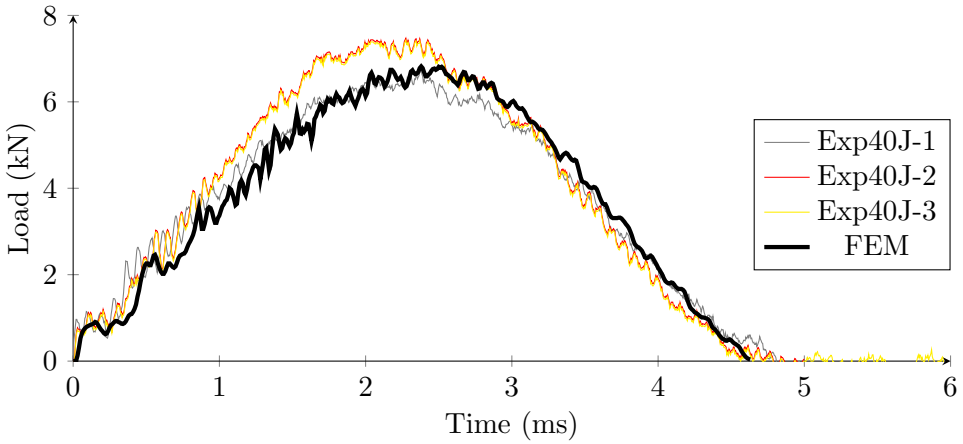


Figure 7.30: FEM prediction of the load-time response for 40 J impact loading on Vectran/MTM57 and compared with three experimental results

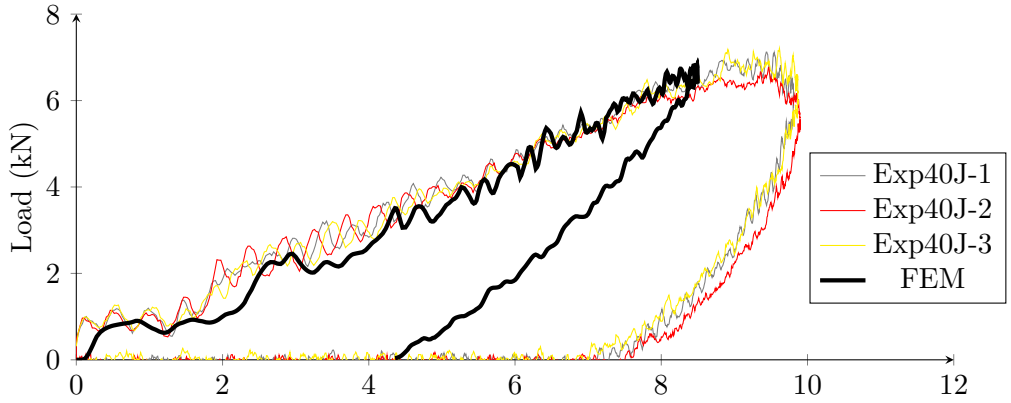
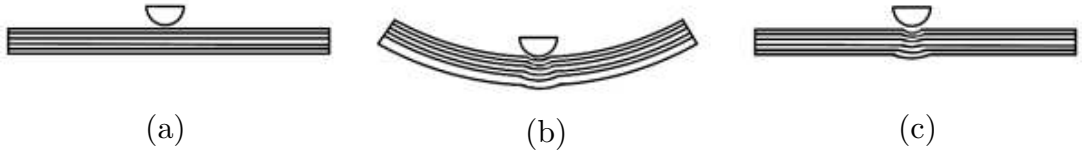


Figure 7.31: FEM prediction of the load-deflection response for 40 J impact loading on Vectran/MTM57 and compared with three experimental results

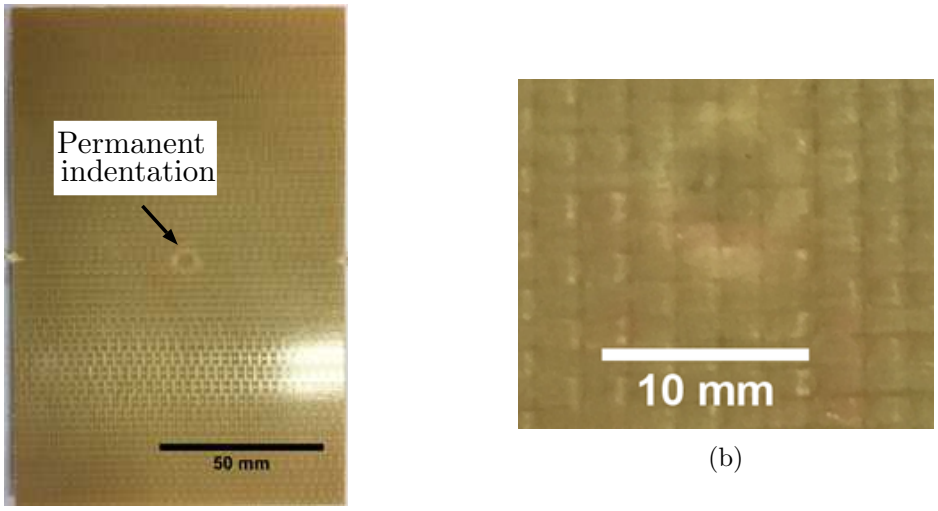
This may be due to a number of reasons. First, it is observed that the experimental laminate experiences a local indentation, in addition to a global flexural response of the laminate. This is diagrammatically shown in Figure 7.32, in which at the apex of

the impact event, local deflection (indentation) allows the laminate to deform further, hence enabling the impactor to further travel downwards with respect to the laminate. This mechanism often results in an observable permanent indentation, which is visible in the impacted specimens, as discussed in subsection 5.4.1. This effect is even more pronounced at higher impact energies, if full penetration does not occur. It can be clearly seen in Figure 7.33 that a circular white 'ring' is present on the laminate front face, due to a localised tensile straining upon impact.



(a) (b) (c)

Figure 7.32: Impact response mechanism of Vectran/MTM57 laminates under low velocity impact loads (a) Before impact (b) During impact (c) After impact



(a) (b)

Figure 7.33: Front face of Vectran/MTM57 after 40 J impact loading (a) Experimental front face damage (b) Close-up view of the permanent indentation

The highly localised damage seen in Figure 7.33 may also be influenced by Vectran's fabric architecture, where the stitches present in the fabric promote localised through-thickness damage, resisting further delamination damage throughout the laminate [210]. This effect is more pronounced on polymer fibres with poor compressive properties (such

as Dyneema and Vectran), in which significant permanent indentation can be observed on the laminate after impact [63].

Second, the inherent nature of the shell element often results in an insufficient prediction of the surface indentation behaviour [110] due to the zero-stress through-thickness assumption. While the β term was included to define the irreversible strain, the localized deformation observed may be due to the high dominance of through-thickness shear, which is not accounted for in the current formulation, due to the plane-stress assumptions. Third, transverse compression properties of Vectran fibres are also suggested to exhibit some form of irreversible deformation, owing to its fibrillar structure [201, 202]. In addition, the nature of polymeric epoxy resins often displays some form of plastic deformation [151], further promoting permanent indentation in the laminate.

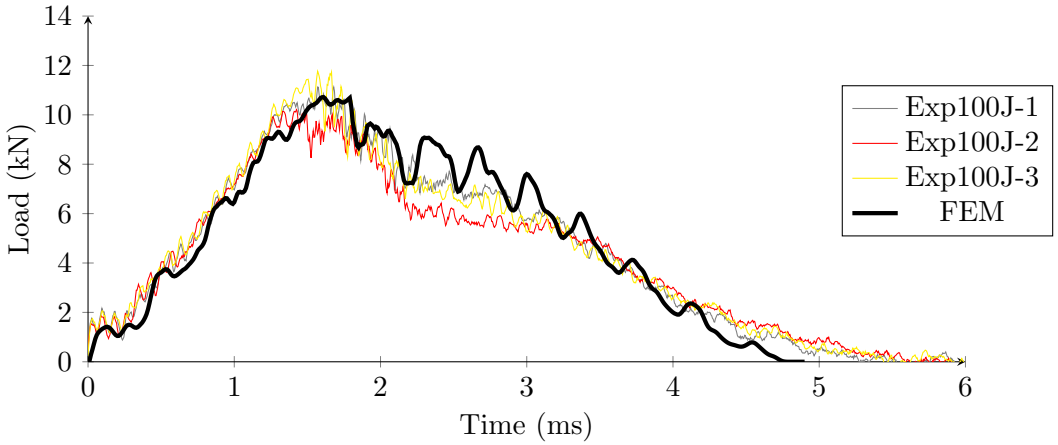


Figure 7.34: FEM prediction of the load-time curve for 100 J impact loading on Vectran/MTM57 and compared with three experimental results

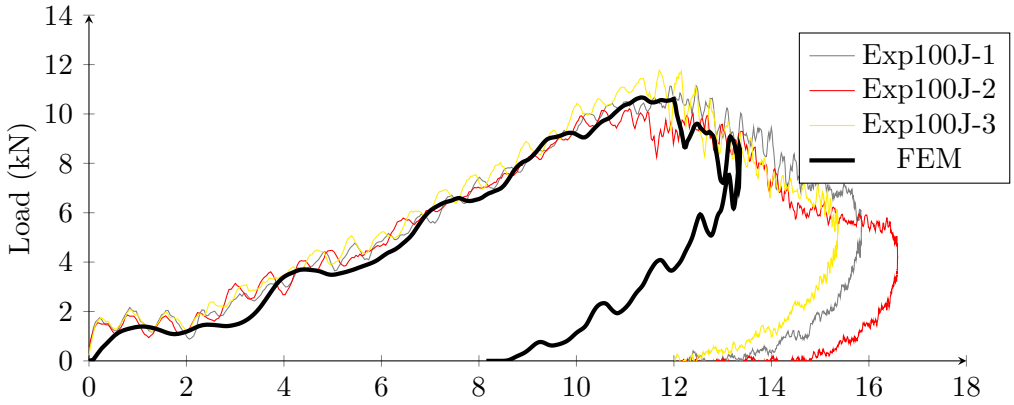


Figure 7.35: FEM prediction of the load-deflection curve for 100 J impact loading on Vectran/MTM57 and compared with three experimental results

Figures 7.34 and 7.35 presents the load-time and load-deflection histories for the 100 J LVI loading on Vectran/MTM57 laminates. While the load-time response is in a good agreement with the experimental results, Figure 7.34, a similar underestimation of the through-thickness deformation can be observed in the load-deflection history, Figure 7.35, resulting in an understimation of the energy absorption by the FEM model. As stated earlier, the underestimation in the through-thickness deformation is largely due to the influence of through-thickness stresses, particularly in shear. Thus, an explicit definition of the through-thickness stress must be included in the material formulation to capture this response.

In addition to the significant permanent indentation, some evidence of fibre failure can be observed on the rear face of the laminate, Figure 7.36a, due to the large tensile strain experienced under LVI. The FEM prediction, shown in Figure 7.36b, was also observed to predict fibre failure, in line with the experimental observation seen in Figure 7.36a.

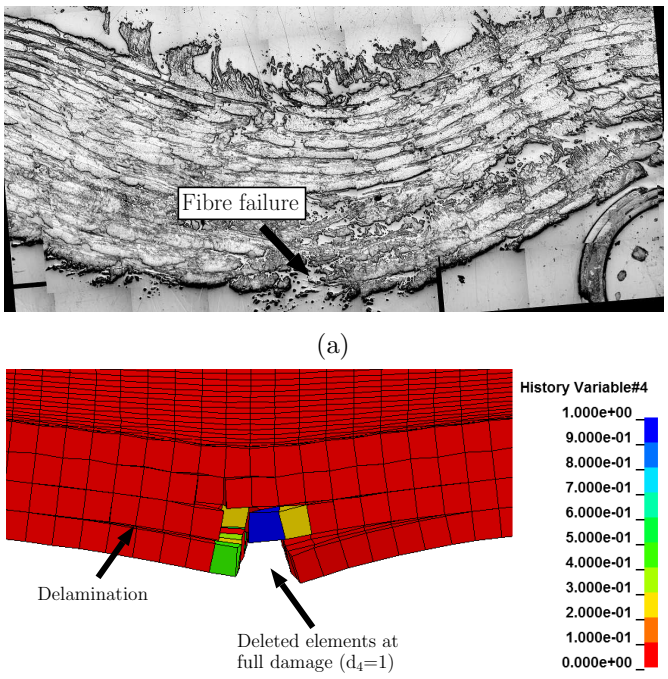
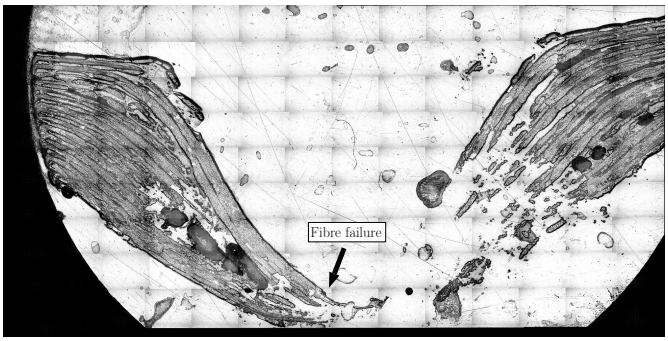
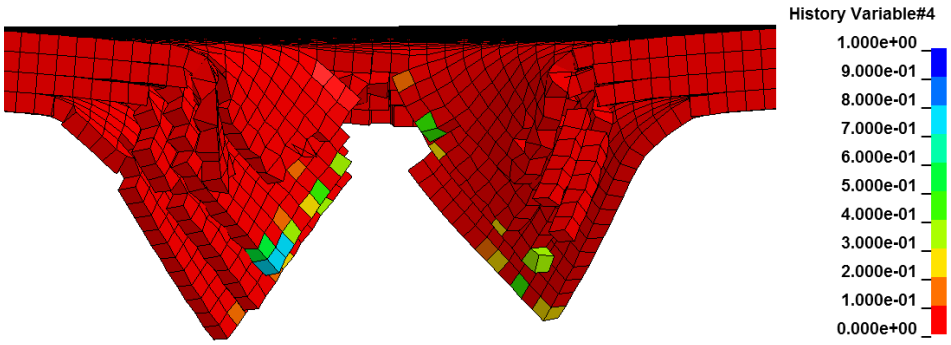


Figure 7.36: Damage observed in the Vectran/MTM57 specimen under 100 J of LVI loading (a) Optical micrograph showing fibre failure (b) Predicted failure in the FEM model including fibre failure and delamination. Contours representing fibre tensile damage

Finally, for the 160J impact case, both the load-time and load-deflection histories showed very good correlation with the experimental results. Complete penetration can be observed in both the experimental result and the FEM prediction, shown in Figure 7.37. However, the post-impact response (after penetration has occurred) was not captured in the FE model, as this was due to the friction between the impactor and the laminate after penetration has occurred, identified as 'F' in Figures 7.38 and 7.39.



(a)



(b)

Figure 7.37: Damage observed in the Vectran/MTM57 specimen under 160 J of LVI loading (a) Optical micrograph showing extensive fibre failure at every ply (b) Damage prediction from the FEM model showing complete penetration. Contours representing fibre tensile damage

An underestimation on the delamination damage can be observed in the FEM model when compared to the experimental results. Similar to the case of IM7/8552 and S2-Glass/MTM57, the simplistic bi-linear formulation does not account for specific toughening mechanisms in delamination behaviour, particularly fibre-bridging effects, which is highly dominant in Vectran/MTM57 composites. Figures 7.40 to 7.42 presents the delamination prediction by the FEM model, as well as the experimentally observed de-

lamination damage. Also shown in Figures 7.40 to 7.42 are a comparison between the FEM model and the experimental observations of the damage observed on the back face of the laminate.

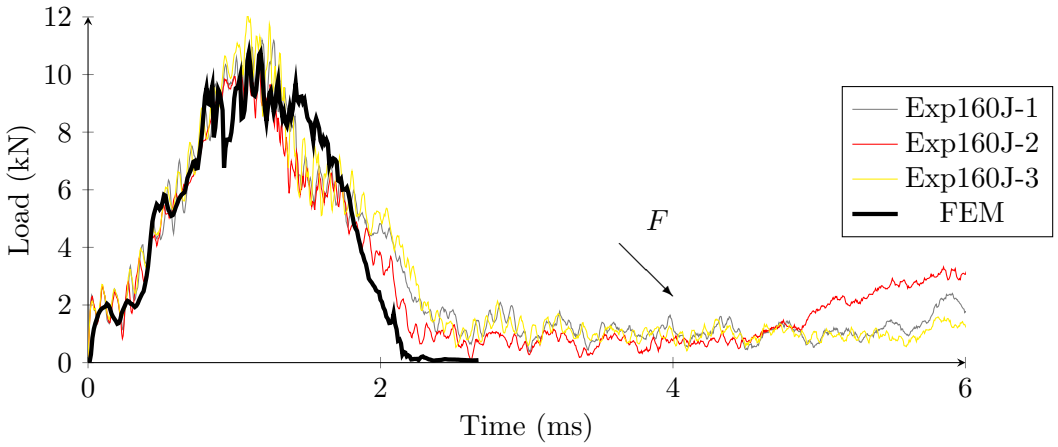


Figure 7.38: FEM prediction of the load-time curve for 160J impact loading on Vectran/MTM57 and compared with three experimental results

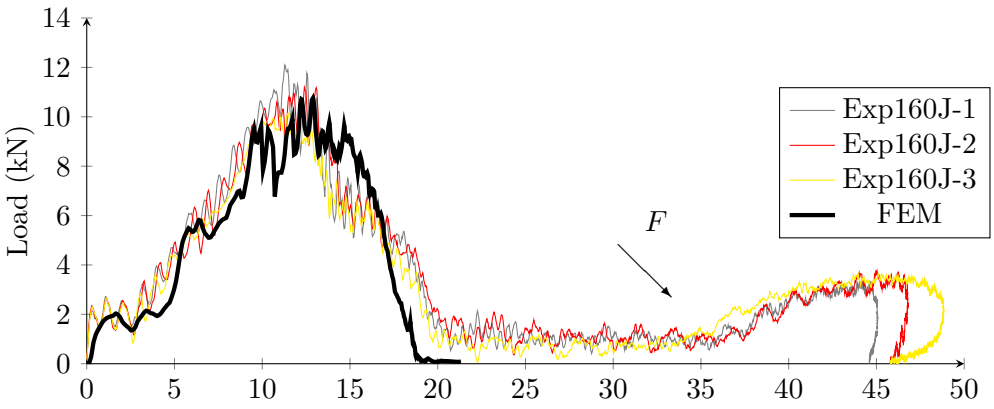
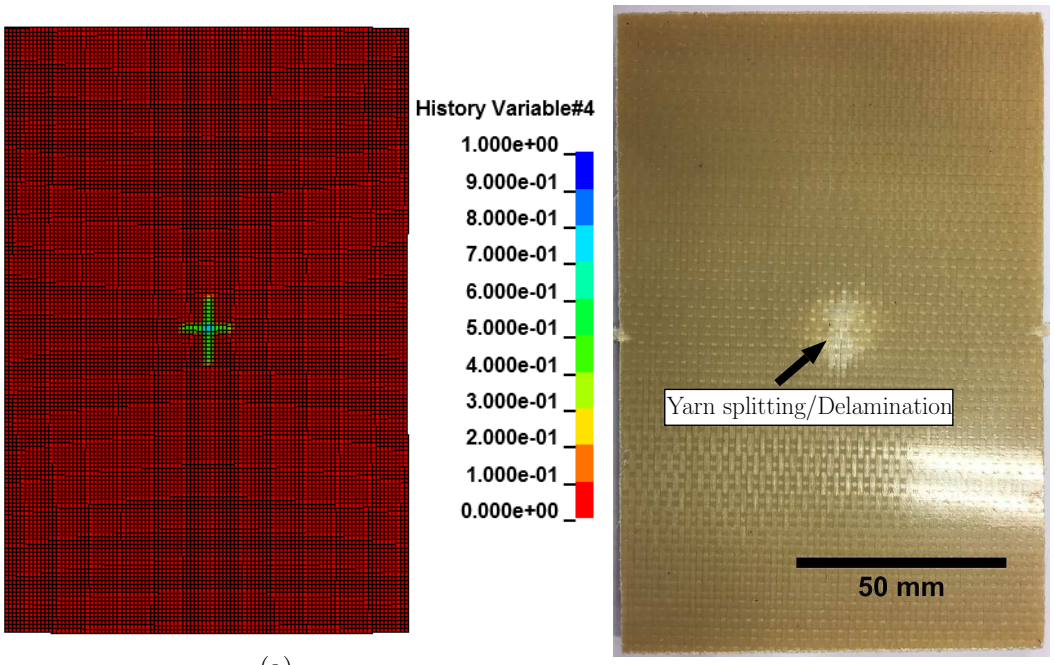


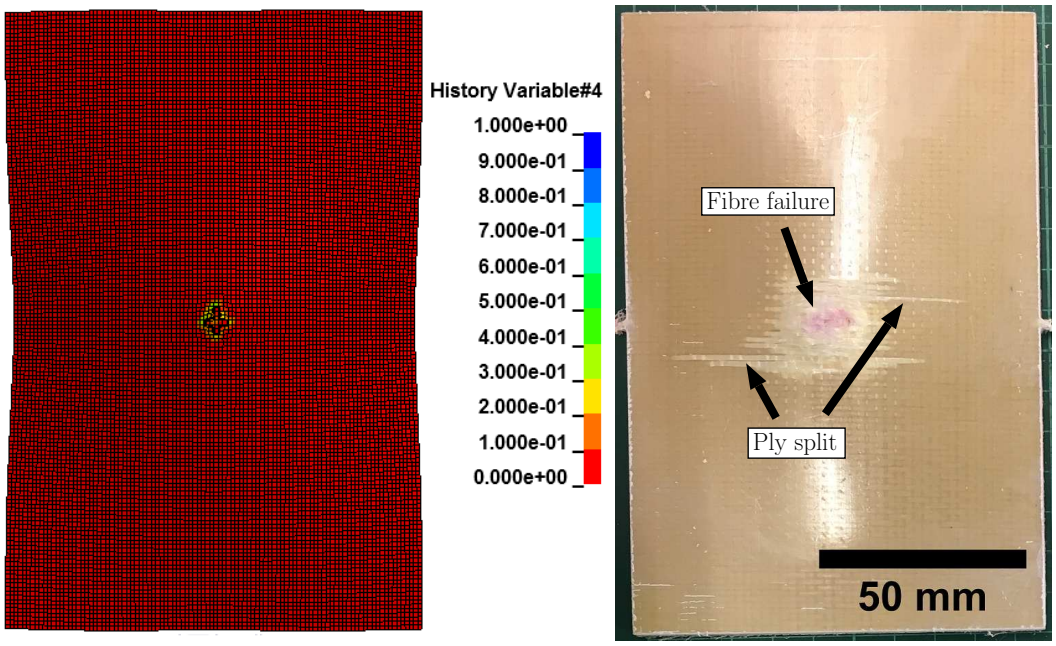
Figure 7.39: FEM prediction of the load-deflection curve on for 160J impact loading on Vectran/MTM57 and compared with three experimental results



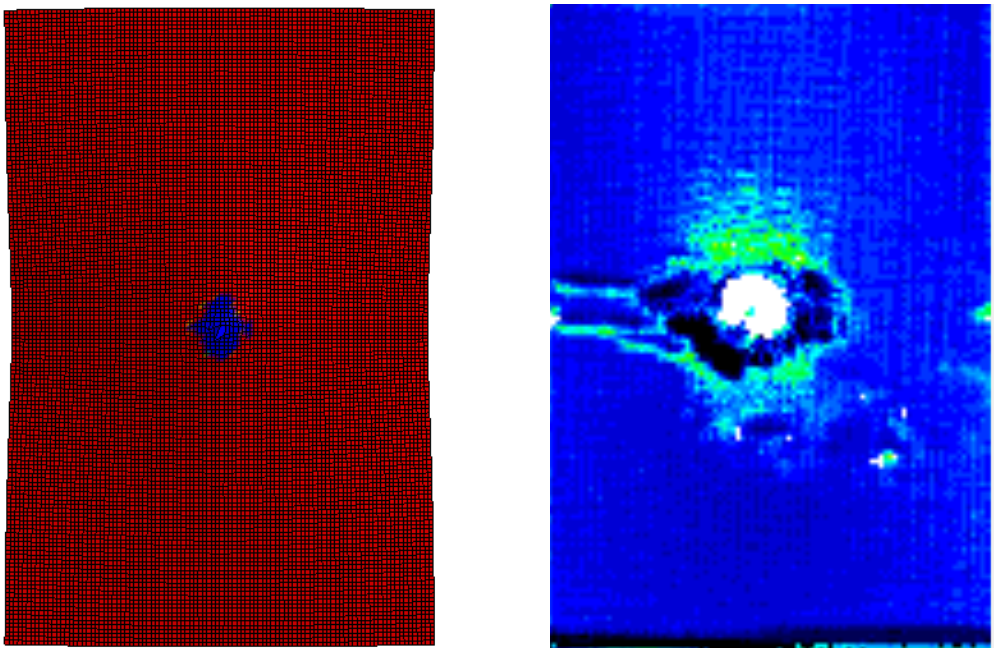
(a) (b)

(c) (d)

Figure 7.40: Comparison of the simulation and experimental results for 40 J impact load on Vectran/MTM57 (a) FEM prediction of damage on the laminate back face (b) Experimental back face damage (c) FEM prediction on delamination damage (d) C-scan results

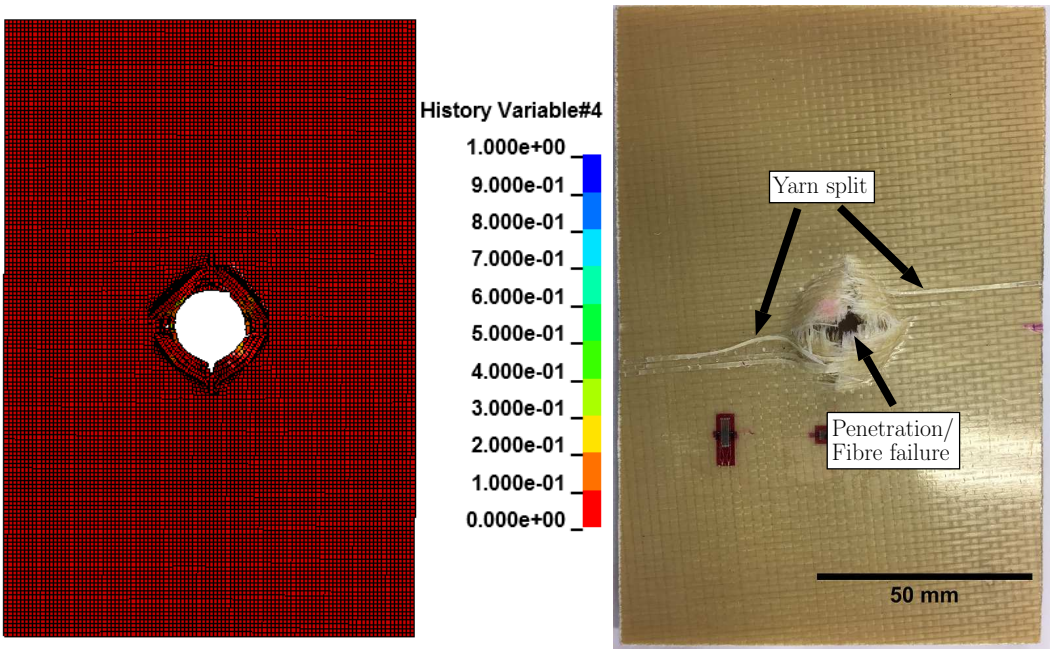


(a) (b)

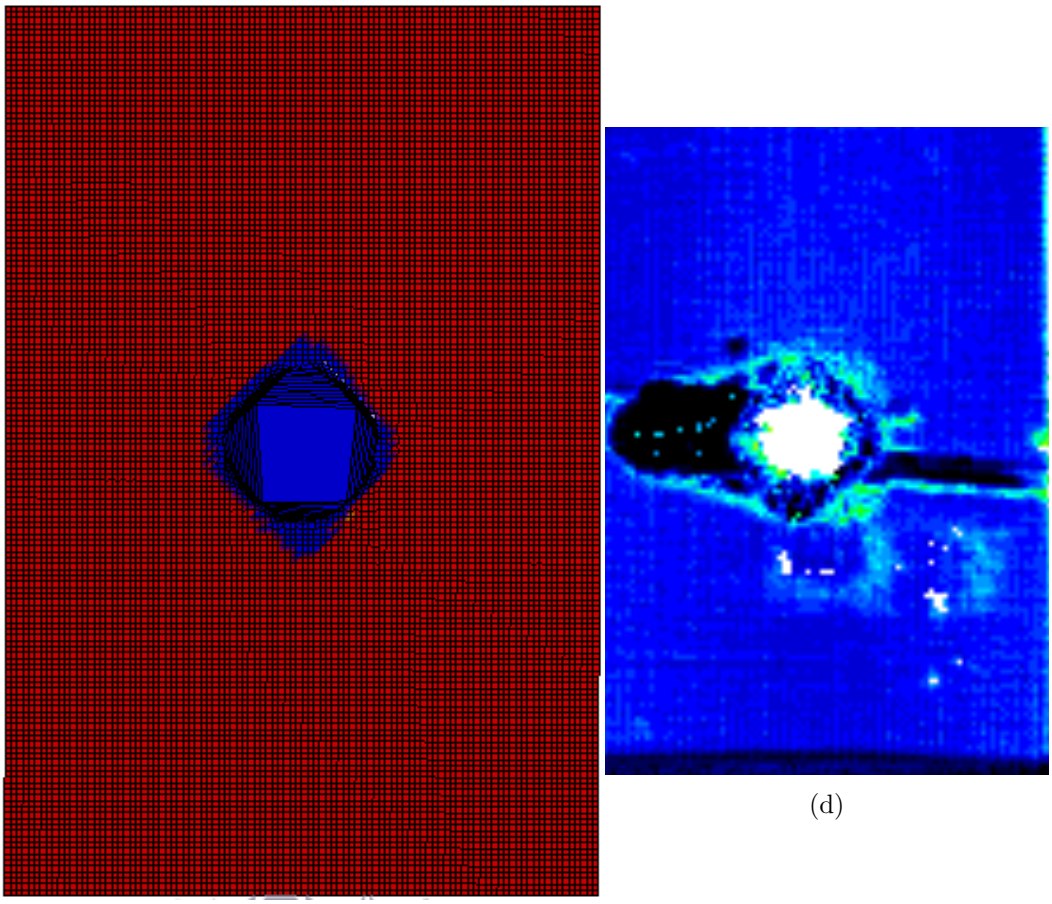


(c) (d)

Figure 7.41: Comparison of the simulation and experimental results for 100 J impact load on Vectran/MTM57 (a) FEM prediction of damage on the laminate back face (b) Experimental back face damage (c) FEM prediction on delamination damage (d) C-scan results



(a) (b)



(c) (d)

Figure 7.42: Comparison of the simulation and experimental results for 160J impact load on Vectran/MTM57 (a) FEM prediction of damage on the laminate back face (b) Experimental back face damage (c) FEM prediction on delamination damage (d) C-scan results

7.3.2 High velocity impact

IM7/8552

The ballistic curve for IM7/8552 is shown in Figure 7.43, where it can be observed that the FEM predictions were in close agreement with the experimental results, albeit with an overestimation at each impact level ($V_{50}^{FE} \approx 115$m/s; $V_{50}^{Exp} \approx 90$ m/s).

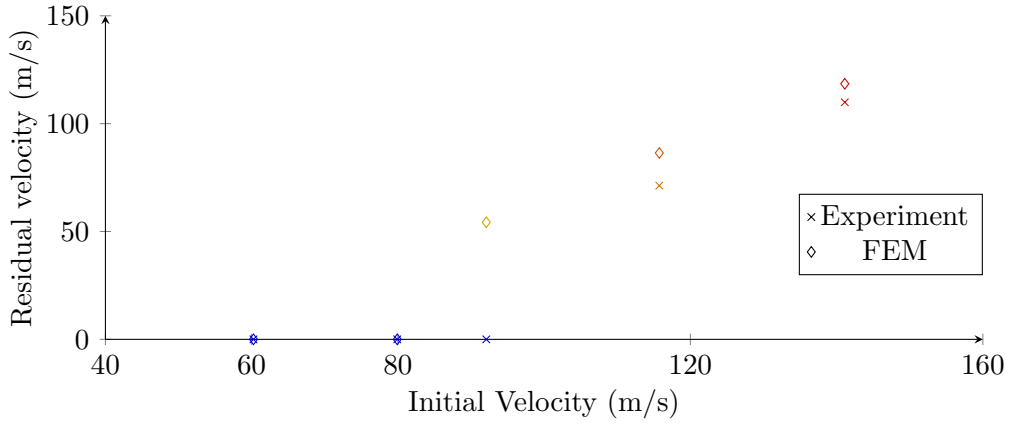


Figure 7.43: Impact versus residual velocity for FEM predictions and experimental measurements for IM7/8552

The experimental and FEM predicted HVI events are also shown in Figure 7.44, where extensive ply-splitting can be observed on the laminate back face, upon projectile impact. This was not predicted by the FEM model, as it requires extensive mesh refinement, modelling each layer of ply (in this case, 32 plies), connected with the cohesive algorithm. However, this would result in a high computational time, due to the significant number of elements involved, as well as the amount of cohesive algorithm used.

Also shown in Figure 7.45 is the delamination prediction by the numerical model using a contact algorithm as explained in subsection 7.2.3. It can be observed that the FEM prediction underestimated the delamination area when compared to the C-scan results - Figure 7.45d (FEM: 1972 mm^2; Exp: 3138 mm^2). This is because the cohesive algorithm used in the FEM model defines a single linear softening curve, which may not be suitable for predicting the fibre-bridging effects. Thus, the use of advanced cohesive algorithms such as the bi-linear or a multi-linear softening model may improve the delamination prediction, as it more accurately represents fibre-bridging effects in

the formulation.

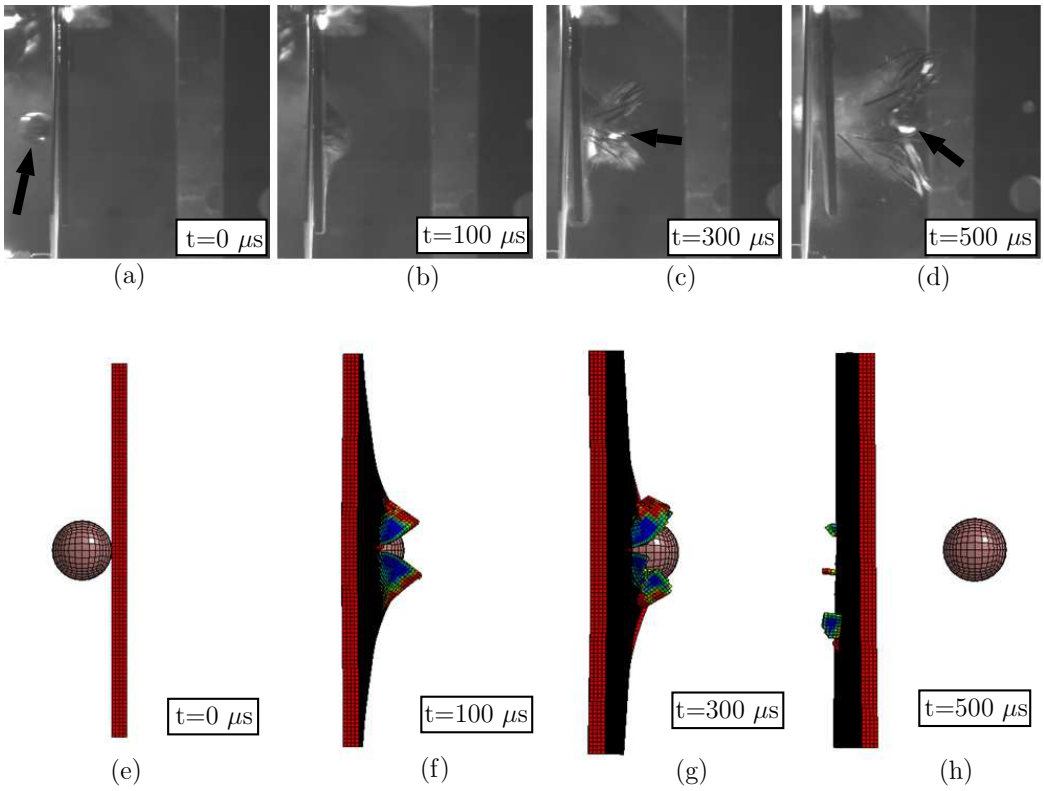
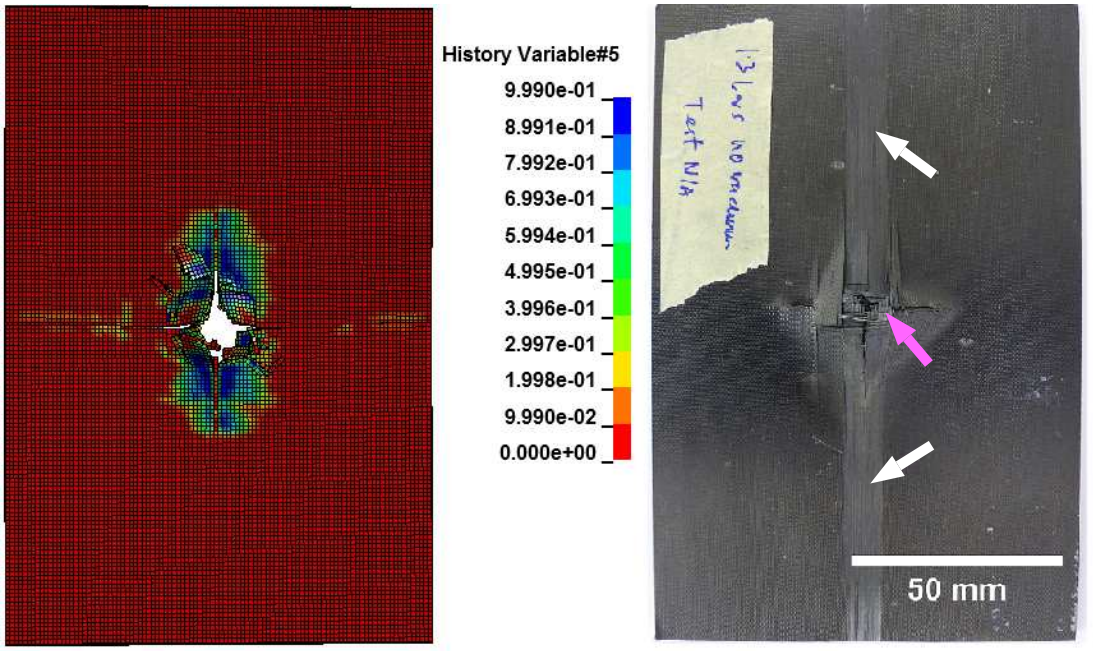
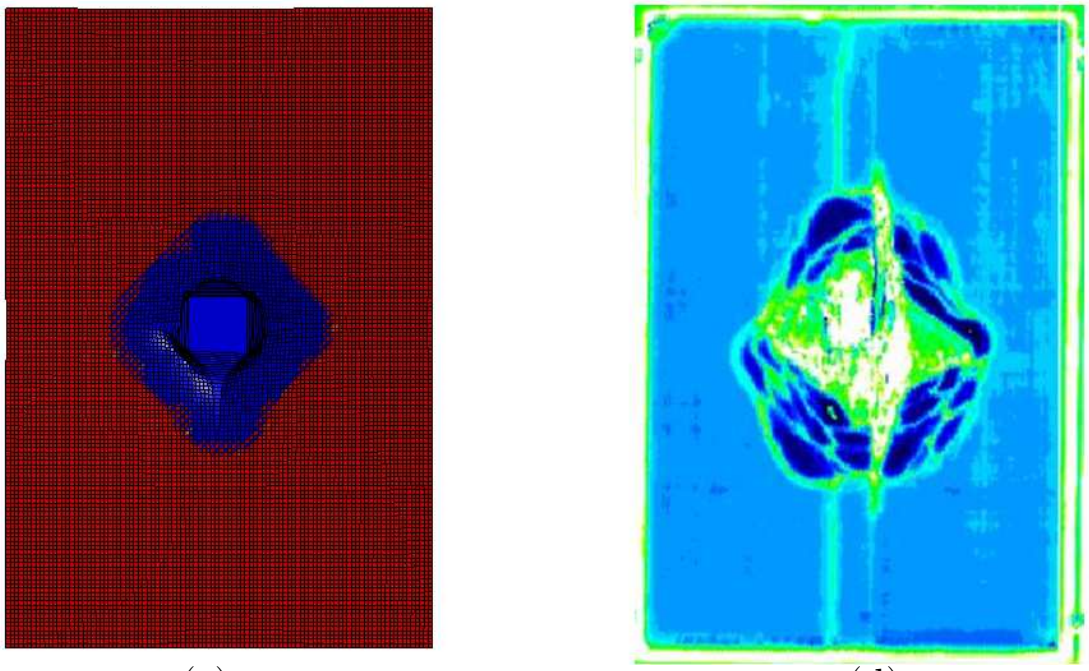


Figure 7.44: HVI events on IM7/8552 at $V_i \approx 115$ m/s. (a) - (d) Experimental HVI events (e) - (h) FEM predictions. Black arrow showing projectile



(a) (b)



(c) (d)

Figure 7.45: Comparison of damage on IM7/8552 laminate under ≈ 92 m/s impact velocity. The black arrows represent ply-splitting whilst the red arrow represents fibre fracture. Contours represents fibre damage. (a) FEM prediction (b) Experimental specimen (c) FEM delamination prediction (d) C-scan results

S2-Glass/MTM57

The sensitivity of S2-Glass/MTM57 laminates to strain-rate effects was a significant issue which must be included in the FEM analysis, with some literature reporting an increase of up to 70% in the tensile properties [211]. Although both IM7/8552 and S2-Glass/MTM57 are brittle in nature, the strain-rate sensitivity, along with other advantageous properties such as a high tensile strain-to-failure, results in a superior performance of the latter composite compared to the former under HVI loading. In the current material model used (MAT262), there is no direct method to include the strain-rate effects for the tensile and compressive components. Therefore, the properties have been adjusted manually according to the available literature [71, 211–213]

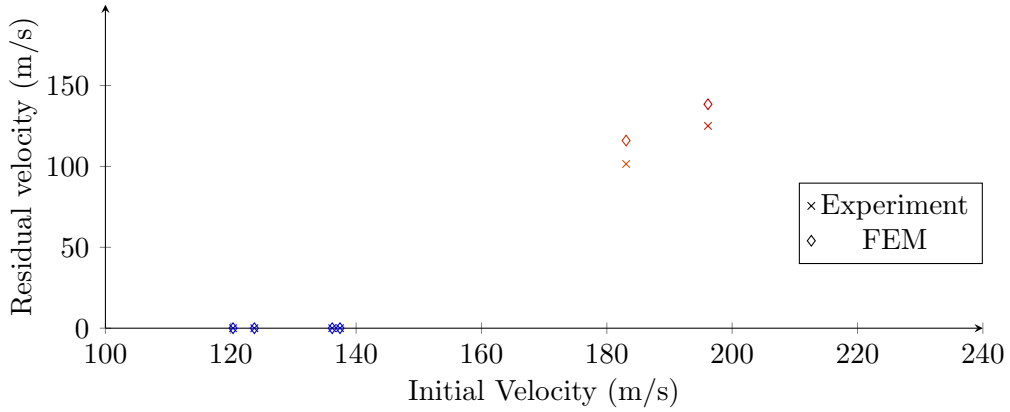


Figure 7.46: Impact versus residual velocity for FEM predictions and experimental measurements for S2-Glass/MTM57

Figure 7.46 presents the ballistic curve of S2-Glass/MTM57 under HVI loading, where it can be observed that the numerical model overestimates the experimental V_{50} by approximately 15% ($V_{50}^{FE} \approx 149$ m/s; $V_{50}^{Exp} \approx 128$ m/s). The extensive ply-splitting that can be observed at the laminate back face upon projectile penetration, Figure 7.47, was not predicted by the model since this requires further modifications to the model to accommodate ply-splitting damage.

Figure 7.48c presentes the predicted delamination damage by the FEM model. It should be noted that particularly for S2-Glass/MTM57, gross delamination was observed which extends towards the laminate boundaries. This resulted in a considerable difficulty to scan the laminate using the ultrasonic C-scan. Further, the NCF architecture poses additional complications due to the presence of stitches and minimal crimps in the

laminate. It was found that the FEM prediction again resulted in an underestimation in delamination damage, when compared to the experimental observations. As seen in Figure 7.48, it was found that the gross delamination with an arbitrary propagation path further complicates the scanning results. This is different to the FEM predictions, which grows radially towards the laminate boundaries. Interestingly, the gross delamination area predicted by the numerical model is considerably close if compared to the experimental result (FEM $\approx$ 6422 mm^2; Exp $\approx$ 6541 mm^2) although the delamination mapping is different.

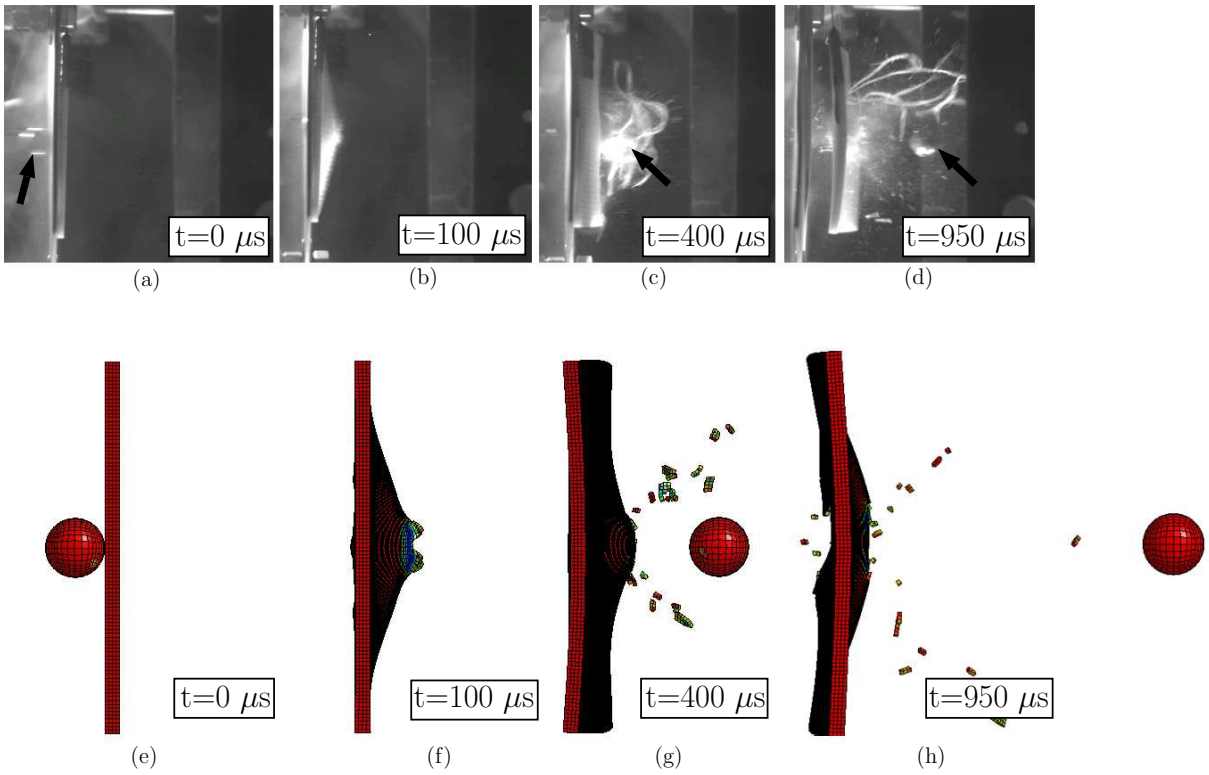


Figure 7.47: HVI events on S2-Glass/MTM57 at $\approx$ 183 m/s. (a) - (d) Experimental HVI events (e) - (h) FEM predictions. Black arrow showing ply-splitting

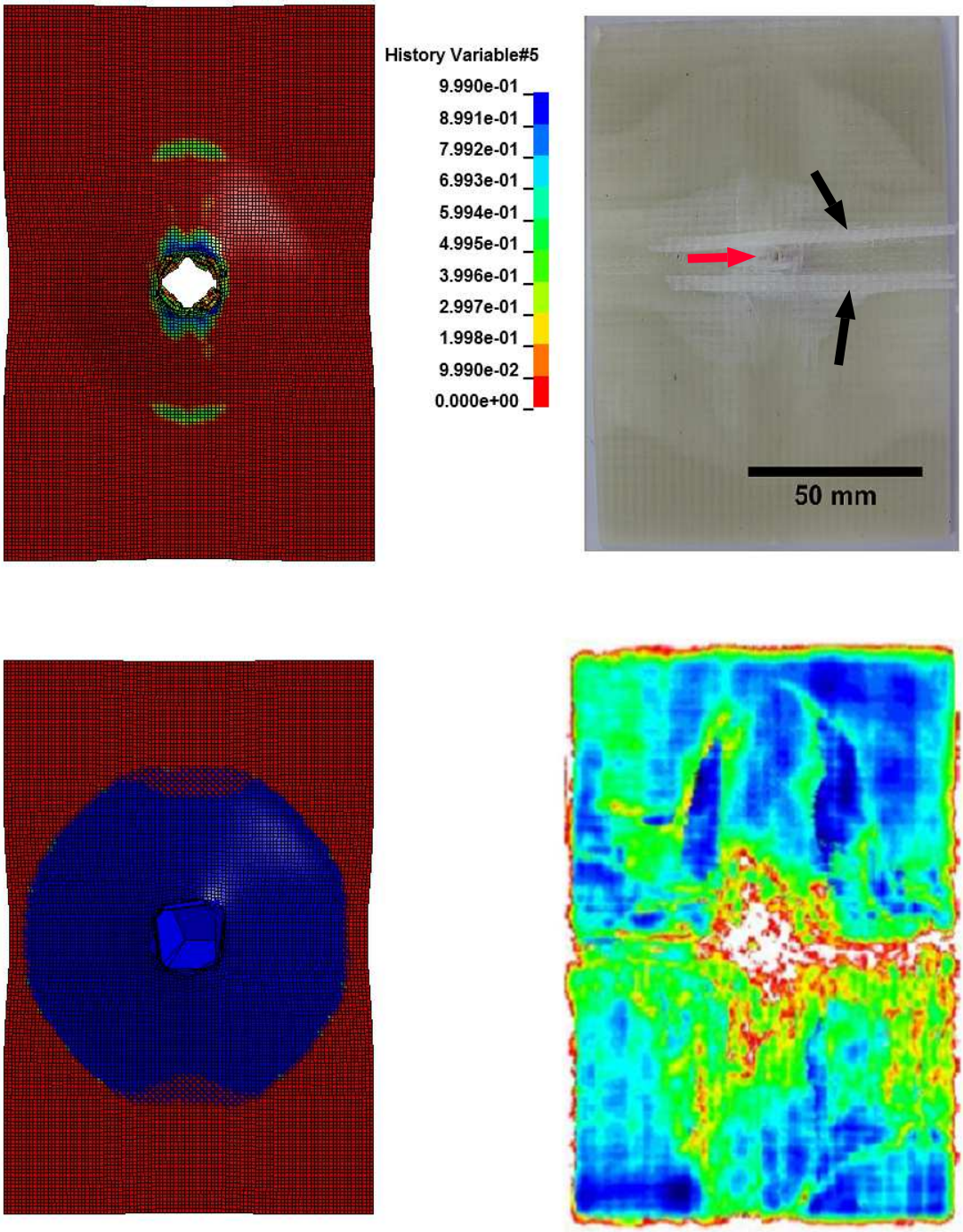


Figure 7.48: Comparison of damage on IM7/8552 laminate under ≈ 92 m/s impact velocity. White arrows represent ply-splitting whilst blue arrow represents fibre fracture. Contours represents fibre damage. (a) FEM prediction (b) Experimental Vectran/MTM57 specimen (c) FEM delamination prediction (d) C-scan results

Vectran/MTM57

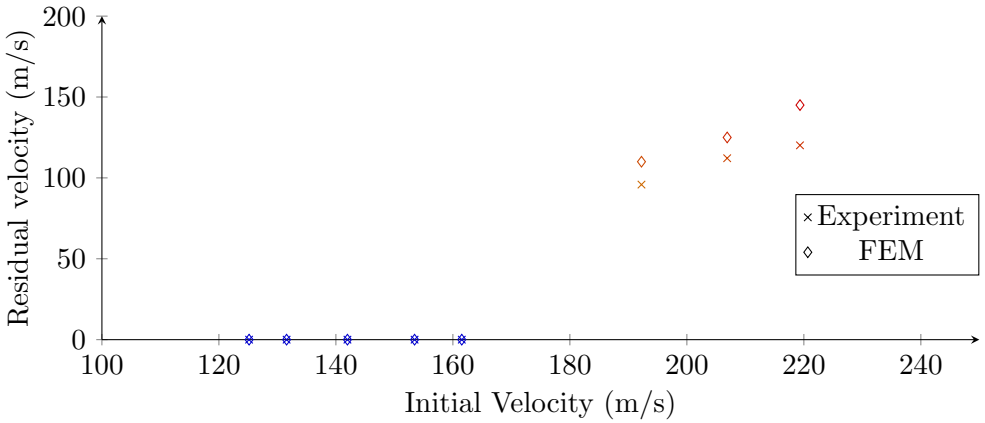


Figure 7.49: Impact versus residual velocity for FEM predictions and experimental measurements for Vectran/MTM57

Figure 7.49 presents the ballistic curve for Vectran/MTM57 laminates under HVI loading. It can be observed that the developed UMAT is in good agreement with the experimental results ($V_{50}^{FEM} \approx 153$ m/s; $V_{50}^{Exp} \approx 161$ m/s), although at higher velocities, the FEM prediction tends to overestimate the residual velocity. It can be seen from Figure 7.50 that extensive ply-splitting has occurred at the back of the laminate, which was not predicted by the UMAT.

However, closer inspection of the laminate revealed extensive compressive damage on the laminate front face, Figure 7.51, extending along both directions. This is suggested to exist initially due to shear damage, in which the front face of the laminate undergoes irreversible shear (shear strain/stress exceeding its linear elastic strain/stress, Figure 7.51 (a), therefore damaging the matrix. As a result of matrix damage, the compressive strength (due to damage in the matrix) is reduced hence yielding a damage pattern as observed in Figure 7.50 (c), due to the flexural motion experienced upon impact.

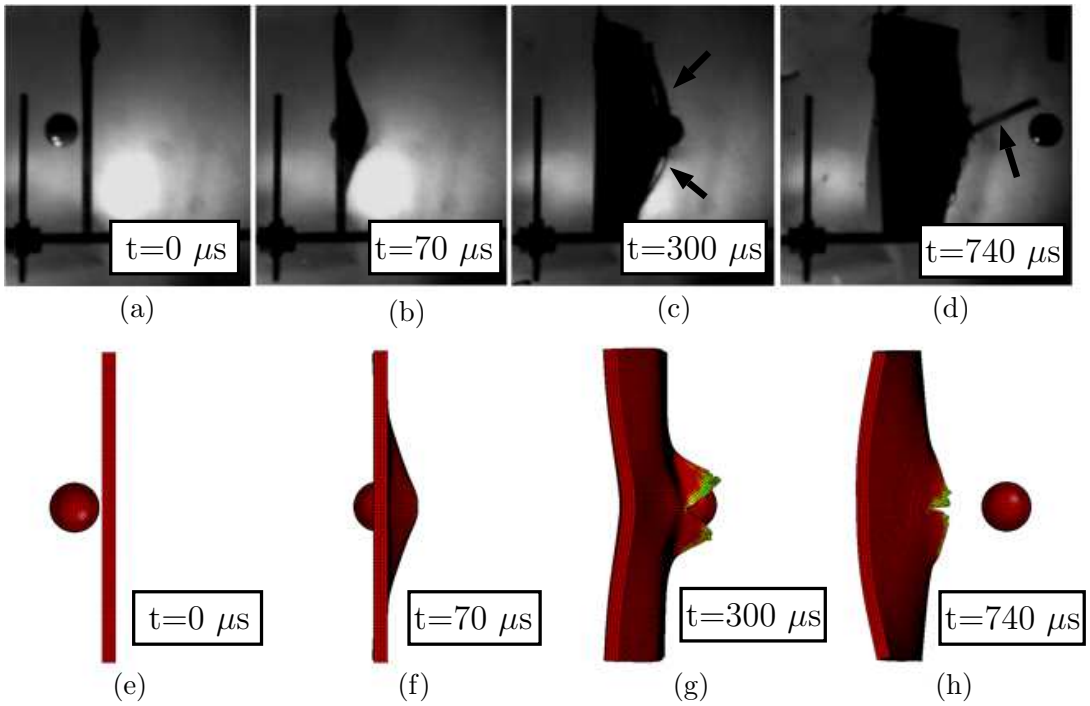


Figure 7.50: HVI events on Vectran/MTM57 at ≈ 170 m/s. (a) - (d) Experimental HVI events (e) - (h) FEM predictions. Black arrow showing ply-splitting

Also shown in Figure 7.51 is the numerical prediction of the delamination damage. Similar to the other composites, the FEM model resulted in an underestimation of the delamination area, similar to the case of IM7/8552 and S2-Glass/MTM57 (FEM ≈ 2092 mm^2; Exp ≈ 3871 mm^2).This is thought to be due to the simplified bi-linear law of the cohesive algorithm. Further, the inherent NCF characteristics which involve stitches often lead to an arbitrary crack propagation path due to the crack arresting mechanism promoted by the stitches.

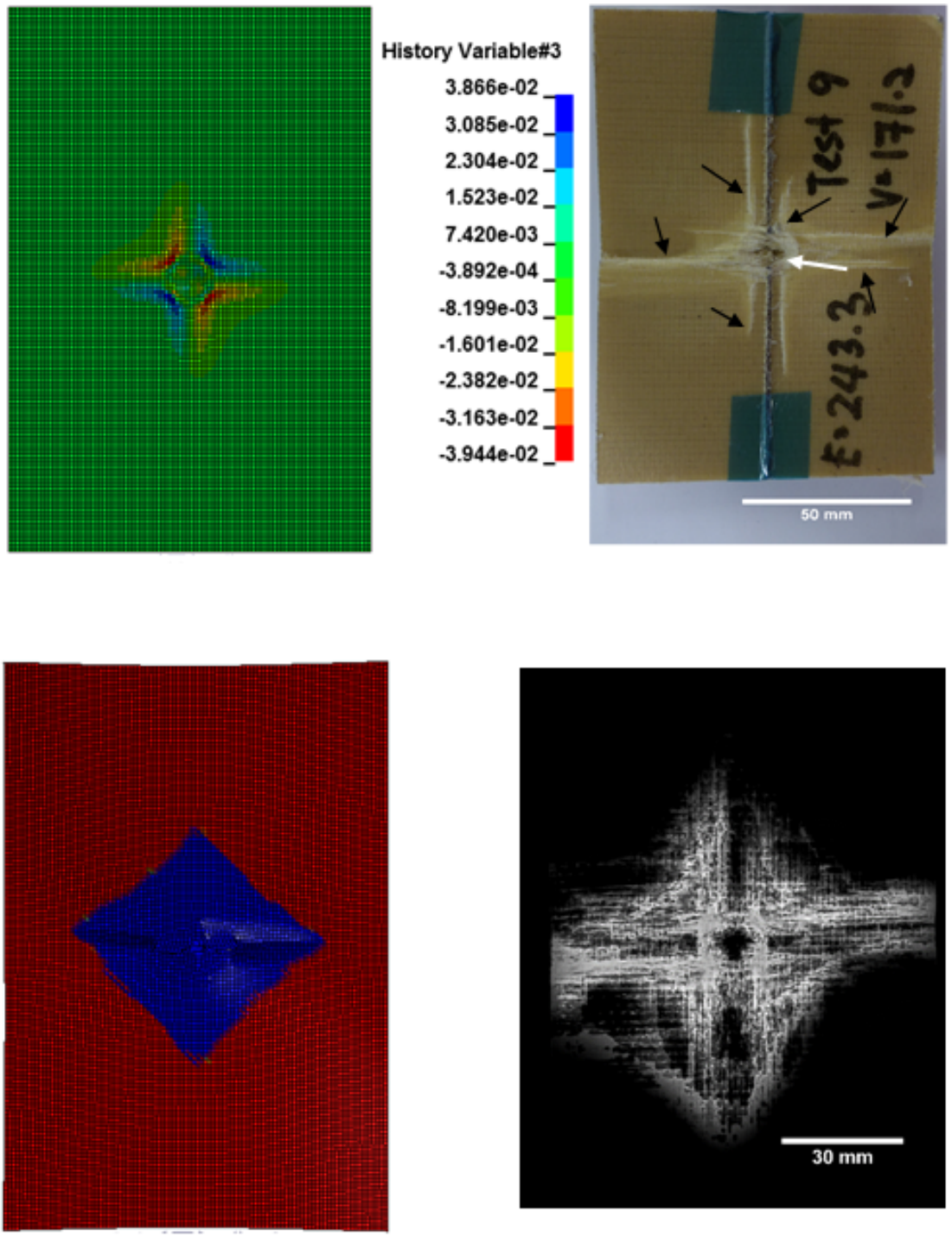


Figure 7.51: Comparison of damage on Vectran/MTM57 laminate under ≈ 170 m/s impact velocity. Black arrows represent matrix damage. Contours representing shear strain. White arrow represent penetration/fibre failure (a) FEM prediction (b) Experimental Vectran/MTM57 specimen (c) FEM delamination prediction (d) C-scan results

7.4 Discussion

7.4.1 Permanent indentation

The occurrence of the permanent indentation on the laminate surface is seen as an energy absorption mechanism to resist impactor penetration. This is particularly true for Vectran/MTM57 composites since a small region of damage was observed under LVI loading for the 40 J and 100 J case. While the β term (discussed previously in subsection 6.3.1) controls the amount of irreversible strain in the in-plane direction for both tensile and compressive direct stresses, the through-thickness behaviour was not modelled within the present UMAT framework, particularly the through-thickness shear. Moreover, although the 'penalty' method was utilised to represent the normal and through-thickness shear stresses, it is possible that the approach could not adequately predict the stress localization due to the local indentation. This is because the 'penalty' approach used in the current UMAT formulation assumes a linear stress-strain relationship in the through-thickness direction, which may be an oversimplification of the actual through-thickness behaviour in Vectran/MTM57 composite.

For S2-Glass/MTM57, permanent indentation is observed together with other damage modes such as matrix cracking and fibre failure. However, a significant underestimation in the load-deflection response is observed, Figure 7.22, due to the absence of any explicit permanent strain definition in the tensile and compressive failure modes, such as the β term in the developed UMAT formulation. Furthermore, the plane-stress assumptions imposed in both material models (MAT262 and UMAT) place strict limitations on predicting the through-thickness behaviour of S2-Glass/MTM57 and Vectran/epoxy laminate, hence resulting in the underestimation in terms of the impact energy absorption.

One strategy in capturing the effects of permanent indentation in composite laminates is by discretizing the model into 'strips' and connecting them using a cohesive algorithm based on the intralaminar (matrix) energy release rate. This was been shown by Bouvet et al. [39], when modelling the effects of permanent indentation in CFRP laminates. The approach was observed to capture very well the permanent indentation seen on CFRP laminates under LVI loading, with excellent correlation between the FEM

model and the experimental results. However, apart from the long computational times, and complex meshing techniques, the approach requires through-thickness effects to be defined.

7.4.2 Strain-rate effects

The significance of the strain-rate effects in transverse impact loading is particularly important, especially for Glass Fibre/Epoxy (GF/Epoxy) and polymer fibre based composites [71, 73, 211–214]. For S2-Glass/MTM57, the dependence on strain-rate, particularly under tensile and compressive modes [71, 213] poses difficulties when correlating the numerical and experimental observations. Furthermore, MAT262 does not offer any enhancement on the tensile and compressive modes from strain-rate effects. Hence the enhancement must be performed manually to obtain a good correlation with experimental results. In contrast, Carbon Fibre/Epoxy (CF/Epoxy) composites were found to be strain-rate independent under tensile and compressive modes [71]. Under $\pm 45\,^{\circ}$ in-plane shear, a considerable improvement was evident in the initial shear stiffness and strength, as well as the shear strength at failure (G^0_{12}, τ^0_{12}, and τ^u_{12}, respectively) with increasing strain-rates [71, 88]

Due to the lack of information on the strain-rate effects in Vectran fibres (or laminated composite), it is proposed that laminated composites based on Vectran fibres would behave differently under different strain-rate. This is because other polymers, especially those having a similar 'skin-core' structure as Vectran, behaves differently with respect to strain-rate, with an average improvement of approximately 30% in the fibre tensile strength and modulus [72, 73, 214]. As a composite, the sensitivity with strain-rate is greater, with some researchers reporting an increase of up to 50% in its tensile properties (strength and modulus) [212, 213, 215].

The fibre-matrix interface also plays a major role in determining the composite sensitivity to strain-rate effects. A weak interface strength is often an indicator of high sensitivity to strain-rate effects, and vice versa [216]. It has been reported that the fibre-matrix interfacial shear strength, τ_i, in a Vectran/Epoxy composite system is approximately 19.5 MPa [184]. This is considerably low compared to that of Carbon/Epoxy

composites ($\tau_i > 40$ MPa [217]). Thus, this indicates a stronger dependency on strain-rate effects. Although the effect may not be as large under LVI compared to HVI, some improvements on the material properties may still exist with increasing velocity. Thus, the material inputs should be adjusted accordingly to account for the effect of strain-rate. Finally, future work on Vectran composites should also be dedicated to characterising these strain-rate effects.

7.4.3 Delamination

The experimental observations present a spectrum of damage modes, which translate into potential sources of energy dissipation, hence defining the impact performance of a composite material. While most of the damage modes such as delamination, fibre failure, and matrix failure (using MAT262) were captured by the numerical model, there still exists other types of damage modes which cannot be predicted using the current material models. In particular, the effect of stitches which is an inherent characteristic of NCF composites remains elusive, since the use of the cohesive algorithm in this study considers a single linear softening curve, hence neglecting any effect of stitching or fibre-bridging. This results in a generic delamination mapping which follows the local element orientation based on the material inputs. However, the propagation of delamination, especially under HVI loading is difficult to predict due to the presence of stitches which results in an undeterminate change of crack path in the laminate. This is not accounted for in the current cohesive algorithm formulation. Further, due to the fibrillar nature of Vectran fibres, fibre-bridging is particularly important as a toughening mechanism under delamination damage. This requires advanced cohesive algorithms which employ a bi-linear or multi-linear softening curve to define the effect of the fibre-bridging mechanism. Table 7.3 presents a summary of the FEM prediction on the delamination damage, as well as the measurements from the experimental observations for LVI. Here, the variation on predicted delamination damage with respect to the energy level can be observed.

Table 7.3: Comparison of FEM prediction and experiments on the measured delamination area under LVI. Units in mm^2

Composite	40 J		100 J		160 J	
	Experimental	FEM	Experimental	FEM	Experimental	FEM
IM7/8552[5]	1,728	1,526	1,677	1,383	1,646	1,251
S2-Glass/MTM57 [5]	140	0	173	0	186	0
Vectran/MTM57[6]	163	65.14	272	204	303	428

Under HVI loading, the difference between numerical predictions and experimental observations were ultimately larger. In most cases, the delamination area predicted by the FEM model is approximately 50% smaller than the experimental results. However, numerical prediction on the delamination damage for S2-Glass/MTM57 laminates was found to be very close with the experimental results, even though the delamination mapping is different. This is due to indeterminate delamination growth in the experiments, in contrast with the FEM model where delamination is observed to grow radially towards the laminate boundaries.

7.4.4 Numerical accuracy

While it can be observed that the material models used in the current PhD study (MAT262 and UMAT) are able to simulate the LVI and HVI response of IM7/8552, S2-Glass/MTM57 and Vectran/MTM57 composites, it is important to fully investigate the accuracy of the numerical model, particularly the developed UMAT for Vectran/MTM57. Figure 7.52 presents a comparison from the average normalized energy absorption between the numerical prediction and the experimental results. Here, two observations can be made. First, the FEM predictions can be observed to underestimate the experimental results for both LVI and HVI loading conditions. Under LVI, the load-deflection response for all composites are considerably underestimated, resulting in a significant underestimation in the energy absorption, particularly in the case of S2-Glass/MTM57 under 40 J of impact energy using MAT262. As stated before, this is because the material formulation does not consider any effects on permanent strain

[5]Using MAT262
[6]Using UMAT

in the tensile and compressive failure modes. It should be noted that MAT262 was developed based on the response of carbon fibre composites, which are well known to have little to no plastic component apart from the ±45 ° in-plane shear [14, 15]. Thus, the effects of permanent strain is neglected in the material formulation.

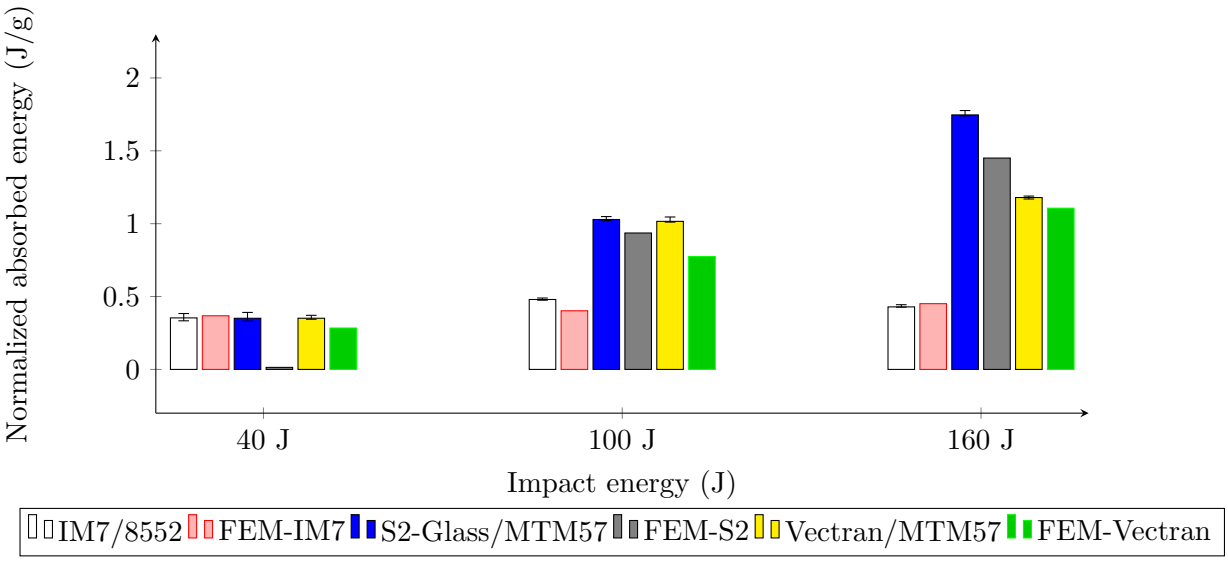


Figure 7.52: A comparison between the average normalized absorbed energy for all laminates under LVI loading - FEM versus experiments

Secondly, a bi-linear approach in modelling the ±45 ° in-plane shear of laminates is seen to be a slight oversimplification of the shear response. This is illustrated in Figure 7.53, where it can be observed that the ±45 ° in-plane shear component using MAT252 results in an overestimation, particularly in the non-linear region where the composite undergoes strain-hardening. This could result in a stiffer response in the numerical model, hence yielding an underestimation in the Back Face Deflection (BFD), particularly under HVI loading. This is shown in Figure 7.54, where it can be observed that the FEM prediction always result in an underestimation of the absorbed impact energy, due to the larger residual velocity, V_i, upon projectile penetration. The FEM underestimation on other damage types such as delamination, wil also influence the amount of impact energy absorption predicted by the numerical model. This is because delamination damage is the most severe under HVI loading, particularly for Vectran/MTM57 laminates.

In addition, damage types such as ply-splitting and stitch failure, particularly for

NCF based architecture, should also be included to yield a more realistic numerical prediction, hence resulting in a better correlation with the experimental observations.

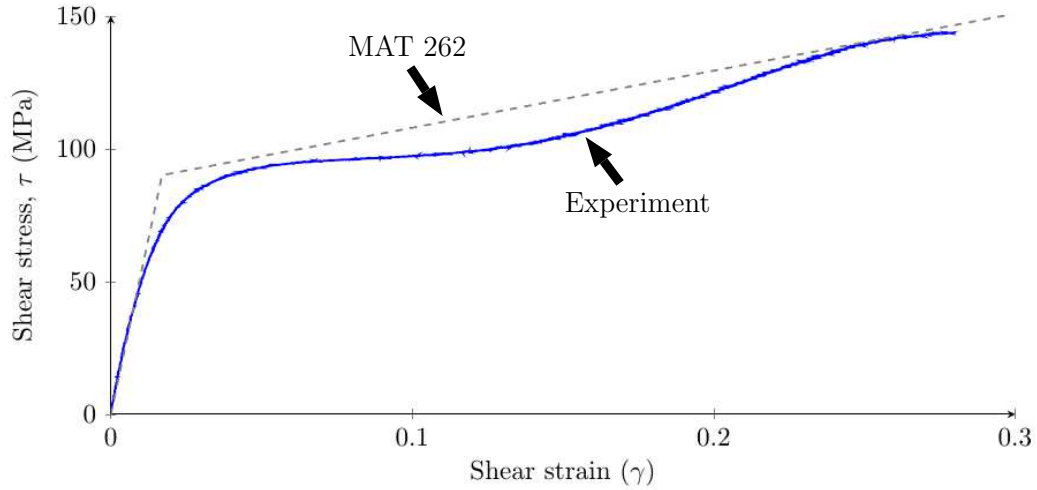


Figure 7.53: Illustration of the bi-linear approach using MAT262 for the ±45° in-plane shear response of IM7/8552

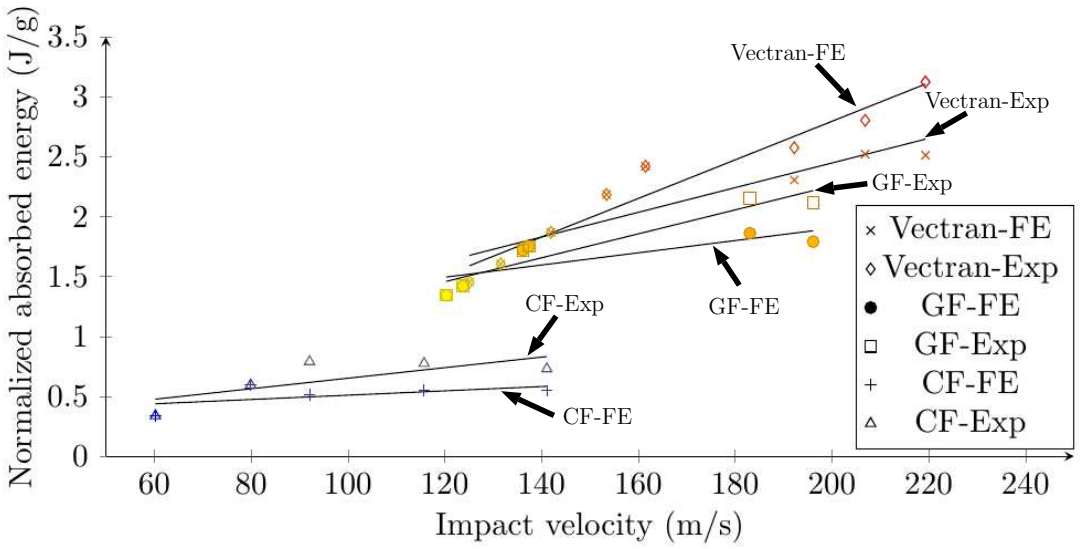


Figure 7.54: Average normalized energy absorption per unit weight under HVI loading between the FEM and experimental results

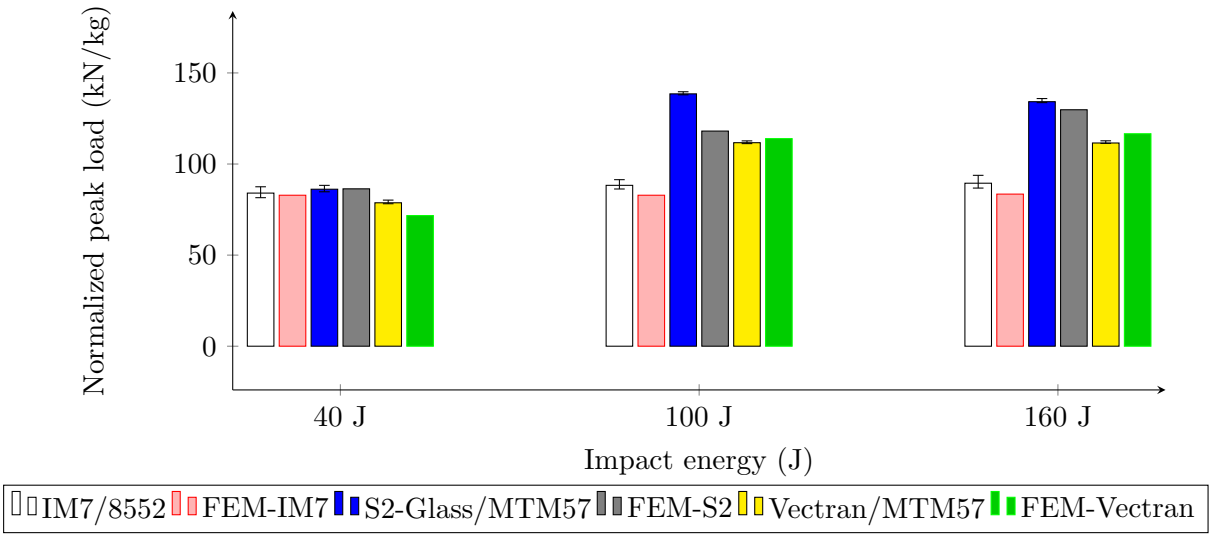


Figure 7.55: A comparison between the average normalized peak load for all laminates under LVI loading - FEM versus experiments

Figure 7.55 presents the average normalized peak loads for all laminates under LVI loading. It can be seen that the numerical model, both MAT262 and UMAT 41v are able closely predict the peak load with the experimental results with a considerable accuracy. This is an excellent feature which could be attributed to the energy-based modelling approach utilised by both material models in this PhD. In contrast with other modelling approaches such as the strain/stress failure criteria, failure does not occur when the stress reaches its maximum strength. Rather, failure is taken at full damage ($d = 1$), which allows the laminate to continue carrying load even when the maximum stress has been reached. This is the great advantage of the energy-based modelling strategy, which compensates the longer computational time compared to the more simpler strain/stress failure criteria approach.

7.5 Summary

This chapter present outcomes from the FEM modelling of IM7/8552, S2-Glass/MTM57, and Vectran/MTM57 under LVI and HVI loadings. It was found that MAT262 predicted with a considerable accuracy the LVI and HVI response of IM7/8552 and S2-Glass/MTM57 composites, despite a number of drawbacks due to the formulation of the material model. First, a large underestimation on the permanent deflection is ob-

served from the load-deflection histories of IM7/8552 and S2-Glass/MTM57. This is because MAT262 does not consider any definition of permanent strain in its material formulation, such as the β component in the developed UMAT. Secondly, the effects of strain-rate on the tensile and compressive failure modes have to be manually adjusted, particularly for S2-Glass/MTM57 composites, due to the strain-rate sensitivity.

The developed UMAT for Vectran/MTM57 composite was observed to be in good agreement with the experimental results under LVI and HVI loadings. Similar to the case of MAT262, an underestimation is observed in the load-deflection response, although the effects of permanent deflection was explicitly included in the material formulation. This is thought to be due to the large influence in the through-thickness stresses, particularly the shear component. Therefore, a 3D formulation should be developed to fully capture the composite response under LVI loading.

Finally, it was found that the cohesive algorithm employed in the FEM model underestimated the delamination behaviour for the composite materials under LVI and HVI loadings. This is especially true for S2-Glass/MTM57 and Vectran/MTM57 composites, where fibre-bridging is one of the dominant toughening mechanism, apart from the effects of NCF stitches, discussed in section 3.8.4. This is largely due to the simplistic nature of the bi-linear approach, which does not explicitly include any effects of fibre-bridging. Thus, advanced cohesive formulation should be employed, such as the multi-linear or exponential softening formulation, to be able to better predict the extent of delamination damage in composite materials under impact loadings.

Chapter 8

Further Discussions

8.1 Introduction

Some of the key topics explored during the course of this PhD are highlighted below:

1. Quasi-static in-plane mechanical characterisation (tension, compression, and $\pm 45^\circ$ in-plane shear) of the composite materials (IM7/8552, S2-Glass/MTM57, and Vectran/MTM57), as well as the out-of-plane interlaminar fracture toughness characterisation using the DCB (Mode I) and 4ENF (Mode II) approaches;

2. Mode I translaminar fracture toughness characterisation of Vectran/MTM57 composite using the modified Compact Tension (CT) specimen initially developed by Katafiasz et al. [70]. The NCT specimen was further refined using the Finite Element Method (FEM) modelling to prevent unwanted plastic deformation in the specimen outside of the intended crack growth region. It was found that fibre pull-out is the main failure mechanism which contributes to the fracture toughness, G_{Ic} of Vectran/MTM57 composite. In addition, the energy dissipated from Vectran fibre failure is also relatively large, when compared Carbon and Glass Fibres;

3. All three composite materials used in this study were placed under LVI and HVI loading and their performance under impact ranked, with all damage modes discussed in detail. It was found that under LVI, both Vectran/MTM57 and S2-Glass/MTM57 showed superior performance, with S2-Glass/MTM57 being the best performing composite. Under HVI, Vectran/MTM57 emerges as the best

performing composite of the three laminates. Finally, IM7/8552 was found to be the worst performing composite among all three under both impact loading conditions;

4. The development of an energy-based damage model for Vectran/Epoxy composite laminate. The numerical model was developed based on previous works by Iannucci et al. [88, 204, 205], modified to accommodate the non-linear stress-strain response under tensile loading. The model could also replicate the non-linear shear behaviour up to the experimental failure strain. Under dynamic loading (both LVI and HVI), a good correlation was found between the developed numerical model and the experimental results.

Section 8.2 discusses key findings and completed objectives.

8.2 Key research areas

8.2.1 Material characterisation

The quasi-static in-plane mechanical characterisation provided important initial insights on the behaviour of the composite materials selected in this study. Particularly for Vectran/MTM57, where it was found that under tensile and compressive loading, a non-linear response was observed due to the 'skin-core' behaviour of Vectran fibres. Similarly, under compressive loading, aside from the very low compressive strength, a strain-hardening response was found upon passing its yield strength, indicating the onset of kink-band failure, with a growing kink-band width as the stress increases. This is a clear indication of a weak (van der Waals) bond between molecules, as well as the fibrillar nature of the fibre which defibrillates almost instantly when loaded under compression [149, 150]. Under $\pm 45^\circ$ in-plane shear, the yield strength was also seen to be the lowest when compared to IM7/8552 and S2-Glass/MTM57, due to the poor fibre-matrix interfacial properties, enabling irreversible matrix deformation to occur very early in the test. In spite of this, the shear strain-to-failure was found to be the largest among all three composites, with an average shear strain of up to 75%, compared to the rest of the composites, which have an average shear strain of approximately 30%.

The measurement of the Fibre Volume Fraction (FVF) was performed using two approaches. For IM7/8552, an optical method was used. The thickness measurement method was chosen for S2-Glass/MTM57 and Vectran/MTM57 composites. The thickness measurement method was selected for Vectran/MTM57 and S2-Glass/MTM57 largely because the method allows for the influence of stitches in the NCF architecture to be excluded. More importantly, the method is suitable to be used for Vectran/MTM57 composite since Vectran fibres have a significantly lower melting temperature of approximately 330°C. In addition, images from the optical microscope were utilised to validate the information provided by the fabric manufacturer.

Next, considering the interlaminar fracture toughness behaviour of S2-Glass/MTM57 and Vectran/MTM57 laminates, experimental observations revealed a toughened Interlaminar Fracture Toughness (IFT) response resulting in a high G_c for both composites under Mode I and II testing. This is partly due to the NCF architecture tha incorporates stitches in the fabric, which act as a crack arrestor, diverting the propagation of cracks parallel to the stitches (i.e. perpendicular to the initial crack path). This is evident from a detailed fractographic study on the fracture surface of both composites, revealing an apparent change in the crack path around the vicinity of a stitch. Moreover, the effect of fibre-bridging, particularly in Vectran/MTM57 composites provided additional toughness to delay the opening (or sliding) of the top and bottom arms of the specimen. It must also be noted that the IFT response is dependent on the FVF of each composite, especially for S2-Glass/MTM57 laminates, as pointed out by Davies et al. [164]. In general, the G_c for both S2-Glass/MTM57 and Vectran/MTM57 was found to be at least six times higher under Mode I, and around four times higher under Mode II compared to IM7/8552 composites.

In all cases, both the quasi-static in-plane and the out-of-plane IFT tests proved highly repeatable with low scatter in each test for all composites used in this study. This is important since the derived experimental values will be used in LS-Dyna for numerical modelling purposes.

8.2.2 Translaminar fracture toughness of Vectran fibre composites

A relatively large fracture energy was calculated from the translaminar fracture toughness characterisation of Vectran/MTM57 composites. It was found that the energy dissipation due to fibre pull-out significantly contribute to the fracture toughness of Vectran/MTM57. This is evidenced by multiple long fibrils observed on the fractured surface, along with shear cusps on the side of the fibres indicating the occurrence of interfacial shear during fibre pull-out. Furthermore, the 'skin-core' nature of the fibre results in a further toughening mechanism upon fibre failure initiating at the skin (due to the improved microstructure at the skin resulting in a high tensile stiffness and low tensile strain) which then progress inwards to the core. Further tensile loading from this point results in an improvement in the fibre's chain orientation resulting in an additional energy absorbing mechanism. The reliability of the obtained G_c was validated using a developed FEM UMAT under transverse dynamic loading, where an excellent correlation was found with regards to the load-time/deflection histories under LVI, as well as impact and residual velocities under HVI.

The modifed Compact Tension (CT) specimen, initially developed by Katafiasz et al. [70] was utilised in this study due to the low compressive and shear properties of the composite, hence mitigating any undesirable failure such as buckling or compressive failures. Initial analysis was performed in LS-Dyna explicit and further developed to achieve the thickness in which undesirable failures could be prevented. Post-test radiographic images of Vectran/MTM57 specimens have also confirmed the absence of irreversible damage such as buckling or compressive failures. The use of the CT specimen has also resulted in a low scatter values which provides a reliable dataset for future use in the FEM modelling.

8.2.3 Impact performance of composite materials

Investigation of the impact performance of the composite materials considered in this study was detailed in Chapter 5. Under LVI, superior impact performance was observed for S2-Glass/MTM57 laminates whilst under HVI, Vectran/MTM57 offers the best ballistic protection compared to IM7/8552 and S2-Glass/MTM57 composites at the same

unit mass. IM7/8552 was observed to perform poorly under both impact types (LVI and HVI).

S2-Glass/MTM57 laminates under LVI have a superior performance for a number of reasons. First, the high tensile strain-to-failure, allows the laminate to be more compliant in absorbing energy by way of flexural deformation. The relatively low $\pm 45^\circ$ in-plane shear properties are also important in allowing the laminate to deform by way of flexure thus enabling more energy to be absorbed. Secondly, the NCF architecture enhances the impact performance by improving the IFT properties particularly in Mode II, due to the shear dominance under LVI loading. This is demonstrated by the minimal amount of delamination when compared to IM7/8552, which possesses a UD architecture. Although Vectran/MTM57 is ranked second in the LVI performance, its response is comparable to that of S2-Glass/MTM57, evidenced by the average normalised energy absorption, presented in subsection 5.54. In addition, the high fibre fracture energy for Vectran/MTM57 (G_{Ic}=260 kJ/m^2 [68]) further enhances its impact performance by absorbing a large impact energy, compared to IM7/8552 (G_{Ic}=147.2 kJ/m^2 [169]) and S2-Glass/MTM57 (G_{Ic}=154.2 kJ/m^2 [70]).

Under HVI, a larger deformation was observed for all composites, particularly for Vectran/MTM57. This was due to the low $\pm 45^\circ$ in-plane shear properties (both stiffness and strength), allowing the composite to further deform to delay projectile penetration. The Back Face Deflection (BFD) was found to be the largest for Vectran/MTM57, whilst the smallest for IM7/8552 laminates. Apart from the large tensile strain-to-failure and higher fibre fracture energy for Vectran/MTM57, the sensitivity to strain-rate effects, particularly for Vectran/MTM57 under the tensile and $\pm 45^\circ$ in-plane shear failure modes further enhance its impact resistance in the high velocity regimes.

All of the commonly observed damage types under LVI and HVI loadings was found in the composites used in this study, such as matrix cracking, delamination, and fibre failure. Particularly for Vectran/MTM57, permanent indentation can be seen in non-penetrating impact energies, especially under the LVI loading. Delamination damage was considerably reduced for S2-Glass/MTM57 and Vectran/MTM57 under LVI loadings, largely due to the effect of stitches in the NCF architecture. However, the inter-

laminar enhancement from the NCF architecture has no influence under HVI loadings, resulting in a more severe delamination failure. For Vectran/MTM57, laminates were found to split into two halves when impacted close to its V_{50}, indicating a significant energy absorption from delamination.

8.2.4 Development of a plane-stress material model for Vectran/MTM57

Chapter 6 focuses on the development of an energy-based damage model for Vectran/epoxy composite. The damage model was based on previous works by Iannucci et al. [88, 204, 205] on thin laminated carbon and glass fibre composites. The constitutive equations were modified to accommodate the non-linearity observed in its tensile stress-strain response, as well as its $\pm 45^\circ$ in-plane shear behaviour. It was found that the UMAT was able to accurately predict the quasi-static in-plane response of Vectran/MTM57, particularly under its tensile stress-strain behaviour, despite the use of a single secant modulus in the constitutive equations. Excellent agreement was also observed in the $\pm 45^\circ$ in-plane shear response of the composite.

However, inaccuracies exist in the local transverse and longitudinal strain after a global shear strain value of approximately 20%. Although this has a small influence in the global shear response, the numerical prediction on the damaged model yields a small difference in the width of the deformed gauge region when compared to the experimental results by approximately 2 mm. This difference was due to the formulation not considering the effects of fibre rotation (scissoring effects) since the local element direction (fibre direction) was kept at a constant 90° relative to each other throughout the analysis. In addition, specific formulations which accounts for the fibre alignment and the angle of rotation should be employed to include the effects of fibre rotation. Under compression, a similar response to the tensile component was incorporated. Upon reaching the 'yield' strength, incompressibility was imposed where the stress was held constant with increasing strain, simulating an elastic-perfectly plastic response. While this assumption was found to be adequate to represent its general behaviour (as well as the composite's behaviour under impact loading), improvements can be made to simulate the strain-hardening response of the composite, therefore obtaining similar response to

the experimental observations.

The use of a secant modulus to represent the tensile and compressive modulus of the composite can also be improved by implementing the physically based two (or three) tier model which is associated with the 'skin-core' structure of Vectran's fibre. One approach is to use Kelvin's viscoelastic model [218] which incorporates two springs and one dashpot two represent the constitutive equation.

8.2.5 Numerical modelling of impact loading

Finally, Chapter 7 focuses on the numerical modelling of all composite materials under LVI and HVI loadings using LS-Dyna explicit. It was found that MAT262, was able to adequately represent the behaviour of IM7/8552 and S2-Glass/MTM57 under impact loads, though with a few drawbacks. First, for non-penetrating energies under LVI loadings, an underestimation can be observed in the load-deflection history, particularly for S2-Glass/MTM57. Secondly, strain-rate effects were only incorporated in the $\pm 45^\circ$ in-plane shear component. While no pronounced strain-rate sensitivity was indicated for IM7/8552 [88], considerable strain-rate effects on S2-Glass/MTM57 was reported under the tensile and compressive modes [71, 211–213].Therefore, the mechanical properties related to the tensile and compressive failure modes needs to be manually adjusted as a constant material input.

The impact response predicted by the UMAT were in close agreement with the experimental results, especially the load-time histories under LVI loadings. However, an underestimation was observed in the load-deflection histories (particularly under the 40 J and 100 J energy levels), due to the absence of through-thickness stress definitions, particularly the transverse shear stress. Therefore, a full 3D formulation is suggested to address this issue which will further improve the accuracy of the model. Under HVI loadings, a slight underestimation was observed in the UMAT prediction due to a number of reasons. First, the energy dissipation due to various failure mechanisms were considerably underpredicted by the FEM model. This is particularly true for delamination failure, where the laminate was observed to split into two halves when impacted close to its V_{50}, whilst an underestimation of at least 50% was found in the

EFM model. In addition, no ply-splitting was predicted by the UMAT, since this requires explicit plies to be defined in the FEM model, as well as th e use of cohesive algorithms to define the intra-laminar interactions. Also, a coupling between the $\pm 45^\circ$ in-plane shear and compressive behaviour should be defined to capture the damage seen on the laminate front face under HVI. This is because the low in-plane shear properties (both stiffness and strength) of Vectran/MTM57 often results in a shear deformation past the non-linear threshold, causing irreversible damage in the matrix. Therefore, the compressive strength was greatly reduced causing compressive damage propagation which extends to the laminate boundaries, as seen in Figure 7.51b.

The use of the bi-linear energy-based cohesive algorithm in predicting delamination damage may be inadequate to represent the interlaminar behaviour of S2-Glass/MTM57 and Vectran/MTM57. This was largely due to the NCF architecture, as well as the fibre-bridging effects which acts as as toughening mechanism for both composite materials. The simplified bi-linear law in the formulation of the cohesive algorithm results in a considerable underprediction of the delaminated area. While this approach is effective for UD based architecture possessing minimal effects of fibre-bridging (such as IM7/8552), the use of a bi-linear cohesive algorithm may not be suitable for NCF based architecture, particularly for fibrillar-based fibres such as Vectran. Thus, the use of advanced cohesive algorithms such as the multi-linear softening model may be more appropriate to represent the delamination behaviour for S2-Glass/MTM57 and Vectran/MTM57 composites.

Chapter 9

Conclusion and Future Work

9.1 Introduction

The increasing use of high performance fibre composites in the aerospace and defence industries highlights a need for further research to improve their performance, particularly under impact loads. It is important to design structures which not only perform well under impact, but possess desirable characteristics under structural loading. For example, the poor compressive properties of Vectran fibre composites limits its application as a structural material, in spite of the excellent performance under impact conditions - unlike carbon fibre composites, which have superior structural properties. This calls for an alternative approach such as hybridization, to harness the superior qualities of both aforementioned materials, yielding a composite which performs well under impact and possesses excellent compressive properties to be used as a structural material.

9.2 Conclusion

A summary of the main outcomes from the research are as follows:

i. The quasi-static in-plane characterisation shows a typical linear elastic behaviour for IM7/8552 and S2-Glass/MTM57 under tensile, and compressive loading. Under the $\pm 45^\circ$ in-plane shear loading, all materials exhibited a non-linearity in terms of strain hardening due to the initial fibre-matrix damage and the subsequent fibre rotation. It was found that Vectran/MTM57 possesses the lowest shear

strength and modulus, which partly explains the superior performance under impact loading. A non-linear behaviour was exhibited by Vectran/MTM57 under tensile and compressive loading due to the difference in the 'skin-core' structure - the skin is attributed to high crystallinity and very high fibre orientation whilst the core is less oriented and amorphous in nature. Hence, when loaded in tension, failure will initiate at the skin first, which propagate inwards to the core, which then re-orients itself enabling further energy absorption. However, when loaded in compression, the weak (van der Waals) bond results in an almost instant failure of the composite, which defibrillates exhibiting a non-linear strain-hardening seen in the compressive stress-strain response;

ii. Characterisation of the interlaminar fracture toughness was only performed on S2-Glass/MTM57 and Vectran/MTM57 composite since a large amount of literature exists for IM7/8552. The fibrillar nature of Vectran fibres provided a significant toughening mechanism by way of fibre-bridging in both Modes I and II. More importantly, the presence of stitches in the NCF architecture enhances the Interlaminar Fracture Toughness (IFT) of both composites by demanding a higher fracture energy to further propagate the crack, since the stitch acts as a crack arrestor, diverting the path of crack parallel to the stitch orientation;

iii. The modifed Compact Tension (CT) specimen was able to successfully mitigate any undesirable failures which could invalidate the test. A relatively high fracture toughness was found for Vectran/MTM57 when compared to IM7/8552 and S2-Glass/MTM57, with considerable evidence of fibre pull-out observed on the fracture surface, with observations of shear cusps on the fibre side. It can be concluded that fibre pull-out is the main energy contribution to the fracture energy, in addition to the energy contribution from interfacial debonding and fibre fracture;

iv. Experimental investigation on the impact behaviour of composite laminates showed superior impact performance for the S2-Glass/MTM57 and Vectran/MTM57 under both LVI and HVI loading. Furthermore, under HVI loading, Vectran/MTM57 showed a markedly superior response due to the large Back Face Deflection (BFD) when compared to IM7/8552 and S2-Glass/MTM57 composites. This was also evi-

denced by the large impactor travel in the load-deflection response under LVI loadings. In addition, minimal delamination was observed for both S2-Glass/MTM57 and Vectran/MTM57 under LVI loadings due to the enhancement provided by the NCF architecture. A considerable permanent indentation (with minimal fibre failure on the laminate) was seen for Vectran/MTM57 especially at the 100 J energy level, due the low transverse shear properties of the composite. For S2-Glass/MTM57 and IM7/8552 laminates, a finite amount of "permanent indentation" was observed on the laminate front face under LVI, with considerable fibre failure at the laminate back face;

v. The numerical model developed for Vectran/MTM57 was seen to be able to closely simulate the experimental response of the laminate, despite the simplifications performed in the constitutive equations. However, a drawback of this modelling strategy is the need to have essential data with regards to the fracture energy of each relevant modes. This would mean additional testing to be performed so as to obtain the required information. The smeared methodology implemented in the numerical model is only suitable for use with structured quadrilateral mesh since no modifications were made on the element shape functions. Concerning the FEM prediction on damage, it was observed under that under LVI loading, damage was comparable to the experimental results. However, under HVI, the numerical prediction was unable to capture the propagation of compressive damage as observed in Figure 7.51;

vi. Apart from the drawbacks discussed previously concerning the UMAT, the numerical model has successfully simulated the impact response of Vectran/MTM57 laminates up to a considerable accuracy. This is an important achievement which provides users with a simplified approach to model polymer fibre composites, especially for fibres which display a non-linear behaviour under tensile and compressive loads, such as Vectran fibre composites. MAT262 was found to be able to accurately simulate the impact response of IM7/8552 and S2-Glass/MTM57, although a significant underestimation was observed on the load-deflection histories, particularly for S2-Glass/MTM57. The effects of strain-rate particularly for

S2-Glass/MTM57 was not included since MAT262 does not include any strain-rate effects in the tensile and compressive modes. Hence, the effects of strain-rate was manually included as a constant value in the material inputs depending on the level of impact energy.

9.3 Future work

The work presented in this thesis has indicate a number of direction for future work. These include:

i. In this research, the results and findings obtained from the material characterisation activities has been presented and clearly discussed. However, it is strongly encouraged that future characterisation Vectran fibre based composites are performed on a UD based architecture, since this could provide the actual properties in a lamina without the influence from the NCF architecture, such as stitches. Further, the effects of strain-rate could be investigated in the relevant loading regime. This is important since it would provide important information for use in numerical simulations involving high strain-rate applications;

ii. Additional studies on translaminar fracture behaviour of Vectran fibre composites is encouraged particularly on the effects of specimen dependence or laminate lay-up on the R-curve behaviour. Further investigation on the influence of temperature on the tensile properties of Vectran fibres would be useful to understand its failure mechanism, since intermolecular friction due to chain slippage in the 'core' region of the fibre structure is likely to increase the local fibre temperature. Thus, the local tensile strength of the fibres would be slightly decreased, resulting in a decrease in the composite fracture toughness;

iii. Although the newly developed material model can successfully predict the response of Vectran fibre composites, a full 3D implementation is highly encouraged. Focus should also be directed to consider the material response under compressive loadings, particularly the kink-band effects observed in Vectran fibre composites. Investigations on the strain-rate effects of Vectran composites (or Vectran fibre)

would also benefit the numerical model. The compression-shear coupling proposed will also enhance the constitutive model to capture the effects arising from the low shear strength (and modulus), as well as the inherently poor compressive properties. The use of advanced cohesive algorithms such as the multi-linear softening model may further improve the predictions due to the extensive fibre-bridging effects observed on the interlaminar properties;

iv. Further research could also be performed using different impactor/projectile dimension and shapes, as well as different projectile velocities. In addition, the use of composite structures in space related applications calls for an extensive research in the hypervelocity impact regime. This would benefit the aeronautical industry, since any improvements made could be used in commercial aircraft to enhance impact resistance to threats such as hail ice and bird strikes;

9.4 Potential application of Vectran fibres

Apart from investigating the impact response of high performance fibre composites, this research has been focused on characterising and understanding the behaviour of Vectran fibre composites. Therefore, a number of potential applications can be highlighted. These include:

i. Vectran fibre composites could be incorporated as part of ballistic protection systems such as vehicle armours, replacing polymer based composites such as Dyneema, due to its higher compressive properties, melting temperature, and creep performance [219];

ii. Vectran fibres could be used as Z-pins or through-the-thickness stitch to enhance delamination toughness due to the ability of the fibre to absorb large amounts of energy when compared to other fibre types such as carbon or glass;

iii. The use of Vectran fibres along with fibres possessing excellent compressive properties such as carbon in a hybrid composite system could result in a superior structural component with an enhanced impact performance;

iv. Vectran could also be used with other polymer fibres such as Aramid or Spectra to produce an improved 'hybrid' fibre by way of braiding thus achieving enhanced tensile properties (both strength and modulus), as well as an improved impact resistance.

Bibliography

[1] W. G. Roeseler, B. Sarh, and M. U. Kismarton. Composite Structures: The first 100 years. In *16th International Conference on Composite Materials*, 2007.

[2] S. Nguyen, E. S. Greenhalgh, R. Olsson, L. Iannucci, and Curtis P. T. Modelling the Lofting of Runaway Debris by Aircraft Tires. *Journal of Aircraft*, 45(5):1701–1714, 2008.

[3] S. Nguyen, E. S. Greenhalgh, J. M. R. Graham, and A. Francis. Runway debris impact threat maps for transport aircraft. *The Aeronautical Journal*, 118(1201):229–266, 2014.

[4] N. Dennis and D. Lyle. Bird strike damage & windshield bird strike. Final report, ATKINS, 2009. [Accessed 10 October 2018].

[5] R. Hedayati and M. Sadighi. *Bird Strike - An Experimental, Theoretical, and Numerical Investigation*. Woodhead Publishing, 2015.

[6] R. Juntikka and R. Olsson. Experimental and modelling study of hail impact on composite plates. In *17th International Conference on Composite Materials*, 2009.

[7] H. Kim, D. A. Welch, and K. T. Kedward. Experimental investigation of high velocity ice impacts on woven carbon/epoxy composite panels. *Composites Part A: Applied Science and Manufacturing*, 34(1):25–41, 2003.

[8] G. Hellard. Composites in airbus: A long story of innovations and experiences. Sevilla, Spain, 2008. EADS Global Investors Forum.

[9] Y. Swolfs, L. Gorbatikh, and I. Verpoest. Fibre hybridisation in polymer composites: A review. *Composites Part A: Applied Science and Manufacturing*, 67:181–200, 2014.

[10] E. S. Greenhalgh. *Fibre-dominated failures of polymer composites.* Woodhead Publishing Limited and CRC Press LLC, Cambridge, England, 2009.

[11] G. A. O. Davies and R. Olsson. Impact on composite structures. *The Aeronautical Journal*, 108(1089):541–563, 2004.

[12] M. O. W. Richardson and W. J. Wisheart. Review of low-velocity impact properties of composite materials. *Composites Part A: Applied Science and Manufacturing*, 27(12):1123–1131, 1996.

[13] D. Roylance. Ballistics of transversely impacted fibers. *Textile Research Journal*, 47(10):679–684, 1977.

[14] P. Maimi, P. P. Camanho, J. A. Mayugo, and C. G. Davila. A continuum damage model for composite laminates: Part I - Constitutive model. *Mechanics of Materials*, 39(10):897–908, 2007.

[15] P. Maimi, P. P. Camanho, J. A. Mayugo, and C. G. Davila. A continuum damage model for composite laminates: Part II - Computational implementation and validation. *Mechanics of Materials*, 39(10):909–919, 2007.

[16] K. Karthikeyan, B.P. Russell, N.A. Fleck, H.N.G. Wadley, and V.S. Deshpande. The effect of shear strength on the ballistic response of laminated composite plates. *European Journal of Mechanics A/Solids*, 42:35–53, 2013.

[17] S. Agrawal, K. K. Singh, and P. K. Sarkar. Impact damage on fibre reinforced polymer matrix composite - A review. *Journal of Composite Materials*, 48(3):313–332, 2014.

[18] S. Abrate. Impact on laminated composite materials. *Applied Mechanics Review*, 44(4):155–190, 1991.

[19] S. Abrate. Impact on laminated composite materials: Recent advances. *Applied Mechanics Review*, 47(11):517–544, 1991.

[20] S. Abrate. *Impact on Composite Structures*. Cambridge University Press, 1998.

[21] U. K. Vaidya. Impact response of laminated and sandwich composites. In S. Abrate, editor, *Impact Engineering of Composite Structures*. SpringerWien-NewYork, 2011.

[22] V. V. Silberschmidt, editor. *Dynamic Deformation, Damage and Fracture in Composite Materials and Structures*. Woodhead Publishing, 2016.

[23] W. J. Cantwell and J. Morton. The impact resistance of composite materials: A review. *Composites*, 22(5):347–362, 1991.

[24] G. A. Schoeppner and S. Abrate. Delamination threshold loads for low velocity impact on composite laminates. *Composites Part A: Applied Science and Manufacturing*, 31:903–915, 2000.

[25] R. Olsson, M. V. Donadon, and B. G. Falzon. Delamination threshold load for dynamic impact on plates. *International Journal of Solids and Structures*, 43:3124–3141, 2006.

[26] P. O. Sjoblom, T. J. Hartness, and T. M. Cordell. On low-velocity impact testing of composite materials. *Journal of Composite Materials*, 22:30–52, 1988.

[27] P. Robinson and G. A. O. Davies. Impactor mass and specimen geometry effects in low velocity impact of laminated composites. *International Journal of Impact Engineering*, 12(2):189–207, 1992.

[28] E. W. Godwin and G. A. O. Davies. *Impact Behaviour of Thermoplastic Composites*. Springer, Edinburgh, Scotland, 1988.

[29] K. S. Pandya, L. Dharmane, J. R. Pothnis, G. Ravikumar, and N. K. Naik. Stress wave attenuation in composites during ballistic impact. *Polymer Testing*, 31(2):261–266, 2008.

[30] P.M. Cuniff. Dimensionless parameters for optimization of textile-based body armor systems. In *18th International Symposium of Ballistics*, pages 1303–1310, 1999.

[31] W.J. Cantwell and J. Morton. Comparison of the low and high velocity impact response of CFRP. *Composites*, 20(6):545–551, 1989.

[32] R. Olsson. Analytical prediction of large mass impact damage in composite laminates. *Composites Part A: Applied Science and Manufacturing*, 32(9):1207–1215, 2001.

[33] J. M. Berthelot. Transverse cracking and delamination in cross-ply glass-fibre and carbon-fibre reinforced plastic laminates: Static and fatigue loading. *Applied Mechanics Reviews*, 56(2):111–147, 2003.

[34] S. Puck and H. Schurmann. Failure analysis of FRP laminates by means of physically based phenomenological models. *Composites Science and Technology*, 58(7):1045–1067, 1998.

[35] K. V. Williams, R. Vaziri, and A. Poursartip. A physically based continuum damage mechanics model for thin laminated composite structures. *International Journal of Solids and Structures*, 40(9):2267–2300, 2003.

[36] W. J. Cantwell and J. Morton. Detection of impact damage in CFRP laminates. *Composite Structures*, 3(3-4):241–257, 1985.

[37] C. H. Jih. Prediction of delamination in composite laminates subjected to low velocity impact. *Journal of Composite Materials*, 27(7):684–701, 1993.

[38] M. de Freitas, A. Silva, and L. Reis. Numerical evaluation of failure mechanisms on composite specimens subjected to impact loading. *Composites Part B: Engineering*, 31(3):199–207, 2000.

[39] C. Bouvet, B. Castanie, M. Bizeul, and J. J. Barrau. Low velocity impact modelling in laminate composite panels with discrete interface elements. *International Journal of Solids and Structures*, 46(14-15):2809–2821, 2009.

[40] S. M. Garcia-Rodriguez, J. Costa, A. Bardera, V. Singery, and D. Trias. A 3d tomographic investigation to elucidate the low-velocity impact resistance, tolerance, and damage sequence of thin non-crimp fabric laminates: effect of ply-thickness. *Composites Part A: Applied Science and Manufacturing*, 31(3):53–65, 2000.

[41] G. Zhou. Prediction of impact damage thresholds of glass fibre reinforced laminates. *Composites Structures*, 31(3):185–193, 1995.

[42] T-W. Shyr and Y-H. Pan. Impact resistance and damage characteristics of composite laminates. *Composite Structures*, 62(2):193–203, 2003.

[43] B. Liaw and F. Delale. Hybrid carbon-glass fibre/toughened epoxy thick composite joints subjected to drop weight and ballistic impacts. Final report, U.S. Army Research Office, 2007. [Accessed 20 October 2018].

[44] V. Crupi, G. Epasto, and E. Guglielmino. Internal damage investigation of composites subjected to low-velocity impact. *Experimental Techniques*, 40(2):555–568, 2016.

[45] G. A. O. Daview and P. Robinson. Predicting failure by debonding/delamination. In *AGARD 74th Structures and Materials Meeting Debonding/Delamination of Composites*, 1992.

[46] R. Olsson. Analytical model for delamination growth during small mass impact on plates. *International Journal of Solids and Structures*, 47(2010):2884–2892, 2010.

[47] D. Liu. Impact-induced delamination - A view of bending stiffness mismatching. *Journal of Composite Materials*, 22(7):674–692, 1988.

[48] M. R. Wisnom. The role of delamination in failure of fibre-reinforced composites. *Philosophical Transactions of the Royal Society A*, 370:1850–1870, 2012.

[49] N. K. Naik and P. Shrirao. Composite structures under ballistic impact. *Composites Structures*, 66(1-4):579–590, 2004.

[50] N. S. N. Shaktivesh, Ch. V. Sesha-Kumar, and Naik. N. K. Ballistic impact performance of composite targets. *Materials and Design*, 51:833–846, 2013.

[51] N. K. Naik, P. Shrirao, and B. C. K. Reddy. Ballistic impact behaviour of woven fabric composites: Parametric studies. *Materials Science and Engineering: A*, 412:104–116, 2005.

[52] T. Mitrevski, I. H. Marshall, R. Thomson, R. Jones, and B. Whittingham. The effect of impactor shape on the impact response of composite laminates. *Composite Structures*, 67(2):139–148, 2005.

[53] T. Mitrevski, I. H. Marshall, and R. Thomson. The influence of impactor shape on the damage to composite laminates. *Composite Structures*, 76(1-2):116–122, 2006.

[54] G. Dorey. Impact damage in composites - Development, consequences, and prevention. In *Proceedings of the 6th International Conference on Composite Materials (ICCM-6) and the 2nd European Conference on Composite Materials (ECCM-2)*, 1987.

[55] W. J. Cantwell and J. Morton. Geometrical effects in the low velocity impact response of CFRP. *Composite Structures*, 12(1):39–59, 1989.

[56] G. Caprino and V. Lopresto. On the penetration energy for fibre-reinforced plastics under low-velocity impact conditions. *Composites Science and Technology*, 61(1):65–73, 2001.

[57] B. Liaw and F. Delale. Highly instrumented static, dynamic, and impact testing of high performance materials. Phd thesis, Department of Aeronautics, Imperial College London, 2013. [Accessed 20 October 2018].

[58] Hexcel. Hextow IM7 Carbon Fibre. Technical datasheet, Hexcel, 2018. [Accessed 20 October 2018].

[59] Kuraray America. Vectran: Liquid Crystal Technology. Technical report, Kuraray, 2006. [Accessed 20 October 2018].

[60] AGY. High Strength Glass Fibres. Technical datasheet, AGY, 2006. [Accessed 20 October 2018].

[61] S. Heimbs, T. Wagner, J. T. V. Lozoya, B. Hoenisch, and F. Franke. Comparison of impact behaviour of glass, carbon, and dyneema composites. *Proceedings of the Institution of Mechanical Engineers. Part C: Journal of Mechanical Engineering Science*, pages 1–16, 2018.

[62] T. S. Reddy, P. R. S. Reddy, and V. Madhu. Response of e-glass/epoxy and dyneema composite laminates subjected to low and high velocity impact. *Procedia Engineering*, 173:278–285, 2017.

[63] M. K. Hazzard, S. Hallett, P. T. Curtis, L. Iannucci, and R. S. Trask. Effect of fibre orientation on the low velocity impact response of thin dyneema composite laminates. *International Journal of Impact Engineering*, 100:35–45, 2017.

[64] K. Karthikeyan, S. Kazemahvazi, and B.P. Russell. Optimal fibre architecture of soft-matrix ballistic laminates. *International Journal of Impact Engineering*, 88:227–237, 2016.

[65] R. Park and J. Jang. Impact behaviour of aramid fibre/glass fibre hybrid composites: The effect of stacking sequence. *Polymer Composites*, 22(1):80–89, 2004.

[66] R.S. Sikarwar, R. Velmurugan, and N.K. Gupta. Effect of velocity and fibres on impact performance of composite laminates - analytical and experimental approach. *International Journal of Crashworthiness*, 22(6):589–601, 2017.

[67] C. Evci and M. Gulgec. An experimental investigation on the impact response of composite materials. *International Journal of Impact Engineering*, 43:40–51, 2012.

[68] S. I. B. Syed Abdullah, L. Iannucci, and E.S. Greenhalgh. On the translaminar fracture toughness of Vectran/epoxy composite material. *Composite Structures*, 202:566–577, 2018.

[69] M.J. Laffan, S.T. Pinho, P. Robinson, and A.J. Mcmillan. Translaminar fracture toughness of composites: A review. *Polymer Testing*, 31(3):481–489, 2012.

[70] T.J. Katafiasz, L. Iannicci, and E.S. Greenhalgh. Development of a novel compact tension specimen to mitigate premature compression and buckling failure modes within fibre hybrid composites. *Composite Structures*, 207:93–107, 2019.

[71] V. Singh. Literature survey of strain rate effects on composites. Technical report, Swerea SICOMP, 2018. [Accessed 20 October 2018].

[72] Y. Wang and Y. M. Xia. The effects of strain rate on the mechanical behaviour of kevlar fibre bundle: An experimental and theoretical study. *Composites Part A: Applied Science and Manufacturing*, 29(11):1411–1415, 1998.

[73] V. B. C. Tan, X. S. Zeng, and V. P. W. Shim. Characterization and constitutive modelling of Aramid fibres at high strain rates. *International Journal of Impact Engineering*, 35(11):1303–1313, 2008.

[74] A. C. P. Koh, V. P. W. Shim, and V. B. C. Tan. Dynamic behaviour of UHMWPE yarns and addressing impendance mismatch effects of specimen clamps. *International Journal of Impact Engineering*, 37(3):324–332, 2010.

[75] A. Donald, A. Windle, and S. Hanna. *Liquid Crystal Polymers as Structural Materials*. Cambridge University Press, Cambridge, England, 2006.

[76] R. Park and J. Jang. Impact behaviour of aramid fibre/glass fibre hybrid composite: Evaluation of a four-layer hybrid composites. *Journal of Materials Science*, 36(9):2359–2367, 2001.

[77] A.K. Bandaru, S. Ahmad, and N. Bhatnagar. Ballistic performance of hybrid thermoplastic composite armors reinforced with kevlar and basalt fabrics. *Composites Part A: Applied Science and Manufacturing*, 97:151–165, 2017.

[78] L. Iannucci. Design of composite ballistic protection systems. In C. H. Zweben and P. W. R. Beaumont, editors, *Comprehensive Composite Materials II*, chapter 8, pages 308–331. Elsevier, 2018.

[79] L. M. Kachanov. Rupture time under creep conditions. *International Journal of Fracture*, 97(1-4):11–18, 1999.

[80] Y. N. rabotnov. Creep rupture. In *Proceedings of the XII International Congress on Applied Mechanics*, 1969.

[81] F-K. Chang and K-Y. Chang. A progressive damage model for laminated composites containing stress concentrations. *Journal of Composite Materials*, 21(9):834–855, 1987.

[82] S. W. Tsai and E. M. Wu. A general theory of strength for anisotropic materials. *Journal of Composite Materials*, 5(1):58–80, 1971.

[83] Z. Hashin. Failure criteria for unidirectional fibre composites. *Journal of Applied Mechanics*, 47(2):329–334, 1980.

[84] P. Ladeveze and E. LeDantec. Damage modelling of the elementary ply for laminated composites. *Composites Science and Technology*, 43(3):257–267, 1992.

[85] A. Matzenmiller, J. Lubliner, and R.L. Taylor. A constitutive model for anisotropic damage in fiber-composites. *Mechanics of Materials*, 20(2):125–152, 1995.

[86] K. V. Williams and R. Vaziri. Application of a damage mechanics model for predicting the impact response of composite materials. *Computers and Structures*, 79(10):997–1011, 2001.

[87] L. Iannucci, R. Dechaene, M. Willows, and J. Degrieck. A failure model for the analysis of thin woven glass composite structures under impact loadings. *Computers and Structures*, 79(8):785–799, 2001.

[88] L. Iannucci and J. Ankersen. An energy based damage model for thin laminated composites. *Composites Science and Technology*, 66(7-8):934–951, 2006.

[89] L. Iannucci and M. Willows. An energy based damage mechanics approach to modelling impact onto woven composite materials - Part I: Numerical models. *Computers: Part A*, 37(11):2041–2056, 2006.

[90] L. Iannucci and M. Willows. An energy based damage mechanics approach to modelling impact onto woven composite materials - Part II: Experimental and numerical results. *Computers: Part A*, 38(2):540–554, 2007.

[91] L. Iannucci, D. J. Pope, and M. Dalzell. A constitutive model for dyneema ud composites. In *Proceedings of the 17th International Conference on Composite Materials (ICCM17)*, 2009.

[92] C. G. Davila, C. A. Rose, and P. P. Camanho. A procedure for superimposing linear cohesive laws to represent multiple damage mechanisms in the fracture of composites. *International Journal of Fracture*, 158(2):211–223, 2009.

[93] Z.P. Bažant and B.H. Oh. Crack band theory for fracture of concrete. *Materiaux et Construction*, 16(3):155–177, 1983.

[94] G. A. O. Davies and X. Zhang. Impact damage prediction in carbon composite structures. *International Journal of Impact Engineering*, 16(1):149–170, 1995.

[95] S. T. Pinho. Modelling failure of laminated composites using physically-based failure models. Phd thesis, Department of Aeronautics, Imperial College London, 2005. [Accessed 9 September 2018].

[96] F. Ehrich. Low velocity impact on psre-loaded composite structures. Phd thesis, Department of Aeronautics, Imperial College London, 2013. [Accessed 20 October 2018].

[97] J. Oliver. A consistent characteristic length for smeared cracking models. *International Journal for Numerical Methods in Engineering*, 28(2):461–474, 1989.

[98] M.V. Donadon, L. Iannucci, B.G. Falzon, J.M. Hodgkinson, and S.F.M. de Almeida. A progressive failure model for composite laminates subjected to low velocity impact damage. *Computers and Structures*, 86(11):1232–1252, 2008.

[99] M. V. Donadon and L. Iannucci. An objectivity algorithm for strain softening materials. In *Proceedings of the 9th International LS-DYNA users conference*, 2006.

[100] L. Raimondo, L. Iannucci, P. Robinson, and P.T. Curtis. A progressive failure model for mesh-size-independent FE analysis of composite laminates subject to low-velocity impact damage. *Composites Science and Technology*, 72(5):624–632, 2012.

[101] C. Bouvet, S. Rivallant, and J. J. Barrau. Low velocity impact modelling in composite laminates capturing permanent indentation. *Composites Science and Technology*, 72(16):1977–1988, 2012.

[102] C. Bouvet, S. Rivallant, and J. J. Barrau. Failure analysis of CFRP laminates subjected to compression after impact: FE simulation using discrete interface elements. *Composites Part A: Applied Science and Manufacturing*, 55:83–93, 2013.

[103] C. S. Lopes, S. Sadaba, C. Gonzalez, J. Llorca, and P. P. Camanho. Physically-sound simulation of low-velocity impact on fibre reinforced laminates. *International Journal of Impact Engineering*, 92:3–17, 2016.

[104] J. Llorca, C. Gonzalez, J. M. Molina-Aldareguia, J. Segurado, R. Seltzer, F. Sket, M. Rodriguez, S. Sadaba, R. Munoz, and L. P. Canal. Multiscale modelling of composite materials: A roadmap towards virtual testing. *Advanced Materials*, 23:5130–5147, 2011.

[105] B. B. Liao, H. C. Tan, J. W. Zhou, and L. Y. Jia. Multiscale modelling of dynamic progressive failure in composite laminates subjected to low velocity impact. *Thin-Walled Structures*, 23:695–707, 2011.

[106] K. K. Jin, Y. Huang, Y. H. Lee, and S. K. Ha. Distribution of micro stresses and interfacial tractions in unidirectional composites. *Journal of Composite Materials*, 42(18):1825–1849, 2008.

[107] H. Kim, D. Whisler, Chen. Z. M., C. Bisagni, M. Kawai, and D. Krueger, editors. *Multiscale modelling strategy for low-velocity impact on FRP*, San Diego, California, 2014. American Society for Composites (ASC).

[108] S. Dai and P. R. Cunningham. Multi-scale damage modelling of 3D woven composites under uni-axial tension. *Composite Structures*, 142:298–312, 2016.

[109] C. C. Chamis. Simplified composite micromechanics equation for hygral thermal and mechanical properties. Technical memorandum, Lewis Research Center, National Aeronautics and Space Administration (NASA), 1983. [Accessed 20 October 2018].

[110] R. Bogenfeld, J. Kreikemeier, and T. Wille. Review and benchmark study on the analysis of low-velocity impact on composite laminates. *Engineering Failure Analysis*, 86:72–99, 2018.

[111] A. Tabiei and W. Zhang. Composite laminate delamination simulation and experiment: A review of recent development. *Applied Mechanics Review*, 70(3):1–23, 2018.

[112] R. Krueger. Virtual crack closure technique: History, approach, and applications. *Applied Mechanics Review*, 57(2004):109–143.

[113] B. Y. Chen, S. T. Pinho, N. V. De Carvalho, P. M. Baiz, and T. E. Tay. A floating node method for the modelling of discontinuities in composites. *Engineering Fracture Mechanics*, 127:104–134, 2014.

[114] D. S. Dugdale. Yielding of steel sheets containing slits. *Journal of the Mechanics and Physics of Solids*, 8(2):100–104, 1960.

[115] G. I. Barenblatt. The formation of equilibrium cracks during brittle fracture. general ideas and hypothesis. axially-symmetric cracks. *Journal of Applied Mathematics and Mechanics*, 23(3):622–636, 1959.

[116] Y. Mi, M. A. Crisfield, and G. A. O. Davies. Progressive delamination using interface elements. *Journal of Composite Materials*, 32(14):1246–1272, 1998.

[117] P. W. Harper and S. R. Hallett. Cohesive zone length in numerical simulations of composite delaminations. *Engineering Fracture Mechanics*, 75(16):4774–4792, 2008.

[118] A. Turon, C. G. Davila, P. P. Camanho, and J. Costa. An engineering solution for mesh size effects in the simulation of delamination using cohesize zone models. *Engineering Fracture Mechanics*, 74:1665–1682, 2007.

[119] R. Gutkin, M.L. Laffan, S.T. Pinho, P. Robinson, and P.T. Curtis. Modelling the R-curve effect and its specimen-dependence. *International Journal of Solids and Structures*, 48(11-12):1767–1777, 2011.

[120] B. F. Sorenson and T. K. Jacobsen. Large-scale bridging in composites: R-curves and bridging laws. *Composites Part A: Applied Science and Manufacturing*, 29(11):1443–1451, 1998.

[121] B.J. Briscoe and D.R. Williams. Interlaminar fracture toughness of aramid/epoxy laminates. *Composites Science and Technology*, 46(3):277–286, 1993.

[122] S. Hashemi, A. J. Kinloch, and J. M. Williams. The analysis of interlaminar fracture in uniaxial fibre-polymer composites. *Proceedings of the Royal Society A*, 427(1872):173–199, 1990.

[123] A.C. Garg. Delamination - A damage mode in composite structures. *Engineering Fracture Mechanics*, 29(5):557–584, 1988.

[124] L. Iannucci. Dynamic delamination modelling using interface elements. *Computers and Structures*, 84(15-16):1029–1048, 2006.

[125] S. T. Pinho, L. Iannucci, and P. Robinson. Formulation and implementation of decohesion elements in an explicit finite element code. *Composites Part A: Applied Science and Manufacturing*, 37(5):778–789, 2006.

[126] P. P. Camanho, Davila. C. G., and M. F. deMoura. Numerical simulation of mixed-mode progressive delamination in composite materials. *Journal of Composite Materials*, 27(16):1415–1438, 2003.

[127] V. Q. Bui, L. Iannucci, P. Robinson, and S. T. Pinho. A coupled mixed-mode delamination model for laminated composites. *Journal of Composite Materials*, 45(16):1717–1729, 2011.

[128] M. M. Shokrieh, Z. Daneshjoo, and M. Fakoor. A modified model for simulation of Mode I delamination growth in laminated composite materials. *Theoretical and Applied Fracture Mechanics*, 82:107–116, 2016.

[129] M. Heidari-Rarani, M. M. Shokrieh, and P. P. Camanho. Finite element modelling of Mode I delamination growth in laminated DCB specimens with R-curve effects. *Composites Part B: Engineering*, 45(1):897–903, 2013.

[130] M. L. Benzeggagh and M. Kenane. Measurement of mixed-mode delamination fracture toughness of unidirectional glass-epoxy composites with mixed mode bending apparatus. *Composite Science and Technology*, 56(4):439–449, 1996.

[131] J. R. Reeder. An evaluation of mixed-mode delamination failure criteria. Technical memorandum, NASA Langley Research Center, 1992. [Accessed 20 October 2018].

[132] M F. S. F. de Moura, J. P. M. Goncalves, and F. G. A. Silva. A new energy based mixed-mode cohesive zone model. *International Journal of Solids and Structures*, 102-103:112–119, 2016.

[133] N.V. De Carvalho, B. Y. Chen, S. T. Pinho, J. G. Ratcliffe, P. M. Baiz, and T. E. Tay. Modeiing delamination migration in cross-ply tape laminates. *Composites Part A: Applied Science and Manufacturing*, 71:192–203, 2015.

[134] Y. Shi, C. Pinna, and C. Soutis. Interface cohesive elements to model matrix crack evolution in composite laminates. *Applied Composite Materials*, 21:57–70, 2014.

[135] D. Kumar, R. Roy, J. H. Kweon, and J. H. Choi. Numerical modelling of combined matrix cracking and delamination in composite laminates using cohesive elements. *Applied Composite Materials*, 23(3):397–419, 2016.

[136] T. J. Katafiasz. Hybridization of Carbon and Glass Fibre Composites for Automotive Applications. Phd thesis, Department of Aeronautics, Imperial College London, 2018. [Accessed 1 November 2018].

[137] ASTM D3039/D3039M-17. Standard Test Method for Tensile Properties of Polymer Matrix Composite Materials. ASTM International, West Conshohocken, PA, 2017, https://doi.org/10.1520/D3039_D3039M-17.

[138] F. L. Matthews. *Compression*. Woodhead Publishing, Cambridge, England, 2000.

[139] ASTM D3410/D3410M-16. Standard Test Method for Compressive Properties of Polymer Matrix Composite Materials with Unsupported Gage Section by Shear Loading. ASTM International, West Conshohocken, PA, 2016, https://doi.org/10.1520/D3410_D3410M-16.

[140] ASTM D3518/D3518M-13. Standard Test Method for In-Plane Shear Response of Polymer Matrix Composite Materials by Tensile Test of a ±45° Laminate. ASTM International, West Conshohocken, PA, 2013, https://doi.org/10.1520/D3518_D3518M-13.

[141] Hexcel Corporation. Hexply 8552: Epoxy matrix. Technical datasheet, Hexcel, 2016. [Accessed 20 October 2018].

[142] Cytec Industrial Materials. MTM57 Series. Technical datasheet, Cytec, 2012. [Accessed 20 October 2018].

[143] A. R. Bunsell, editor. *Handbook of tensile properties of textile and technical fibres.* Woodhead Publishing, 2009.

[144] K. Naito. Tensile properties and weibull modulus of some high-performance polymeric fibres. *Journal of Applied Polymer Science*, 128(2):1185–1192, 2013.

[145] A. Pegoretti, A. Zanolli, and C. Migliaresi. Preparation and tensile mechanical properties of unidirectional liquid crystal single-polymer composites. *Composites Science and Technology*, 66(213):1970–1979, 2006.

[146] L. C. Sawyer and M. Jaffe. The structure of thermotropic copolyesters. *Journal of Materials Science*, 21:1897–1913, 1986.

[147] L. C. Sawyer, R. T. Chen, M. G. Jamieson, I. H. Musselman, and P. E. Russell. The fibrillar hierarchy in liquid crystalline polymers. *Journal of Materials Science*, 28(1):225–238, 1993.

[148] K.K.V. Bhagwat. Testing of high performance fibres. Master's dissertation, Department of Aeronautics, Imperial College London, 2016. [Accessed 9 September 2018].

[149] M. G. Dobb, D. J. Johnson, and B. P. Saville. Compressional behaviour of Kevlar fibres. *Polymer*, 22(7):960–965, 1981.

[150] J. H. Greenwood and P. G. Rose. Compressive behaviour of Kevlar 49 fibres and composites. *Journal of Materials Science*, 9:1809–1814, 1974.

[151] S. Yamini and R. J. Young. The mechanical properties of epoxy resins: Part 1 - mechanisms of plastic deformation. *Journal of Materials Science*, 15:1814–1822, 1980.

[152] M. C. Waterbury and L. T. Drzal. Determination of fibre volume fractions by optical numeric volume fraction analysis. *Journal of Reinforced Plastics and Composites*, 8:627–636, 1989.

[153] M. T. Cann, D. O. Adams, and C. L. Schneider. Characterization of fibre volume fraction gradients in composite laminates. *Journal of Composite Materials*, 42:447–466, 2009.

[154] P. T. Curtis. CRAG (Composite Research Advisory Group) test methods for the measurement of the engineering properties of fibre reinforced plastics. Final Report, Defence Technical Information center, 1988.

[155] ASTM D3171-15. Standard Test Methods for Constituent Content of Composite Materials. ASTM International, West Conshohocken, PA, 2015, https://doi.org/10.1520/D3171-15.

[156] A. Szekrenyes. Overview on the experimental investigations of the fracture toughness in composite materials. *Hungarian Electronic Journal fro Sciences, Mechanical Engineering and Transport Section (2002)*, (MET-020507-A):1–19, 2002.

[157] P. Hansen and R. Martin. DCB, 4ENF, and MMB delamination characterisation of S2/8552 and IM7/8552. Technical report, United States Army, European Research Office, 1999. [Accessed 20 October 2018].

[158] M.W. Czabaj and J.G. Ratcliffe. Comparison of intralaminar and interlaminar Mode I fracture toughnesses of unidirectional IM7/8552 carbon/epoxy composite. *Composites Science and Technology*, 89:15–23, 2013.

[159] S. Psarras. Investigating failure in composite stiffener run-outs. Phd thesis, Department of Aeronautics, Imperial College London, 2013. [Accessed 9 September 2018].

[160] ASTM D5528. Standard Test Method or Mode I Interlaminar Fracture Toughness of Unidirectional Fibre-Reinforced Polymer Matrix Composites. ASTM International, West Conshohocken, PA, 2013, https://doi.org/10.1520/D5528-13.

[161] P. Robinson and J. M. Hodgkinson. *Interlaminar Fracture Toughness*. Woodhead Publishing, Cambridge, England, 2000.

[162] R. H. Martin and B. D. Davidson. Mode II fracture toughness evaluation using four point bend, end notched flexure test. *Plastics, Rubber, and Composites*, 28(8):401–406, 1999.

[163] G. Dietmar and T. Seelig. *Linear Elastic Fracture Mechanics*. Springer, Darmstadt, Germany, 2006.

[164] P. Davies, P. Casari, and L.A. Carlsson. Influence of fibre volume fraction on Mode II interlaminar fracture toughness of glass/epoxy using the 4ENF specimen. *Composites Science and Technology*, 65(2):295–300, 2005.

[165] B. D. Schuecker, C.; Davidson. Effect of friction on the perceived Mode II delamination toughness from three and four-point bend end-notched flexure tests. *ASTM Publications*, pages 334–344, 2001.

[166] J. Kalantar and L.T. Drzak. The bonding mechanism of Aramid fibres to epoxy matrices. Part 1: A review of the literature. *Journal of Materials Science*, 25(10):4186–4193, 1990.

[167] D. Hull and T.W Clyne. *Toughness of composites*. Cambridge University Press, Cambridge, England, 1996.

[168] T. Bru, P. Hellstrom, R. Gutkin, D. Ramantani, and P. Goran. Characterisation of the mechanical and fracture properties of a uni-weave carbon fibre/epoxy non-crimp fabric composite. *Data in Brief*, 6:680–695, 2016.

[169] M.J. Laffan, S.T. Pinho, P. Robinson, and L. Iannucci. Measurement of the in situ ply fracture toughness associated with the mode I fibre tensile failure in FRP. Part I: Data reduction. *Composites Science and Technology*, 70:606–613, 2010.

[170] S.T. Pinho, L. Iannucci, and P. Robinson. Fracture toughness of the tensile and compressive fibre modes in laminated composites. *Composites Science and Technology*, 66(13):2069–2079, 2006.

[171] G. Catalanotti, P.P. Camanho, G. Xavier, C.G. Davila, and A.T. Marques. Measurement of resistance curves in the longitudinal failure of composites using digital image correlation. *Composites Science and Technology*, 70(13):1986–1993, 2010.

[172] N. Blanco, D. Trias, S. T. Pinho, and P. Robinson. Intralminar fracture toughness characterisation of woven composite laminates. part I: Design and analysis of a compact tension (CT) specimen. *Engineering Fracture Mechanics*, 131:349–360, 2014.

[173] R.F. Teixeira, S.T. Pinho, and P. Robinson. Translaminar ply fracture toughness of advanced composites. In *18th International Conference on Composite Materials*, 2011.

[174] Livermore Software Technology Corporation (LSTC). LS-Dyna Theory Manual. Software manual, LSTC, 2006. [Accessed 20 October 2018].

[175] Livermore Software Technology Corporation (LSTC). LS-Dyna Manual Volume II. Software manual, LSTC, 2018. [Accessed 20 October 2018].

[176] Livermore Software Technology Corporation (LSTC). LS-Dyna Manual Volume I. Software manual, LSTC, 2018. [Accessed 20 October 2018].

[177] ASTM E399-17. Standard Test Method for Linear-Elastic Plane-Strain Fracture Toughness K_{Ic} of Metallic Materials. ASTM International, West Conshohocken, PA, 2017, https://doi.org/10.1520/E0399-17.

[178] D. Porter, J. Guan, and F. Vollrath. Spider silk: Super material or thin fibre. *Advanced Materials*, 25(9):1275–1279, 2013.

[179] S. Pimenta and S. T. Pinho. An analytical model for the fracture toughness of fibre composites with stochastic quasi-fractal fracture surfaces. *Journal of the Mechanics and Physics of Solids*, 66:78–102, 2014.

[180] J.K. Kim and Y.W. Mai. High strength, high fracture toughness fibre composites with interface control - a review. *Composites Science and Technology*, 41:333–378, 1991.

[181] Y.W. Mai and F. Castino. Fracture toughness of Kevlar-epoxy composites with controlled interfacial bonding. *Journal of Material Science*, 19:1638–1655, 1984.

[182] A. Kelly and W.R. Tyson. Tensile properties of fibre-reinforced metals: Copper/tungsten and copper/molybdenum. *Journal of the mechanics and physics of solids*, 13(6):329–338, 1965.

[183] Dupont. Kevlar Aramid fibres Technical Guide. Technical data, Dupont, 2018. [Accessed 20 October 2018].

[184] J. Zeng and N. Netravali. Tensile properties of fibre-reinforced metals: Copper/tungsten and copper/molybdenum. *Journal of Adhesion Science and Technology*, 20(5):387–409, 2012.

[185] Ticona. vectra liquid crystal polymer. Technical datasheet, Ticona, 2001. [Accessed 10 November 2018].

[186] D. E. Beers and J. E. Ramirez. Vectran high performance fibre. *The Journal of The Textile Institute*, 81(4):561–574, 1990.

[187] ASTM D7136/D7136M-15. Standard Test Method for Measuring the Damage Resistance of a Fiber-Reinforced Polymer Matrix Composite to a Drop-Weight Impact Event. ASTM International, West Conshohocken, PA, 2015, https://doi.org/10.1520/D7136_D7136M-15.

[188] E. B. Zaretsky. *Light Gas Gun.* Springer International Publishing, Switzerland, 2016.

[189] N.K. Bourne. A 50 mm bore gas gun for dynamic loading of materials and structures. *Measurement Science and Technology*, 14:273–278, 2003.

[190] A.E. Siegel. The theory of high speed guns. Final report, United States Naval Ordnance Laboratory, 1965. [Accessed 20 October 2018].

[191] E.A. Ferriter, I.A. McCulloh, and W. deRosset. Techniques used to estimate limit velocity in ballistics testing with small sample size. Final report, United States Military Academy, 1965. [Accessed 20 October 2018].

[192] J.D. Walker. Ballistic limit of fabric with resin. In *19th International Symposium of Ballistics*, pages 1239–1246, 2001.

[193] L. Sorrentino, C. Bellini, A. Corrado, W. Polini, and Aricò. Ballistics performance evaluation of composite laminates in kevlar 29. *Procedia Engineering*, 88:255–262, 2014.

[194] J.P. Lambert and G.H.. Jonas. Towards standardization in terminal ballistics testing: Velocity representation. Technical report, US Ballistics Research Laboratories, 1976. [Accessed 20 October 2018].

[195] R.F. Recht and T.W. Ipson. Ballistics perforation dynamics. *Journal of Applied Mechanics*, 30(3):384–390, 1963.

[196] M. R. O'Masta, D. H. Crayton, V. S. Deshpande, and H. N. G. Wadley. Mechanisms of penetration in polyethylene reinforced cross-ply laminates. *International Journal of Impact Engineering*, 86:249–264, 2015.

[197] E. S. Greenhalgh, V. M. Bloodworth, L. Iannucci, and D. Pope. Fractographic observations of Dyneema composites under ballistic impact. *Composites Part A: Applied Science and Manufacturing*, 44(1):51–62, 2013.

[198] B. A. Cheeseman and T. A. Bogetti. Ballistic impact into fabric and compliant composite laminates. *Composite Structures*, 61(1-2):161–173, 2003.

[199] C. Wang, X. Ji, A. Roy, V. V. Silberschmidt, and Z. Chen. Shear strength and fracture toughness of carbon fibre/epoxy interface: effect of surface treatment. *Materials & Design*, 85:800–807, 2015.

[200] A. Godara, L. Gorbatikh, G. Kalinka, A. Warrier, O. Rochez, L. Mezzo, F. Luizi, A. W. van Vuure, S. V. Lomov, and I. Verpoest. Interfacial shear strength of a glass fiber/epoxy bonding in composites modified with carbon nanotubes. *Composites Science and Technology*, 70(9):1346–1352, 2010.

[201] M. Cheng, W. Chen, and T. Weerassoriya. Mechanical properties of Kevlar KM2 single fibre. *Journal of Engineering Materials and Technology*, 127(2):197–203, 2005.

[202] S. Sockalingam, R. Bremble, J. W. Gillisepie Jr., and M. Keefe. Transverse compression behaviour of Kevlar KM2 single fibre. *Composites Part A: Applied Science and Manufacturing*, 81:271–281, 2016.

[203] P. Maimi, J.A. Mayugo, and P.P. Camanho. A three-dimensional damage model for transversely isotropic composite laminates. *Journal of Composite Materials*, 42(25):2717–2745, 2008.

[204] L. Iannucci and M.L. Willows. An energy based damage mechanics approach to modelling impact onto woven composite materials - Part I: Numerical models. *Composites: Part A*, 37(11):2041–2056, 2006.

[205] L. Iannucci and M.L. Willows. An energy based damage mechanics approach to modelling impact onto woven composite materials - Part II: Experimental and numerical results. *Composites: Part A*, 38(2):540–554, 2007.

[206] S. Murakami. *Material Damage and Continuum Damage Mechanics*. Springer, Netherlands, 2012.

[207] R. Edmunds and N. A. Wadee. On kink banding inidvidual PPTA fibres. *Composites Science and Technology*, 65(7-8):1284–1298, 2005.

[208] M. A. Wadee, G. W. Hunt, and M. A. Peletier. Kink band instability in layered. *Journal of the Mechanics and Physics of Solids*, 52(5):1071–1091, 2004.

[209] M. V. Donadon, S. F. M. de Almeida, M. A. Arbelo, and A. R. de Faria. A three-dimensional ply failure model for composite structures. *International Journal of Aerospace Engineering*, pages 1071–1091, 2009.

[210] P. Potluri, P. Hogg, M. Arshad, D. Jetavat, and P. Jamshidi. Influence of fibre architecture on impact damage tolerance in 3D woven composites. *Applied Composite Materials*, 19(5):799–812, 2012.

[211] S. Gurusideswar, N. Srinivasan, R. Velmurugan, and N. K. Gupta. Tensile response of Epoxy and S2-Glass/Epoxy composites at low and medium strain rate regimes. *Procedia Engineering*, 173:686–693, 2017.

[212] J. Harding and L. Welsh. Effect of strain rate on the tensile failure of woven reinforced polyester resin composites. *Journal de Physique Colloques*, 46:405–414, 1985.

[213] I. M. Daniel and T. Liber. Strain rate effects on mechanical properties of fibre composites. Technical report, National Aeronautics and Space Administration (NASA), 1976. [Accessed 20 October 2018].

[214] D. Zhu, B. Mobasher, J. Erni, S. Bansal, and S. D. Rajan. Strain rate and gauge length effects on tensile behaviour of Kevlar 49 single yarn. *Composites Part A: Applied Science and Manfacturing*, 43(11):2021–2029, 2012.

[215] S. C. Woo and T. W. Kim. High strain rate impact in kevlar-woven composites and fracture analysis using acoustic emission. *Composites Part B: Engineering*, 60:125–136, 2014.

[216] Y. Termonia. Effect of strain rate on the mechanical properties of composites with a weak fibre/matrix interface. *Journals of Materials Science*, 60:4878–4882, 2014.

[217] J. Koyanagi, S. Ogihara, H. Nakatani, T. Okabe, and S. Yoneyama. Mechanical properties of fibre/matrix interface in polymer matrix composites. *Advanced Composite Materials*, 23(5-6):551–570, 2014.

[218] S. P. C. Marques and G. J. Creus. *Computational Viscoelasticity*. Springer, 2012.

[219] Kuraray America Inc. Vectran liquid crystal polymer. Technical data, Kuraray Co. Ltd., 2006. [Accessed 20 October 2018].

Appendix A

New Sabot Stripper Design

It was found that the 50 mm calibre single stage gas gun could not be used to characterise the V_{50} of IM7/8552, S2-Glass/MTM57, and Vectran/MTM57, since low projectile velocities (to not penetrate the composite laminates) could not be achieved. Therefore, a steel sabot was utilised to reduce the projectile impact velocity. Consequently, a modified sabot catcher was designed to 'catch' the sabot upon reaching the muzzle of the gas gun. Figure A.2 illustrate a schematic of the final sabot catcher manufactured.

Initial design was made usign the relationship first proposed by Siegel [190] given by:

$$F = ma = P_0 A \left[1 - \frac{(\gamma - 1)v}{2c_0}\right]^{\frac{2\gamma}{(\gamma-1)}} \tag{A.1}$$

where γ is the adiabatic exponent of the gas (for air γ=1.4), c_0 is the sonic velocity (for air, C_0=342 m/s at 0°), v is the gas velocity travelling in the barrel, and P_0 is the initial gas pressure. Using Equation A.1, the impact velocity versus firing pressure relationship was established and presented in Figure A.1. Note that Figure A.1 also presents the velocity with different sabot materials.

Information obtained from Figure A.1 was used to select the spring type which would be installed on the modified sabot catcher, Figure A.2. This was achieved by utilising the principles of conservation of momentum (inelastic collision) between the sabot (and projectile) impacting the sabot catcher main frame, which then collided with the spring.

The use of the modified sabot catcher was observed to 'catch' the steel sabot safely,

without inducing any damage to the gun, but also reduces the amount of debris generated from impact if a brittle material is used, such as Polypropylene.This is an important aspect since the impacted (damaged) laminates should not be subjected to any further damage post-impact.

Figures A.3 to A.5 presents the main parts used in the modified sabot catcher.

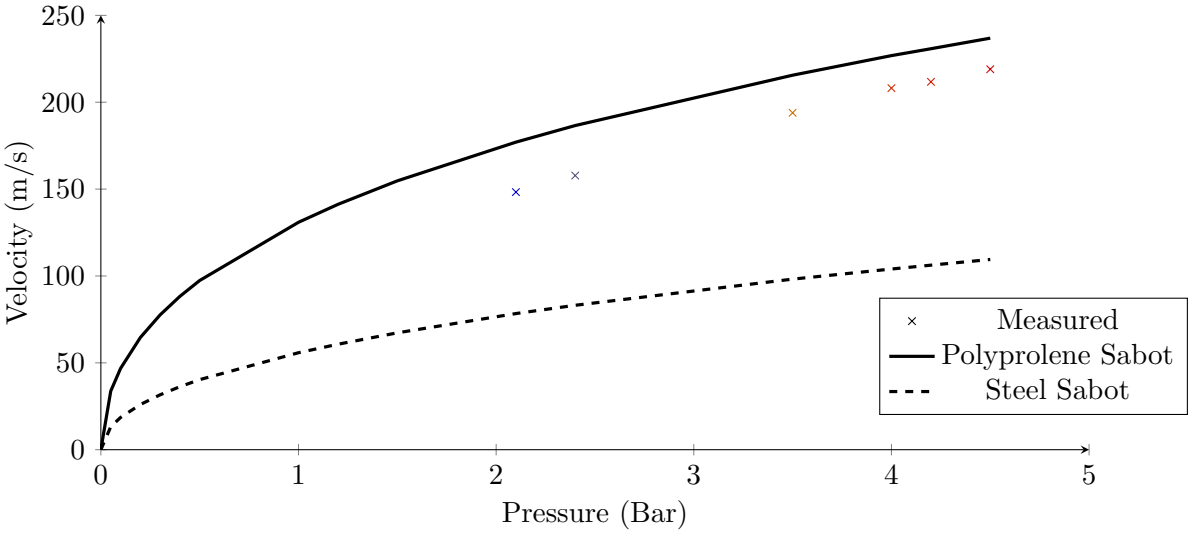


Figure A.1: Velocity-Pressure calibration curve. Note the change in velocity with respect to pressure with different sabot material

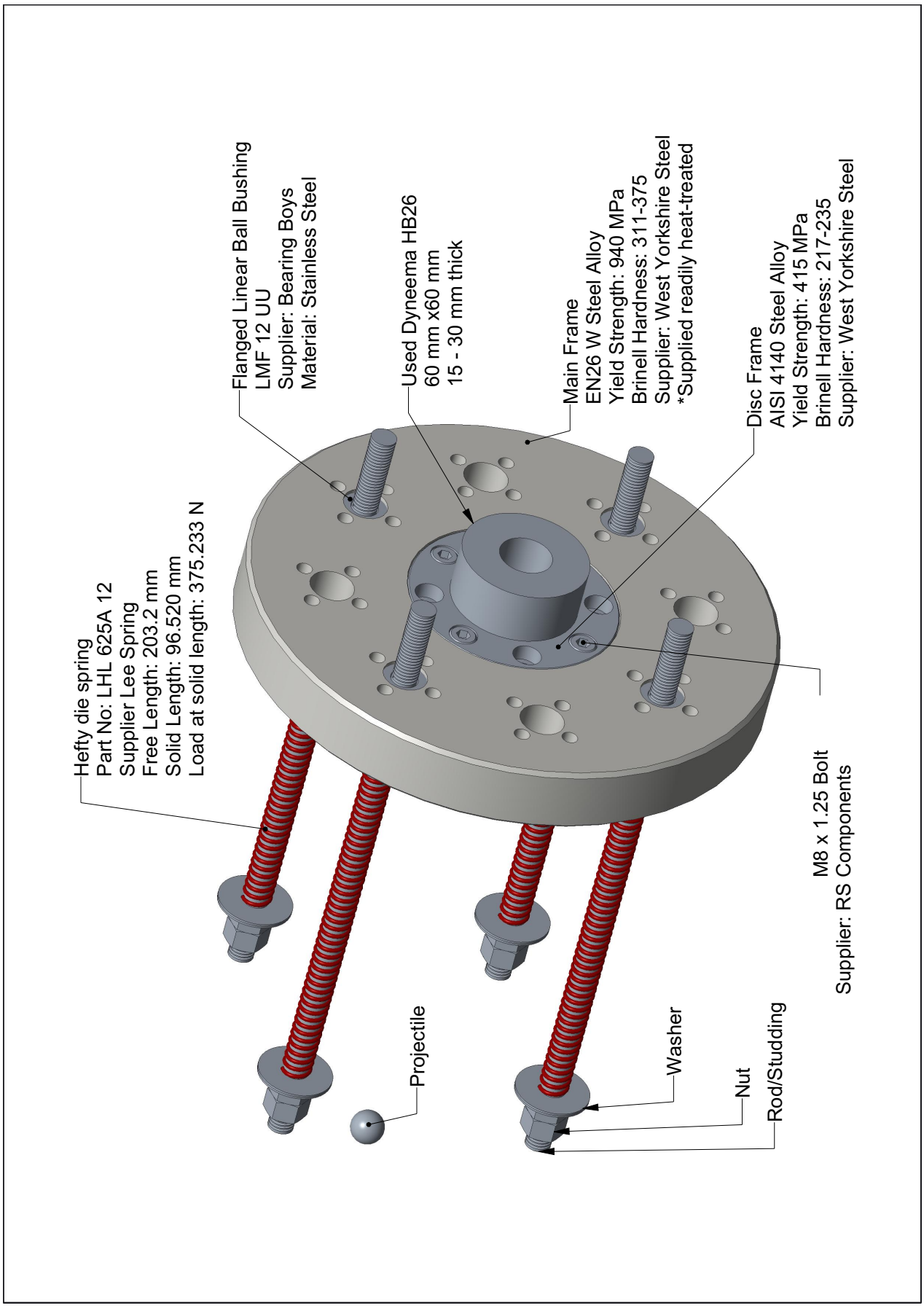


Figure A.2: Complete schematic of the modified sabot catcher

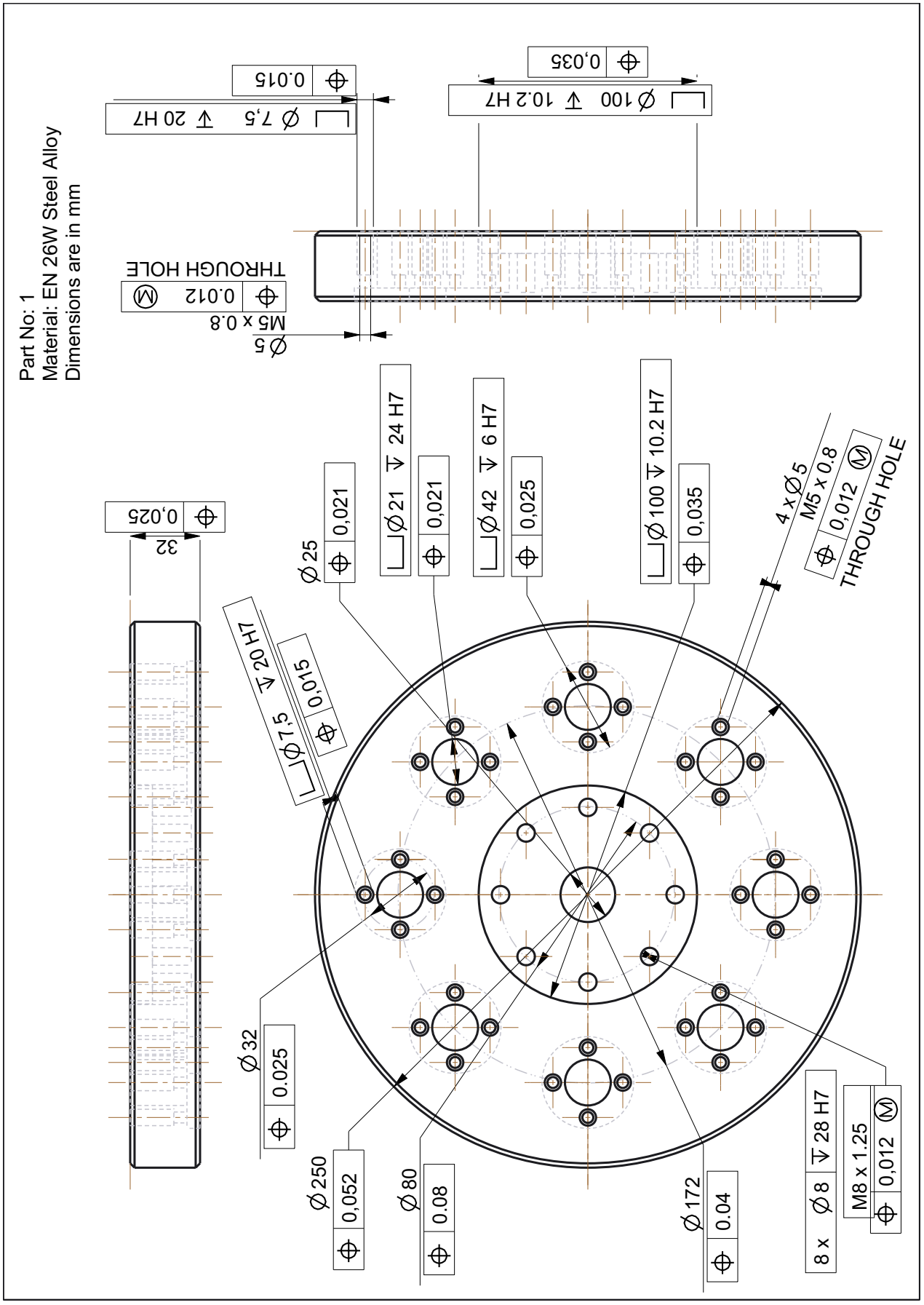


Figure A.3: Main Frame

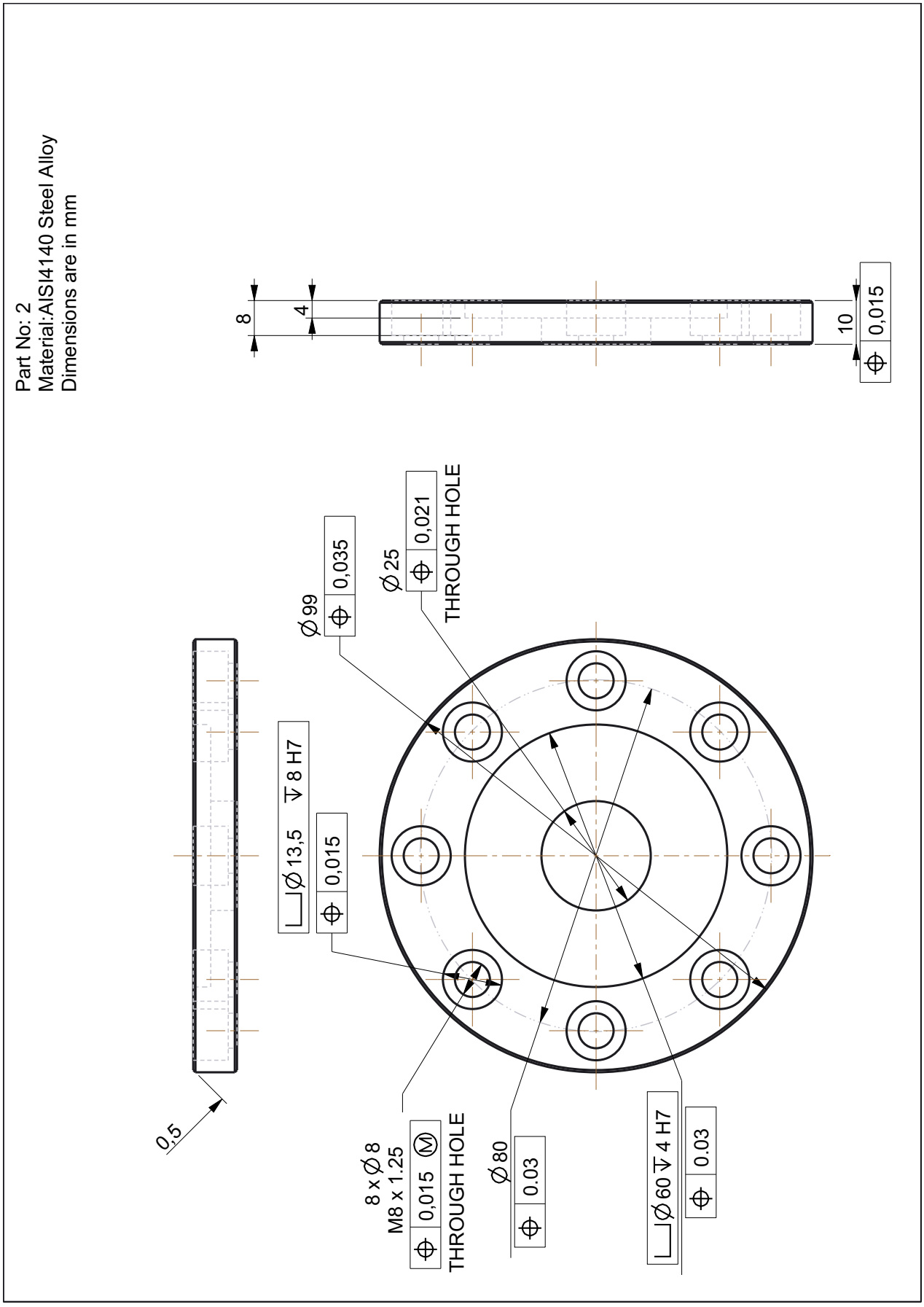


Figure A.4: Disc Frame

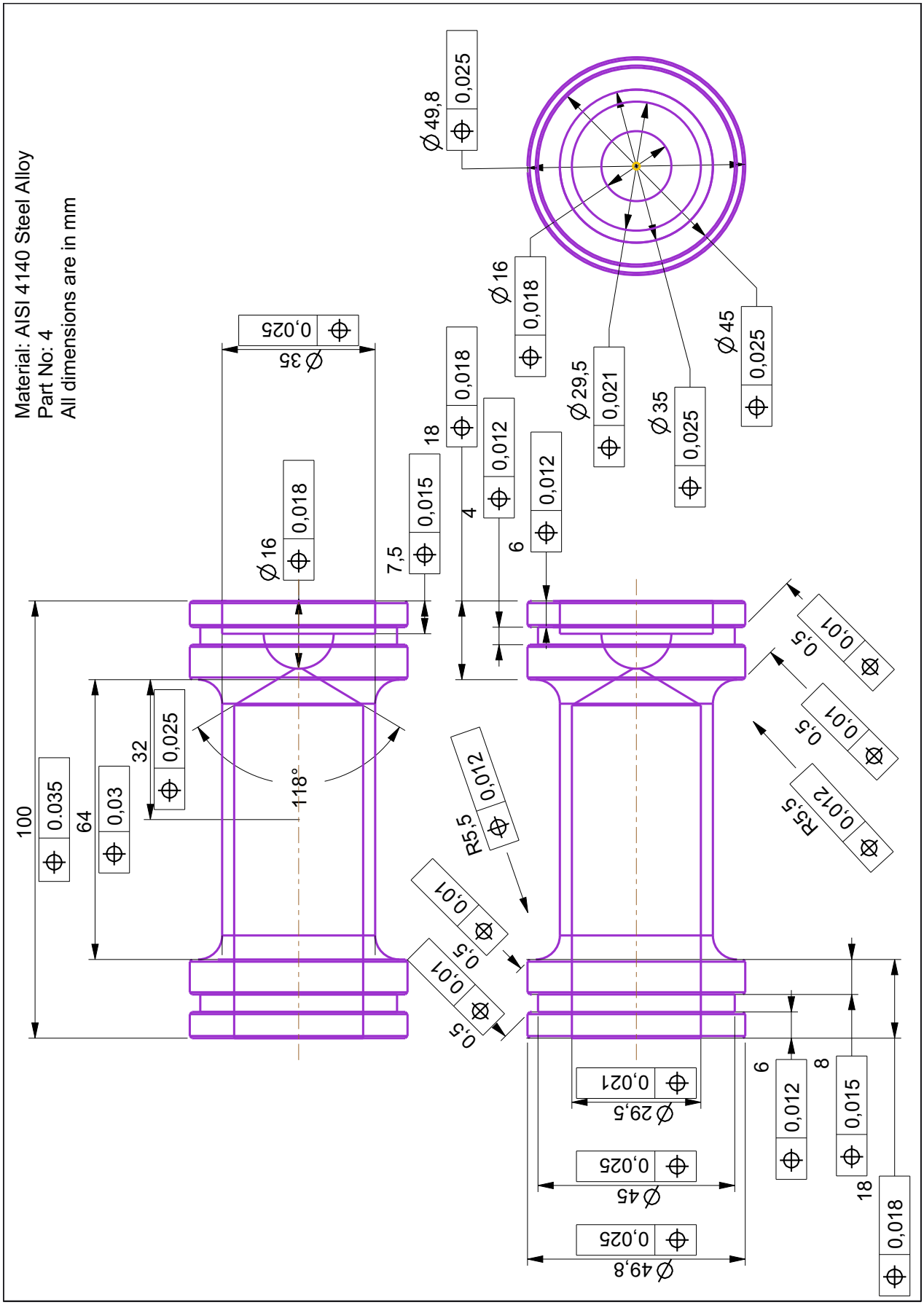


Figure A.5: Sabot

Appendix B

Analytical prediction on the ballistic limit

The selection of initial firing velocity, V_i, can either be calculated analytically, using existing analytical techniques [30, 192, 193], or numerically by performing FEM simulations. The latter approach is normally preferred due to the accuracy and relaibility of the results. However, numerical simulations can take excessive amount of CPU time, depending on the complexity of the analysis. Therefore, analytical techniques may be attractive if time is a constraint.

In this PhD, the approach proposed by Walker [192] was selected due to the simplicity of the technique. The author observed that dry fabrics of low areal density tend to have a better ballistic performance compared to a composite laminate having similar areal density. However, as the areal density of the laminate increases, its ballistic performance improves due to the enhancement in flexural stiffness. The author concluded that an increase in flexural stiffness will result in an enhancement in the laminate ballistic performance.

The ballistic limit for 100% dry fabric is given by [192]:

$$V_{bl} = \frac{9}{2}(1+\beta X)c_f\varepsilon_f\left\{\left(\frac{R_{bl}}{R_p}\right)^{2/3} - 2\left(\frac{R_{bl}}{R_p}\right)^{1/3} + 3\right\}^{-1} \tag{B.1}$$

where $\frac{R_{bl}}{R_p}$ is given by:

$$\frac{R_{bl}}{R_p} = \sqrt{\frac{9\pi}{8}\left(\frac{1}{X} + \beta\right)} \tag{B.2}$$

where X is the ratio of the armour areal density and projectile areal density; 0 indicates the resin mass fraction of the dry fabric (in this case, none), r is the resin mass fraction, c_f is the fibre wavespeed,ε_f is the fibre strain to failure, and β is a multiplier to give the area of fabric initially involved in this motion. In the current case, a value of β=2.56 was used, following Walker's experimental observation. It was found that the value yielded reasonable V_{50} values, as shown in Table B.1.

Table B.1: Ballistic limit predicted using Walker's relationship

Projectile diameter = 16 mm		
Composite	V_{bl}-Calculated	V_{bl} (m/s)-Experiment (m/s)
S2-Glass/MTM57	187.97	140.56
Vectran/MTM57	154.94	164.05
IM7/8552	119.39	96.67

Appendix C

Flowchart of LS-Dyna implementation

The flowchart shown in Figure C.1 illustrate the implemented flow of the developed UMAT into LS-Dyna explicit. The code employs an incremental Lagrangian formulation, with the time-step governed by the so-called, 'Courant' time step [176]. The size of each time step is controlled by the smallest element size, hence resulting in a conditionally-stable condition.

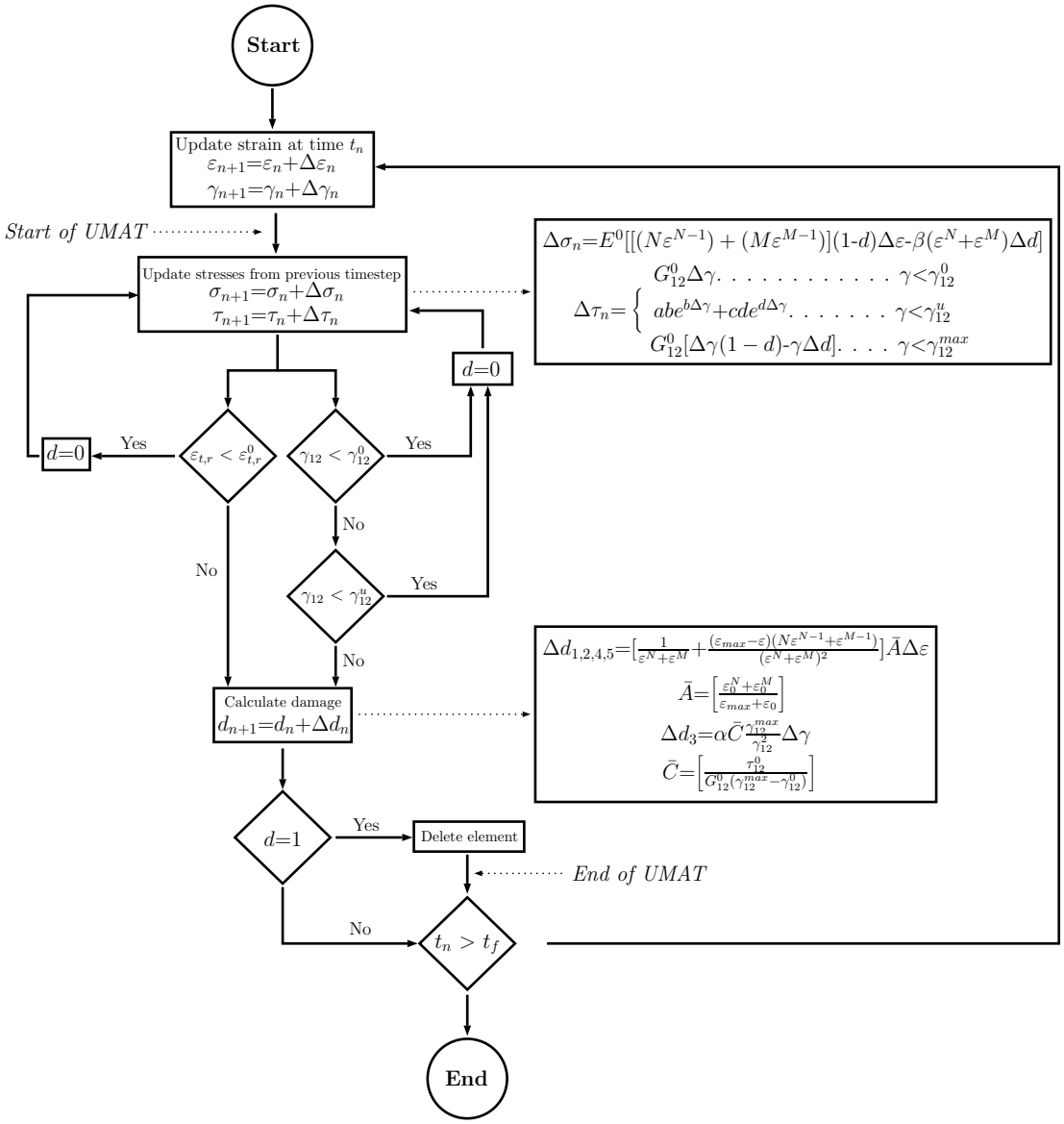


Figure C.1: Flowchart illustrating the implemented UMAT into LS-Dyna explicit. t_n represents the current time, t_f represents the termination (final) time, and $\varepsilon_{t,c}$ represents the strain under tension and compression, respectively

fcure